U.S. DEPARTMENT OF THE INTERIOR
U.S. GEOLOGICAL SURVEY

# Death Valley, California: Surface micro-relief statistics and radar scatterometer data

by

Gerald G. Schaber[1]
Graydon L. Berlin[1,2]

OPEN-FILE REPORT 93-272

Prepared for the National Aeronautics and Space Administration under NASA Contracts WO-8864 and W13,709

[1] 2255 N. Gemini Drive
Flagstaff, Arizona 86001

[2] Northern Arizona University
Flagstaff, Arizona, 86011

1993

# TABLE OF CONTENTS

## Prologue

Recently accelerated interest in terrestrial and planetary radar investigations has revealed the need for a better and more quantitative understanding of radar backscatter from large areas of natural terrain surfaces. Most early backscatter model investigations have had to rely heavily on mathematical models and have applied numerous approximations because of the nearly total lack of natural terrain micro-relief statistics and the unavailability of calibrated radar cross-section measurements (Rice, 1951; Beckmann and Spizzichino, 1966; Valenzuela, 1967, 1968; Moore, 1969; Barrick, 1970, 1972). Calibrated radar backscatter data have only recently become available using multiwavelength, polarimetric SAR sensors. Thus, a resurgence in studies related to radar backscatter modeling of natural surfaces has been encouraged (e.g., Schaber and others, 1980, 1986; Ulaby and others, 1981 Elachi, 1987; Engman and Wang, 1987; Sabins, 1987; van Zyl and others, 1987, 1991; Zebker and others, 1987; van Zyl, 1989, 1991; Campbell and others, 1989; Ulaby and Elachi, 1990; Avery and Berlin, 1992; Evans and others, 1992; Farr, 1992). Because a "true" mathematical description of all but the most unique ground surface appears out of the question, models are necessary to describe the radar return from natural surfaces (Moore, 1969). Thus, at present, the role of theory should be simply to aid us in interpreting these measurements, and to suggest how the empirical relationships may be extrapolated.

A detailed summary of the many methodologies and approaches used to model backscatter from natural terrains of various roughness scales and types is beyond the intent of this report. However, a brief summary of major models follows. Originally, the physical optics (or Kirchhoff-Huygens approach) and related tangent plane method provided the major theoretical tool and stemmed from use of the Helmholtz integral (e.g., Davies, 1954; Beckmann and Spizzichino, 1963; Hagfors, 1964; Semonov, 1966; Kodis, 1966; Barrick and Peake, 1967; Stogryn, 1967; Peake and Barrick, 1968; Blanchard and Rouse, 1980, and others).

In an attempt to incorporate depolarization effects, noted by experimental evidence, Rice (1951) introduced the small pertubation method as an incoherent solution which uses essentially the same method derived by Lord Rayleigh for acoustics. Various modifications of the pertubation method (e.g., the Bragg-Rice method) were then pursued in a theoretical manner by Peake (1959), Fung (1967, 1868) and Valenzuela (1967, 1968), among others. Models for composite surface roughness were introduced after it was realized that natural terrain surfaces simply cannot be described by any single theoretical model (e.g., Semenov, 1966; Fuks, 1966; Valenzuela, 1968; Barrick and Peake, 1968).

The physical mechanism of the interaction of radar waves with natural terrain surfaces today remains the most poorly known of the parameters necessary for empirical derivation of backscatter models. Peake and Barrick (1967) have reviewed the various theories for scattering from surfaces with different roughness scales (summary in Barrick and Peake, 1968). Experimental and theoretical modeling of the scattering of radar waves from large areas on the ocean surface using various modifications of the tangent plane, Bragg-Rice, and Rayleigh models has been considerably more successful than backscatter studies of natural terrain surfaces because of the systematic (mathematical) nature of sea-state waves and ripple roughness (Wright, 1966. 1968; Barrick, 1968; Daley, 1973; Valenzuela, 1974, 1978; Thompson and others, 1983; Brown and others, 1975).

What follows is a comprehensive documentation by the authors of the extensive database of surface micro-roughness statistics and radar scatterometer data acquired of the Death Valley saltpan and fan gravels between 1973 and 1983. The Death Valley saltpan and adjacent fan gravel surfaces were selected early as good radar backscatter test sites because of their diversity of surface roughness types and scales, and the general absence of vegetation. Problems subsequently recognized with the unique hydrology of the valley floor, in regard to radar backscatter modeling, are discussed below.

## INTRODUCTION

Death Valley, California, has long been a site for the comparison of a wide range of multispectral remote sensing data, including investigations of the correlations between radar backscatter and diverse types of micro-roughness (Schaber and others, 1976a,b; Dailey and others, 1978a,b, 1979). A resurgence in the interest in Death Valley within remote sensing communities has arisen as a result of the (1) availability of state-of-the-art airborne, multispectral (C-, L-, and P-bands) and fully polarimetric synthetic aperture radar (SAR) sensors, (2) selection of the Valley as a prime study site in NASA's recent Geologic Remote Sensing Field Experiment (GRSFE) (Evans and others, in press), and (3) use of the Valley as a major surface calibration site during the Third Shuttle Imaging Radar Experiment (SIR-C/X-SAR) (first mission - April, 1994)(Evans and others, 1993).

In this report, we make available radar scatterometer data, terrain microrelief, and surface electrical properties data that were acquired from Death Valley between 1973 and 1983 as part of a NASA Planetary Geology (PG) Program contract to the USGS to investigate radar backscatter from natural terrain surfaces. Part of this extensive dataset has been reformatted, tabulated and cross-correlated for this open-file report, but only a limited amount of interpretation of these data is provided here. It is our hope that these previously unpublished databases will provide information useful to the general remote sensing community in evaluating contemporary multispectral, polarimetric SAR, and other remote sensing and ground data collected from Death Valley as part of the GRSFE and SIR-C/X-SAR Missions. *To the knowledge of the authors, no natural terrain site has been so throughly documented for terrain micro-relief statistics over such a wide range of sampling intervals (3 mm to ~100 m) for the primary purpose of understanding radar backscatter.*

The saltpan and adjoining gravel fans within Death Valley National Monument were first considered as potentially useful sites for the correlation between radar backscatter and surface micro-topography following acquisition of experimental L-band (25-cm wavelength) SAR images of this region by the Jet Propulsion Laboratory in 1969 and 1970 (Schaber and others, 1976a) (Figs. 1, 2). Our initial geologic evaluation of these images, as well as earlier X-band (3-cm wavelength) SAR images obtained by the Goodyear Aerospace Corporation in 1964 (Schaber and others, 1976b; Berlin and others, 1980), showed that there is a first order correlation between the average relief of the surface scatterers on the saltpan and fan gravel surfaces and the relative density of radar image film (i.e., backscattered return). In this early investigation, the Rayleigh criterion (Beckmann and Spizzichino, 1963) that predicts the size of surface scatterer transition between radar rough and radar-smooth, was verified from field studies to occur at L-band between 4 cm (0.16λ) and 7 cm (0.28λ). Subsequent papers (Dailey and others, 1978a,b; 1979; Berlin and others, 1980) describe the excellent discrimination of Death Valley geologic units using multipolarization, multifrequency radar images, Multispectral Scanner (MSS) images, and various combinations of these data sets. Many X-band, L-band, and three-frequency polarimetric SAR images have been acquired over Death Valley since the early 1970s. Because of the limited scope of this Open-File Report, the reader is referred to Hunt and Mabey (1966), Hunt and others (1966), and Hunt (1975) for detailed descriptions of the geology, structure, and hydrology of Death Valley and vicinity (see Fig. 1, Table 2).

Early in our investigation of radar backscatter in Death Valley, It became clear that detailed micro-topography of the saltpan and fan gravel surfaces would have to be acquired at a variety of slope lengths, and then analyzed statistically prior to any serious attempt to "quantify" the relationship between the radar backscatter cross section ($\sigma^o$) and microrelief statistics. As a result, the major objectives of our subsequent radar-geology investigations in Death Valley were divided into two major tasks: (1) collection of detailed micro-topography data and the calculation of terrain statistical data from this topography; and (2) the empirical derivation of one or more radar backscatter inversion models, from which we hoped to estimate the surface properties (e.g., dielectric constant, microrelief) given a knowledge of the radar backscatter cross-section behavior, and visa versa. In this report, we simply present the scatterometer database and describe the methodologies that were successfully developed for (1) collecting detailed micro-topography information, and (2) statistical analysis of these data. Earlier relevant reports describing selected aspects of this methodology are referenced below as appropriate.

The empirical derivation of a unified backscatter inversion model that would be applicable to the wide range (and diverse types) of micro-relief in Death Valley was recognized to be a complex and difficult task early in our investigation. Our basic approach to this task during the late 1970s and early 1980s involved the development of a "modified Bragg-Rice model", summarized in an abstract presented by Brown and Schaber (1980). In the course of this early study, we and our JPL collaborator (Walter E. Brown Jr.) developed serious concerns as to whether the modified Bragg-Rice model, or any other "single" backscatter inversion algorithm, could satisfactorily represent the backscatter that resulted solely from the surface of the diverse saltpan and fan gravel terrains in the valley. *Our major concern was (and still is) the degree to which radar backscatter from the saltpan deposits, and to a lesser degree from the gravel fans, is influenced by volume scattering, multiple scattering, and complex dielectric effects.*

Additional problems during our early radar-geology studies in Death Valley included: (1) the dependability (at all incidence angles and frequencies) and the absolute calibration of radar scatterometer data obtained in 1977 and 1979 (described below) in support of our NASA investigation; and (2) the unavailability at that time of calibrated ($\sigma^o$), multispectral and polarimetric SAR images. The availability of calibrated multispectral and fully polarimetric SAR image data is especially important to enable the researcher to justify the spatial extrapolation of any inversion model through follow-up field studies. Fortunately, such databases are now becoming available.

Volume scattering and multiple scattering effects (Ulaby et al., 1982) were found to be most prevalent at the lower frequencies (L-band and P-band) in both the saltpan and gravel surfaces. Surface and near-surface dielectric anomalies are encountered predominantly within the saltpan, and at all radar frequencies investigated (X-, C-, L- and P-bands). Lenses of damp to wet silts and clays, hygroscopic salts, and hollow hummocks (near-surface cavities) are characteristic of the valley floor year round (Fig. 3). The Death Valley saltpan is dominantly below sea level, reaching a minimum elevation of -86 m in Badwater Basin (Figs. 1, 2b). Excessive near-surface moisture and sand and clay lensing is especially troublesome within the smoothest (and lowest elevation) floodplain deposits, which cover about one third of the saltpan. The slightly rough sulphate and carbonate units within the saltpan are characterized by near-surface salt heaving and are pitted with solution cavities (Fig. 3).

Both the damp zones (salt saturated) and the void spaces act as complex dielectric inhomogeneities that produce increased backscatter in both radar scatterometer data and SAR images. The damp areas of the floodplain, for example, are best delineated on the VV polarization images (See section - Hydrologic Problems in Death Valley.) Such returns are extremely difficult, if not impossible, to separate from backscatter signatures that are entirely the result of measured "surface" roughness variations.

A state-of-the-art Airborne Synthetic Aperture Radar (AIRSAR) has become available in recent years for radar-geologic and radar polarimetric investigations (e.g., van Zyl, 1989, 1990; van Zyl and others, 1991, 1989, 1987; Nguyen and others, 1990; Sheen and others, 1989; Evans and others, 1988; Zebker and others, 1987). This fully digital, calibrated SAR, developed and built at the Jet Propulsion Laboratory (Pasadena, Calif.), is mounted aboard a DC-8-72 aircraft which is maintained and operated out of NASA's Moffett Field (Mountain View, California). This SAR has the capability to acquire simulataneous C-, L-, and P-band data in four polarizations (HH-HV, VV-VH), and records both the amplitude and phase of the returning signals. AIRSAR is a powerful contemporary tool for investigating the feasibility of deriving radar backscatter inversion models in Death Valley and elsewhere (e.g., van Zyl and others, 1991).

*Researchers interesting in using AIRSAR data to pursue backscatter inversion modeling within Death Valley are strongly cautioned about the potential effects of spurious volume scattering and anomalous dielectrics, especially within the various saltpan deposits on the valley floor, as described above.*

## background information on databases collected between 1973 and 1983

### Surface Profiles From Stereo Models

Two types of stereo terrain photography (ground level and helicopter borne) were acquired during the 1970s and early 1980s for the purpose of documenting terrain micro-topography for a total of eight saltpan and four fan gravel sites within Death Valley (Figs. 1, 4-13; Tables 1, 2). However, all 12 surface stations are not always included in each separate tabulation and correlation of the radar scatterometer and terrain roughness data discussed below because of limited coverage of some sites by the available scatterometer flightlines.

A templet device for obtaining in situ topographic profiles at low cost was first tested and found to produce satisfactory results (0.5-m vertical resolution and 1-2 cm horizontal resolution).

However, this method was abandoned in lieu of photogrammetric reduction of conventional stereomodels in order to insure the desired documentation of the highest frequency component of the terrain microrelief that may be important in Bragg-like scattering (see Schaber and Berlin, 1980). Similar templet measuring devices have been utilized with satisfactory results in contemporary studies of radar backscatter from lava flows (e.g., Gaddis and others, 1989).

The ground level Hasselblad (model MK-70 with 60 mm lens) photographs were taken (handheld) in 1977 from about 2 to 2.5 m above the surface in overlap and convergent stereo. The stereomodels have a ground resolution of 1-2 mm. High resolution surface profiles, 1.1 to 2.9 m in length, were obtained by photogrammetric reduction of the stereomodels using analytical stereoplotters at the U.S. Geological Survey (Flagstaff Field Center, Flagstaff, Arizona). The profiles were digitized at a 3-mm equivalent ground spacing for input into a terrain analysis software program (described below). A stereomodel baseline was established in the ground-level stereopairs by placing two "leveled" meter sticks at orthogonal angles in the field of view.

The helicopter-borne Hasselblad photographs were taken (handheld) on May 9, 1981 from about 100 m above the ground surface in overlap and convergent stereo, and have a ground resolution of 2 to 3 cm. The stereomodels were photogrammetrically reduced to produce two orthogonal profiles, 50 to 94 m in length. The models were digitized to an equivalent ground interval of 10 cm for terrain analysis (Figs. 14-21). Two white posterboard targets (45.5 cm on a side) with large black circles and a 10 cm bar scale were spaced 50 m apart and leveled on each geologic calibration surface just prior to the helicopter overflights. A more sophisticated, boom-mounted stereo camera system on a helicopter platform was utilized by Wall and others (1991) to acquire microrelief information in support of contemporary studies of SAR and other remote sensing data in Death Valley.

The profiles made from the ground level and helicopter-borne stereo photographs described in this Open-File Report statistically represent both the large-scale variations in the topography and the terrain micro-structure on the Death Valley saltpan and gravel fans <u>at that time</u> (mid 1970s to early 1980s). The locations of the ground level and helicopter based photography sites for terrain micro-relief calibration were covered by one or more of the footprints of the JSC radar scatterometer, as described below (see Table 4). The ground level and helicopter-borne stereo photography in Death Valley was supplemented between 1977 and 1979 with NASA airborne radar-scatterometer data (Figs. 22-29, Table 4).

### Radar Scatterometer Data

A radar scatterometer is a non-imaging radar system designed to measure the radar backscatter cross-section ($\sigma^o$) from radar reflectivity time-histories as a function of incidence angle ($\theta_o$) at a particular wavelength and polarization. Such measurements, when made with a continuous-wave Doppler radar, have some unique advantages such as (a) the simultaneity of the received signal from a long narrow swath of terrain, (b) the capability of receiving information forward and aft of the nadir, and (c) the capability of filtering a narrow portion of the Doppler spectrum by analog or computer methods to yield information from a particular ground cell of the irradiated terrain (Kennedy and Janza, 1969; Thompson, 1983). The Doppler frequency shift in the received signals is provided by the relative motion between the aircraft and the overflown terrain. The basic scatterometer equation is given by

$$f_d = (2V/\lambda) \sin(\theta_i) \qquad (1)$$

where $f_d$ = Observed Doppler shift
$V$ = Aircraft velocity
$\lambda$ = Radar wavelength
$\theta_i$ = Angle of incidence

A particular Doppler frequency is associated with a specific angle of incidence, whereas the Doppler is zero at nadir. The scattering area has a footprint which is a parallelogram aligned with the aircraft's ground track. Thus, the scattering area is the product of the width (cross track) and a length (along track) of this footprint. The length of the scattering areas is determined by Doppler filtering of the echo (Thompson, 1983). Thus:

$$L = R\Delta\theta_i = \frac{H\Delta\theta_i}{\cos(\theta_i)} = \frac{H\Delta f\lambda}{2V\cos^2(\theta_i)} \qquad (2)$$

where $L$ = Scattering area length (along track)
$R$ = Range
$H$ = Aircraft altitude above the ground
$\Delta f$ = Spectral resolution

The width (cross-track dimension) of the footprint is determined by antenna bandwidth, thus:

$$W = R\Omega = \frac{HB}{\cos(\theta i)} \qquad (3)$$

where W = Scattering area width (across track)
$\Omega$ = Antenna beamwidth
B = Radar bandwidth

Scatterometer radar-backscatter cross section measurements of the type described above were obtained from a Convair-130 aircraft flying at 460 m above ground level with a forward velocity of 280 km/hr over selected areas of Death Valley in May and June, 1977 and April and May, 1979 (Figs. 22-29, Table 4). The radar antenna footprints over Death Valley from this altitude were 69 m and 23 m for the L-band and X-band systems, respectively (Fenner and others, 1978). The radar scatterometer system used in this investigation was operated by the Johnson Space Center (JSC) (Experiment System Division-Microwave Section) Houston, Texas, and transmitted several frequencies: 0.4 Ghz (P-band, 0.75 m), 1.6 Ghz, (L-band, 0.187 m), 4.75 Ghz (C-band, 0.063 m), and 13.3 Ghz (K-band 0.023 m), though most areas do not have a complete set of usable observations at all four frequencies (Table 4). The 13.3 Ghz scatterometer, which acquired data only in VV polarization, produced little usable data from Death Valley. The total system dynamic range for the scatterometers is in excess of 50 dB (Fenner and others, 1978).

The JSC scatterometer system was capable of transmitting one polarization (either horizontal or vertical) and receiving both like- and cross-polarized components (H or V, but not both simultaneously). Each frequency and polarization combination was recorded at five-degree increments of incidence angle over a usable range of 15 to 50 degrees. Five flightlines of data were collected, four in VV-VH polarization and one in HH-HV polarization. Color photographs was obtained at 1:3000 scale during the data runs. These data were used to establish aircraft flight paths relative to the selected terrain analysis sites on different geologic surfaces.

The resulting graphs of radar backscatter per unit area ($\sigma_o$) versus incidence angle, shown in Figures 22-29, coarsely delineate the backscatter "envelope" of nine of the saltpan and fan gravel sites studied within the valley. The degree of absolute calibration of the radar backscatter cross-section data reduced from the JSC scatterometer radar reflectivity time histories was never well defined, but is estimated to be approximately ±3 dB (Steve Reid, Lockheed Aerospace, Houston TX, personal commun., 1979).

## TERRAIN ANALYSIS

Parametric description of natural topography, for practical applications such as radar-backscatter modeling is a highly complex subject (Pike, 1963; Pike and Rozema, 1975). Research in this area is commonly referred to as terrain analysis. Many studies in terrain analysis were undertaken to develop a classification scheme for a highly specific set of circumstances. Accordingly, the descriptive statistics that we have applied to micro-roughness in Death Valley for the purpose of understanding radar backscatter thus constitute only one way to address the general problem--modeling the geometry of natural terrains. The application to radar tends to restrict descriptive variables to those expressing surface roughness rather than other, more exotic characteristics of larger scale terrains (Pike, 1978; Pike and Rozema, 1975). Moreover, the statistical description of topography at a millimeter to 100 m scale represents an application of terrain analysis to one extreme of the scale with which there is still little experience on the part of earth scientists (Schaber and others, 1980).

### The U.S. Geological Survey's Terrain Analysis Software

The terrain statistics presented below were generated using the U.S. Geological Survey's Terrain Analysis Module (TAM) software, originally developed under NASA funding for trafficability analysis for the Apollo Lunar Rover Vehicle (LRV) and for incidental studies of lunar morphology (Pike and Rozema, 1975; Pike, 1978; Schaber and others, 1979, 1980). It is important to note here that the TAM software, as written, cannot presently accept three-dimensional topographic models as input. Therefore, terrain statistics performed on the Death Valley terrains described in this report were computed from orthogonal, linear topographic profiles digitized at equally-spaced intervals.

The Terrain Analysis Module is written in FORTRAN IV and consists of seven integrated data analysis and plotting routines. The program furnishes nearly one hundred individual items of graphical and tabular data dealing with six major statistical parameters, including: (1) topographic relief, hypsometric analyses, (2) topographic grain, (3) power ("variance") spectral density

(Rozema, 1969; Pike and Rozema, 1975), and (4) mean slope angles at various relief profile sampling intervals (Schaber and others, 1979, 1980). Appendix A includes a brief description of the seven subprograms that comprise TAM, and an example printout from TAM is included in Schaber and others (1980).

## Statistics of Relief, Slope and Curvature

The photogrammetrically generated topographic profiles from ground level and helicopter-based photography obtained at selected saltpan and fan gravel sites in Death Valley (Figs. 1,2, 4ab, 14-21; Tables 1, 2) were digitized at 3-mm and 10-cm ground intervals, respectively. The resulting elevation profiles were used as input in the TAM software in order to calculate various parameters related to surface roughness. Selected statistics on relief, slope, curvature, and power spectral density functions computed for selected saltpan and fan gravel calibration sites (shown in Figs. 1,2, 5-13 and Tables 1 and 2) are tabulated in Tables 5-30. Graphical representations of the probability density of elevation (relief) and slope, and the power spectral density (PSD) curves (described below) computed from the helicopter-derived profiles for the selected saltpan and fan gravel sites, are shown in Figures 30-39. The parameters for the regression line-fit to the PSD data are shown in Table 31.

The probability density functions for micro-relief on natural terrain surfaces are very poorly known because of the rather specialized need for such information and the extreme difficulty in acquiring these data over large uniformly rough areas. Information of this type is, however, required for proper empirical modeling of radar backscatter. A totally random set of elevation measurements on an isotropically rough, natural surface should follow the "Gaussian" or normal distribution of the probability density functions. We can test the validity of the normal distribution for micro-relief within Death Valley by elevation frequency analysis of the profile data (Figs. 4, 14-21). If a variable X, representing deviation from mean relief, is distributed as:

$$F(x) = 1/\sqrt{2\pi Sx^2} * e^{-(X-h)^2/2Sx^2}$$

where Sx = standard deviation of relief and h = mean relief, then X is said to have the normal distribution of the probability density functions (Miller and Kahn, 1962). From the values of standard deviation of relief and mean relief listed in Tables 4-13 we can calculate true normal distribution of the probability density for the selected saltpan and gravel surfaces in Death Valley used in this study. The measured probability density functions for both relief and slope are shown in Figures 30-38. For purposes of radar backscatter model investigations, it is important to know how closely these surfaces approximate a normal or other distribution of the probability density functions.

Examples of the correlations between normalized radar backscatter cross section at L-band (for HH, HV and VV, VH polarization, and at various angles of incidence) and mean relief, relief variance, and mean slope for nine surface calibration sites are graphically presented in Figures 40-45. Breaks in the slope of the curves are seen to occur at about 4 cm for mean relief, 4 $cm^2$ for relief variance, and about 8° for mean slope (e.g., Fig. 40-41). These flexures are thought to represent the transition between Rayleigh (i.e., specular) and diffuse scattering at L-band, as earlier reported (Schaber and others, 1976). Similar graphs for the remaining scatterometer frequencies (X-, C- and P-bands) have not been produced; however, they can be generated in part from the tabular and graphical data presented in this report.

## Mean Slope Versus Profile Sampling Interval

The slope portion of the TAM software calculates the algebraic and absolute slope statistics for varying profile sampling intervals and absolute slope statistics for varying profile sampling intervals, and furnishes a regression line fit equation for these data (See Appendix A). Figure 46 illustrates a graphical presentation of these data for the 12 ground-level and helicopter-derived topographic profiles shown in Figures 4 and 14-21 (Table 2). Note the relative insensitivity of relief profile sampling interval versus mean slope angle for the rougher saltpan surfaces characterized by stations A ,B and C (See Figs. 4, 5, 46a). The extreme smoothness of the floodplain surface (Stations G,H -see Fig. 9) is shown by its mean slope of zero degrees at a rather short sampling interval of about 50 to 60 mm. Similarly for the fine-grained fan gravels on Artist's Drive (station K, Fig. 12) and the desert pavement surface on Tucki Wash Fan (station L, Fig. 13), the mean slope goes essentially to zero at sampling intervals of 100 and 50 mm, respectively. The values of these statistics lies in the equivalence of the profile sampling interval and radar wavelength sensitivity to surface irregularities and relief facets.

## Spectral Analysis of Surface Roughness

[Actual and line-fit power spectral density curves for the orthogonal X and Y profiles computed for the nine saltpan and fan gravel sites from the ground-level stereo models are compared in Figure 39. The parameters for the regression line functions for the PSD curves derived from both the ground-level and helicopter-derived topographic profiles are given in Table 30.]

Power spectral or time series analysis enables examination of the frequency content of topographic or surface roughness profiles. In natural terrain surfaces, profiles are generally statistically random functions that can be represented by the continuous variance spectrum. Elevation amplitudes that contribute to variability of a random isotropic surface above its mean height value are thus associated with a continuum of wavelengths. Separating a random profile into wavelength bands yields the spectral density of the relief variance which is given as the square of the amplitude per unit bandwidth of the contributing wavelength bands (Pike and Rozema, 1975). This value has been called the power spectral density (PSD). The actual PSD curves for the studied Death Valley surface profiles are shown as parts e and f of Figures 30 through 38 and Figure 39a-d, while the regression line fit curves to these data are shown in Figure 39e and f.

The variance spectral density program used in this study derives the autocovariance function and the Fourier transform of the autocovariance function which is the spectral density function of the variance, and vice versa (Pike and Rozema, 1975). Autocorrelation is applied to the relief data to bring out any periodicities that may be present in the topographic profile.

The variance, or power spectral density graphs, are sloping lines representing continuous functions of topographic (spatial) wavelength. Because the greatest relief within a surface profile (natural terrain) is generally associated with the longer wavelengths, the spectral density decreases rapidly with decreasing terrain wavelengths. The slopes of the PSD curves describe a relation between the relief content of the long and short wave features (Bryson and Dutton, 1967). An overall slope of -3 is thought to indicate a "uniformity" of topographic slope for all relief features in the sample area, regardless of their size (Lettan, 1967; Bekker, 1969). A slope less steep than -3 indicates that small topographic features (high frequency) are rougher than large (low frequency) features. This is a common aspect of the surface profiles of Death Valley saltpan surfaces. Likewise, a spectrum slope steeper than -3 suggests more rough, coarse-grained features and fewer smooth, fine-grained relief forms. The average PSD curve slopes for the Death Valley saltpan and gravel geologic surfaces using the ground level topographic profiles (shown in Fig. 4) are -2.418 and -1.892 respectively, indicating a surplus of high frequency small-scale relief over large-scale relief (see Fig. 39a-d).

Digital bandpass filtering of the very low frequency data in the surface profiles is performed prior to calculation of the PSD functions. This operation is included since a long-term trend in the profiles affects the PSD function in two ways: (1) it may result in a non-stationary profile (i.e., a profile whose statistical properties are affected by a change in origin), and (2) because the amplitude of the profile associated with the low frequency of a long trend would likely be relatively large, enough power would be contributed by the low frequency to obscure that contributed by higher frequencies (Rozema, 1969). The overturn on the upper left side of the Death Valley PSD curves (Fig. 38) is the result of this high pass filtering of the low frequency trends on the ground-level topographic profiles.

## CORRELATION BETWEEN SAR IMAGE FILM DENSITY AND TERRAIN ANALYSIS DATA FOR SALTPAN AND GRAVEL FAN SURFACES

### Background

Between 1964 and the mid-1980s, many dozens of flightlines of uncalibrated (i.e., for normalized radar backscatter cross-section) X-band and L-band SAR images of Death Valley were acquired by aircraft-borne SARs operated by several different organizations and facilities (e.g., Jet Propulsion Laboratory, Air Force Systems Command, Goodyear Aerospace, Corp., Motorola Aerospace Corp., Johnson Space Center). Spaceborne L-band SAR images of Death Valley were first acquired by Seasat in 1978. Earlier, digitally-correlated, L-band SAR images (dual polarization, HH and HV or VV and VH) were acquired by the Planetology and Oceanography Section of the Jet Propulsion Laboratory (JPL) utilizing the NASA Convair-990 that was maintained and operated out of NASA/Ames Research Center (Moffett Field, Calif). The 990 aircraft was destroyed by fire on 17 July 1985 and was replaced by the current DC-8-72 ("AIRSAR"), described above. For a complete listing of JPL-acquired SAR data (both aircraft and Seasat) of Death

Valley and vicinity, the reader is referred to the radar data library at JPL (Don Harrison, phone 818-354-2386).

## Methods

Following the technique described in Schaber and others (1976), several of these uncalibrated airborne X-band images and airborne and Seasat L-band SAR images of Death Valley were scanned at 25 or 50 micrometers in an attempt to correlate relative film density values or digital number (DN) from diverse saltpan and fan gravel surfaces with documented surface relief and slope statistics (described above). To minimize the effect of varying incidence angle on returned power (film density) from the surface, only those SAR images that contain geologic units of interest within a limited incidence angle range were selected for digital analysis of film densities. Given that the SAR images obtained early in our study were not calibrated (i.e., they have an unknown relation between return power and film density), the film density values, after correcting for digitizer transformation function and film gamma were used to show a relative correlation with various surface relief and slope statistics.

A computer program ("STAT") (written by Pat Chavez, U.S. Geological Survey, Flagstaff, Arizona), originally developed for analysis of Landsat MSS film density values, was utilized in our density analysis of the radar images. In the STAT program, five separate "samples" within five saltpan and four fan gravel units were measured for the average and standard deviation of film density value (DN). The DN samples were selected from the same geologic unit from which specific calibration sites were selected for terrain analysis (as described above).

Image picture element ("pixel") arrays of 10 X 10 and 20 X 20 were used in this analysis. An analysis of film DN for the selected geologic surfaces, versus changes in angle of incidence across the central portion of the images, indicated differences were within the "noise". Thus, small differences in incidence angle effects (few tenths to 1 degree) were not taken into consideration in subsequent calculations. After correction of the mean DN values for the digitizer transformation function, DN values were "normalized" to the roughest of the salt pan surfaces (Station A or B) measured in each radar image (Figs. 5a, 10).

**<u>The "Interesting" Results</u>** - Figures 47-52 show the resulting line-fit graphs correlating normalized film DN values on X- and L-band SAR images with several of the measured surface relief and slope parameters described above. The gravel and saltpan surfaces are clearly distinguishable on the graphs derived from DN analysis of both the airborne, X-band (HH and VV) and the airborne and Seasat L-band (HH) images. The gravels show a higher normalized DN relative to the saltpan units on all of the airborne HH and VV images. On the 1975 airborne L-band HV polarization image, shown in Figure 50, the saltpan and gravel surfaces are indistinguishable.

For the DN analysis of the Seasat L-band (HH) image (Fig. 52), however, the saltpan surfaces show a distinctly higher backscatter relative to the fan gravels. This is just the opposite of that seen on the analysis of the HH and VV airborne images (Figs. 47-51). This effect is tentatively attributed as a consequence of the steep 20° (off nadir) incidence angle at which the Seasat data were acquired. (compared with the airborne images that are generally acquired with incidence angles between 45° and 70°). At a 20° incidence angle, the Seasat SAR returns are characteristic of the steeper part of normal radar backscatter cross-section curves (versus incidence angle) for natural terrains (e.g., Ulaby and Dobson, 1989a,b; Ulaby and Elachi, 1990; Ulaby and others, 1981, 1982, 1986).

These overall results suggest the strong possibility that radar returns from the saltpan and gravel fans result from uniquely different scattering mechanisms, and that acquisition of a wide variation in the angle of incidence may be useful for separating these different radar-scattering mechanisms. Multiple scattering might be more significant in both the X- and L-band SAR returns from the fan gravels than the saltpan; thus indicating possible stronger total return power from the gravels relative to the saltpan surfaces when each has an equivalent mean relief, or relief variance.

Interestingly, DN analysis of the VH image from the JSC ANAPQ-102A SAR sensor showed a dramatic steepening of the fan gravel DN curve relative to that of the saltpan (Fig. 49). The reason for this effect is not yet well understood. However, the same effect did not appear on DN curves that were derived from an L-band image acquired in HV polarization (see Fig. 51a,b,c). The DN curves derived from analysis of both an aircraft L-band VV and HV images and a Seasat HH L-band image (Figs. 50-51) show a break-in-slope at the smoothest end of the roughness scale. The reversal in the relative positions of the fan gravel and saltpan points on the Seasat image DN curves was noted at the beginning of this section.

The flexures or breaks-in-slope observed in the DN curves for the L-band gravel and saltpan units occur in the range of 2 to 8 cm mean relief, 4 to 6 $cm^2$ relief variance, and 4° to 8° mean slope at a 25-cm profile sampling interval. As mentioned above, these breaks-in-slope are thought to represent the "Rayleigh breakpoint", or transition from quasi-specular to dominantly diffuse backscatter which we showed to be well defined based on density analysis of the first L-band SAR images obtained of Death Valley (Schaber and others, 1976). This change in scattering mechanism to Rayleigh scattering at X-band (higher frequency) is not resolved on Figures 47-49 because it occurs at only a few millimeters surface-relief scale at the higher radar frequencies (e.g., K- and X-band)(McDonald and Waite, 1973).

Because the radar images digitized for film density DN values were not calibrated for absolute values of return radar power, the slopes of the curves shown in Figures 47-52 differ slightly for each sample of X-and L-band image data and should not be taken as meaningful parameters. The intercept of these curves with the ordinate (ratio of normalized film DN) is interpreted to be controlled by differing photographic and image processing procedures used on the radar image data to maintain maximum dynamic range (number of film gray levels).

The relative correlation shown between normalized radar film density and various surface roughness parameters in Death Valley was expected, based on the results of our earlier studies (Schaber and others, 1976a,b). However, the apparent, distinct separation of the saltpan and fan gravel surfaces on the digital image data was unexpected. Verification of this separation was not confirmed during our analyses of the comparison of terrain relief statistics with the JSC radar scatterometer data (refer to Figures 40-45). However, the separation of the saltpan from the gravel surfaces may have been more pronounced on the SAR images because of the spatially "more representative" samples of the geologic surfaces that were analyzed, as compared to the narrow footprint and lower surface resolution of the JSC scatterometers. The consistently steeper ground slope of the large gravel fans in Death Valley relative to the saltpan was taken into consideration during the selection of the SAR film DN values; however, it could still be an important factor in the observed results that should be investigated. Further investigation into possible different scattering behaviors of the saltpan and the gravel surfaces in Death Valley is now possible using JPL's calibrated, multispectral radar polarimeter (AIRSAR).

## MOISTURE PROBLEMS IN DEATH VALLEY AND THEIR POSSIBLE ADVERSE EFFECTS ON THE MODELING OF RADAR BACKSCATTER

In terms of direct precipitation, Death Valley is the driest part of the United States, with rainfall averaging only about 42 mm per year. However, the paucity of precipitation is misleading because Death Valley receives more water from springs, seeps, and streams than most of the surrounding basins (Sharp, 1972). There are two primary reasons for this. First, the floor of Death Valley, the saltpan, is the drainage sink or sump for a fairly large hydrologic basin (about 24,350 $km^2$) in southeastern California and adjacent parts of Nevada. The saltpan collects the surface-water and ground-water discharge from (1) the Amargosa River, which enters the saltpan from the south, (2) Salt Creek, which enters the saltpan from the north, and (3) numerous side canyons from the adjoining mountains east (Black and Funeral Mountains) and west (Panamint Range) of the valley floor. Second, almost 50 percent of the water entering Death Valley comes via faults that serve as underground conduits from mountains and valleys lying outside the hydrologic basin. The principal source for this water is thought to be the Spring Mountains, the third range east of Death Valley, and some 80 km away (Hunt, 1975).

Elevated moisture levels in the saltpan, and especially the floodplain areas, are attributable to both seasonal sheet flooding and the capillary rise of shallow ground water (See Appendix B.) When precipitation is above normal in the hydrologic basin, the floodplain areas in Cottonball, Middle, and Badwater Basins (Fig. 2) can be covered by standing water. Most of the time, however, the floodplain deposits are damp and covered with a very thin (often quite dry) coating of nearly pure salt.

How floodplain moisture influences visible, mid-infrared (IR), and radar returns is illustrated in Figures 53 And 54. Figure 53 shows Landsat Thematic Mapper (TM) band 3 (0.63-0.69 µm, red) and band 5 (1.55-1.75 µm, mid-IR) images of Death Valley. The band 3 image displays the floodplain areas in bright tones, which is indicative of strong surface reflectance from the salt coating in the visible spectrum (Fig. 9). By comparison, the band 5 image shows the same area in dark tones because it was responding to changes in the moisture content of the floodplain deposits (reflectance decreases as moisture content increases).

Figure 54 shows two X-band, VV images of Cottonball Basin and Badwater Basin. Although the floodplain areas have a very smooth playa surface (Figs. 2 and 9), note that the image tones are much brighter than the dark signature one would expect for a specular surface. This is because the VV polarization is extremely sensitive to changes in the dielectric constant due to moisture variations (reflectance increases as moisture increases). Figure 26 clearly shows the influence of floodplain moisture in Cottonball Basin on multifrequency radar scatterometer backscatter cross-section values.

## ACKNOWLEDGMENTS

The authors thank the personnel at the National Park Service at Death Valley National Monument for their excellent support of our field work between 1970 and 1983. The authors also acknowledge Kevin Horstman and Richard Kozak for their assistance in the field, in the sedimentary petrology laboratory, and with data processing. tasks.

The authors also thank Robert Gurule for his support in terrain analysis, Sherman Wu and his photogrammetric Group (USGS-Flagstaff) for providing reduction of stereo photography, and H. F. Gonzalez and James A. Harmon of the the U.S. Army White Sands Missile Range (New Mexico) Calibration Division for providing the laboratory measurements of sample dielectric properties.

Special thanks goes to the NASA Planetary Geology Program for providing funding support for this work; Steve Reid (Lockheed Aerospace, Houston, Texas) and Dick Fenner (Johnson Space Center, Houston, Texas) for support in acquiring and reducing the radar scatterometer data; Walter Brown Jr., Mike Kobrick, Charles Elachi, Don Harrison, Annie Richardson, and other personnel of the Terrestrial and Planetary Radar Group at the Jet Propulsion Laboratory for acquiring and processing "numerous" airborne SAR passes over Death Valley in support of our research during the 1970s and early 1980s.

## REFERENCES CITED

Arvidson, R.E. and others, 1993, Characterization of lava flow degradation in the Pisgah and Cima volcanic fields, California using Landsat Thematic Mapper and AIRSAR data: Geol. Soc. Am. Bull., v. 105, no. 2, 175-188.

Avery, T.E., and Berlin, G.L., 1992, Fundamentals of remote Sensing and airphoto interpretation: Fifth Edition, Macmillan Publishing Company, New York, 472 p.

Barrick, D.E., 1970, Unacceptable height correlation coefficients and the quasispecular components in rough surface scattering:

__________, 1972, First order theory and analysis of MF/HF/VHF scatter from the sea: IEEE Trans. Ant. Propog., v. 20, pp. 2-10.

Barrick, D.E., and Peake, W.H., 1967, Scattering from surfaces with different roughness scales: Analysis and interpretation: Research Rept. No. BAT-197A-10-3, Battelle Memorial Institute, Columbus Laboratories, Columbus, Ohio, AD 662751: also published under separate cover as Rept. No. 1388-26, ElectroScience Laboratory, Ohio State Univ., Columbus, Ohio, N67-39091.

Barrick, D.E., and Peake, W.H., 1968, A review of scattering from surfaces with different roughness scales: Radio Science, v. 3 (New Series), pp. 865-868.

Beckmann, P., 1965, Scattering by composite rough surfaces: Proc. IEEE, v. 53, pp. 1012-1015.

Beckmann, P., and Spizzichino, A., 1963, The scattering of electromagnetic waves from rough surfaces: pp. 80-89, Macmillan Co., New York.

Bekker, M.G., 1969, Introduction to terrain-vehicle systems: Ann Arbor, University of Michigan Press, pp. 158-378.

Berlin, G.L., Schaber, G.G., and Horstman, K.C., 1980, Possible fault detection in Cottonball Basin, California: An application of radar remote sensing: Remote Sensing of Environ., v. 10, 33-42.

Brown, W.E. Jr., Elachi, C., and Thompson, T.W., 1975, Radar imaging of ocean surface patterns: J. Geophys. Res., v. 81, p. 2657.

Brown, W.E. Jr., and Schaber, G.G., 1980, Radar backscatter: A modified Bragg-Rice model (abst): Second Terrain and Sea Scatter Workshop Proceedings, Washington D.C. (March 1-2, 1980), 1p.

Bryson, R.A., and Dutton, J.A., 1679, The variance spectra of certain natural series, in Garrison, W.L., and Marble, D.F., eds., Evanston, Illinois, Northwestern University Press, pp. 1-24.

Campbell, B.A., Zisk, S.H., and Mouginis-Mark, P.J., 1989, A quad-pol radar scattering model for use in remote sensing of lava flow morphology: Remote Sensing of Environment, v. 30, pp. 227-237.

Croxton, F.E., Cowden, D.J., and Klein, S., 1967, Applied general statistics: Third Edition, Prentice-Hall, Englewood Cliffs, N.J., 745 p.

Dailey, J.C., 1973, Wind dependence of radar sea return: J. Geophys. Res., v. 78, pp. 7823-7833.

Dailey, M., Elachi, C., Farr, T., and Schaber, G., 1978a, Discrimination of geologic units in Death Valley using dual frequency and polarization imaging radar data: Geophys. Res. Lettr., v. 5, pp. 889-82.

Dailey, M.I., Elachi, C., Farr, T., Stromberg, W., Williams, S., and Schaber, G.G., 1978b, Application of multispectral radar and Landsat imagery to geologic mapping in Death Valley: Jet Propulsion Laboratory Techn. Rept. 78-19, 47 p.

Dailey, M.I., Farr, Tom. and Schaber, G.G., 1979, Geologic interpretation from composited radar and Landsat imagery: Photog. Eng. and Remote Sensing, v. 45, No. 8, pp.1109-1116.

Davies, H., 1964, The reflection of electromagnetic waves from a rough surface: Proc. IEE (London), v. 101, part IV, pp. 209-214.

Elachi, C., 1987, Introduction to the physics and techniques of remote sensing: Wiley and Sons, New York, 413 p.

Elandt, R.C., 1961, The folded normal distribution: Two methods of estimating parameters from moments: Technometrics, v. 3, no. 4, pp. 551-562.

Engman, E.T. and Wang, J.R., 1987, Evaluating roughness models of radar backscatter: IEEE Trans. on Geoscience and Remote Sensing, v. GE-25, no. 6, pp. 709-713.

Evans, D.L., 1992, Geologic studies using synthetic aperture radar (SAR) data: Episodes, v. 15, pp. 21-31.

Evans, D.L., Elachi, C., Stofan, E.R., Holt, B., Way, J.B., Kobrick, M., Ottl, H., Pampaloni, P., Vogt, M., Wall, S., van Zyl, J., and Schier, M., 1993, The Shuttle Imaging Radar-C and X-SAR Mission: EOS, v, 74, pp. 1, 157-158.

Evans, D.L., and 15 others, The Geologic Remote Sensing Field Experiment: Overview of preliminary results from the Lunar Volcanic Field, Nevada: IEEE Trans. on Geosci. and Remote Sensing, in press.

Evans, D.L., Farr, T.G. and van Zyl, J.J., 1992, Estimates of surface roughness derived from synthetic aperture radar (SAR) data:

IEEE Trans. on Geoscience and Remote Sensing, v. 30, no. 2, pp. 382-389.

Farr, T.G., 1992, Microtopographic evolution of lava flows at Cima Volcanic Field, Mohave Desert, California: J. Geophys. Res., v. 97, no. B11, pp. 15,171-15,179.

Fenner, R.G., Reid, S.C., and Schaber, G.G., 1978, An unconventional approach to imaging radar calibration: Proceedings of the Microwave Remote Sensing Symposium, Houston, Texas (Dec. 6-7, 1977).

Fuks, I., 1966, Contribution to the theory of radio wave scattering on the perturbed sea surface: Izvestia Vyshihk Uchebnikh Zavedeniy, Radiofizika (USSR), v. 9, no. 5, 876-887.

Fung, A.K., 1967, Theory of cross-polarized power return from a random surface: Appl. Sci. Res., v. 18, pp. 56-60.

Fung, A.K., 1968, Mechanisms of polarized and depolarized scattering from a rough dielectric surface: J. Franklin Institute, v. 285, pp. 125-133.

Gaddis, Lisa, Mouginis-Mark, Pete, Singer, Robert and Kaupp, Verne, 1989, Geologic analyses of Shuttle Imaging Radar (SIR-B) data of Kilauea Volcano, Hawaii: Geol. Soc. Am. Bull., v. 101, pp. 317-332.

Greeley, Ronald, and Martel, Linda, 1988, Radar observations of basaltic lava flows, Craters of the Moon, Idaho: Intern. J. Remote Sensing, v. 9, no. 6, pp. 1071-1085.

Grender, C.C., 1976, Topo III, A FORTRAN program for terrain analysis: Computers and Geoscience, v. 32, pp. 195-209.

Hunt, C.B. and Mabey, D.R., 1966, Stratigraphy and structure in Death Valley, California: U.S. Geol. Survey Prof. Paper 494-A., 162p.

Hunt, C.B., Robinson, T.W., Bowles, W.A., and Washburn, A.L., 1966, Hydrologic Basin, Death Valley, California: U.S. Geol. Survey Prof. Paper 494-B, 138p.

Hunt, C.B., 1975, Death Valley: Geology, ecology, archaeology: University of Calif. Press, Berkeley, 234 p.

Kirby, R.P., 1991, Measurement of surface roughness in desert terrain by close range photogrammetry: Phogrammetric Record, v. 13 (78), pp. 855-875.

Kodis, R.D., 1966, A note on the theory of scattering from an irregular surface: IEEE Trans. Ant. Prop. AP-14, No. 1, 77-82.

McDonald, H.C., and Waite, W.P., 1973, Imaging radars provide terrain texture and roughness parameters in semi-arid environments, Modern Geology, v. 4, pp. 145-158.

Miller, R.L., and Kahn, J.S., 1962, Statistical Analysis in the geological sciences; John Wiley and Sons, Inc., New York, 483 p,

Moore, R.,K., 1969, Radar return from the ground: Bull. of Engineering publ. No. 59, Univ. of Kansas , Lawrence, Kansas, 87 p.

Nguyen, L., Pang, A., and Richardson, A., 1990, SAR data catalog system (V5.0) user's guide: Jet Propulsion Laboratory Publ. D-7657 (May 15, 1990), 114 p.

Peake, W.H., 1959, Theory of radar return from terrain: IRE National Convention Record, v. 7, pt. 1, pp. 27-41.

Pike, R.J., 1963, Landform regions of southern New England - quantitative delimitation: M.A. Thesis, Clark University, Worcester, Mass., 80 p.

________ 1978, Lunar landscape morphometry: U.S. Geological Survey Open-File Rept. 78-812, 142 p.

Pike, R.J., and Rozema, W.J., 1975, Spectral analysis of landforms: Annals of the Assoc. of Am. Geographers, v. 65, pp. 499-516.

Pike, R.J., and Wilson, S.E., 1971, Elevation-relief ratio, hypsometric integral, and geomorphic area-altitude analysis: Geol. Soc. Am. Bull., v. 82, pp. 1079-1084.

Ray, T.W., Farr, T.G. and van Zyl, J.J., 1992, Detection of land degradation with polarimetric SAR: Geophys. Res. Lettr., v. 19, no. 15, pp. 1587-1590.

Rice, S.O., 1951, Reflection of electromagnetic waves by slightly rough surfaces, *in* Theory of Electromagnetic Waves, ed. M. Kline, pp. 351-378: Interscience Publ., Inc., New York, New York; Dover Publ. Inc., New York, New York.

Rozema, W.J., 1969, The use of spectral analysis in describing lunar surface roughness: U.S. Geological Surv. Prof. Paper 650-D, pp. 180-188.

Sabins, F.F., Jr., 1987, Remote sensing: Principles and interpretation:, Second edition: W.H. Freeman, San Francisco, 426 p.

Schaber, G.G., Berlin, G.L., and Brown, W.E., Jr., 1976a, Variations in surface roughness within Death Valley, California: Geologic evaluation of 25-cm wavelength radar images: Geol. Soc. Am. Bull., v. 87, pp. 29-41.

Schaber, G.G., Berlin, G.L., and Pitrone, D.J., 1976b, Selection of remote sensing techniques: Surface roughness information from 3-cm wavlength SLAR images: Amer. Soc. Photogram (ASP) Proceedings, Washington, D.C., 42nd Annual Meeting, Feb. 22-27, 1976, pp. 103-117.

Schaber, G.G., Pike, R.J., and Berlin, G.L., 1979, Terrain-analysis procedures for modeling radar backscatter: U.S. Geol. Surv. Open-File Rept., 79-1088, 67 p.

Schaber, G.G., Elachi, Charles, and Farr, T.G., 1980, Remote sensing of SP Mountain and SP lava flow in north-central Arizona: Remote Sensing of Environment, v. 9, pp. 149-170.

Schaber, G.G., McCauley, J.F., Breed, C.S., and Olhoeft, G.R., 1986, Shuttle Imaing Radar: Physical controls on signal penetration and scattering in the Eastern Sahara: IEEE Trans. on Geoscinece and Remote Sensing, v. GE-24, no. 4, pp. 603-623.

Semenov, B., 1966, An approximate calculation of scattering of electromagnetic waves from a rough surface: Radiotekhnika i Elektronika (USSR) 11, no. 8, pp.1351-1361.

Sharp, R.P., 1972, Geology field guide to southern California: Wm. C. Brown Co., Dubuque, 181 p.

Sheen, D.R., Freeman, A., and Kasischke, E.S., 1989, Phase calibration of polarimetric radar images: IEEE Trans. on Geoscience and Remote Sensing, v. 27, no. 6, 719-731.

Siegal, B.S., and Gillespie, A.R., 1980, Remote sensing in geology: John Wiley, and Sons, New York, 702 p.

Speight, J.C., 1974, A parametric approach to landform regions: Special Pub. No. 7, The Institute of British Geographers, pp. 213-230.

_________1977, Landform pattern description from aerial photographs: Photogrammetria, v. 32, pp. 161-182.

Stogryn, A., 1967, Electromagnetic scattering from rough, finitely conducting surfaces: Radio Sci., v. 2 (New Series), no. 4, pp. 415-428.

Strahler, A.N., 1952, Hypsometric (area-altitude) analysis of erosional topography: Geol. Soc. Am. Bull., v. 63, pp. 1117-1142.

Thompson, T.W., 1983, A user's manual for the NASA/JPL synthetic radar and the NASA/JPL L-band and C-band scatterometers: JPL Publication 83-38, 38p.

Thompson, T.W. Weissman, D.E., and Gonzalez, F.I., 1983, L-band backscatter dependence upon surface wind stress: A summary of new Seasat-1 and aircraft observations: J. Geophys. Res., v. 88, no. C3, pp. 1727-1735.

Ulaby, F.T., and Elachi, C., 1990, Radar polarimetry for geoscience applications; Artech House Inc, Norwood, MA., 364 p.

Ulaby, F.T., and Dobson, M.C., 1989a, Handbook of radar scattering statistics for terrain; Artech House, Inc., Norwood MA.

_____________. 1989b, Radar scattering statistics for terrain: software and user's manual; Artech House, Inc., Norwood MA.

Ulaby, F.T., Moore, R.K., and Fung, A.K., 1981, Microwave remote sensing -active and passive, v. 1: Addison-Wesley, Reading, Mass., 456 p.

________ 1982, Microwave remote sensing, and surface scattering and emission theory: *in* Microwave Remote Sensing: Active and Passive, vol. II: Addison-Wesley, Reading, MA, pp. 816-880.

________, 1986, Microwave Remote Sensing-Active and Passive, vol. III: Addison-Wesley, Reading, MA, pp. 1935-1999.

U.S. Geological Survey, 1970, Topographic data analysis system, Administrative Report: Computer Center Division, Flagstaff, Arizona, 100 p.

Valenzuela, G.R., 1967, Depolarization of radar waves by slightly rough surfaces: IEEE Trans. Ant. and Prop., v. AP-15, no. 4, pp. 552-557.

Valenzuela, G.R., 1968, Scattering of electromagnetic waves from a tilted slightly rough surface: Radio Science, vol. 1, 1057-1066.

Valenzuela, G.R., 1978, Theories for the interaction of electromagnetic and ocean waves-a review: Boundary Layer Meteorol., v. 13, pp. 61-85.

van Zyl, J.J., 1989, Unsupervised classification of scattering behavior using radar polarimetry data: IEEE Trans. on Geosci. and Remote Sensing, v. 27, no. 1, pp. 36-45.

__________1990, Calibration of polarimetric radar images using only image parameters and trihedral corner reflector responses: IEEE Trans. on Geosci. and Remote Sensing, v. 28, no. 3, pp. 337-348.

van Zyl, J.J., Zebker, H.A., and Elachi, C., 1987, Imaging radar polarization signatures: Theory and observation: Radio Sci., v. 22, no. 4, pp 529-543.

van Zyl, J.J., Burnette, C.F., and Farr, T.G., 1991, Inference of surface power spectra from inversion of multifrequency polarimetric radar data: Geophys. Res. Lettr., v. 18, no. 9, 1878-1790.

Wall, S.D., Farr. T.G., Muller, J.P., Lewis, P., and Leberl, F.W., 1991, Measurements of surface microtopography: Photogramm. Eng. and Remote Sensing, v. 57, no. 8, 1075-1078.

Wright, J.W., 1966, Backscattering from capillary waves with application to sea clutter: IEEE Trans. Ant. Prop., v. AP-14, no. 8, pp. 749-754.

Wright, J.W., 1968, A new model for sea clutter: IEEE Trans. Ant. Prop., v. AP-16, pp. 217-223.

Wood, W.F., and Snell, J.B., 1960, A quantitative system for classifying landforms: U.S. Army Natick Laboratory Technical Paper EP-124, Natick, Mass., 80 p.

Zebker, H.A., van Zyl, J.J., and Held, D.N., 1987, Imaging radar polarimetry from wave synthesis: J. Geophys. Res., vol. 92, no. B1, 683-701.

## FIGURE CAPTIONS

Figure 1 - Geologic map of Death Valley (after Hunt and Mabey, 1966) showing the general location of six saltpan (A through H) and four fan gravel sites (I through L) selected for micro-terrain analysis. The Devil's Golf Course (DGC) and Cottonball Basin (CBB) are indicated. Not all sites (e.g. C and F) are found in all figures and tables that follow.

Figure 2 -(a) UPD-4, X-band (3-cm wavelength; H-H polarization) SAR image of part of Death Valley showing the locations of the surface calibration stations A, H, and K indicated in Figure 1. Areas labeled include Middle Basin (MB), Artist's Drive Fan (ADF), Devil's Golf Course (DGC), and Badwater Basin (BB). SAR image (3 m resolution) obtained in 1976 by the Air Force Systems Command (Goodyear Aerospace Corp. - Litchfield Park, Ariz.); (b) another part of the same UPD-4 SAR image strip shown in (a), showing locations of surface calibration stations B, C, D, E, G, I, J, and L. Areas labeled include the Furnace Creek Ranch (FCR), Furnace Creek Fan (FCF), Tucki Wash Fan (TWF), and Cottonball Basin (CBB).

Figure 3 - Schematic geologic cross sections of typical saltpan and fan gravel deposits in Death Valley.

Figure 4 - (a) Topographic profiles of saltpan stations A through H, reduced photogrammetrically from ground-level stereo photography (X-profile). Photos acquired from 2.0-2.5 m height (handheld); (b) same as (a) but with Y-profile; (c) same as (a) but for fan gravel stations I-L; (d) same as (b) but for stations I-L.

Figure 5 - (a) View across station A, massive halite (rock salt), (geologic unit Qh; Hunt and Mabey, 1966), Devil's Golf Course. Note Lambertian-like, cavernous roughness; (b) helicopter photograph obtained from approximately 100 m height above the surface of the Devil's Golf Course, showing the extreme level of surface roughness. Area shown in image is 72 m X 91 m.

Figure 6 - Station B, Qhr Massive Rock Salt (halite) in Cottonball Basin. Meter stick held by person for scale.

**Figure 7** - Station D, Saline Facies-Carbonate Zone in Cottonball Basin. Meter stick shown for scale.

**Figure 8** - Station E- Qhs, Silty Rock Salt-Smooth Facies in Cottonball Basin.

**Figure 9** - Station H, Qf, Floodplain deposit in Badwater Basin; the smoothest of the five saltpan surfaces investigated. Meter stick shown for scale.

**Figure 10** - Station I, $Qg_3$ - coarse, boulder gravels on Tucki Wash Fan (located on the west side of the Valley). Orthogonally-placed meter sticks shown for scale.

**Figure 11** - Station J, $Qg_3$ - moderately coarse gravels on Furnace Creek Fan near Furnace Creek Ranch.

**Figure 12** - Station K, $Qg_3$ - fine gravels on Artist's Drive Fan on the east side of the Valley. Meter stick shown for scale.

**Figure 13** - Station L, $Qg_2$ - Desert Pavement on No. 2 Fan Gravels on Tucki Wash Fan. Thirty centimeter long rule with five cm markings shown for scale.

**Figure 14** - (a) Topographic profile across station A on the Devil's Golf Course. Produced in X-direction across stereo model. Note: This and all profiles shown in Figures 14-20 below were obtained by photogrammetric reduction of stereo photographs taken from a helicopter 100 meters height above surface. Profile is 50.5 m long.; (b) same as (a) but in Y (orthogonal to X) direction across stereo model. Profile is 81.4 m long.

**Figure 15** - (a) Topographic profile across station B in the Cottonball Basin. X-direction across stereo model. Profile is 81.2 m long; (b) same as (a) but in Y direction. Profile is 101.1 m long.

**Figure 16** - (a) Topographic profile across station D in the Cottonball Basin. X-direction across stereo model. Profile is 92.6 m long; (b) same as (a) but in Y-direction. Profile is 92.6 m long.

Figure 17 - (a) Topographic profile across station E in Cottonball Basin. X-direction across stereo model. Profile 47.8 m long; (b) same as (a) except in Y-direction. Profile is 93.85 m long.

Figure 18 - (a) Topographic profile across station I on Tucki Wash Fan. X-direction across stereo model. Profile is 50.25 m long.; (b) same as (a) but in Y-direction. Profile is 81.8 m long.

Figure 19 - (a) Topographic profile across station J on Furnace Creek Fan. X-direction across stereo model. Profile is 62.3 m long; (b) same as (a) but in Y-direction. Profile is 59.8 m long.

Figure 20 - (a) Topographic profile across station K on Artist's Drive Fan. X-direction across stereo model. Profile is 73.0 m long; same as (a) but in Y-direction. Profile is 83.0 m long.

Figure 21 - (a) Topographic profile across station L on Tucki Wash Fan. X-direction across stereo model. Profile is 37.2 m long; (b) same as (a) but in Y-direction. Profile is 90.0 m long.

Figure 22 - (a) Multifrequency HH-HV (polarization) radar backscatter cross-section values ($\sigma_o$) versus incidence angle ($\theta_i$) for station A surface. Scatterometer wavelength (in meters) given to right of curves. Data reduced from JSC radar scatterometer data acquired over Death Valley in 1977 and 1979. See text for details; (b) same as (a) but giving VV and VH polarization values; (c) same as (b) but giving the values from a different scatterometer flightline.

Figure 23 - (a) Multifrequency, VV-VH radar backscatter cross-section values versus incidence angle for station B surface. See Figure 21 (a) for more details; (b) same as (a) but giving the values from a different scatterometer flightline.

Figure 24 - Multifrequency, HH-HV radar backscatter cross-section values versus incidence angle for station D.

Figure 25 - (a) Mutifrequency, HH-HV radar scatterometer cross-section values versus incidence angle for station E; (b) same as (a) but giving VV-VH polarization values.

Figure 26 - (a) Multifrequency, HH-HV radar backscatter cross-section values versus incidence angle for station H; (b) same as (a)

but giving the values for a different scatterometer flightline; (c) same as (a) but giving VV-VH polarization values.

**Figure 27** - (a) Multifrequency, HH-HV radar backscatter cross-section values for station I; (b) same as (a) but giving the values from a different scatterometer flightline.

**Figure 28** - Multifrequency, VV-VH radar backscatter cross-section values for station K.

**Figure 29** - Multifrequency, HH-HV radar backscatter cross-section values for station L.

**Figure 30** - (a) Probability density of relief for station A surface derived from analysis of the topographic X-profile shown in Figure 14a; (b) same as (a) but derived from Y-profile shown in Figure 14b; (c) probability density of slopes for X-profile described in (a); (d) same as (c) but derived from Y-profile described in (b); (e) power spectral density (PSD) curves for station A, computed from topographic X-profiles acquired from both ground level and helicopter platform; (f) same as (e) but for Y-profiles.

**Figure 31** -(a-f) Same as for Fig. 30 but for station B.

**Figure 32**- (a-f) Same as for Fig. 30 but for station D.

**Figure 33** - (a-f) Same as Fig. 30 but for station E.

**Figure 34** - PSD curves for station H (Ground-level data only). PSD curve derived from helicopter-based stereo photography were not computed because of extreme smoothness of floodplain surface.

**Figure 35** - (a-f) Same as Fig. 30 but for station I.

**Figure 36** - (a-f) Same as Fig. 30 but for station J.

**Figure 37** - (a-f) Same as Fig. 30 but for station K.

**Figure 38** - (a-f) Same as Fig. 30 but for station L.

**Figure 39** - (a) PSD curves for six saltpan stations. Data computed from ground-level topographic profiles (X-direction in stereo model) using the USGS Terrain Analysis Module (TAM) described above and in

Appendix; (b) same as (a) but computed from Y-direction profile across stereo model (See ground-level profiles, Fig. 4a,b); (c) same as (a) but for fan gravel stations; (d) Same as (b) but computed for fan gravel stations; (e) Same as (a and b) but derived from line-fit equation; produced by TAM software (See Table 31); (f) Same as (c and d) but computed from line-fit equations produced by TAM software (see Table 31.)

Figure 40 - (a) Correlation at five different incidence angles between L-band (VV polarization) radar backscatter cross-section values ($\sigma_0$) and mean relief for six saltpan and fan gravel stations. Values of $\sigma_0$ computed derived from radar scatterometer data (See Figs. 22-29); (b) Same as (a) but correlated with relief variance; (c) Same as (a) but correlated with mean slope. Surface statistical data (i.e., mean relief, relief variance, standard deviation and mean slope) plotted in Figs. 40-45 are taken from Table 4 and derived from statistical analysis of the ground-level topographic profiles shown in Fig. 3.

Figure 41 - (a-c) Same as Fig. 40 but computed for VH polarization.

Figure 42 - (a-c) Same as Fig. 40 but computed for stations I, D, and L, and with HH polarization.

Figure 43- (a-c) Same as Fig. 42 but computed for HV polarization.

Figure 44 - Same as Fig. 40a but for stations K and L.

Figure 45 - Same as Fig. 41a but for stations J and K.

Figure 46 - (a) Absolute slope versus sampling interval derived from terrain analysis of the ground-level topographic profiles for six saltpan and four fan gravel surfaces; (b) same as (a) but from the terrain analysis of helicopter-derived topographic profile.

Figure 47 - (a) Ratio of X-band SAR film density (DN values) versus measured mean relief for five saltpan and three fan gravel surfaces in Death Valley (HH-polarization). The SAR image used was acquired over Death Valley by the Goodyear Aerospace Corporation in 1964. Note clear separation of saltpan and fan gravel surfaces; (b) same as (a) but for relief standard deviation; (c) same as (a) but for

mean slope at 3 cm sampling interval. Surface statistics for this and all following DN plots (through Fig. 52) are taken from Table 4.

Figure 48 - (a-b) Same as Fig. 47a-b but using a high resolution (3 m) X-band SAR image acquired in 1976 by the Goodyear Aerospace Corp. using a UPD-4 SAR sensor (see Fig. 2); (c) same as (a-b) but computed for mean slope at 25 cm sampling interval.

Figure 49 - (a-b) Same as Fig. 47a-b but using a VV-polarization, X-band (3-cm) SAR image obtained with the JSC ANAPQ-102X SAR sensor (VV polarization). Several flightlines of dual polarization (simultaneous HH and HV or VV and VH only) X-band image data were acquired over Death Valley by the Johnson Space Center (JSC) on March 16, 1979 at the request of the senior author (ggs) (See Fig. 54); (c) same as (a) but correlated with mean slope at 3 cm sampling interval; (d-f) same as (a-c) but using VH polarization. Note strong steepening of curve for gravel sites compared to HH or VV polarization (See text); (g) same as (f) but for mean slope at 25 cm sampling interval.

Figure 50 - (a-b) Same as Fig. 47a,b but using an L-band (25-cm wavelength) SAR image (VV polarization) of Death Valley acquired by JPL in 1976. Note break in slope of curves at about 6 cm mean relief (See text); (c) same as (a-b) but for mean slope at 25 cm sampling interval.

Figure 51 - (a-b) Same as Fig. 46a,b but using an L-band SAR image (HV polarization) of Death Valley acquired by JPL in 1975; (c) same as (a-b) but for mean slope 25-cm sampling interval. [Note that, unlike the data shown in Figs. 47-49, the saltpan and gravel surfaces are not distinguishable from the gravels in the plots, but together form a smooth curve].

Figure 52 - (a-b) Same as Fig. 47a,b but for Seasat L-band (HH polarization) image acquired by NASA-JPL in 1978. Note that the position of the saltpan and gravel points are "reversed" compared in position relative to X- and L-band HH and VV airborne radar image data shown in Figs. 47-50 (see text); (c) same as (a-b) but for mean slope at 25 cm sampling interval..

Figure 53 - Landsat Thematic Mapper (TM) images of Death Valley, acquired on November 17, 1982; (a) band 3 image (0.63-0.69μm); (b)

band 5 image (1.55-1.75µm). Note that the floodplain areas in Cottonball, Middle, and Badwater Basins are depicted in bright tones on the band 3 image and darker tones on the band 5 image.

Figure 54 - VV polarization, X-band SAR image of (a) Cottonball Basin (CBB) and Tucki Wash Fan (TWF), and (b) Badwater Basin (BB) and Devil's Golf Course (DGC). The light tones for the floodplain areas (white arrows) indicate damp playa surfaces; these extremely smooth surfaces are radar dark when dry. The SAR images were acquired in 1981 using the ANA/PQ 102A, SAR sensor (RB-57 aircraft) operated by the Johnson Space Center (Houston, Texas). Incidence angle near image center is about 55 degrees off nadir.

## TABLES

Table 1 - Location of surface calibration sites in Death Valley

Table 2 - Quaternary geologic unit descriptions of surface calibration sites.

Table 3 - Summary of general surface roughness parameters for various saltpan and fan gravel stations documented in Death Valley. Data derived from terrain analysis using ground-level topographic profiles ( Fig. 4).

Table 4 - 1977 and 1979 radar scatterometer data for Death Valley

Table 5- Selected relief statistics for station A derived from TAM software analysis of topographic profiles derived from ground-level (GRX, GRY) and helicopter-based (HELX, HELY) stereo photography. X and Y denote orthogonal profiles produced from stereo models (Figs. 3, 13-20).

Table 6 - Same as Table 5 but for station B

Table 7- Same as Table 5 but for station D.

Table 8 - Same as Table 5 but for station E.

Table 9 - Same as Table 5 but for station H.

Table 10 - Same as Table 5 but for station I.

**Table 11** - Same as Table 5 but for station J.

**Table 12** - Same as Table 5 but for station K.

**Table 13** - Same as Table 5 but for station L.

**Table 14** - Selected slope and curvature statistics for station A derived from TAM software analysis of topographic profiles (X-direction only) derived from ground-level stereo models (see Figs. 4a,c.). Statistics for various sampling intervals indicated. Values $LOG_{10}$ (A) and B are parameters in regression line-fit equation for slope of the form Log10 (cumulative percent frequency) = Log10(A) + B* (slope angle)].

**Table 15**- Same as Table 14 but for station B.

**Table 16** - Same as Table 14 but for station D.

**Table 17** - Same as Table 14 but for station E.

**Table 18** - Same as Table 14 but for station H.

**Table 19** - Same as Table 14 but for station I.

**Table 20** - Same as Table 14 but for station J.

**Table 21** - Same as Table 14 but for station K.

**Table 22** - Same as Table 14 but for station L.

**Table 23**- (a) Selected slope and curvature statistics for station A derived from TAM software analysis of topographic profiles (X-direction) derived from topographic profiles reduced from helicopter-derived stereo models (see Figs. 5-21). Statistics for various sampling intervals indicated. Values $LOG_{10}$ (A) and B are parameters in regression line-fit equation for slope of the form Log10 (cumulative percent frequency) = Log10(A) + B* (slope angle)]; (b) same as (a) but for Y-profile.

**Table 24**- (a-b) Same as Fig. 23 but for station B.

**Table 25** - (a-b) Same as Fig. 23 but for station D.

**Table 26** - (a-b) Same as Fig. 23 but for station E.

**Table 27** - (a-b) Same as Fig. 23 but for station I.

**Table 28** - (a-b) Same as Fig. 23 but for station J.

**Table 29** - (a-b) Same as Fig. 23 but for station K.

**Table 30** - (a-b) Same as Fig. 23 but for station L.

Table 31 - Regression Line-Fit Parameters For power spectral density functions shown in Figure 39

## APPENDIX A

## THE U.S. GEOLOGICAL SURVEY'S TERRAIN SOFTWARE MODULE

The photogrammetrically-derived topographic profiles of the five saltpan and four fan gravel surfaces described in this report were digitized and used as input to the U.S. Geological Survey's Terrain Analysis Module (TAM). TAM, written in FORTRAN IV language, consists of seven integrated data analysis and plotting routines. It furnishes nearly 100 individual pieces of graphical and tabular data that describe four major aspects of topographic geometry: (1) relative relief, hypsometry, topographic grain; (2) power (variance) spectral density of relief; (3) slope angles between slope reversals; and (4) base length slope angle and curvature. A sample output from the TAM, including the plotting subroutine products is given in Schaber and others (1980). The seven major programs that make up the TAM are briefly described as follows:

**Program 1. - Data Formatting.** This initial program of TAM simply formats the input data in readable form for subsequent analysis. Input consists of topographic elevations, measured at a constant horizontal increment ('delta-L') along a continuous profile.

**Program 2 - Relief Analysis.** This part of the provides comprehensive data on the statistical variation of topographic elevation along a profile. The output includes relief, mean elevation, variance, standard deviation, and other standard statistical parameters of elevation such as skewness, kurtosis, elevation-relief ratio (E.R.), hypsometric integral (H) (Pike and Wilson, 1971), and topographic grain (Wood and Snell, 1960). This portion of TAM also tabulates the frequency and cumulative percent frequency of elevations within class intervals, so that histograms may be constructed. Ten of these parameters are recalculated from decreasing sample sizes (N), at lengthening sampling intervals (I). This practice reveals the minimum sample size from which stable statistics can be calculated from each data set.

Hypsometric analysis is valuable in radar backscatter analysis because it gives a quantitative assessment for the proportion of the surface area within a unit volume that can easily contribute to radar backscatter and the proportion that would behave quasispecularly to the radar. Hypsometry is the distribution of ground surface area, or horizontal cross-sectional area of a ground surface, with respect to relief or elevation (Strahler, 1952). Wood and Snell (1960) and Pike (1963) have shown that topographic samples may resemble one another with respect to local relief, average slope, or other geometric aspects, and yet may vary appreciably in appearance as demonstrated by values of elevation-relief ratio (E.R.):

$$\text{E.R.} = \frac{\text{mean elevation} - \text{minimum elevation}}{\text{maximum relief}}$$

which was shown by Pike and Wilson (1971) to be equivalent to the hypsometric integral (H), or the proportionate area below the hypsometric function curve. The derivation of the hypsometric function is beyond the scope of this report but has been well documented by Strahler (1952) and Pike and Wilson (1971). Simply defined, the hypsometric function is the proportion of the total surface area of a unit terrain surface containing elevations greater than a measured elevation. A surface that has exactly equal proportions of its area above and below the mean height value would have a hypsometric integral equal to 0.5.

Topographic grain needs to be determined before computing statistics on roughness or any other aspect of terrain geometry. If the profile obtained by the ground level or helicopter photogrammetric technique is of sufficient length to contain most of the relief elements, or is unnecessarily long, then statistical errors will enter the calculations for modeling radar backscatter. Topographic grain of a terrain is essentially the minimum area or linear sample distance on a surface that contains most of the important relief structure (Wood and Snell, 1960). If the size of a progressively larger, nested interval along the horizontal axis of a profile is plotted against the maximum relief within the intervals, relief increases rapidly to a point and then levels off. The sampling interval size corresponding to the point at which relief inflects is the "topographic grain." Most of the topographic characteristics of the sample region will thus be contained within an interval of this size.

**Program 3 - Power Spectral Analysis.** The analysis of relief variance is of significant importance for radar backscatter modeling, as originally demonstrated by Peak (1959), Valenzuela (1967), Barrick (1972), who made use of the covariance spectrum of relief in various perturbations of the Bragg-Rice scattering models.

Brown and Schaber (1980) found that covariance spectra obtained by the photogrammetric and statistical techniques described in the report can be used with a Bragg-Rice scattering model to predict radar cross-section values to some degree of success for saltpan and gravels within Death Valley, depending on the complexities created by volume and multiple scattering in near surface voids, and dielectric inhomogeneities created by dampness, as described in this report (also see van Zyl and others, 1991.)

This power spectral density PSD) subprogram computes the various frequency components of the relief (Rozema, 1969). Power spectral or time series analysis examines the frequency content of topographic or surface-roughness profiles. For natural terrain surfaces, most profiles are statistically random functions that can only be represented by the continuous variance spectrum. Elevation amplitudes that contribute to variability of a random isotropic surface above its mean height value thus are associated with a continuum of wavelengths. Separating a random profile into wavelength bands yields the spectral density of the relief variance, which is given as the square of the amplitude per unit bandwidth of the contributing wavelength bands (Pike and Rozema, 1975). This value is the power spectral density (PSD).

The variance spectral density program used in this study derives the autocovariance function and the Fourier transform of the autocovariance function that is the spectral density function of the variance and vice versa (Pike and Rozema, 1975). Autocorrelation of relief data enhances any periodicities that may be present in the topographic profile.

The "variance" or power spectral density graphs are sloping lines representing continuous functions of topographic (spatial) wavelengths (see Fig. 38). Because the greatest relief within a surface profile (natural terrain) is generally associated with the longer wavelengths, the spectral density decreases rapidly with decreasing terrain wavelength. The slopes of the PSD curves describe a relation between the relief content of the long and short features (Bryson and Dutton, 1967). An overall slope of -3 is thought to indicate a "uniformity" of topographic slope for all relief features in the sample area, regardless of their size (Bekker, 1969). A slope less steep than -3 indicates that small topographic features (high frequency) are rougher than large (low frequency) features. Likewise, a spectrum slope steeper than -3 suggests more rough, coarse-grained features and less smooth, fine-grained relief forms.

Digital bandpass filtering of the very low frequency data in the surface profiles is performed prior to calculation of the PSD functions. This operation is included because a long-term trend in the profiles affects the PSD function in two ways: (1) it may result in a nonstationary profile, that is, a profile whose statistical properties are affected by a change in origin; and (2) because the amplitude of the profile associated with the low frequency of a long trend would likely be relatively large, enough power would be contributed by the low frequency to obscure that contributed by higher frequencies (Rozema, 1969).

**Program 4 - Power Spectrum Plots.** This subroutine plots the elevation variance of relief as frequency (cycles per mm) vs. power spectral density ($mm^2$ per cycle per mm ). Conversion of the PSD values to $m^2$ per cycle per meter involves multiplying each frequency value by $10^3$. Pike and Rozema (1975) have shown that PSD values are interchangeable with variance [amplitude$^2$, per wave number (units$^2$)], in the same fashion: frequency (in cycles per unit) is interchangeable with wave number (units$^{-1}$). Immediately following the PSD plot, a least squares regression line fit equation is given for the PSD data in addition to the total variance of the integrated spectrum (see Schaber and others, 1980.)

**Program 5 - Slope Angle Between Slope Reversals.** There are innumerable ways to characterize topographic slopes. One of them is to identify terrain segments that occur between reversals in slope direction along a profile. Both the length and steepness of the slope are variables. Radar backscatter power is strongly dependent on the number of reflecting facets on the target area at moderate to high angles of incidence. This program can furnish quantitative data on such facets, which are areas between two adjacent slope reversals. Every reversal of slope from the input topographic profile is listed, as are the slope angle and slope length between these reversals. Also given are the three steepest and the three longest slopes, and the number of slope reversals per meter. A regression line is computed for slope length and slope angle.

**Program 6 - Slope Angle Against Slope Interval Plots.** This subroutine plots each slope length against its slope angle on semilog scale. The computer-printed graph is an approximation and may differ slightly from the actual values. Where more than nine values occupy the same position, a letter symbol code is printed indicating the number of points at that location. The steepest slope angle printed out is 20°. This value is too low a cutoff for microterrain applications, where the slopes are very steep (e.g., the Massive Halite unit in Death Valley (see Fig. 5a,b)). This graph is only of minor value in its present format.

**Program 7 - Base Length Slope Angle and Curvature.** This subprogram is exceptionally comprehensive and flexible, and yields a large amount of information on surface roughness. Two parameters, slope angle and the angle of slope curvature, are computed at different values of the unit cell, or base length (delta-L). Slope angle at the smallest delta-L, the input sampling interval, is simply the slope of the line connecting any two adjacent sample elevations. Curvature is the angle subtended by three adjacent elevations along the traverse (Fig. A1). Calculations start with a horizontal sampling interval (delta-L) of X mm (3.0 mm in the example shown in Schaber and others, 1980). The subroutine then calculates algebraic and absolute values of statistics for both slope angle and the angle of curvature, including minimum, maximum, mean, variance, standard deviation, skewness, kurtosis, and median. Absolute values are unsigned. Algebraic values are positive (slopes facing the end of the profile and convex curvatures), and negative (slopes facing the opposite direction and concave curvatures)(Fig. A1). Algebraic frequency distributions are symmetric about the zero values and often approach the Gaussian ideal. Absolute distributions approach the "half-normal" model (Elandt, 1961) and are skewed strongly to the right. Slopes and curvatures calculated by both conventions are necessary and complement one another.

The dispersion coefficient (algebraic standard deviation divided by absolute mean) is analogous to the usual coefficient of variation (Croxton and others, 1967, p. 189), and is an excellent measure of relative dispersion. The "Elandt coefficient" (informal name by Pike, 1978), defined as absolute mean divided by absolute standard deviation (Elandt, 1961), can be used as a rapid initial test for the "half-normality" of an absolute slope frequency distribution (see Pike, 1978, pp. 14-15).

Following a listing of the number of negative and positive values of slope and curvature (and their ratios) are tabulations of algebraic and absolute frequency-distribution statistics. These are intended for histograms and other graphic output. The percent (10 to 90) dispersion of the algebraic values is also listed, in addition to the results of a chi-square test for the normality of the algebraic frequency distribution of both slope and curvature. Regression line-fits are calculated relating cumulative percent frequency and slope angle and cumulative percent frequency and percent mean slope.

Similar regression equations are given for the curvature statistics. These equations enable the histograms to be roughly expressed by only two parameters, slope and coefficient of the fit.

The delta-L value (sampling interval) is then doubled (for example, from 3.0 mm to 6.0 mm in the example given in Schaber and others, 1980) and all calculations are rerun. This steepening of the delta-L value continues until the desired level of sampling interval is reached or until too few cases remain to calculate good statistics. The final calculation in the program are linear regression fits relating delta-L to mean absolute slope and curvature for all iterations. This valuable equation can be used to assess the relation of slope and curvature angles for a specific terrain at various fractions (or multiples) of radar wavelength scales (where delta-L is equated to roughness sampling-interval of the radar).

**Possible Program Improvements.** The Terrain Analysis Module has been found to be almost ideal for radar backscatter modeling studies of fine-scale relief, and can be used with topographic information derived from either in situ templets or photogrammetric reduction of stereo photographs. Experience with this software, however, has indicated the need for at least four additional computations and plotting subroutines of significance to radar backscatter modeling: (1) height correlation coefficient (autocorrelation), or statistical association between various pairs of elevations along a profile; (2) probability density function for surface elevations; (3) probability density functions for surface slopes (Pike and Rozema, 1975; Barrick, 1970); and (4) root mean square (rms) slopes and curvatures for all base lengths. These additional programs and subroutines could simply be added. Autocorrelation of surface heights already is performed as part of the PSD computations (Program 3) and merely needs to be printed out. The information on relief and slope curvature necessary for calculating their probability density functions is available in Programs 2 and 7. Only the rms calculations will require writing an entirely new subprogram.

## APPENDIX A FIGURE

**Figure A1** - Diagrammatic representation of slope curvature along a profile. Dots show ground surface. Circles are sample elevations measured at a constant horizontal increment (delta-L). Positive curvature shown by $\alpha$; negative curvature by $\beta$.

# APPENDIX B

## LABORATORY DIELECTRIC CONSTANT MEASUREMENTS

Samples collected from Death Valley saltpan and fan gravel surfaces during the JSC scatterometer overflight in 1976 and the JSC ANAPQ-102 X-band dual-polarization SAR overflight of in 1981 were measured in the laboratory for both real and imaginary component of dielectric constant, and the resultant dielectric constant (Table B1). The laboratory measurements were performed by H. F. Gonzalez (Secondary Standards Branch) and James A. Harmon (Chief, Calibration Division Quality assurance Officer), both of the U.S. Army White Sands Missile Range, New Mexico. As shown in Table B1, resultant dielectric constant values ($\varepsilon_r$) from 2.7 to 16.6 were measured at 13.3 Ghz for dry to wet samples (1.24 to 24.7% $H_20$, by weight, respectively) from the Quaternary floodplain deposits (Qf) (Stations G and H; Figs. 1, 2, 9). *Because of this wide diversity in dielectric properties, the authors suggest that the floodplain deposits not be used to constrain the low roughness (smooth) end of empirical-derived radar backscatter inversion models that may be developed using the Death Valley saltpan surfaces .*

## APPENDIX B FIGURE

<u>**Figure B1**</u> - Resultant dielectric constant plotted against weight percent water for samples listed in Table B1.

## APPENDIX B TABLE

<u>**Table B1**</u> - Laboratory Measured Dielectric Properties for Death Valley Samples

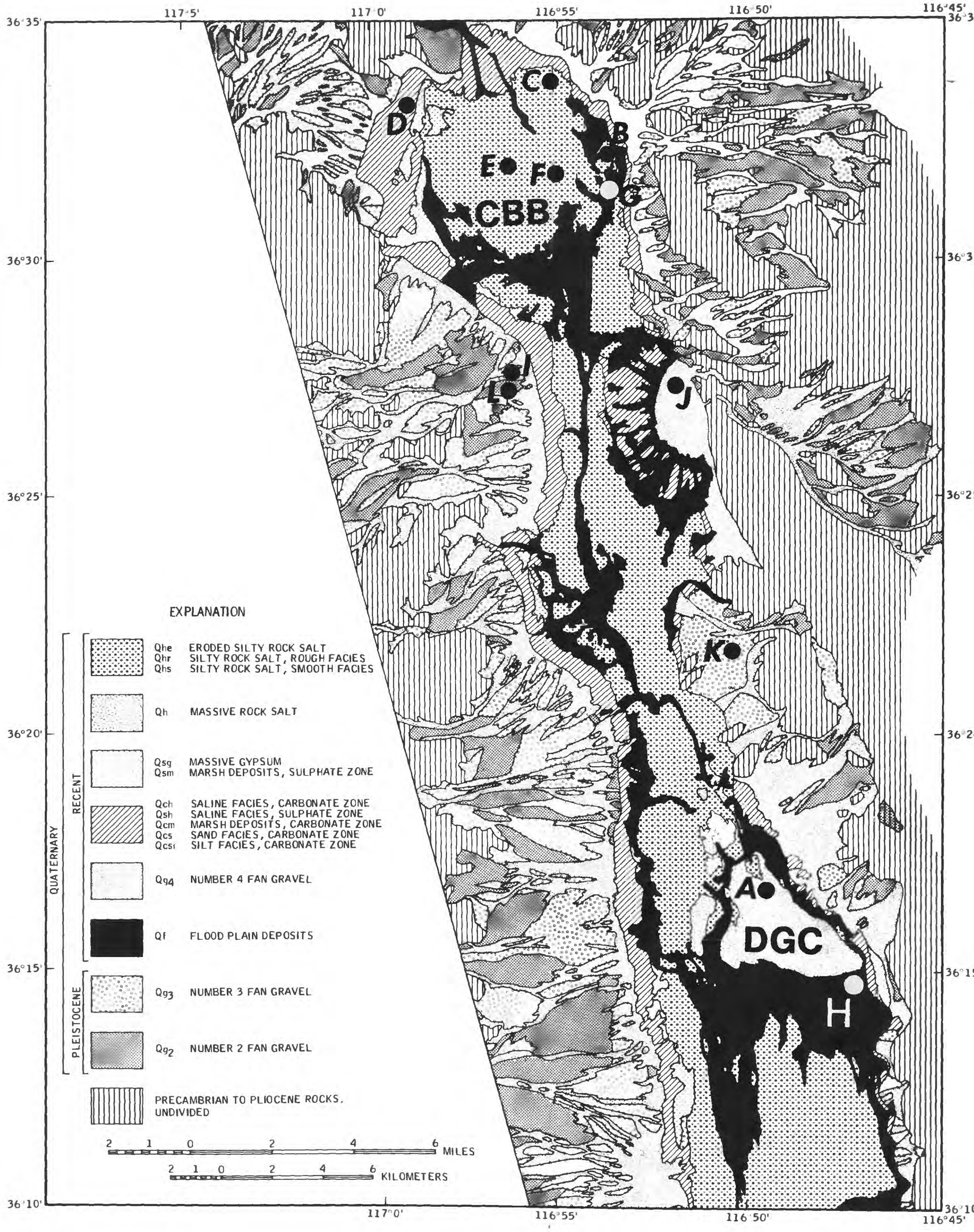
117°5'
117°0'
116°55'
116°50'
116°45'
36°35'
36°30'
36°25'
36°20'
36°15'
36°10'
C
D
B
E
F
G
CBB
I
L
J
K
A
DGC
H
EXPLANATION
QUATERNARY
RECENT
PLEISTOCENE
Qhe ERODED SILTY ROCK SALT
Qhr SILTY ROCK SALT, ROUGH FACIES
Qhs SILTY ROCK SALT, SMOOTH FACIES
Qh MASSIVE ROCK SALT
Qsg MASSIVE GYPSUM
Qsm MARSH DEPOSITS, SULPHATE ZONE
Qch SALINE FACIES, CARBONATE ZONE
Qsh SALINE FACIES, SULPHATE ZONE
Qcm MARSH DEPOSITS, CARBONATE ZONE
Qcs SAND FACIES, CARBONATE ZONE
Qcsi SILT FACIES, CARBONATE ZONE
Qg4 NUMBER 4 FAN GRAVEL
Qf FLOOD PLAIN DEPOSITS
Qg3 NUMBER 3 FAN GRAVEL
Qg2 NUMBER 2 FAN GRAVEL
PRECAMBRIAN TO PLIOCENE ROCKS, UNDIVIDED
2 1 0 2 4 6 MILES
2 1 0 2 4 6 KILOMETERS

Figure 1


K
ADF
MB
A
DGC
H
BB
X BAND 1976 SCANNED 50 MICRON. SPLICED, TONE MATCHED, TBLSTR.
1970 NS FILE

Figure 2a

TOP?

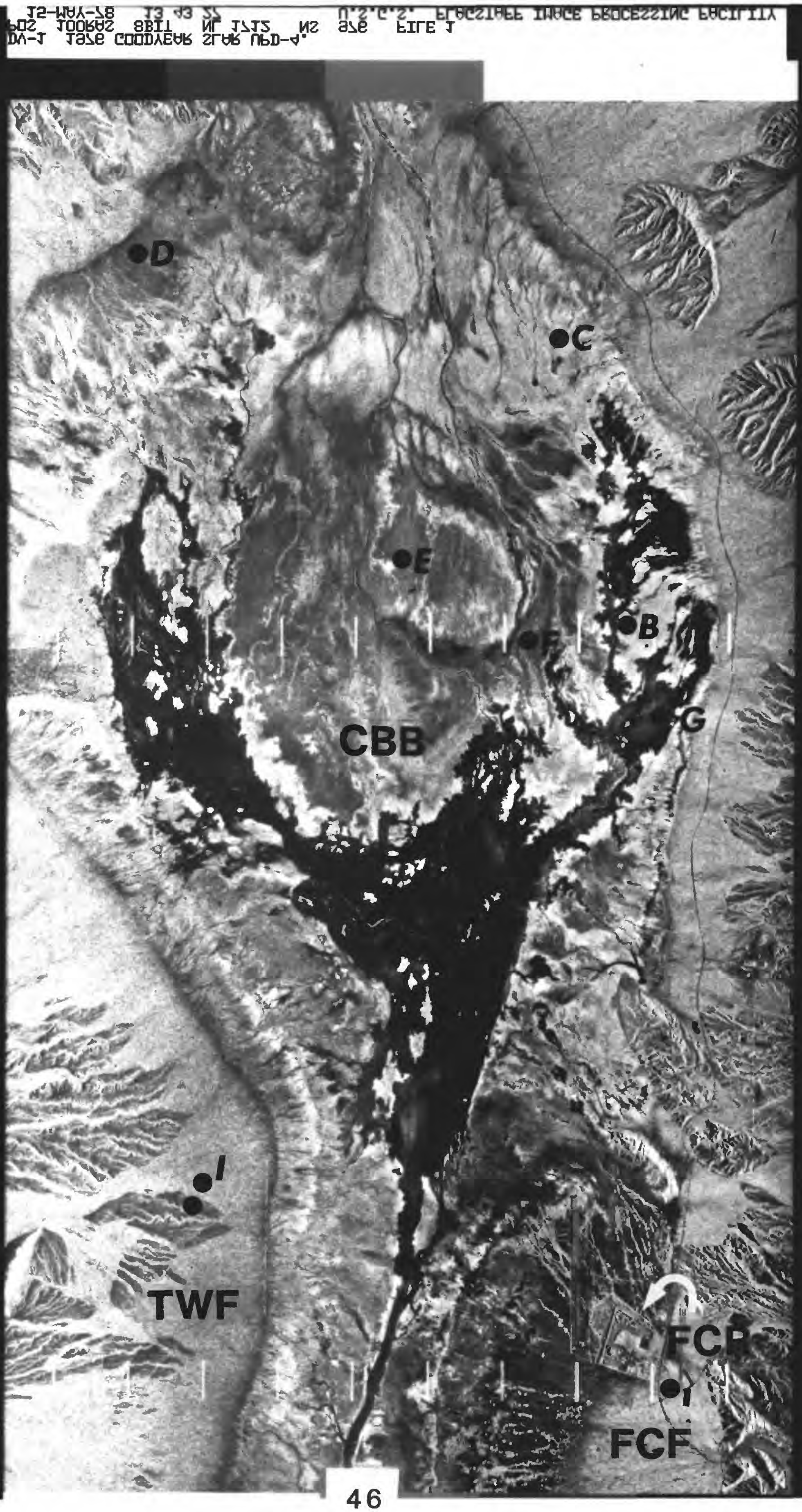

Figure 2b

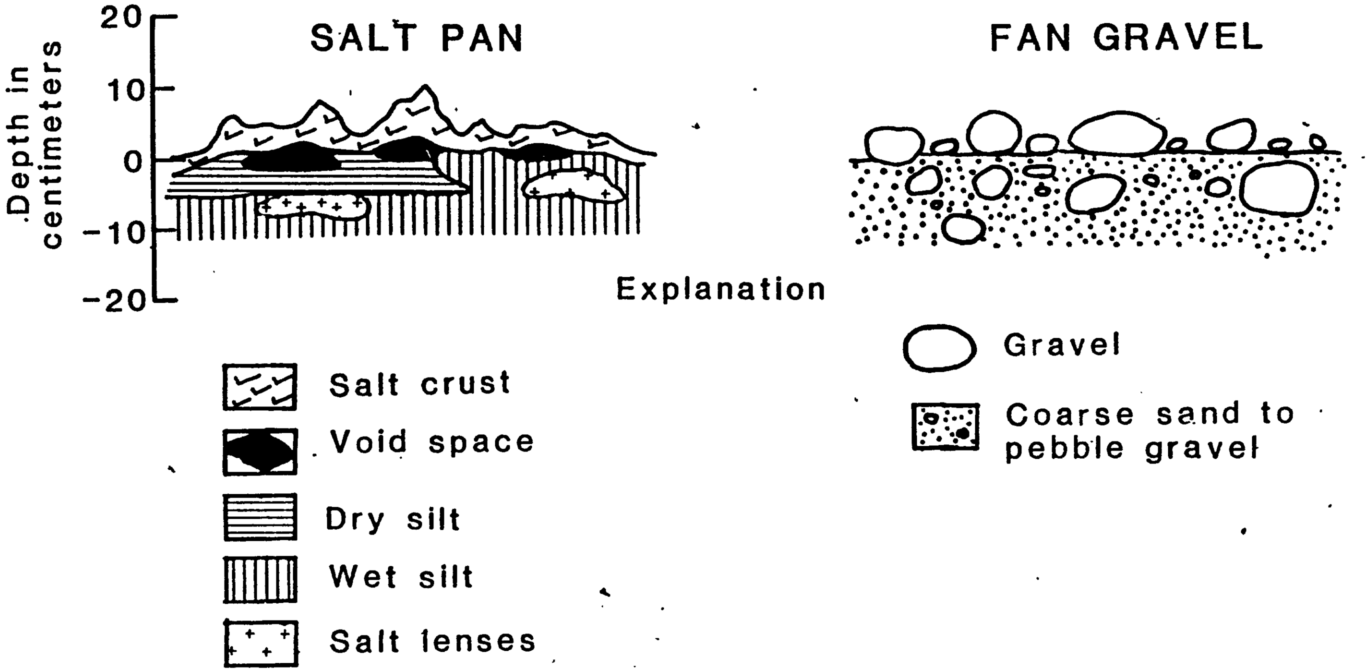
20
10
0
-10
-20
Depth in centimeters
SALT PAN
FAN GRAVEL
Explanation
Salt crust
Void space
Dry silt
Wet silt
Salt lenses
Gravel
Coarse sand to pebble gravel

Figure 3

**TABLE 1 - Death Valley Sample Site Locations (Degrees/Minutes/Seconds)**

| | | | | | |
|---|---|---|---|---|---|
| | | | | | |
| **SITE** | **LOCATION** | | **LATITUDE** | **LONGITUDE** | |
| | | | | | |
| A | Devil's Goilf Course | | 36/16/54 | 16/49/39 | |
| | | | | | |
| B | Cottonball Basin | | 36/31/57 | 116/54/03 | |
| | | | | | |
| C | Cottonball Basin | | 36/33/42 | 116/55/13 | |
| | | | | | |
| D | Cottonball Basin | | 36/32/36 | 116/59/45 | |
| | | | | | |
| E | Cottonball Basin | | 36/31/45 | 116/57/45 | |
| | | | | | |
| F | Cottonball Basin | | 36/31/51 | 116/55/06 | |
| | | | | | |
| G | Badwater Basin | | 36/13/51 | 116/46/49 | |
| | | | | | |
| H | Badwater Basin | | 36/13/57 | 116/46/30 | |
| | | | | | |
| I | Tucki Wash Fan | | 36/27/30 | 116/56/12 | |
| | | | | | |
| J | Furnace Creek Fan | | 26/27/26 | 116/51/46 | |
| | | | | | |
| K | Artist's Drive Fan | | 36/21/38 | 115/50/42 | |
| | | | | | |
| L | Tucki Wash Fan | | 36/27/23 | 116/56/09 | |

Table 1

| | TABLE 2 - QUATERNARY GEOLOGIC UNIT DESCRIPTIONS: DEATH VALLEY, CALIFORNIA | | |
|---|---|---|---|
| **STATION CODE** | **GEOLOGIC UNIT** | **UNIT SYMBOL** | **DESCRIPTION** |
| | | **SALTPAN SURFACES** | |
| A | Massive rock | Qh | Approximately 1 to 2 m thick; 95% sodium chloride. |
| | salt | | Exceedingly rough jagged surface, earning the name "Devil's Golf Course". |
| | | | Elevated and protected against annual flooding. |
| | | | Vegetation lacking. |
| B-C | Silty rock salt | Qhr(1)(2) | Approximately 0.6 to 1.5 m thick. Capped by brown silty layer |
| | Rough facies | | 2.5 to 5 cm thick containing sulfate and borate salts. |
| | | | surface rough. Elevated and protected against most flooding. Vegetation lacking. |
| D | Carbonate Zone | Qch | Sand and silt facies of Pleistocene lake deposits impregnated |
| | | | with Holocene carbonate and sulfate salts. Surface layer 15 to |
| | | | 46 cm thick. Low parts subject to flooding. Runoff |
| | | | is by solution pits. Vegetation when present is most commonly pickleweed. |
| E-F | Silty rock salt | Qhs (1)(2) | Surface layer is brown silt 5 to 46 cm thick containing sulfate |
| | smooth facies | | and borate salts underlain by 5 to 46 cm of silty rock salt. |
| | | | Subject to some flooding from adjacent streams. Vegetation lacking. |
| G-H | Flood plain | Qf (1)(2) | Lowest saline deposit in elevation. Subject to seasonal flooding which |
| | deposits | | produces a smooth playa surface. May be periodically damp with salts |
| | | | held in solution. Vegetation lacking except along washes traversing the carbonate zone. |
| | | **FAN GRAVEL SURFACES** | |
| I-J | Fan gravel | Qg3 (1)(2) | Younger of the upper Pleistiocene and Holocene fan gravels. |
| | facies | | Mostly pebble- to cobble-size gravel with scattered boulders. |
| | | | Older surfaces veneered with desert varnish. Xerophytic vegetation. |
| K | Fan gravel | Qg3 (3) | Pebble- to sand-sized zone, 100-200 m wide, at the base |
| | facies | | of gravel fans. Xerophytic vegetation. |
| L | Desert | Qg2 | Older of the upper Pleistiocene fan gravels. Formed by |
| | Pavement | | disintegration of originally round pebbled, cobbles, and boulders |
| | | | into a smooth interlocking surface usually one layer thick and underlain |
| | | | by silt. Surface coated with desert varnish. Vegetation lacking. |
| Adapted from Hunt and Mabey (1966) | | | |

Table 2

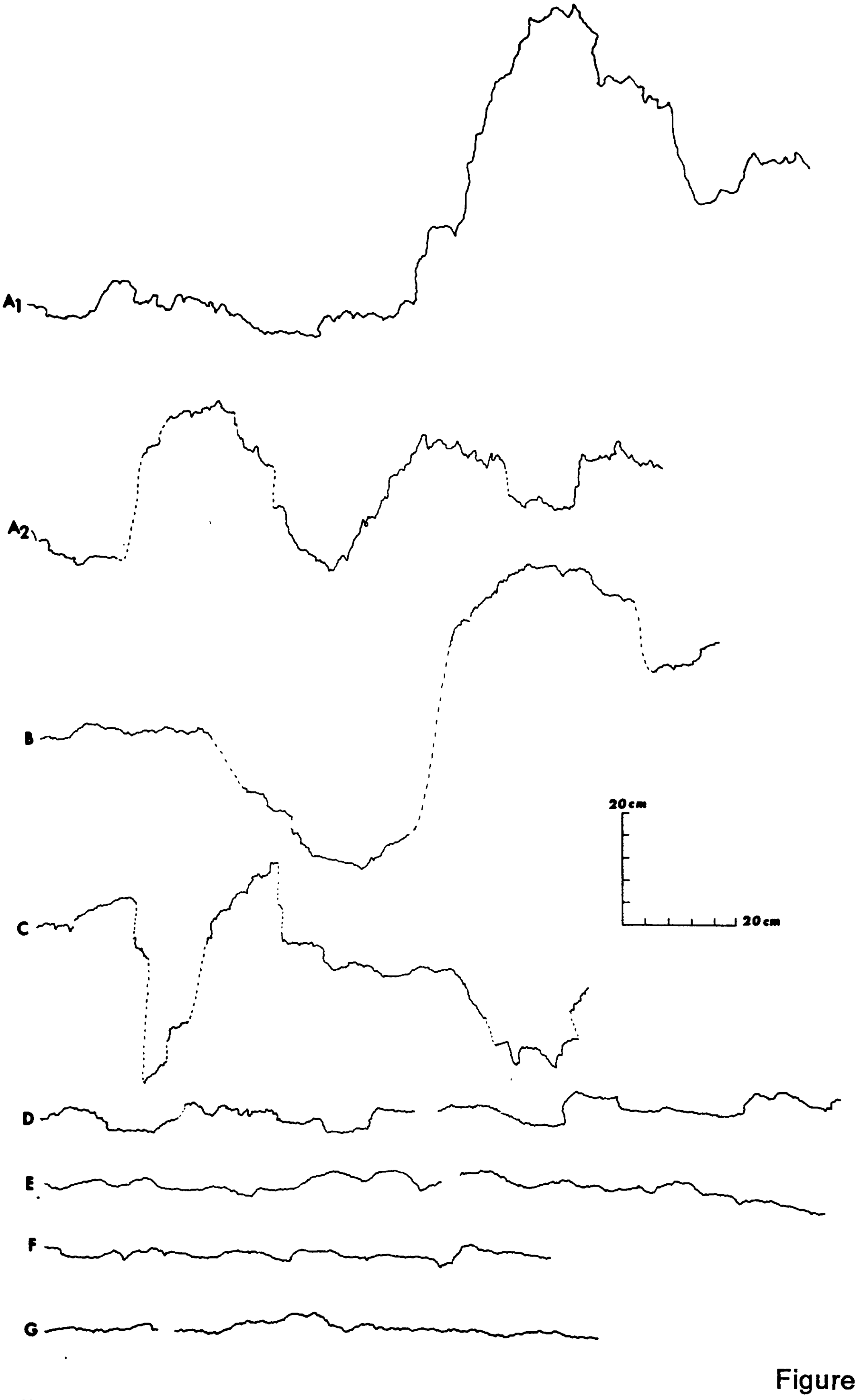

Figure 4a

X-Profile

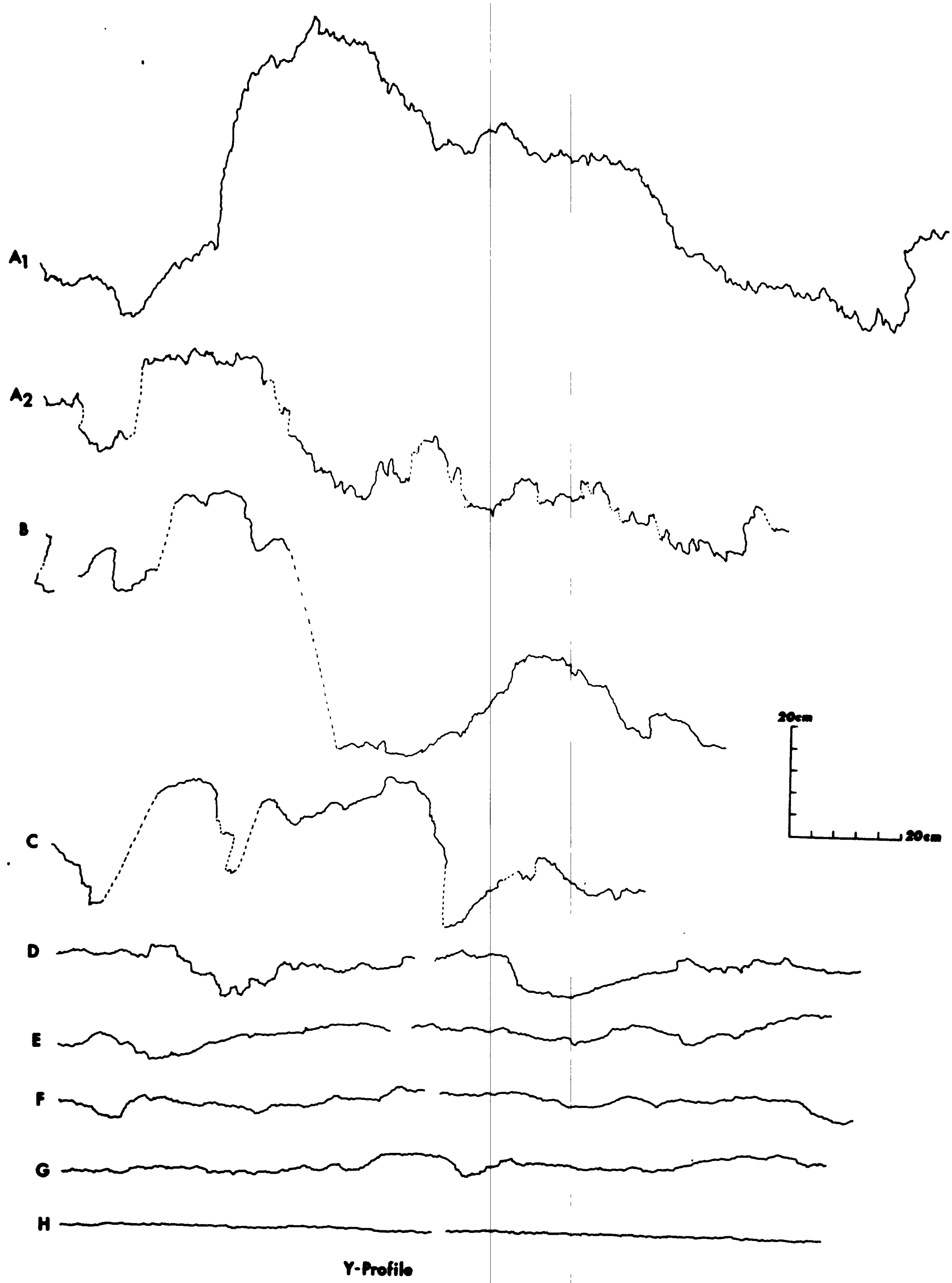

Figure 4b

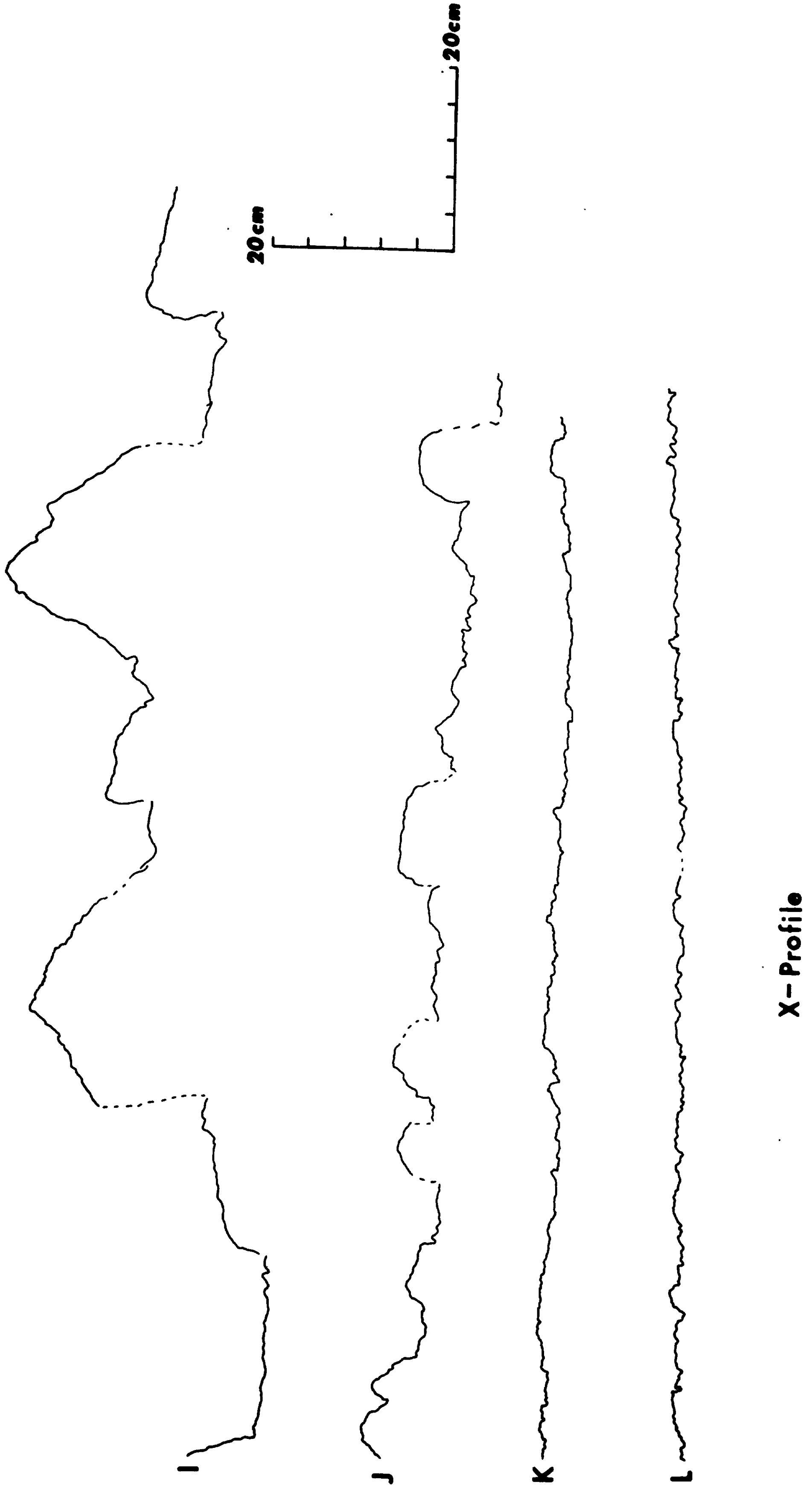

Figure 4c

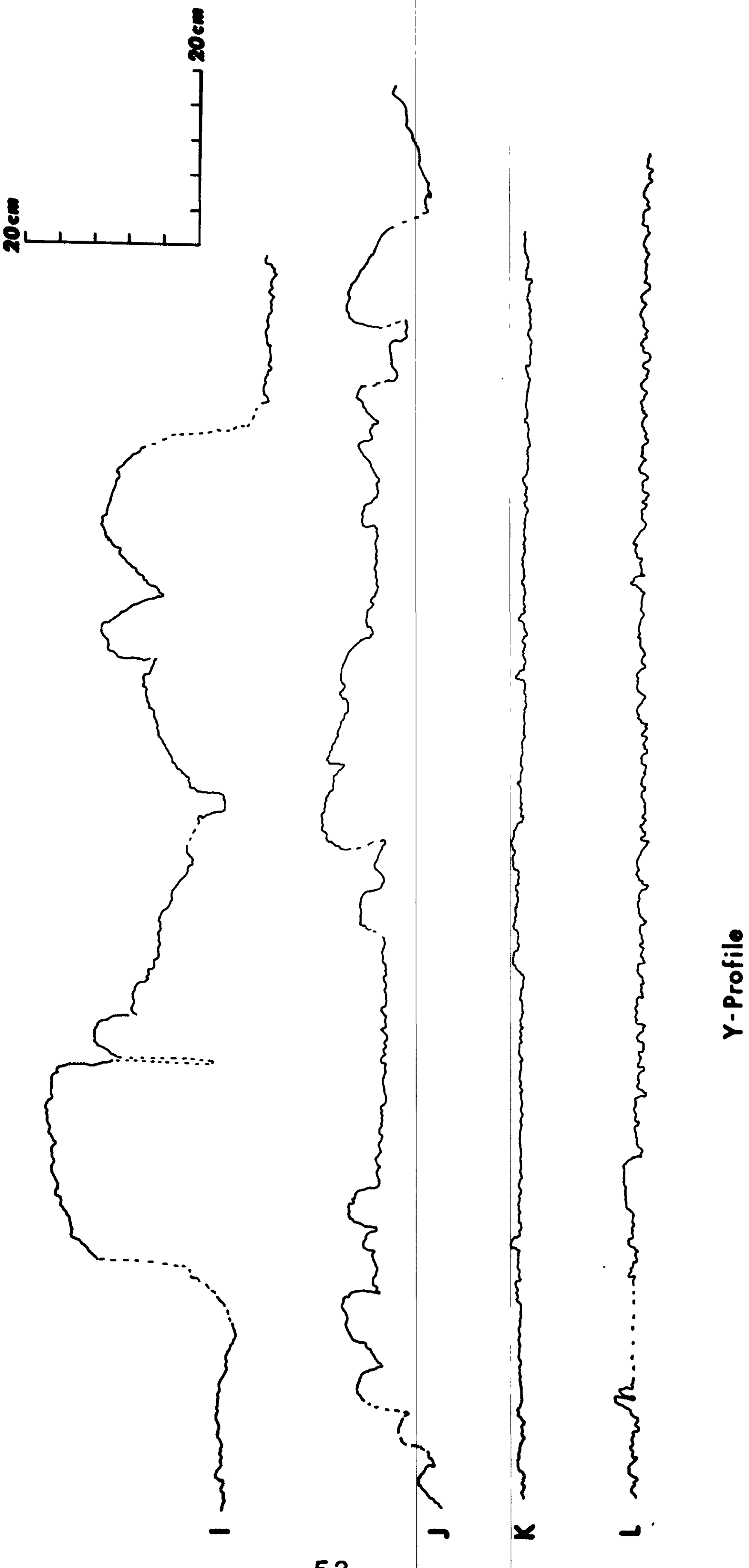

Figure 4d

Figure 5a

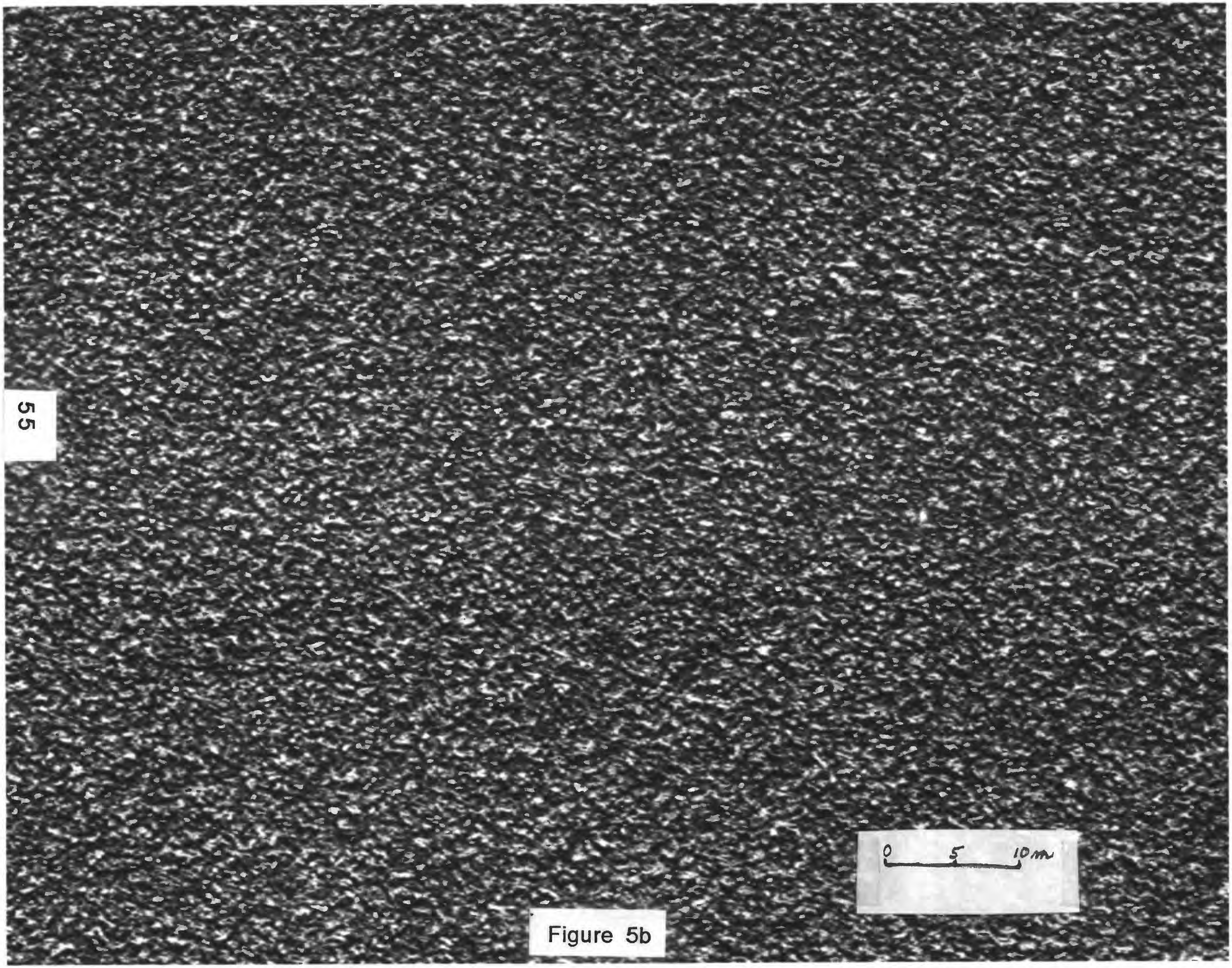

Figure 5b

Sta T7-8/4
Cottonwood Basin

Figure 6

Qch
Cottonball Basin
(Sta L13-14/Qch)

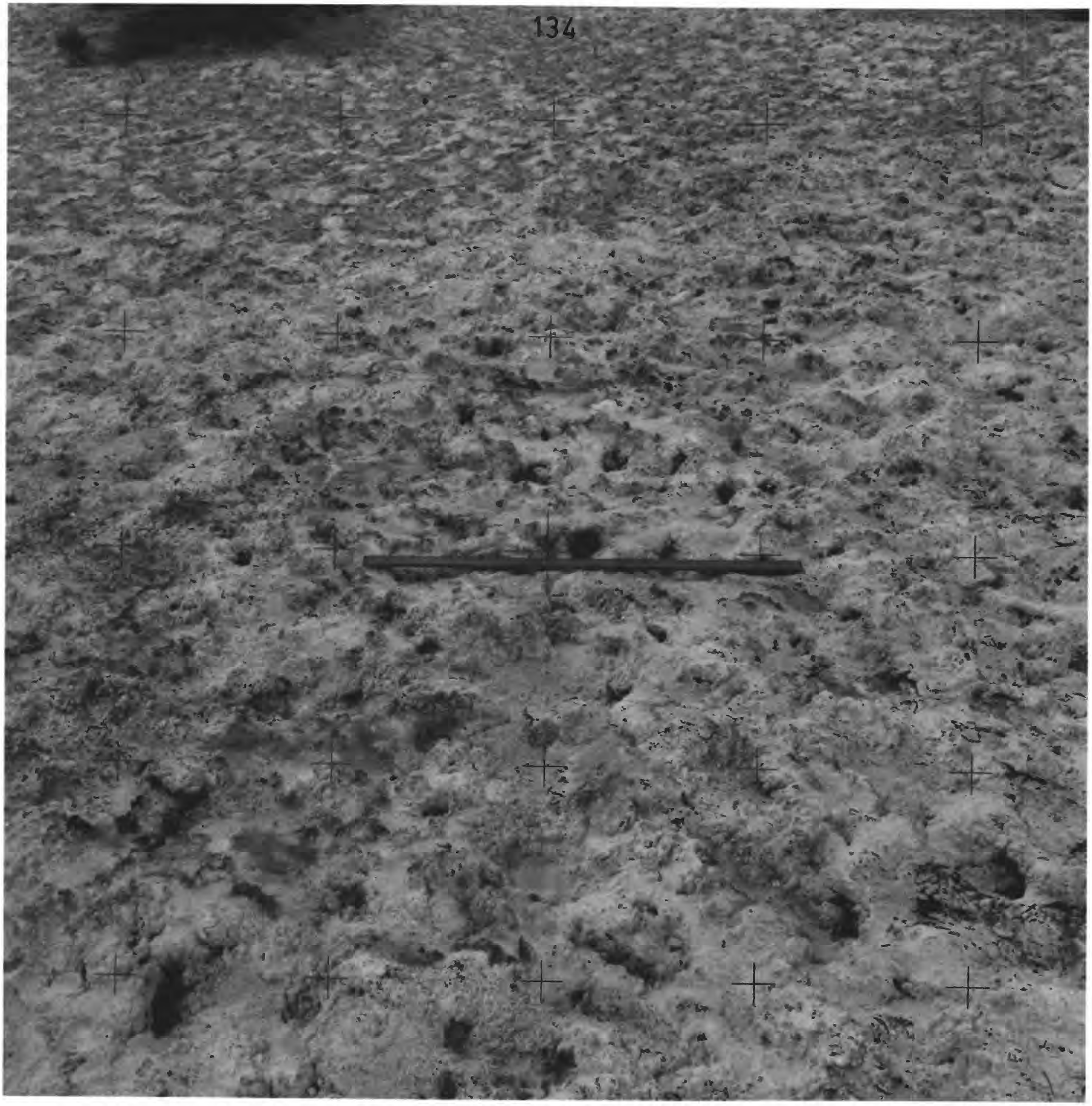

Figure 7

Model 1/Qhs
Cottonball Basin
Station

Figure 8

Model 4/9+
(Smooth) 6-77-13
Badwater

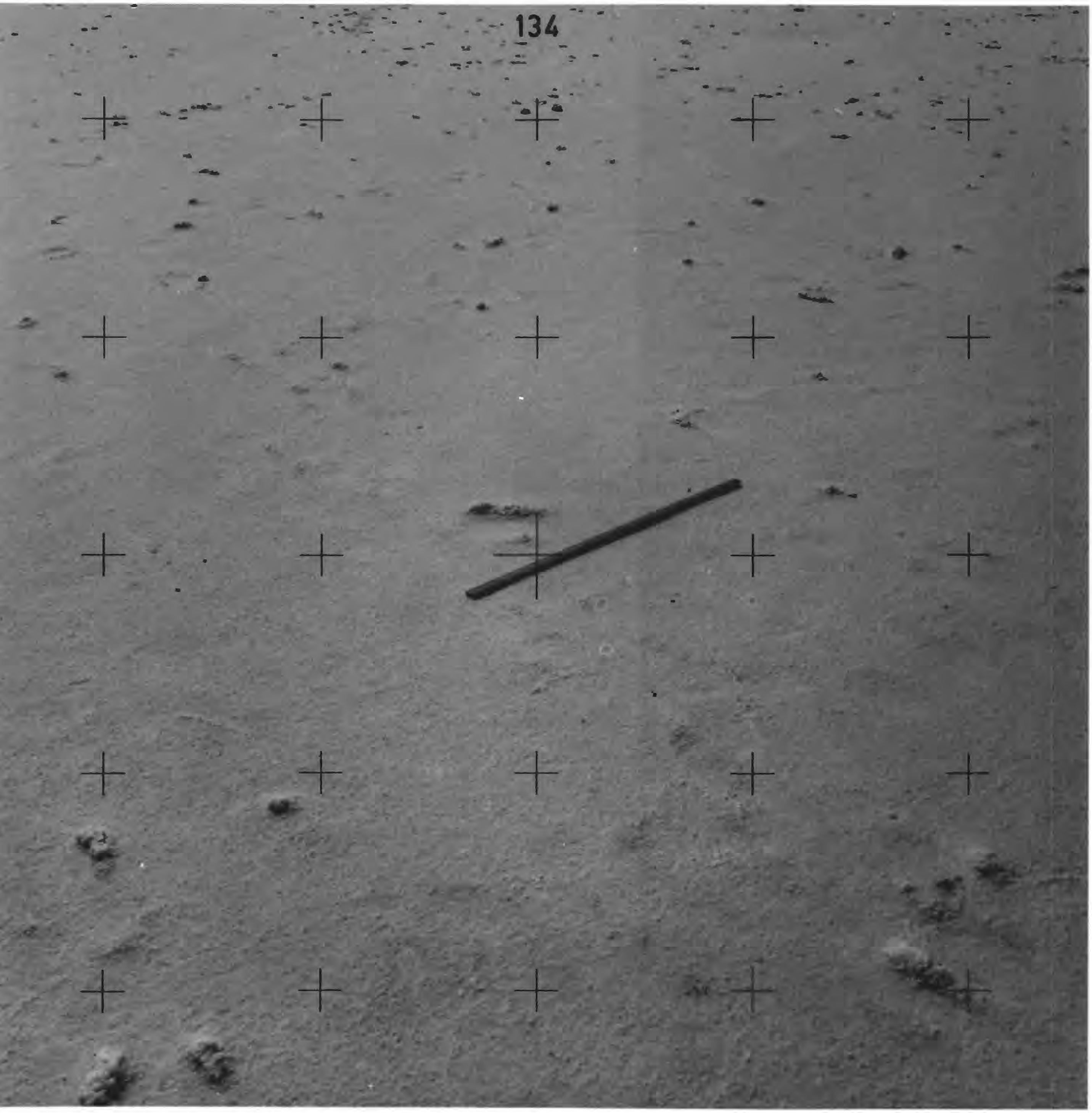

Figure 9

Figure10

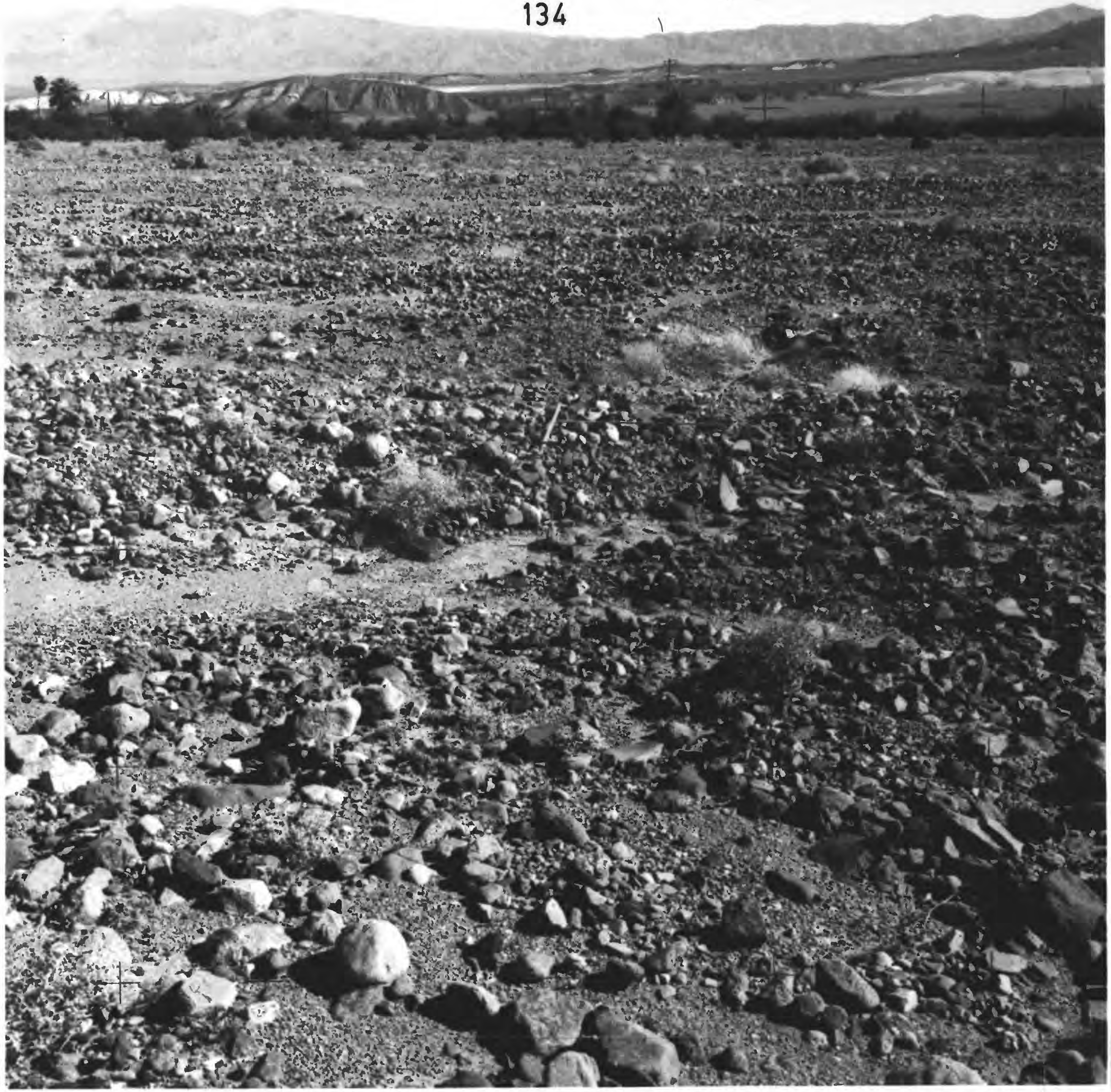

Figure 11

model 3/Qg3 smooth 6-77-5 Roll #1 #2

Qg3 Artists Drive

Figure 12

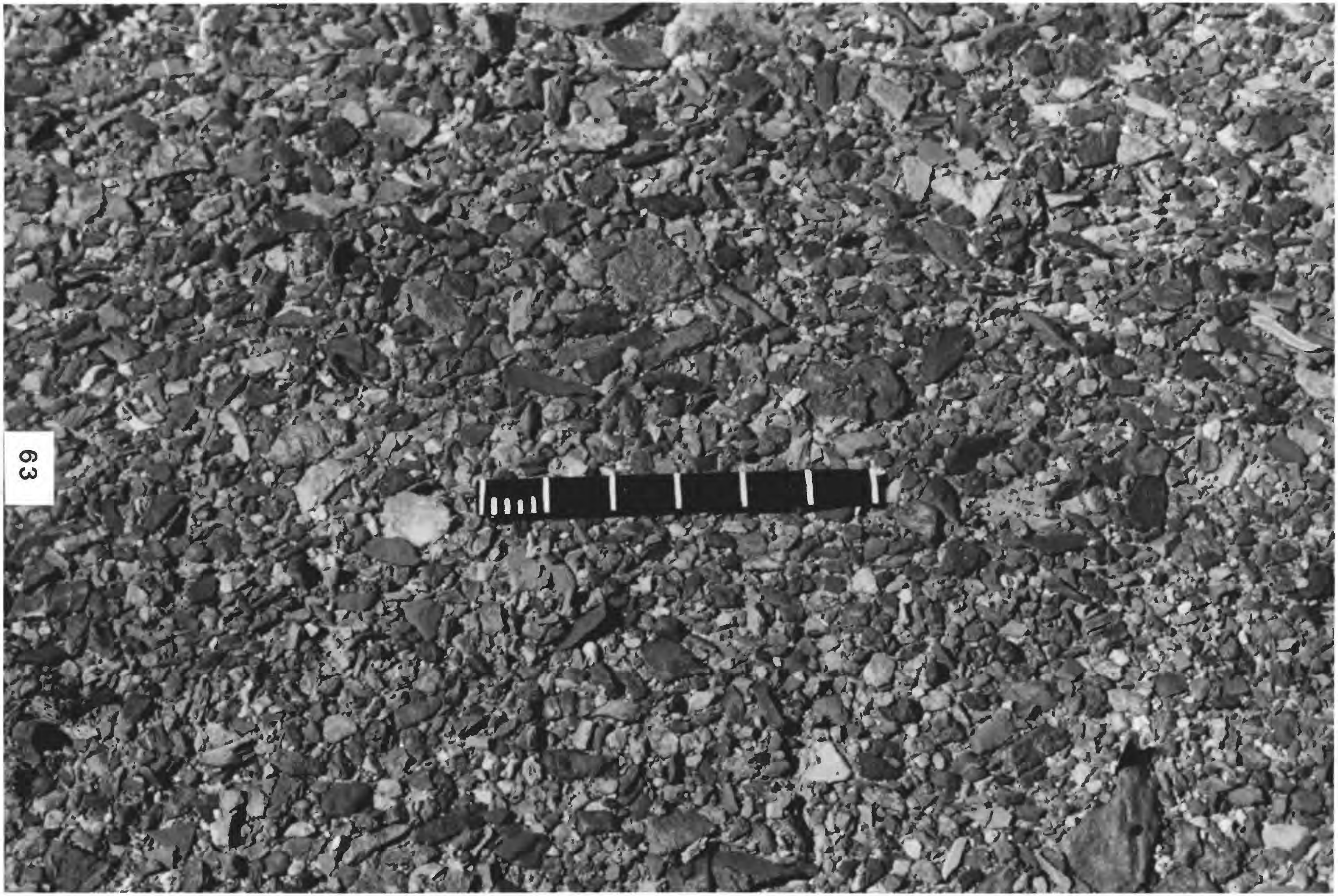

Figure 13

BoTTom

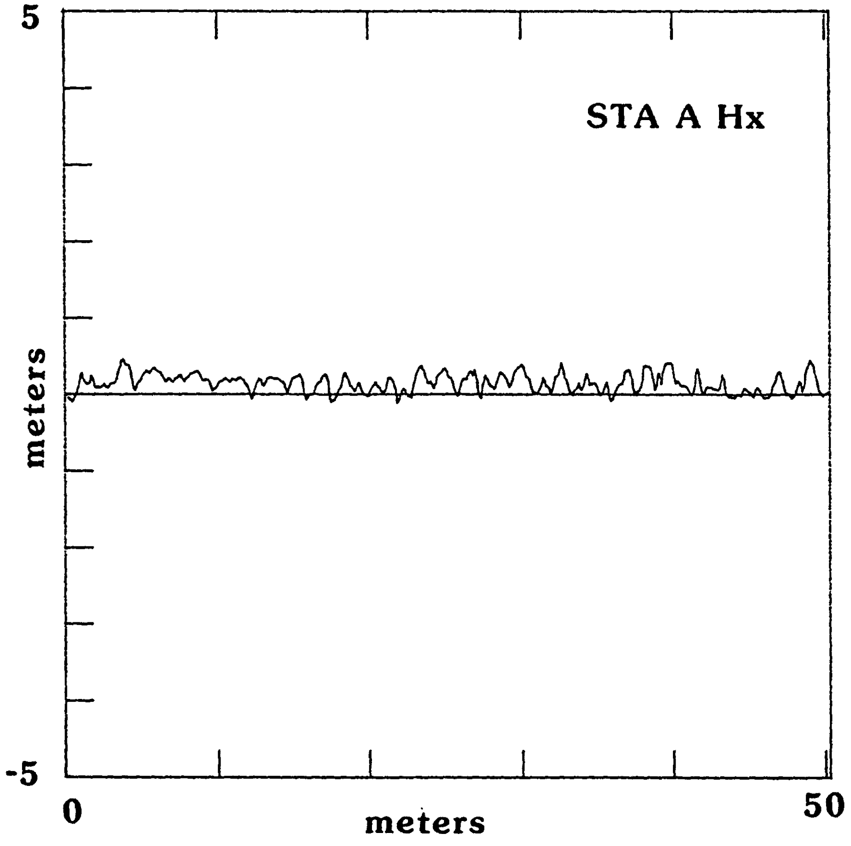

Figure 14a

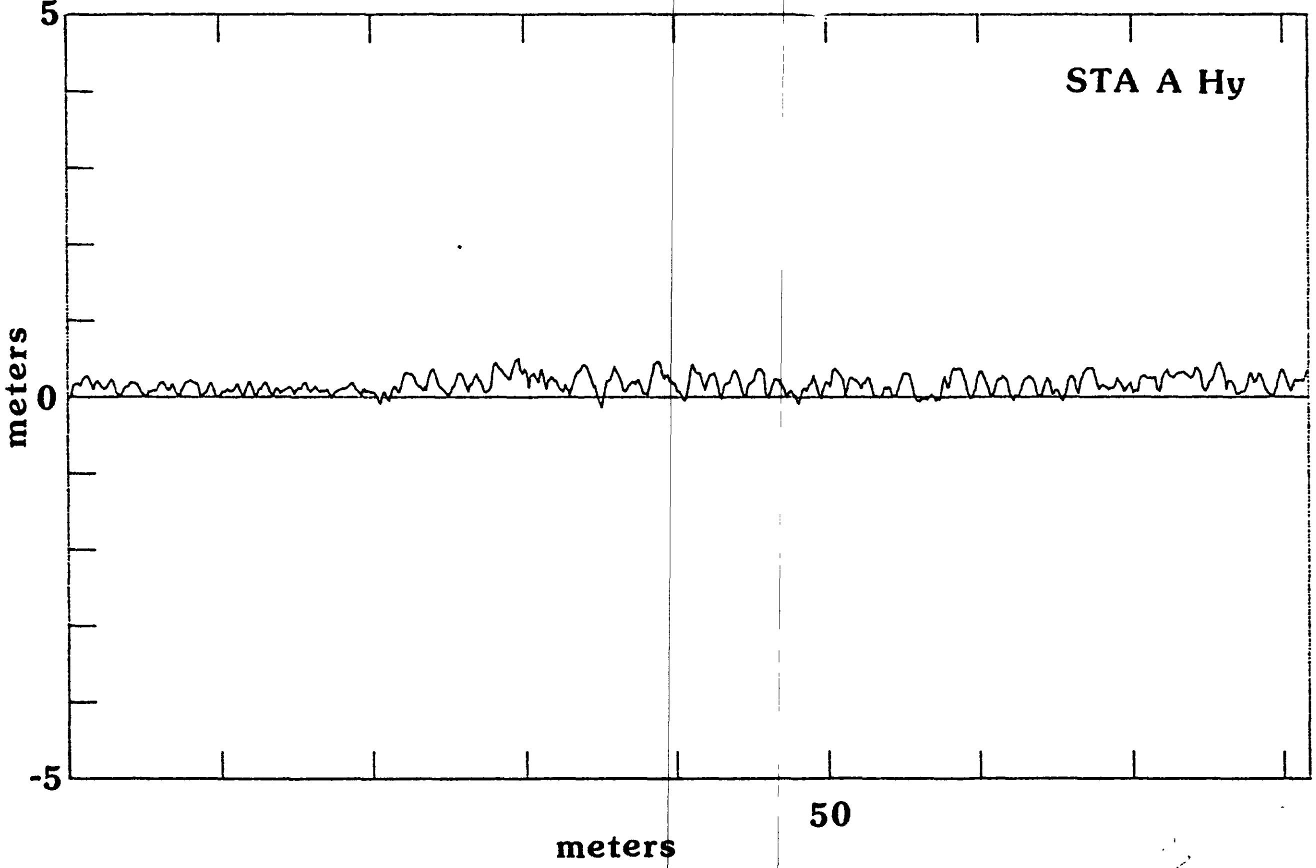

Figure 14b

(pg 67 follows)

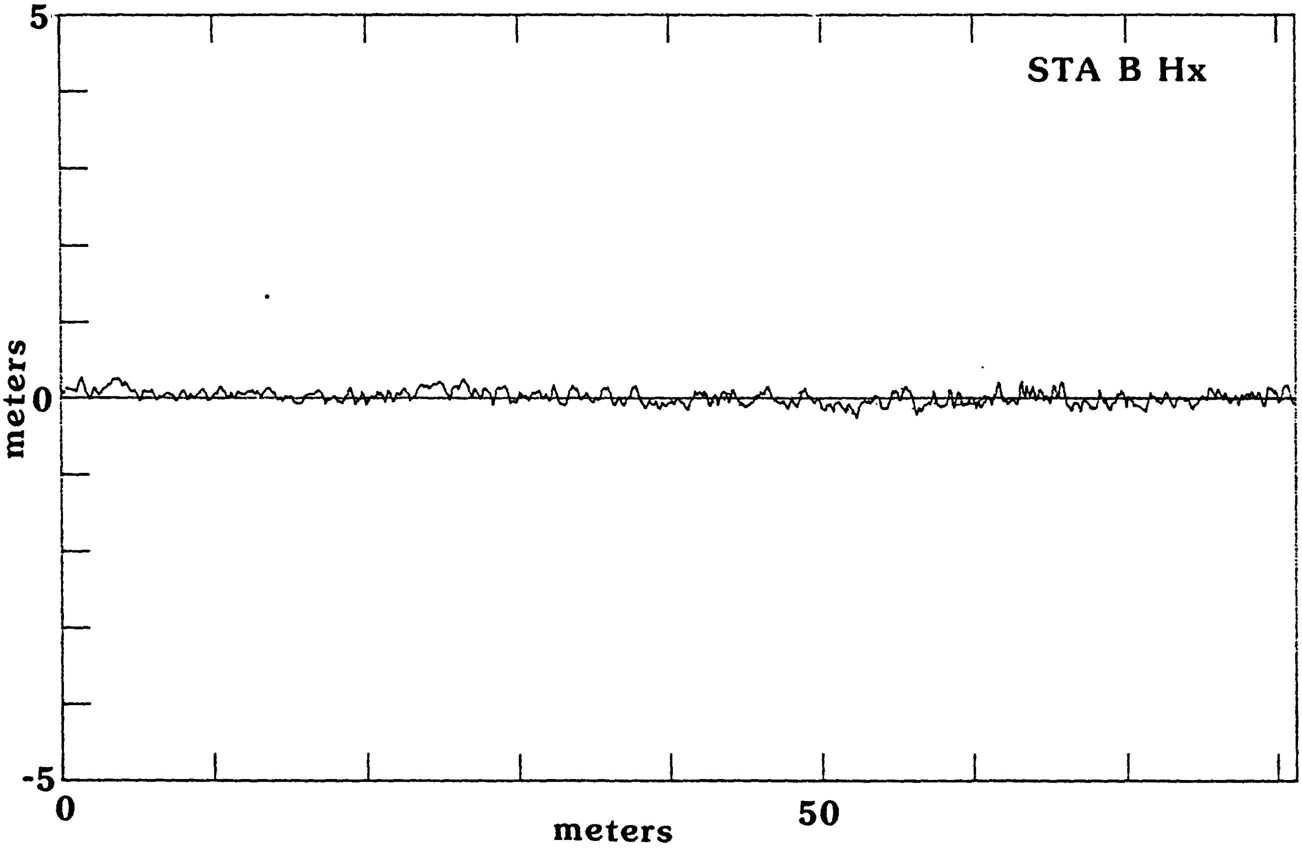

Figure15a

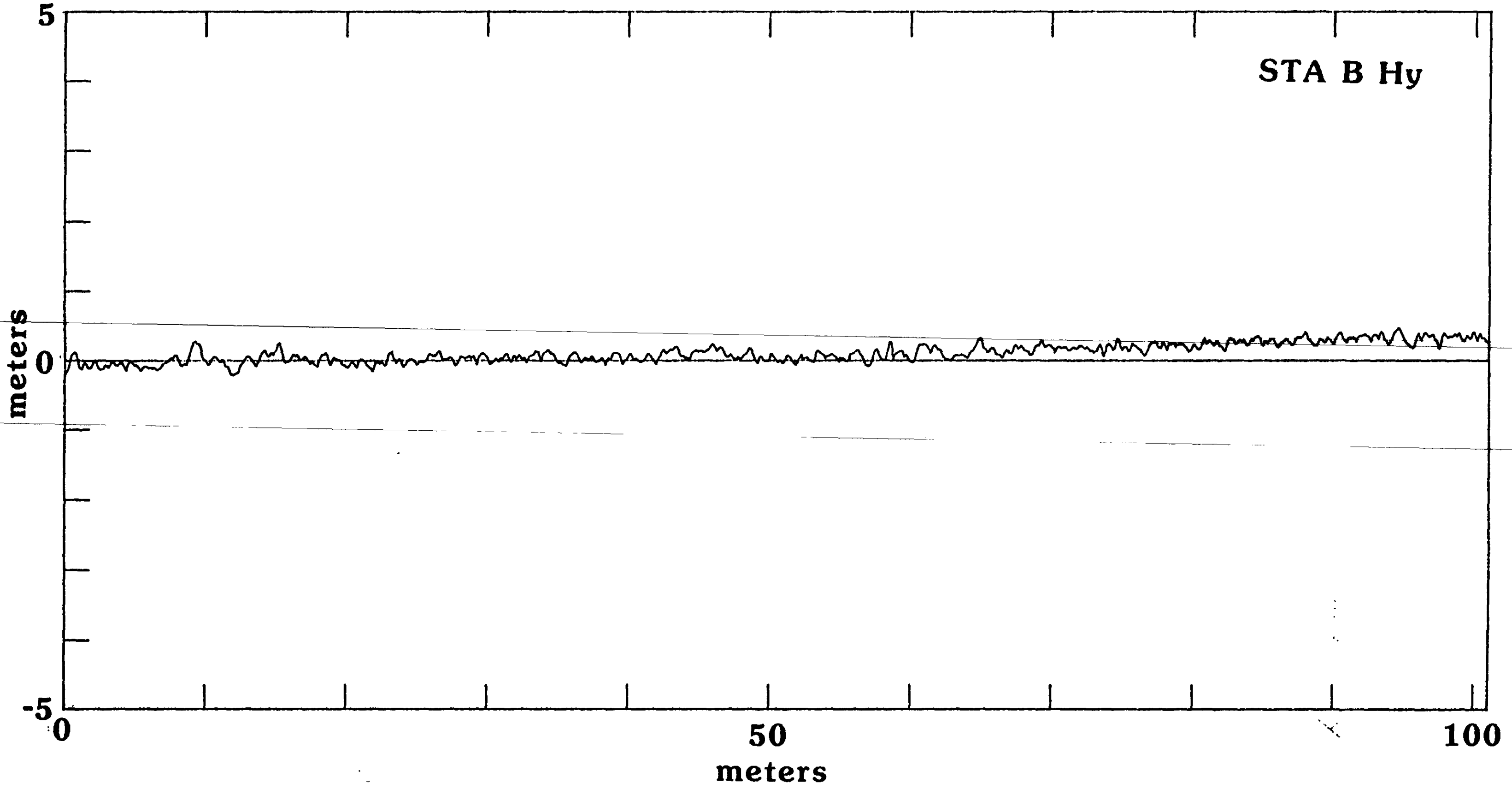

Figure 15b

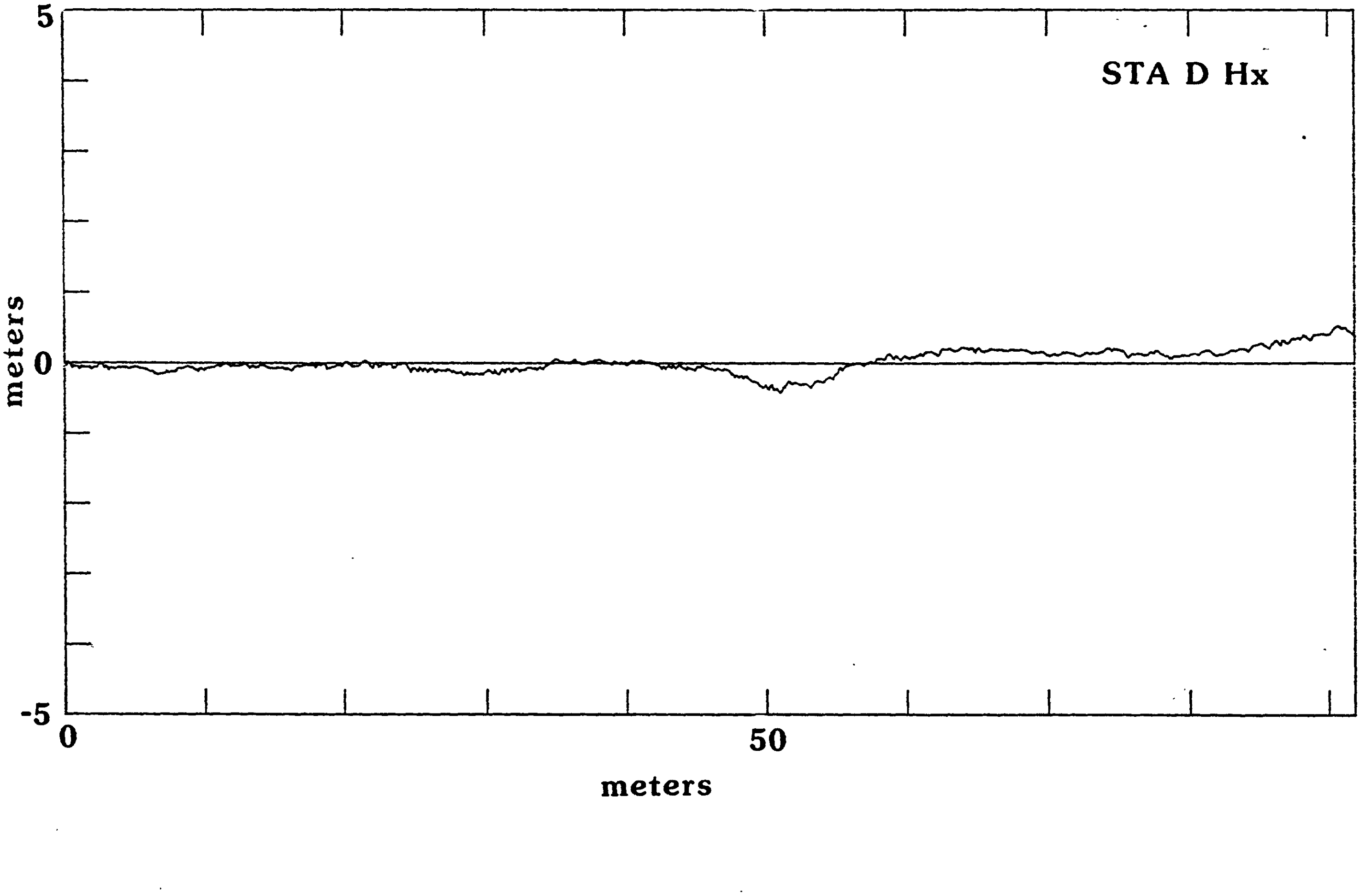

Figure 16a

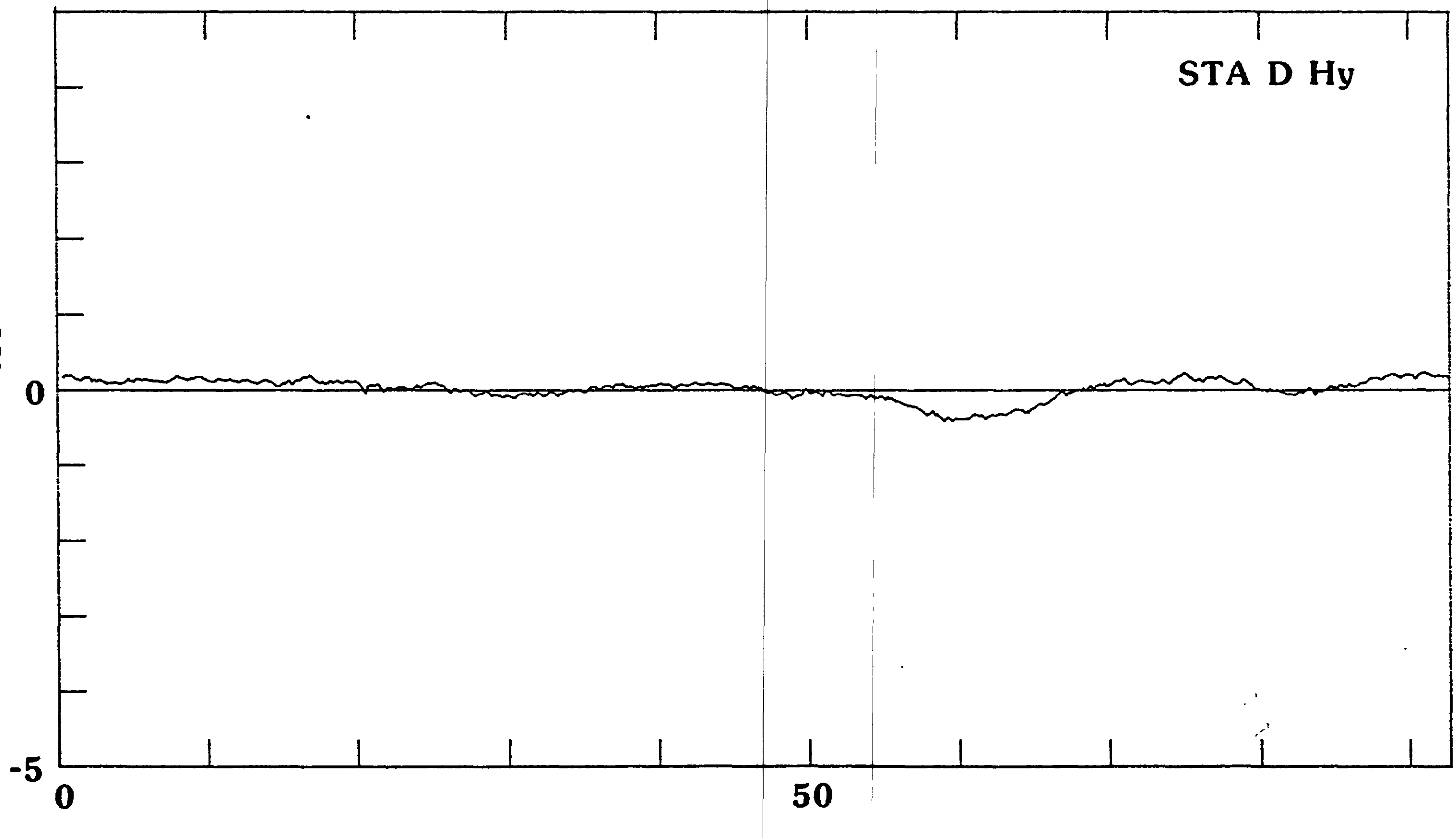

Figure16b

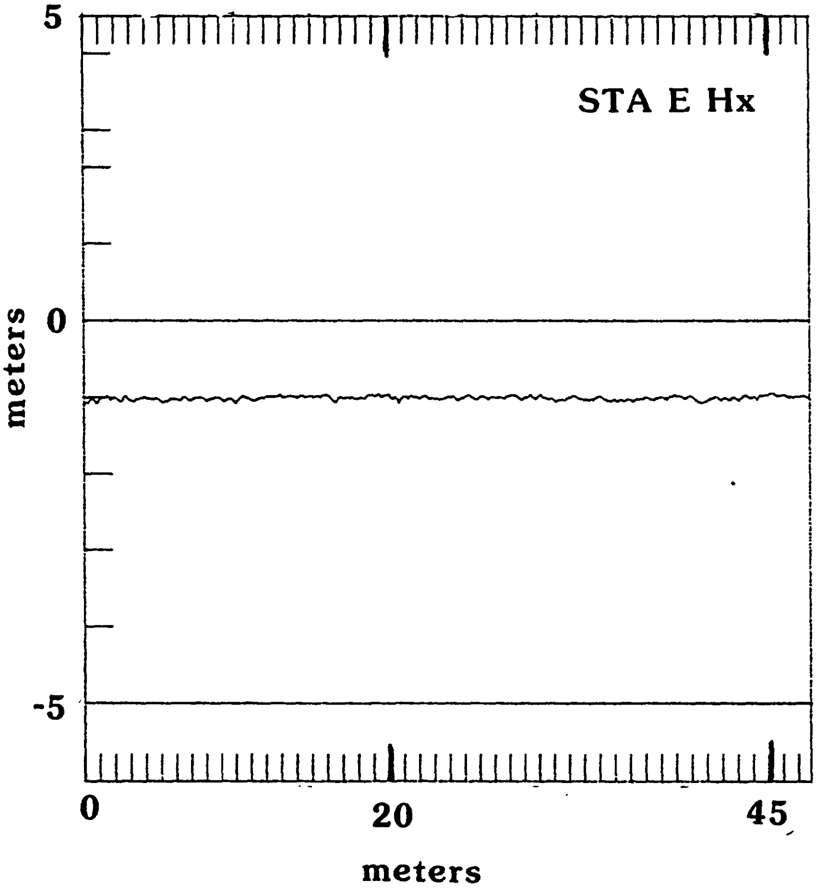

Figure 17a

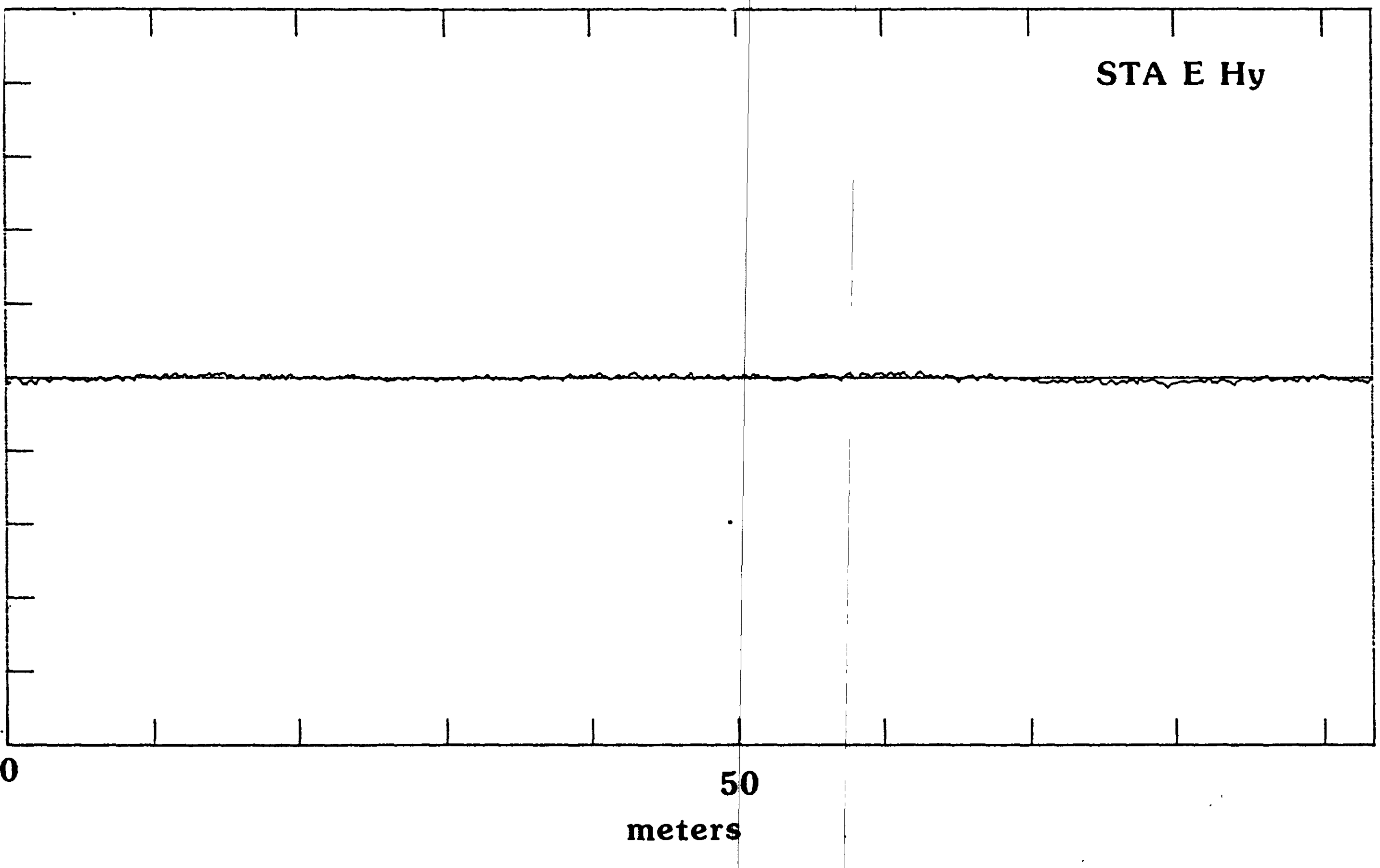

Figure 17b

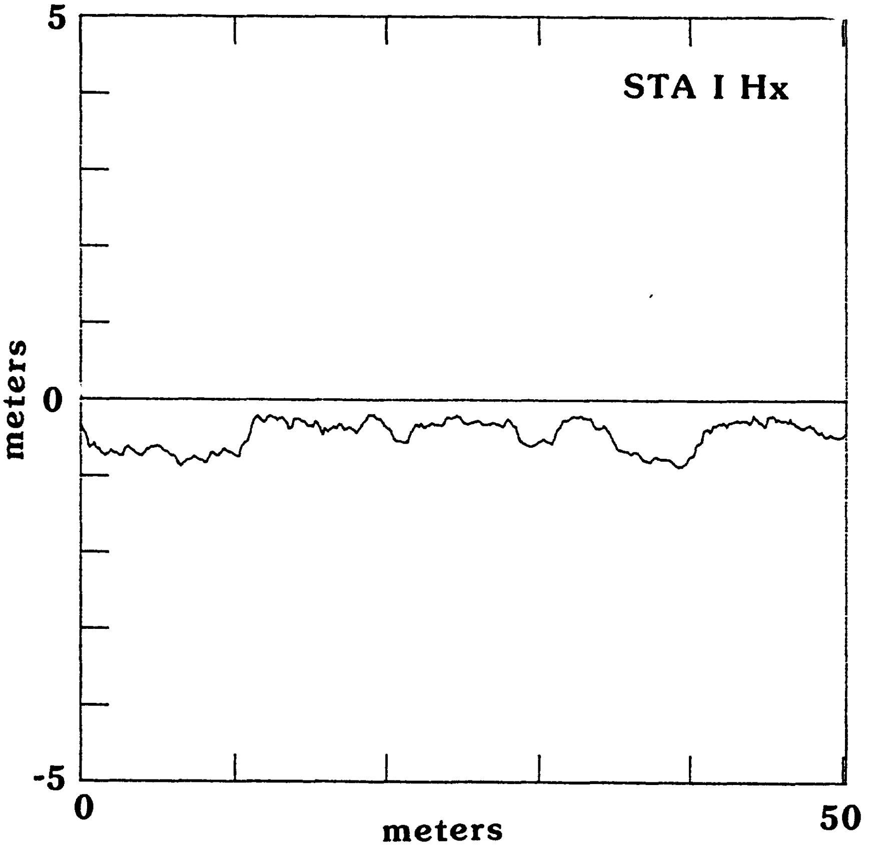

Figure 18a

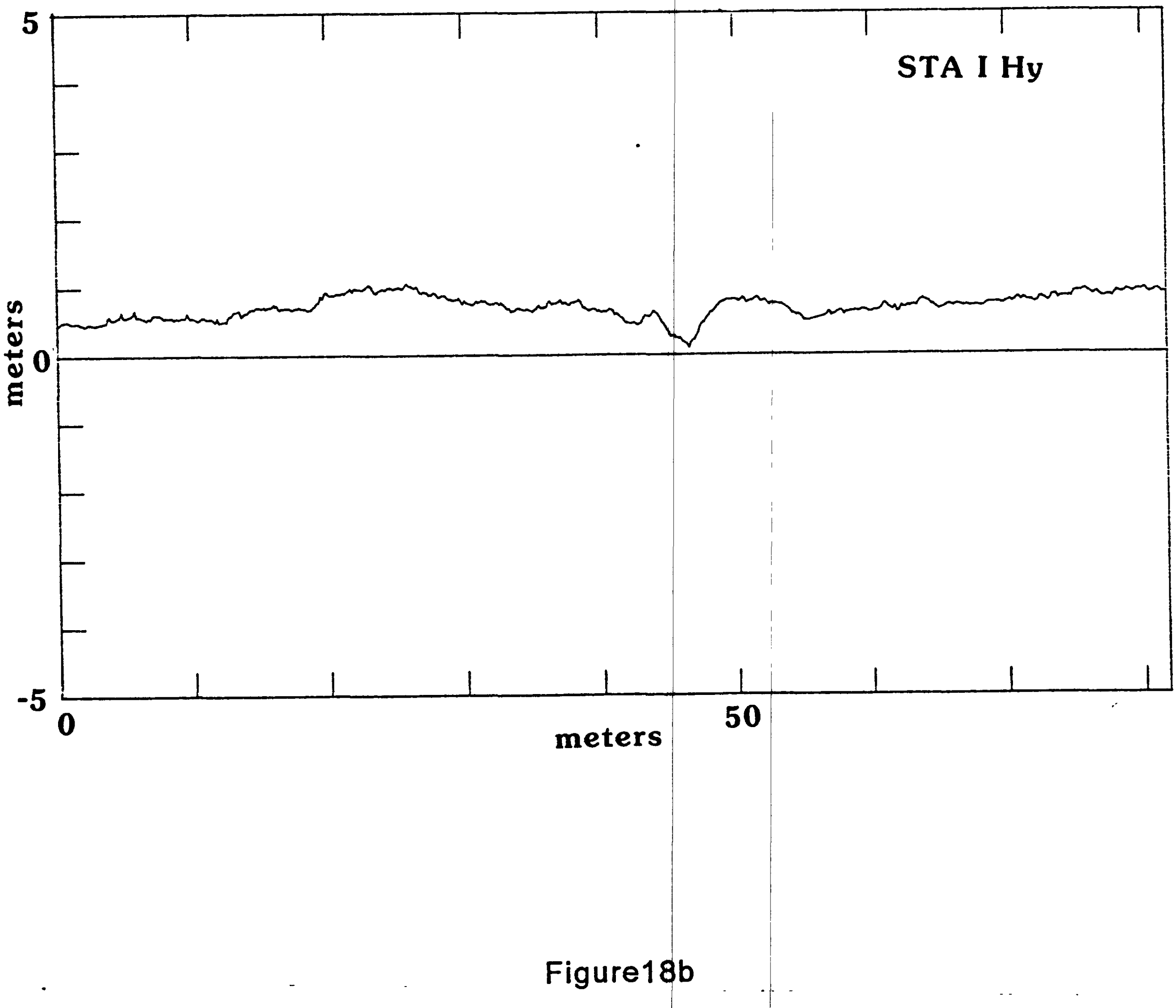

Figure18b

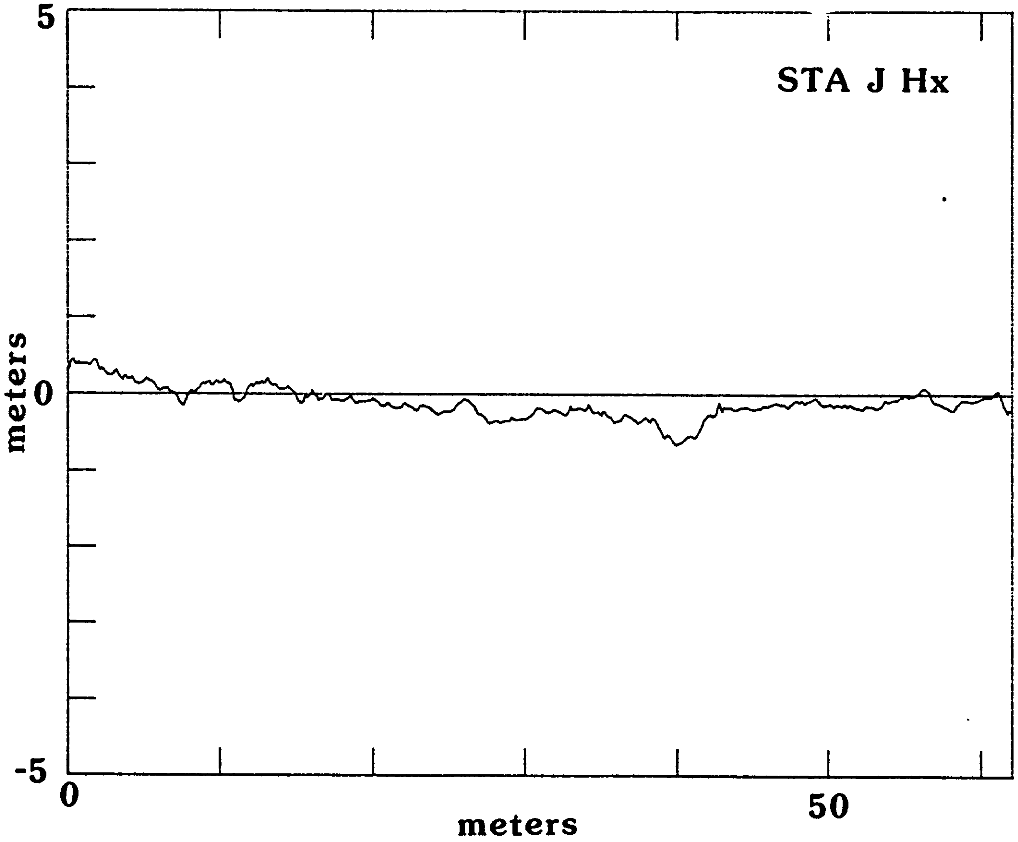

Figure 19a

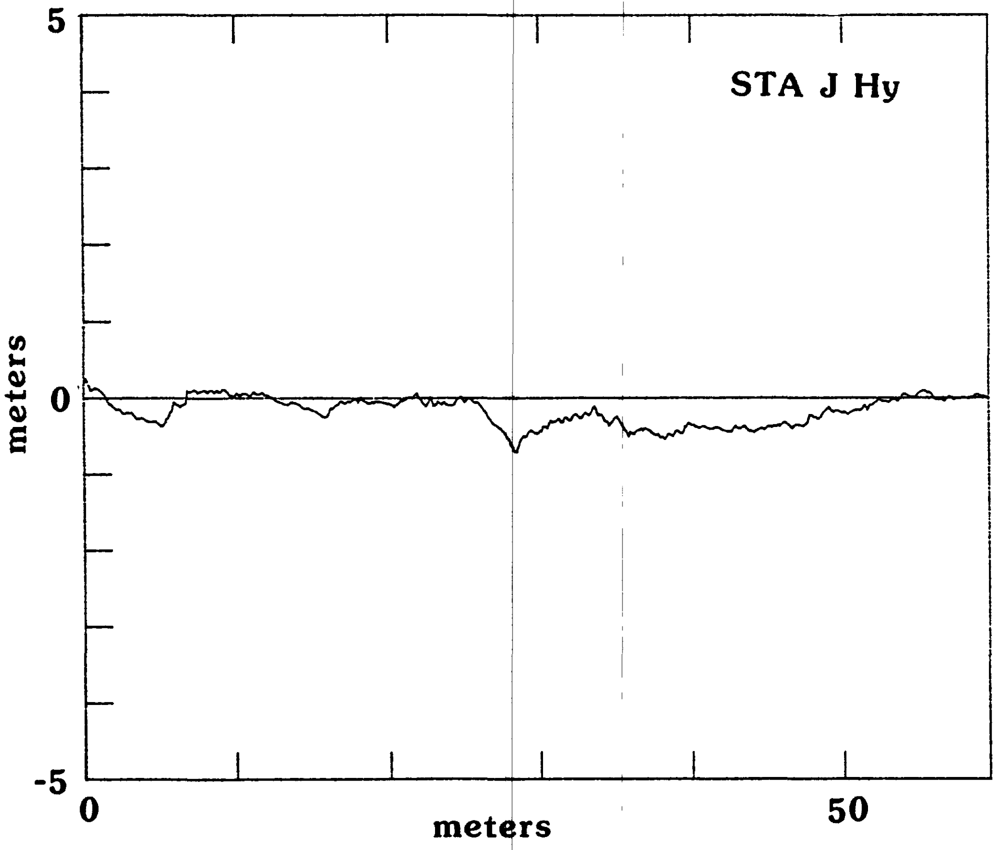

Figure19b

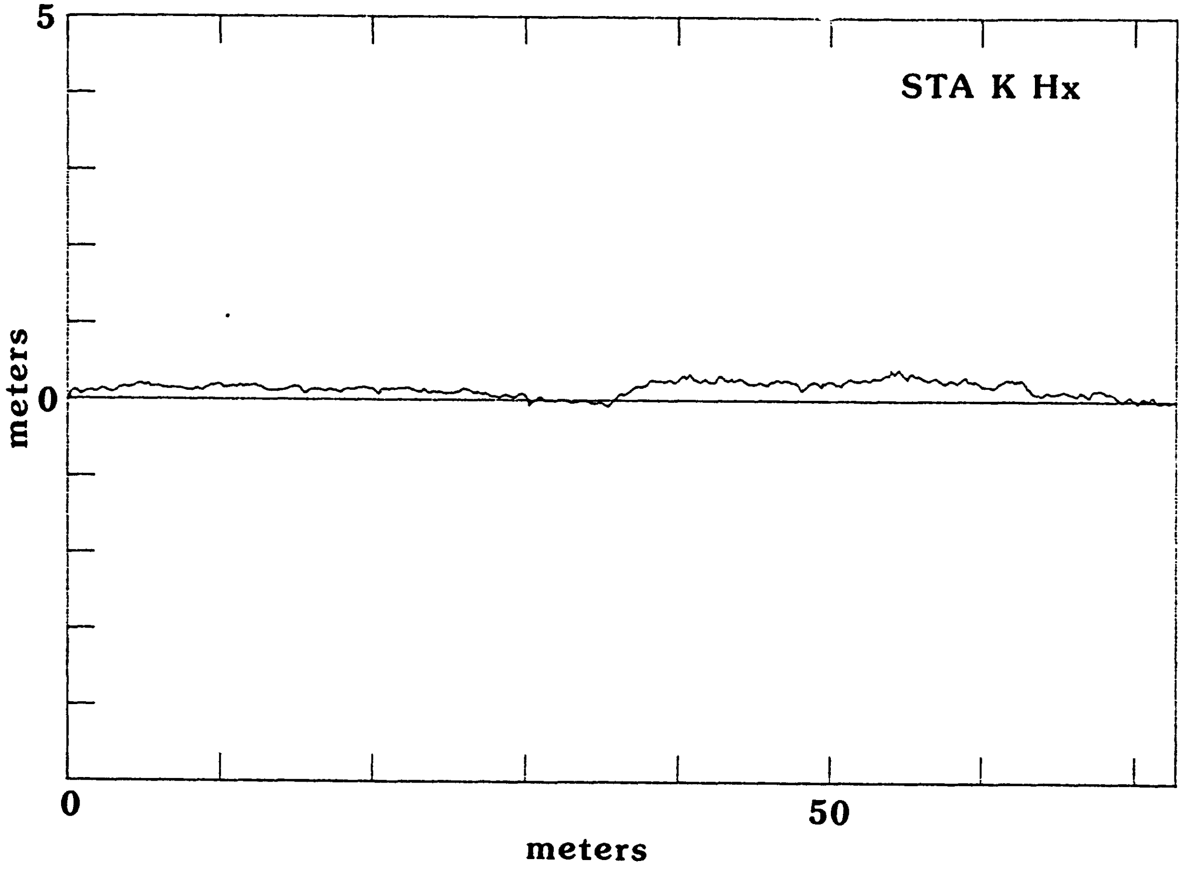

Figure 20a

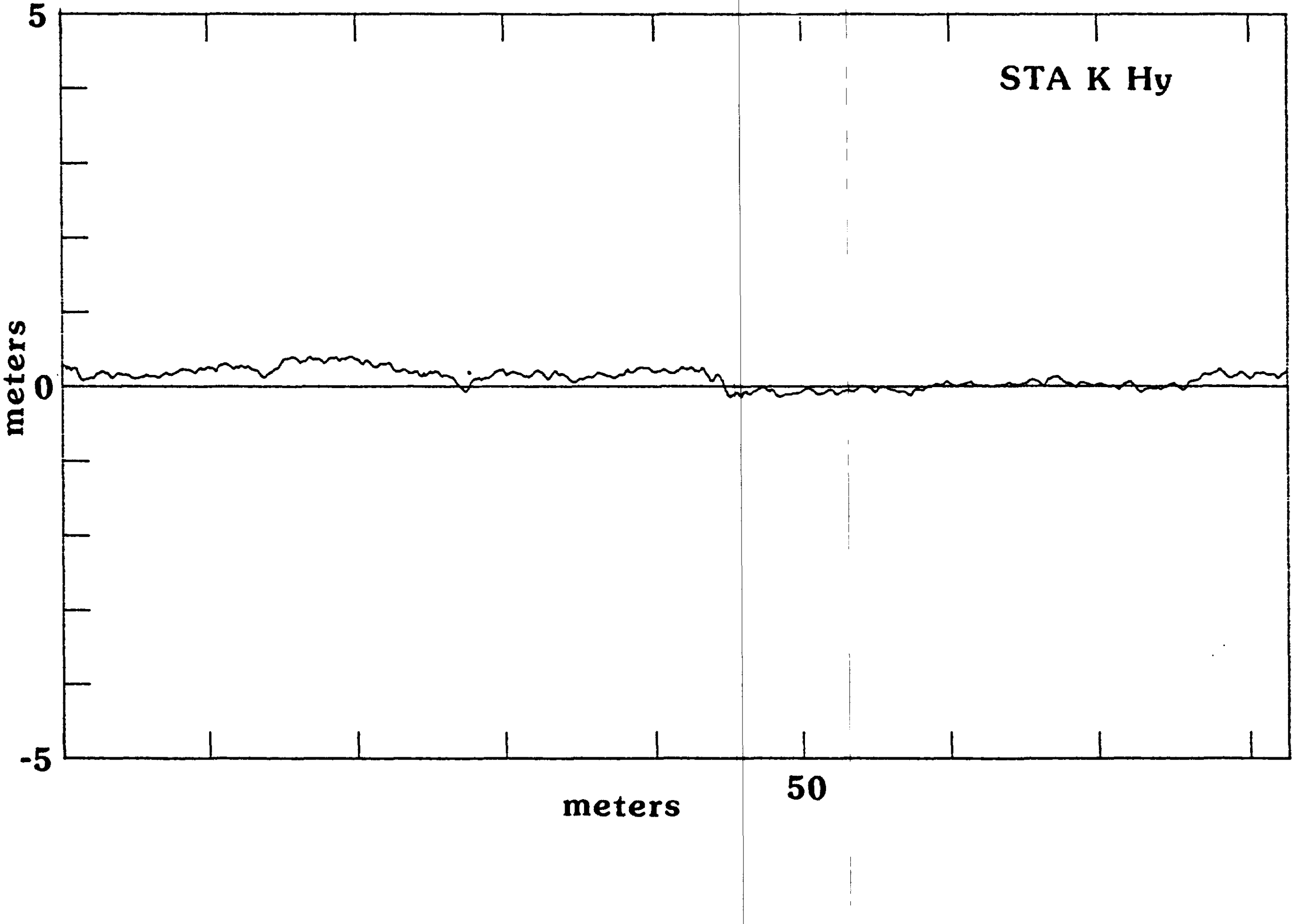

Figure 20b

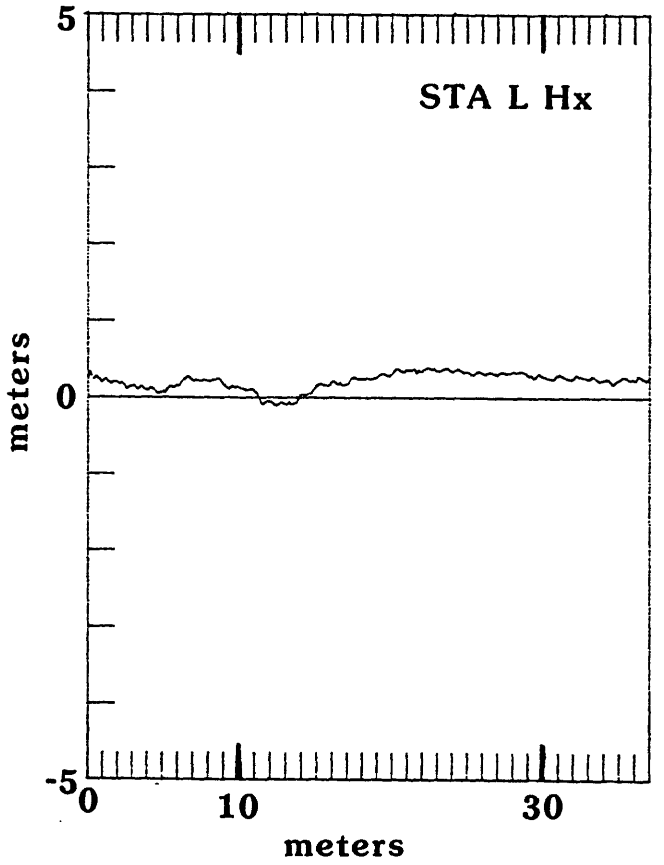

Figure 21a

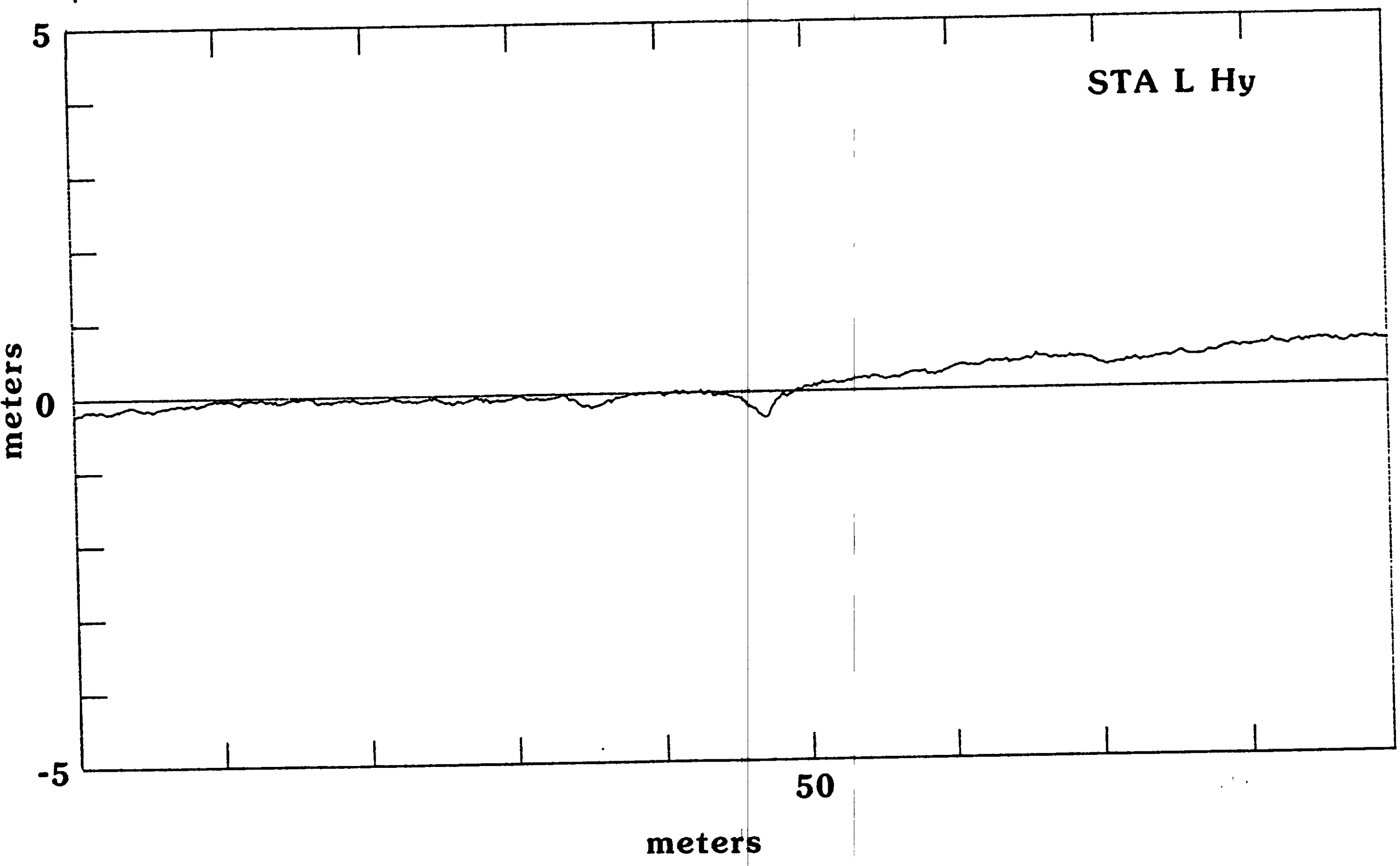

Figure 21b

| TABLE 3 - | 1976 AND 1979 SCATTEROMETER DATA FOR DEATH VALLEY* | | | | | |
|---|---|---|---|---|---|---|
| | | | | | | |
| STATION | UNIT | VV | VH | HH | HV | COMMENTS |
| | | | | | | |
| SALTPAN | | | | | | |
| A | Qh | XXO** | XOO | XX | XX | Complete for 400 MHz, 1.6 Ghz and 4.75 Ghz |
| B,C | Qhr-rough | XXO | XXO | | | |
| D | Qch | | | XO | XO | |
| E | Qhs | XO | XO | X | X | Complete for 400 MHz, 1.6 Ghz and 4.75 Ghz |
| H | Qf | XOO | XOO | XXX | XXX | Complete for 400 Mhz, 1.6 Ghz and 4.75 Ghz |
| | | | | | | |
| FAN GRAVELS | | | | | | |
| I | Qg3-rough | | | XXO | XXO | |
| J | Qg3-moderate | O | 0 | X | X | |
| K | Qg3-smooth | O | 0 | X | X | |
| L | Qg2-pavement | | | XO | XO | |
| | | | | | | |
| *(DATA FOR 1979 INCLUDES 400 HHZ, 1.6 GHZ AND 13.3 GHZ) | | | | | | |
| VV data only for 13.3 Ghz sensor (1979) | | | | | | |
| 1976 data limited to 1.6 GHz only | | | | | | |
| | | | | | | |
| ** O = 1976 data (indivudual passes over geologic units) | | | | | | |
| X = 1979 data (individual passes over geologic unit) | | | | | | |

Table 3

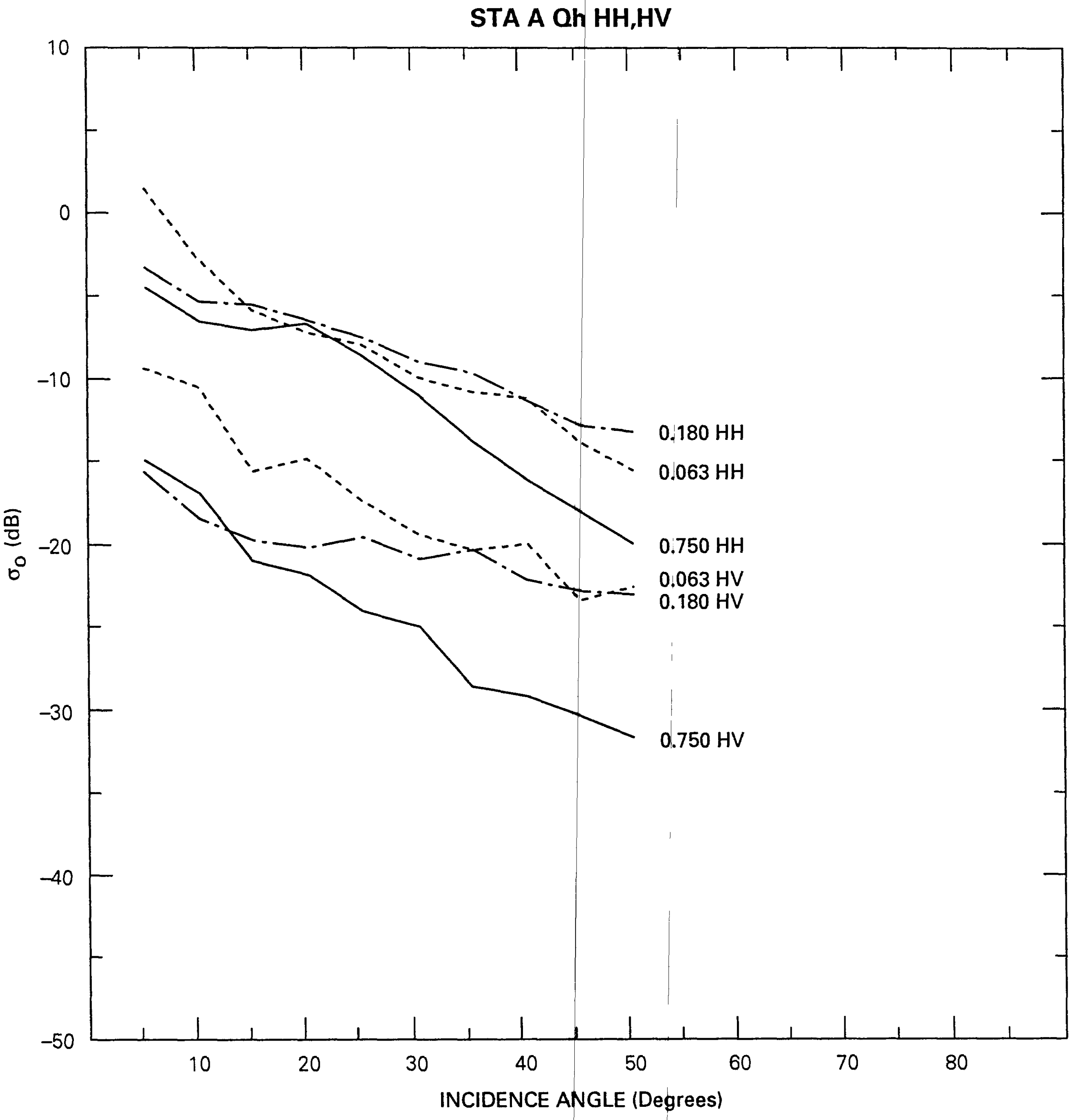
STA A Qh HH,HV
10
0
−10
−20
−30
−40
−50
σ_o (dB)
10
20
30
40
50
60
70
80
INCIDENCE ANGLE (Degrees)
0.180 HH
0.063 HH
0.750 HH
0.063 HV
0.180 HV
0.750 HV

Figure 22a

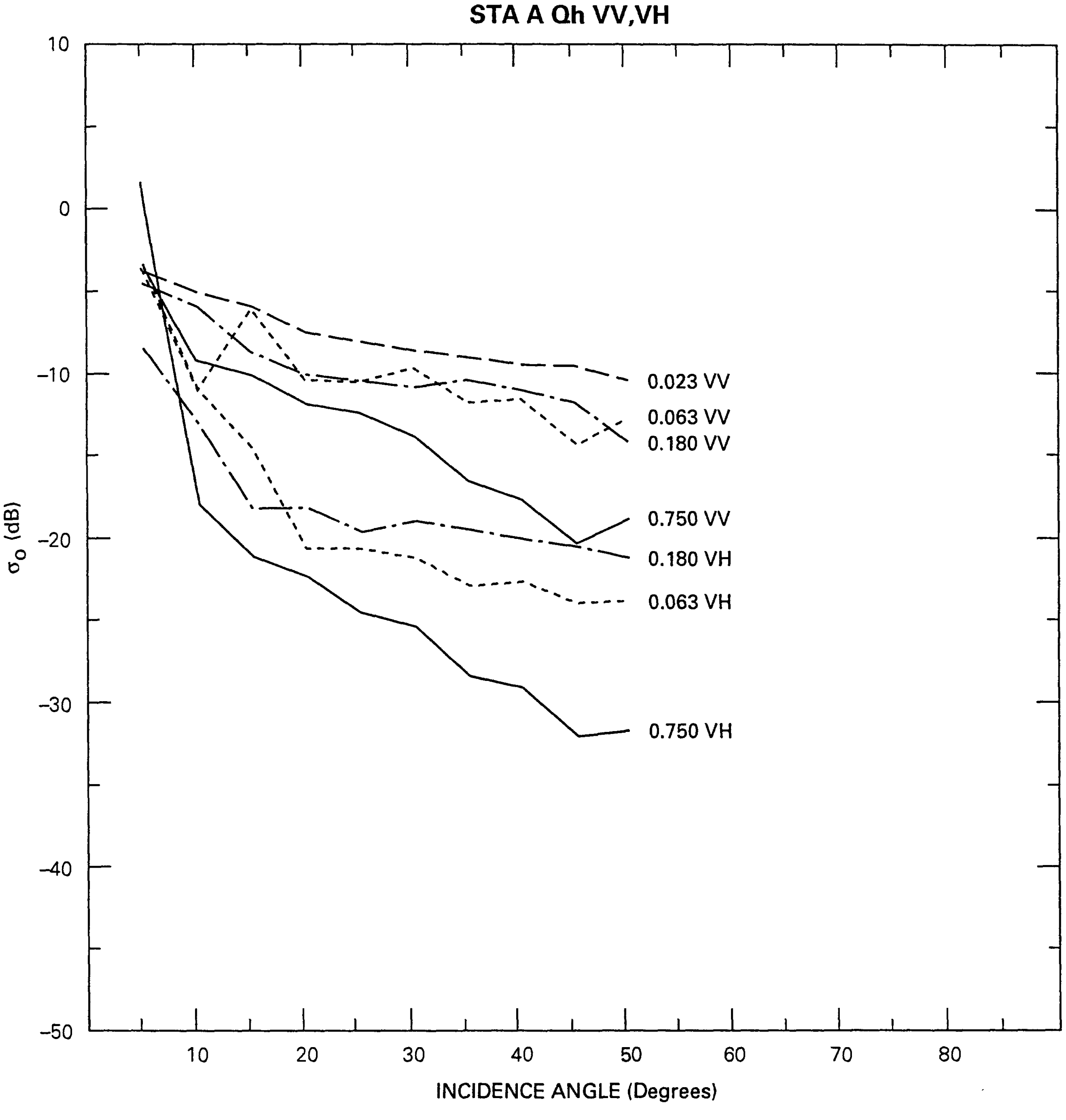
STA A Qh VV,VH
10
0
-10
-20
-30
-40
-50
σo (dB)
10
20
30
40
50
60
70
80
INCIDENCE ANGLE (Degrees)
0.023 VV
0.063 VV
0.180 VV
0.750 VV
0.180 VH
0.063 VH
0.750 VH

Figure 22b

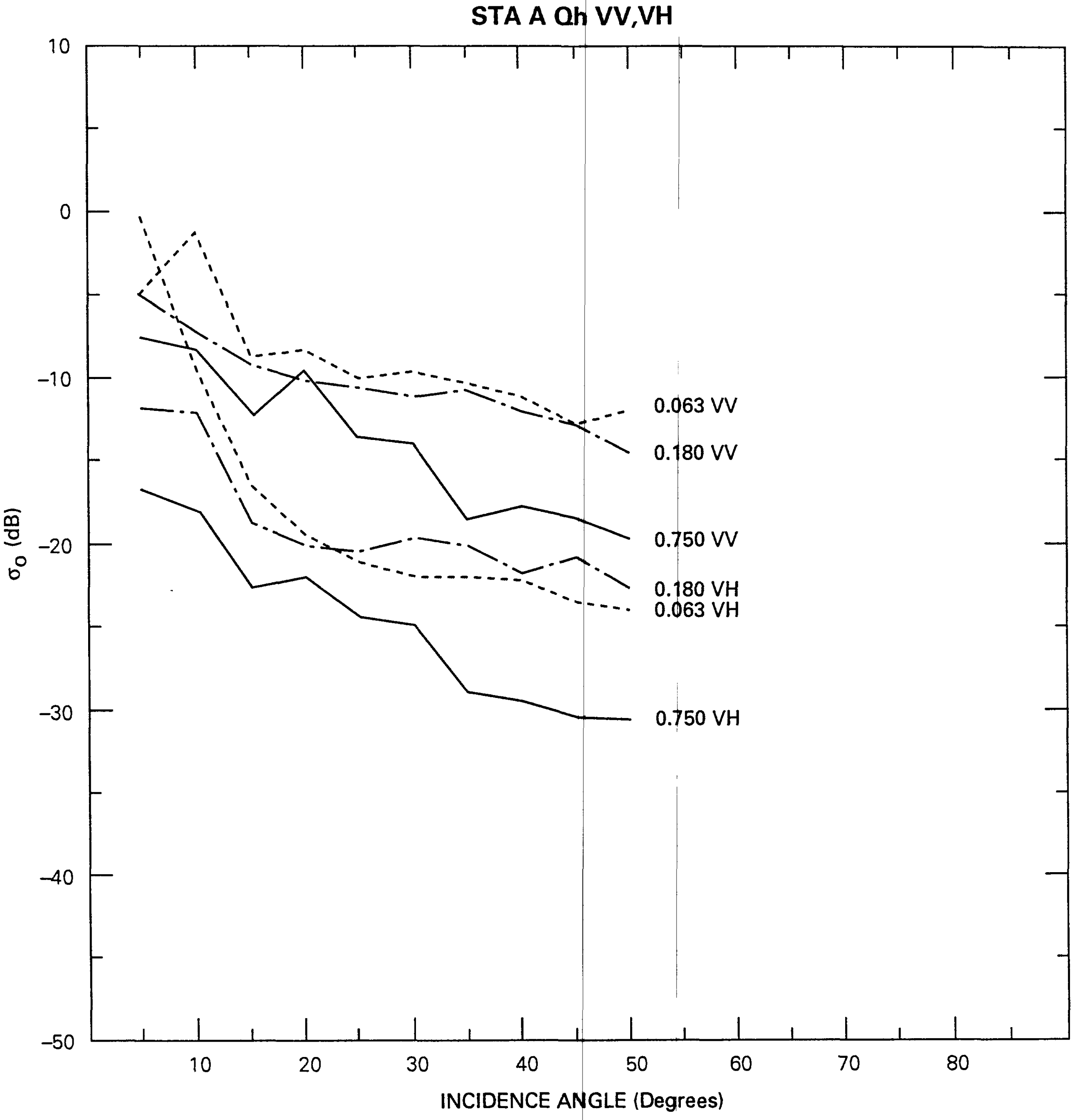
STA A Qh VV,VH
σ₀ (dB)
10
0
−10
−20
−30
−40
−50
10
20
30
40
50
60
70
80
INCIDENCE ANGLE (Degrees)
0.063 VV
0.180 VV
0.750 VV
0.180 VH
0.063 VH
0.750 VH

Figure 22c

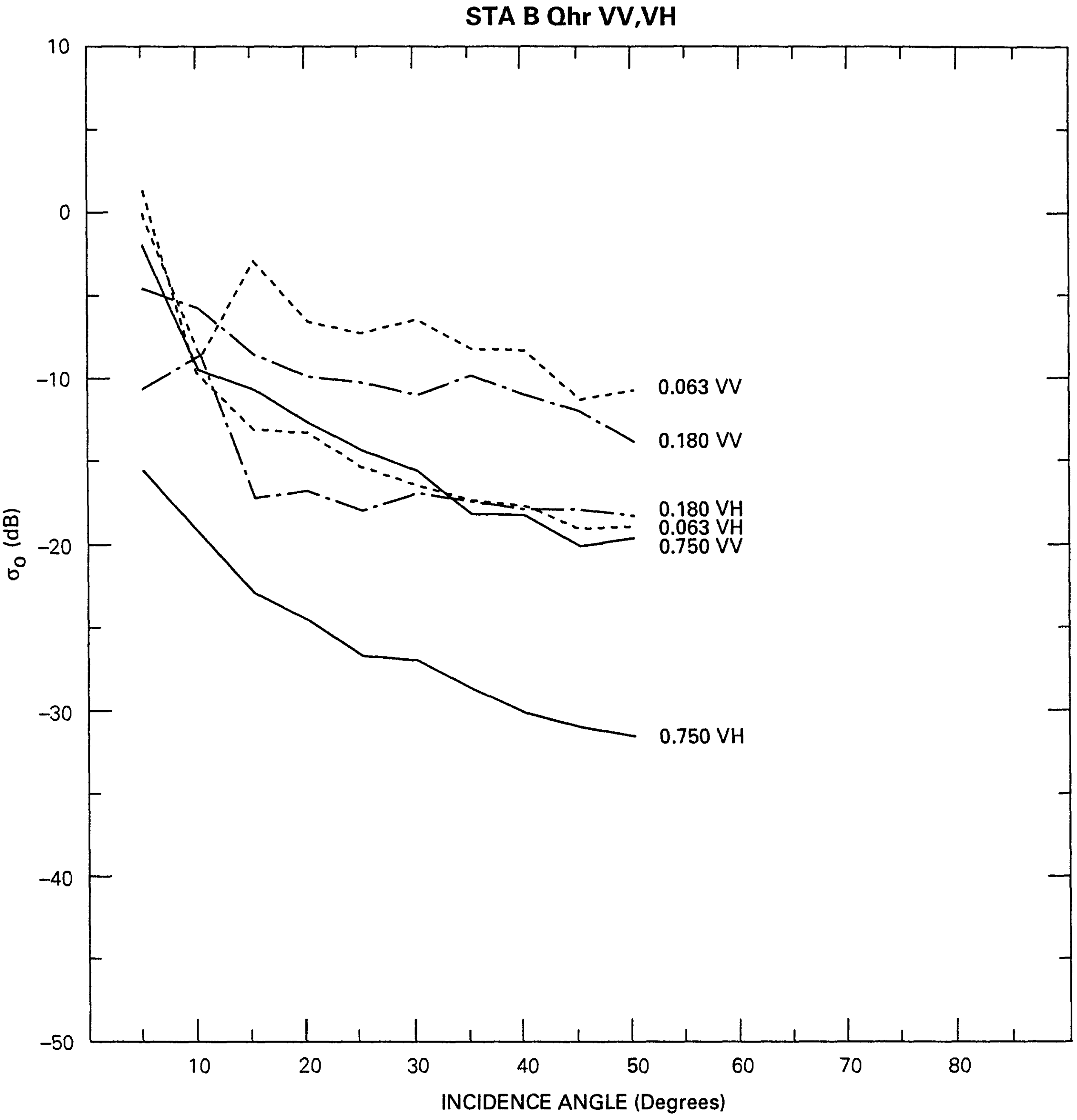
STA B Qhr VV,VH
10
0
-10
-20
-30
-40
-50
$\sigma_o$ (dB)
10
20
30
40
50
60
70
80
INCIDENCE ANGLE (Degrees)
0.063 VV
0.180 VV
0.180 VH
0.063 VH
0.750 VV
0.750 VH

Figure 23a

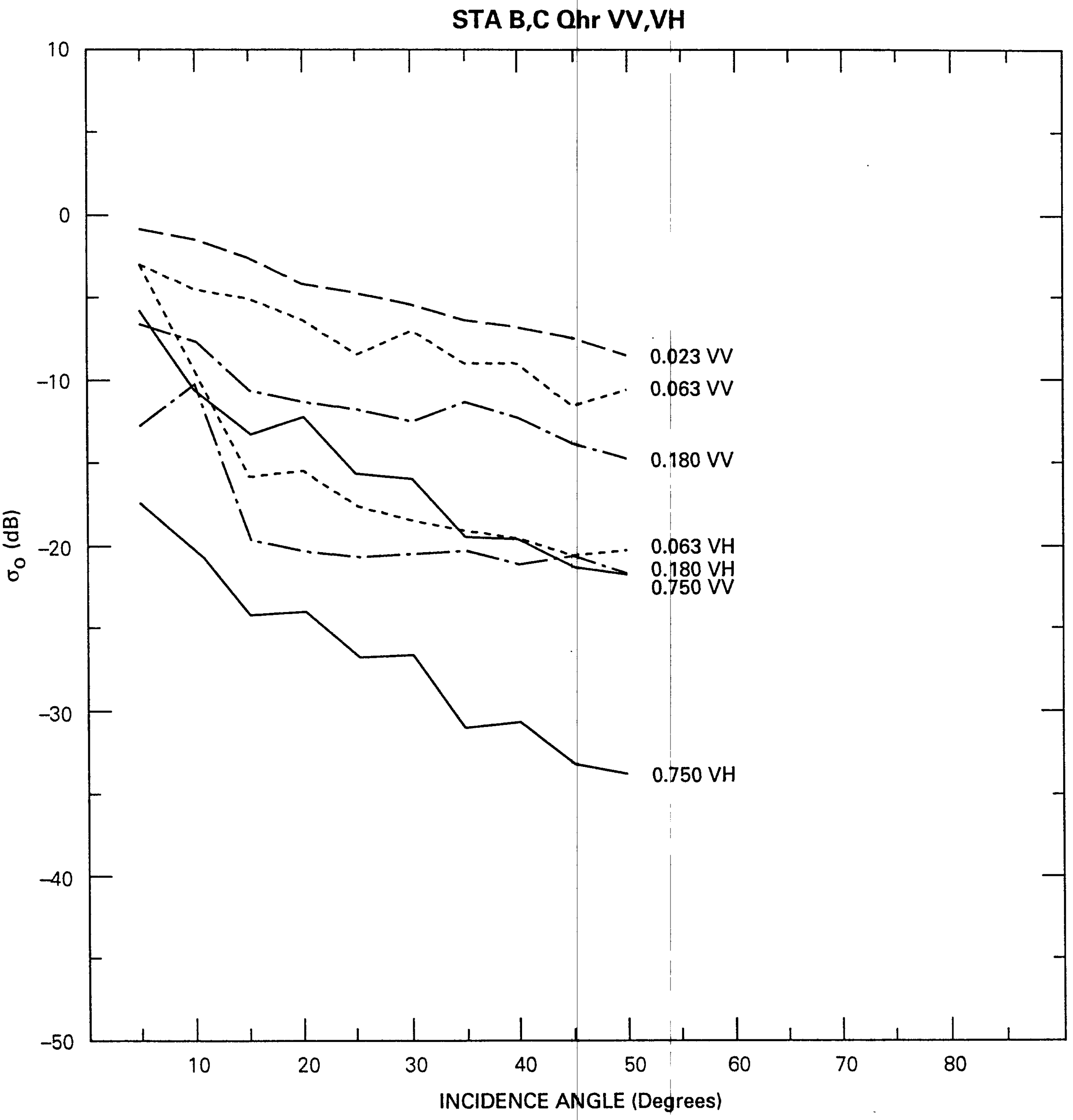
STA B,C Qhr VV,VH
10
0
−10
−20
−30
−40
−50
σo (dB)
10
20
30
40
50
60
70
80
INCIDENCE ANGLE (Degrees)
0.023 VV
0.063 VV
0.180 VV
0.063 VH
0.180 VH
0.750 VV
0.750 VH

Figure 23b

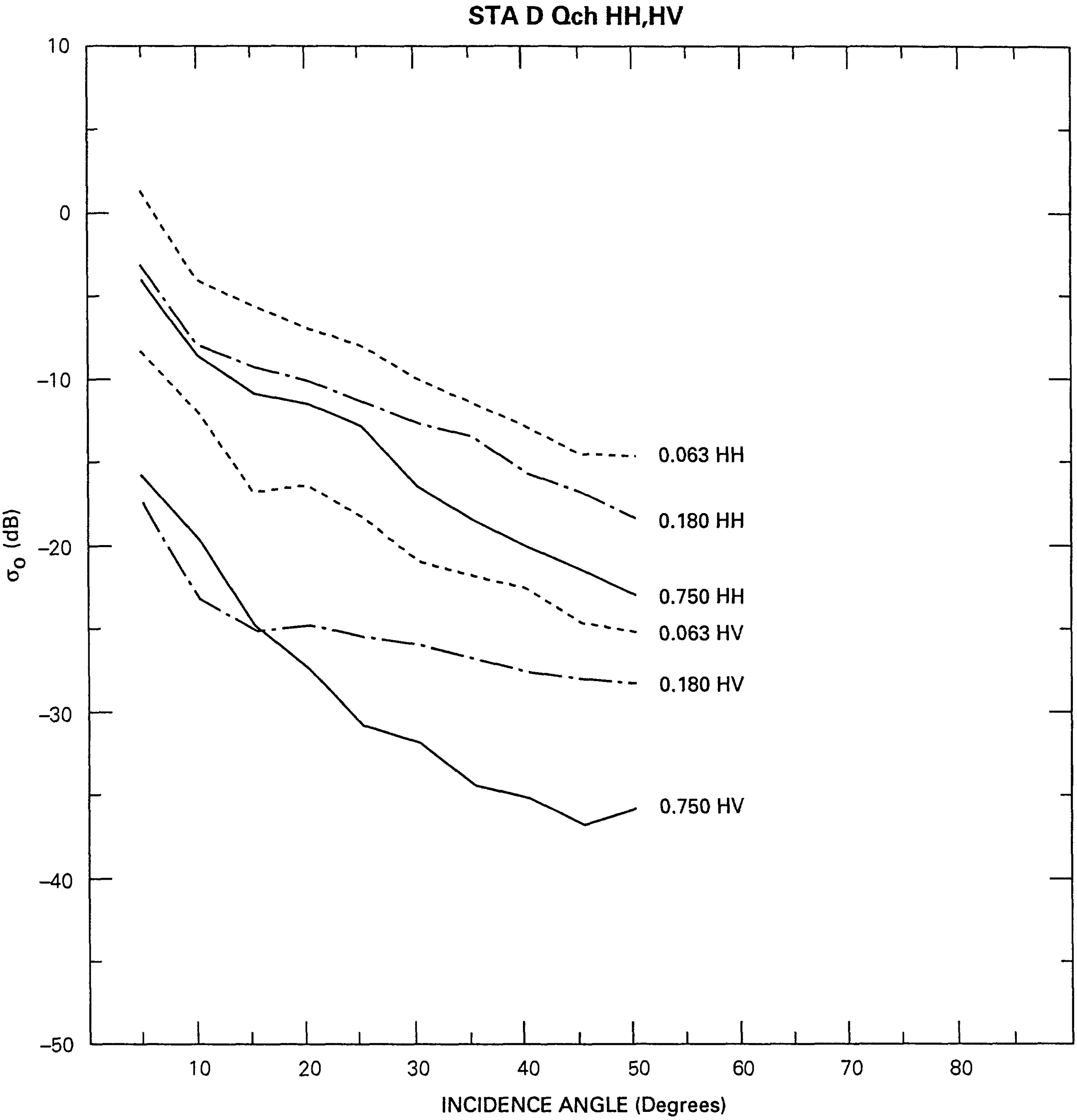

STA D Qch HH,HV

Figure 24

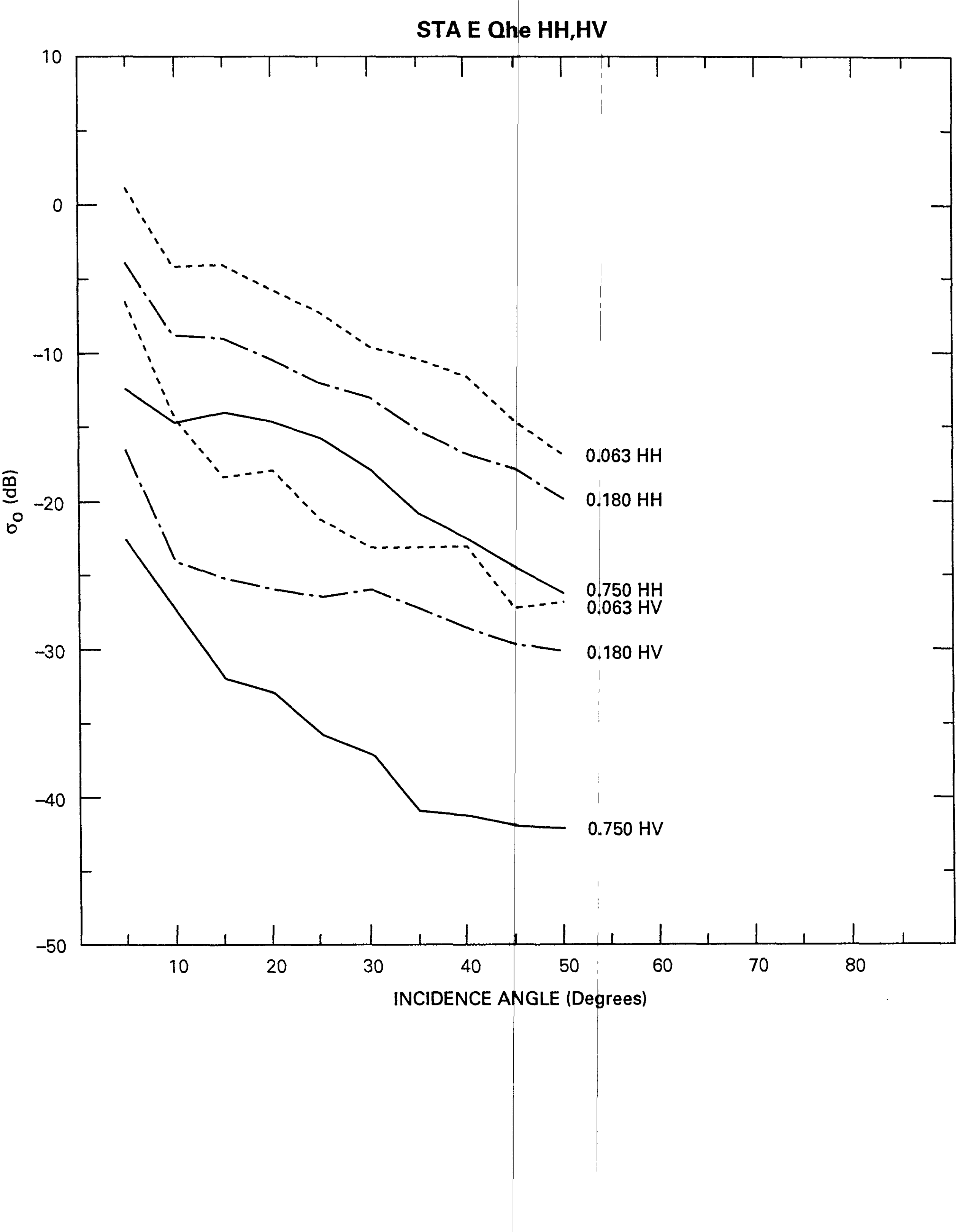
STA E Qhe HH,HV
σo (dB)
10
0
−10
−20
−30
−40
−50
10
20
30
40
50
60
70
80
INCIDENCE ANGLE (Degrees)
0.063 HH
0.180 HH
0.750 HH
0.063 HV
0.180 HV
0.750 HV

Figure 25a

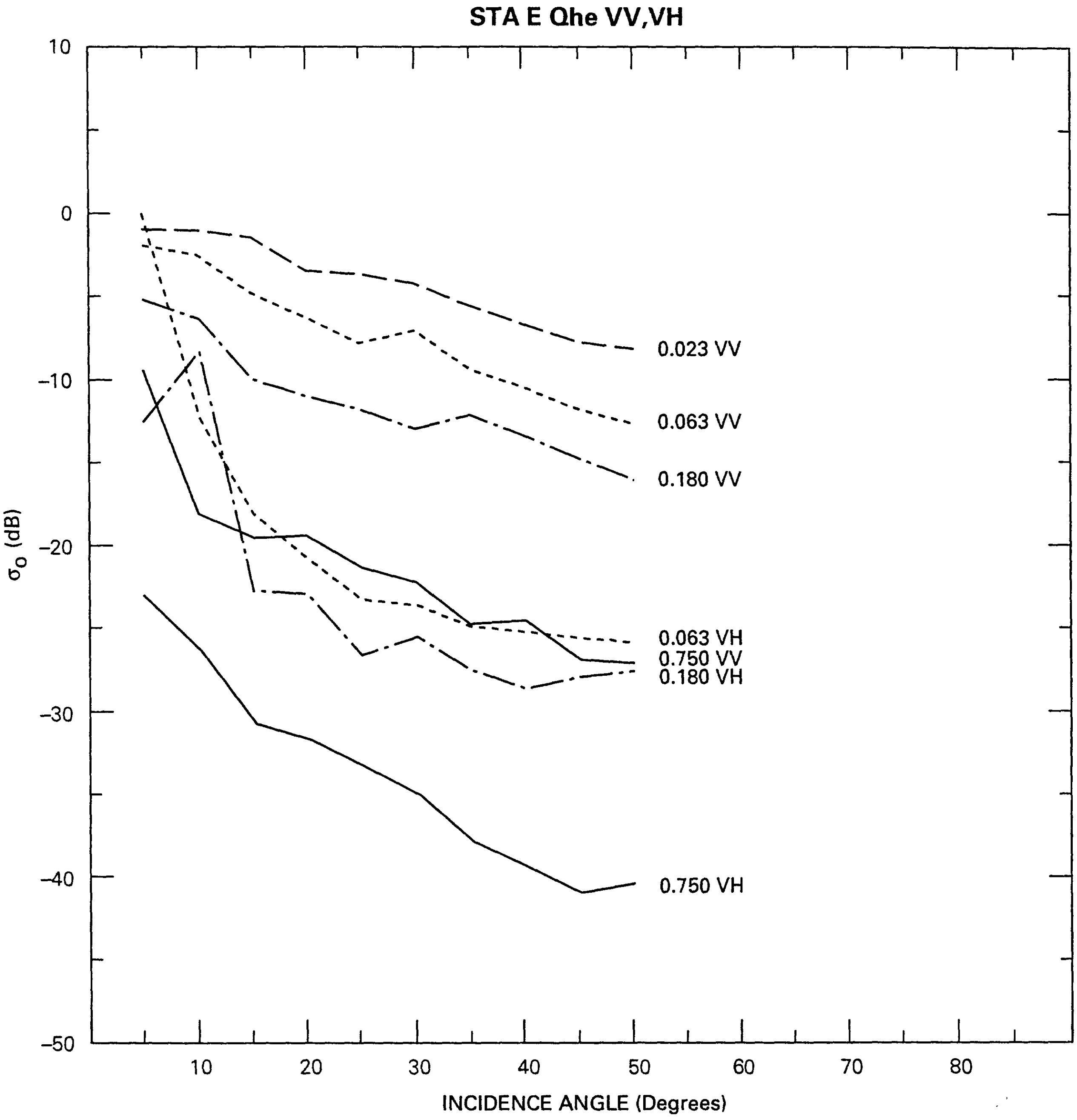
STA E Qhe VV,VH
10
0
-10
-20
-30
-40
-50
σo (dB)
10
20
30
40
50
60
70
80
INCIDENCE ANGLE (Degrees)
0.023 VV
0.063 VV
0.180 VV
0.063 VH
0.750 VV
0.180 VH
0.750 VH

Figure 25b

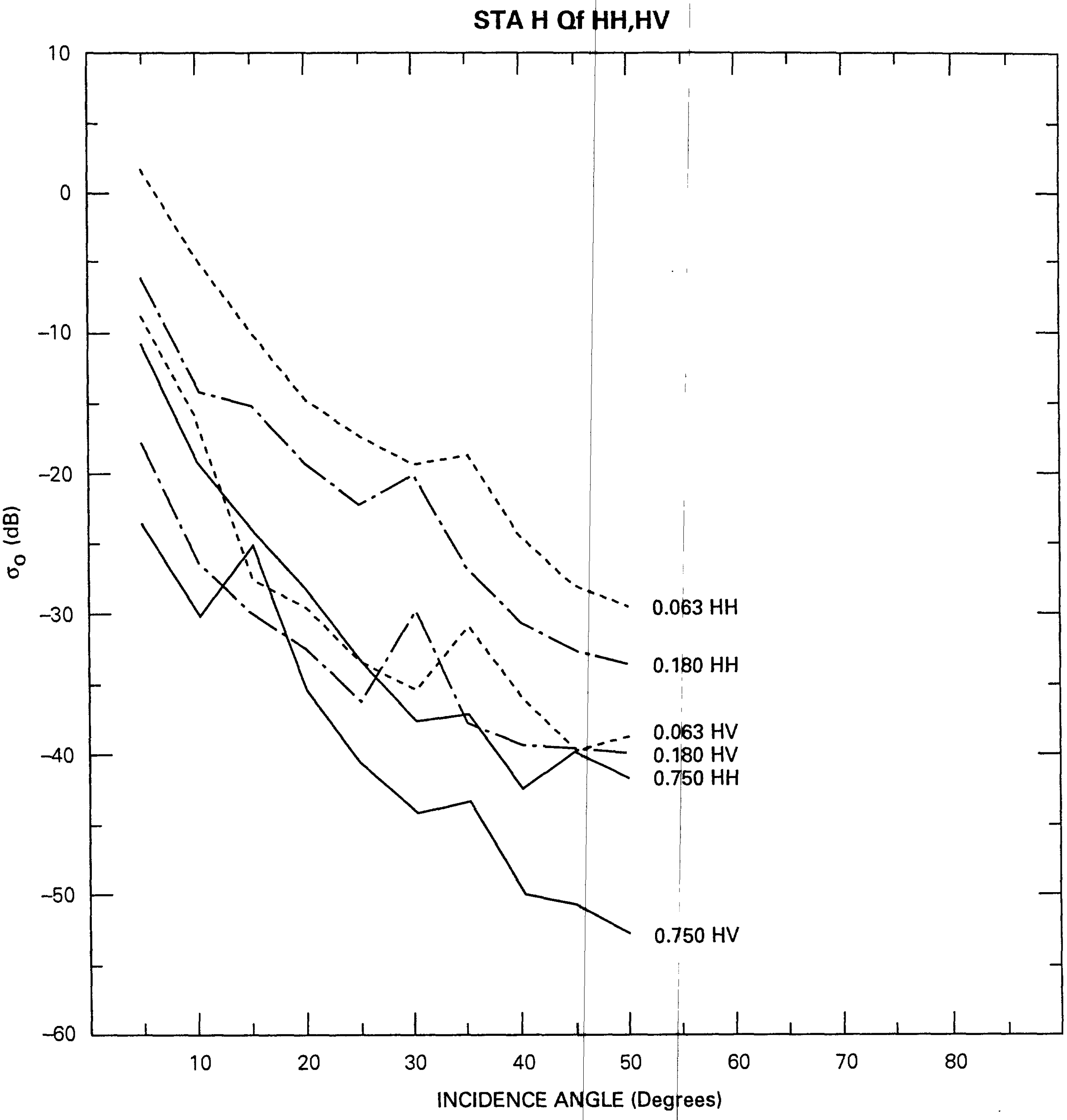
STA H Qf HH,HV
σ_O (dB)
10
0
−10
−20
−30
−40
−50
−60
10
20
30
40
50
60
70
80
INCIDENCE ANGLE (Degrees)
0.063 HH
0.180 HH
0.063 HV
0.180 HV
0.750 HH
0.750 HV

Figure 26a

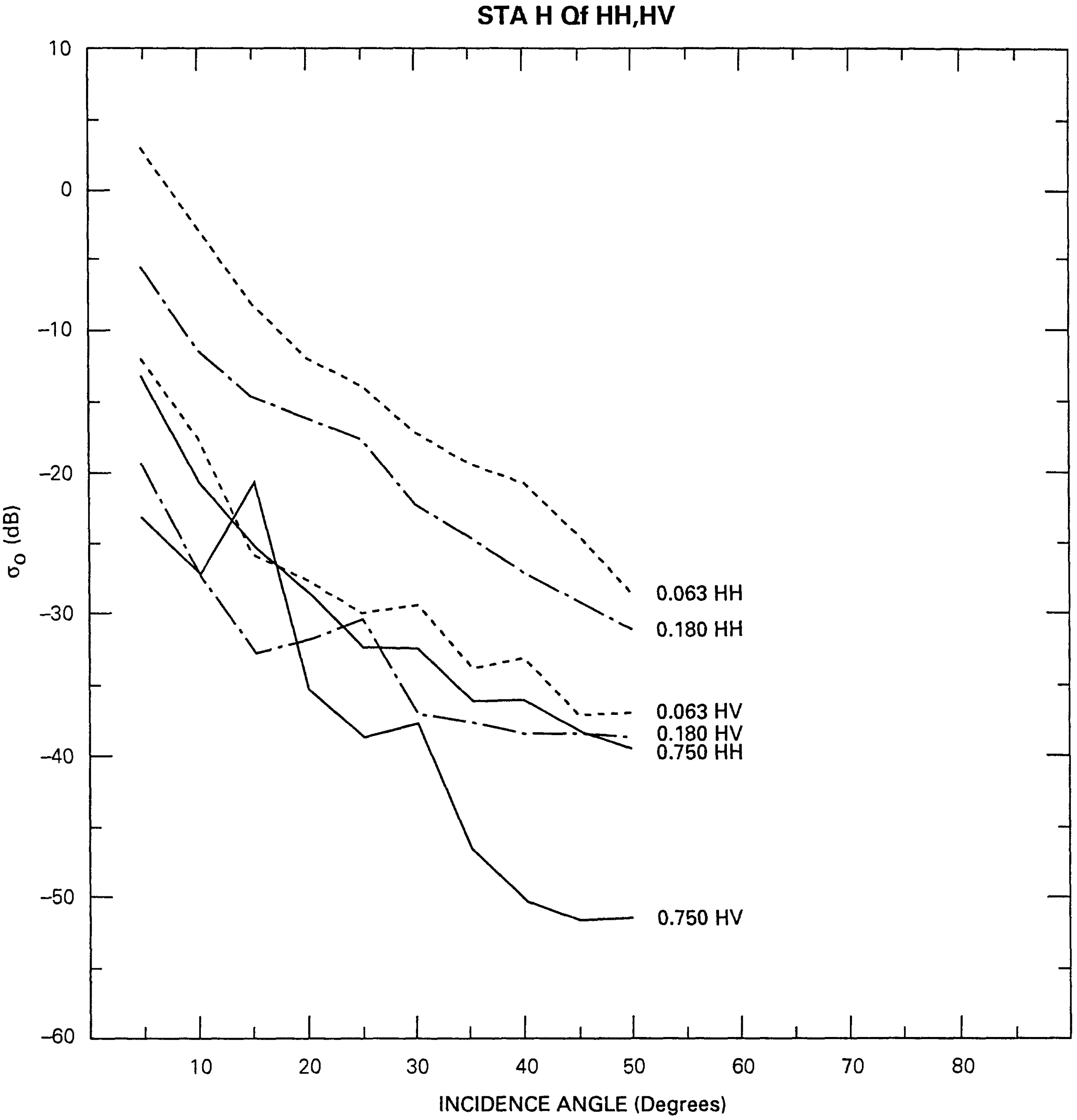
STA H Qf HH,HV
10
0
-10
-20
-30
-40
-50
-60
σo (dB)
10
20
30
40
50
60
70
80
INCIDENCE ANGLE (Degrees)
0.063 HH
0.180 HH
0.063 HV
0.180 HV
0.750 HH
0.750 HV

Figure 26b

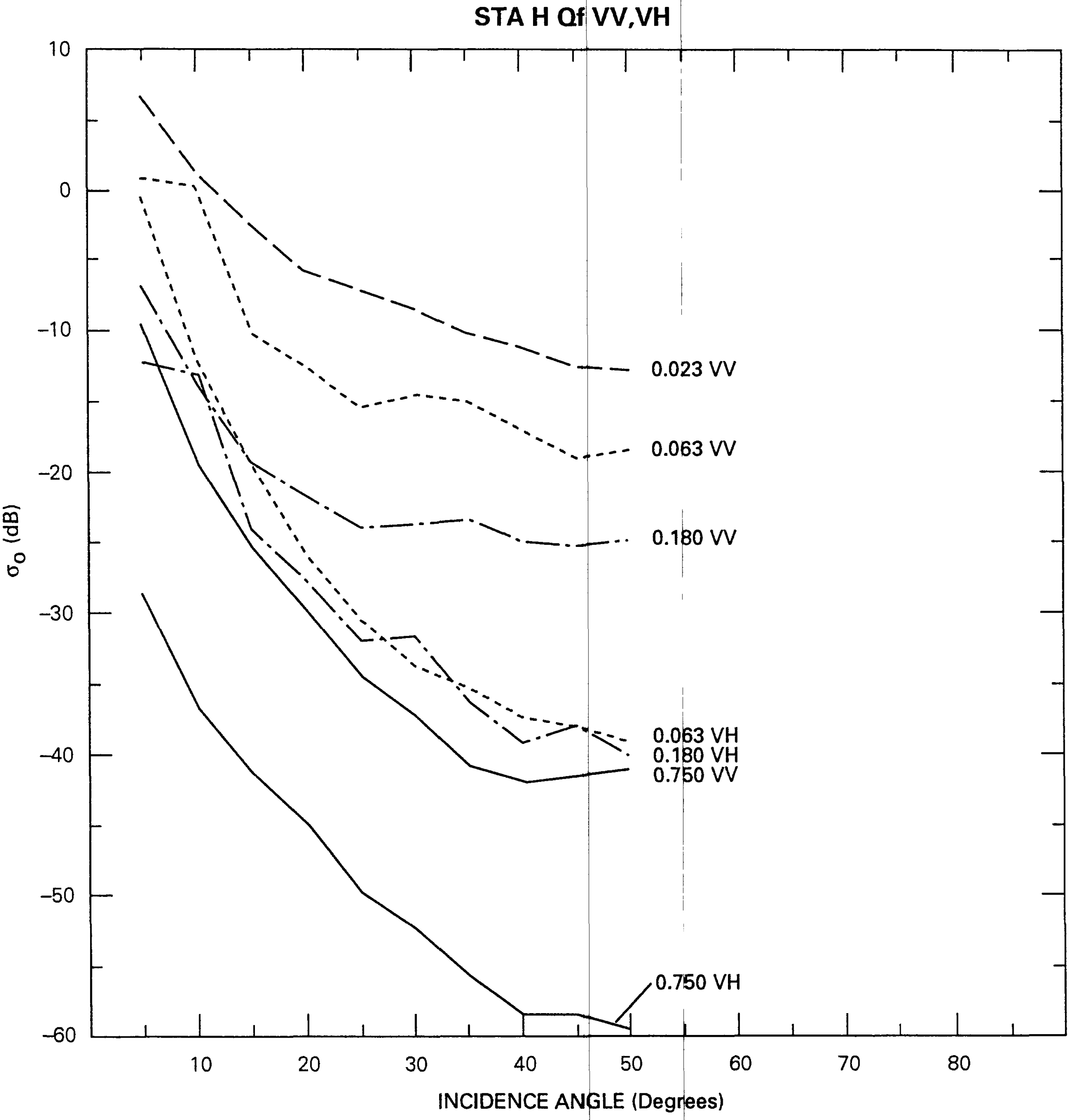
STA H Qf VV,VH
10
0
-10
-20
-30
-40
-50
-60
σ_O (dB)
10
20
30
40
50
60
70
80
INCIDENCE ANGLE (Degrees)
0.023 VV
0.063 VV
0.180 VV
0.063 VH
0.180 VH
0.750 VV
0.750 VH

Figure 26c

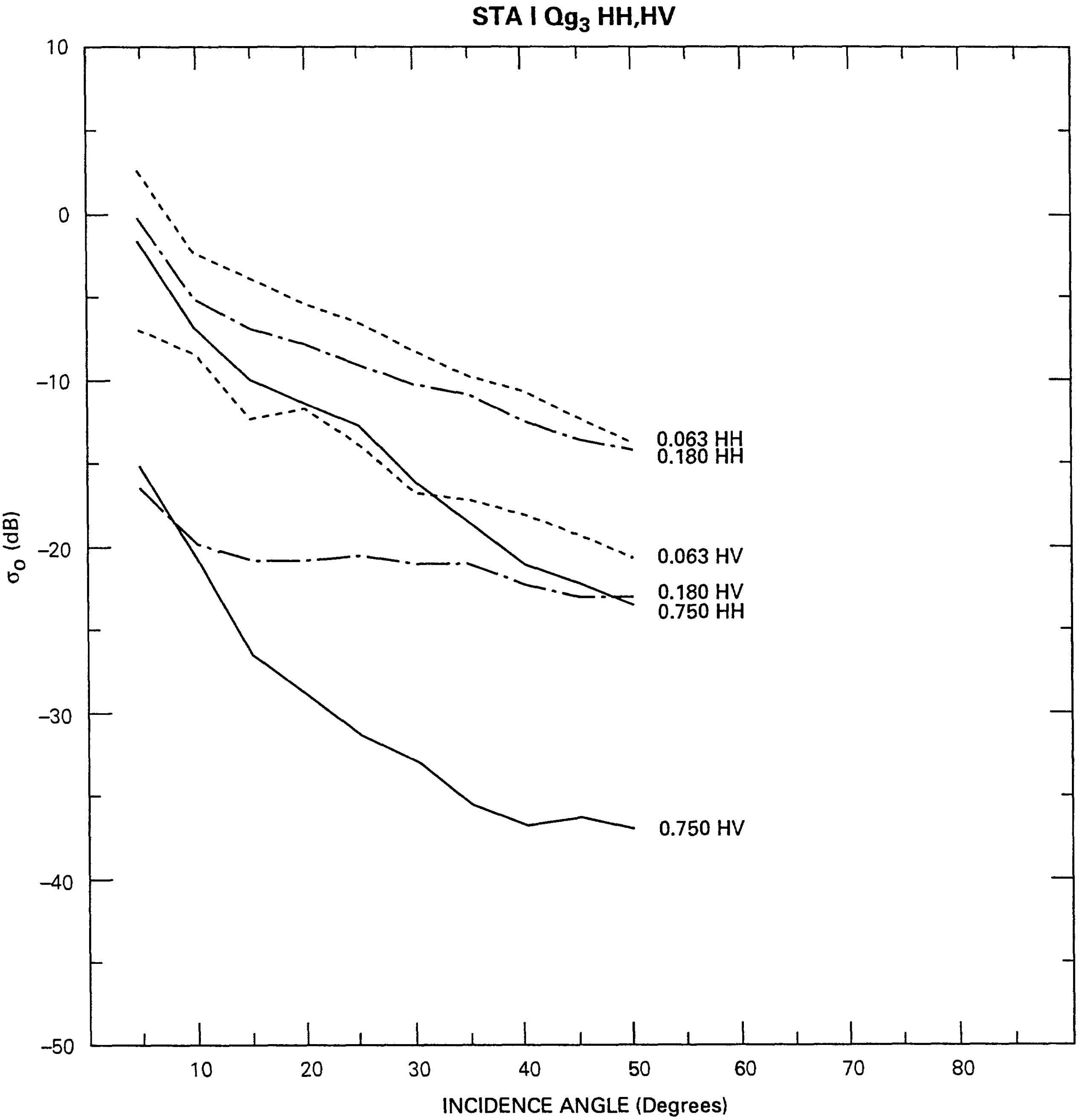
STA I Qg$_3$ HH,HV
10
0
-10
-20
-30
-40
-50
$\sigma_o$ (dB)
10
20
30
40
50
60
70
80
INCIDENCE ANGLE (Degrees)
0.063 HH
0.180 HH
0.063 HV
0.180 HV
0.750 HH
0.750 HV

Figure 27a

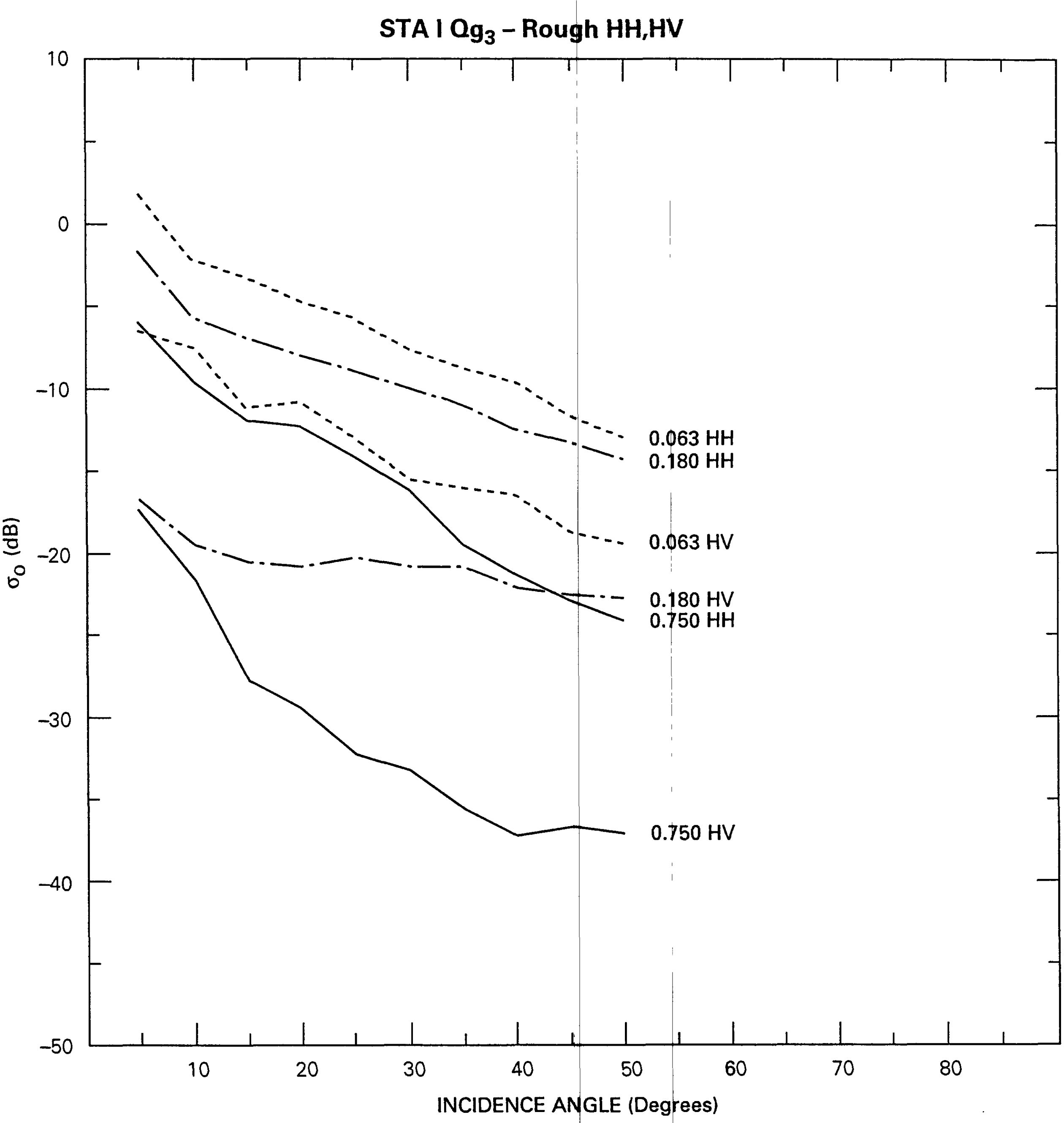
STA I $Qg_3$ – Rough HH,HV
10
0
−10
−20
−30
−40
−50
$\sigma_O$ (dB)
10
20
30
40
50
60
70
80
INCIDENCE ANGLE (Degrees)
0.063 HH
0.180 HH
0.063 HV
0.180 HV
0.750 HH
0.750 HV

Figure 27b

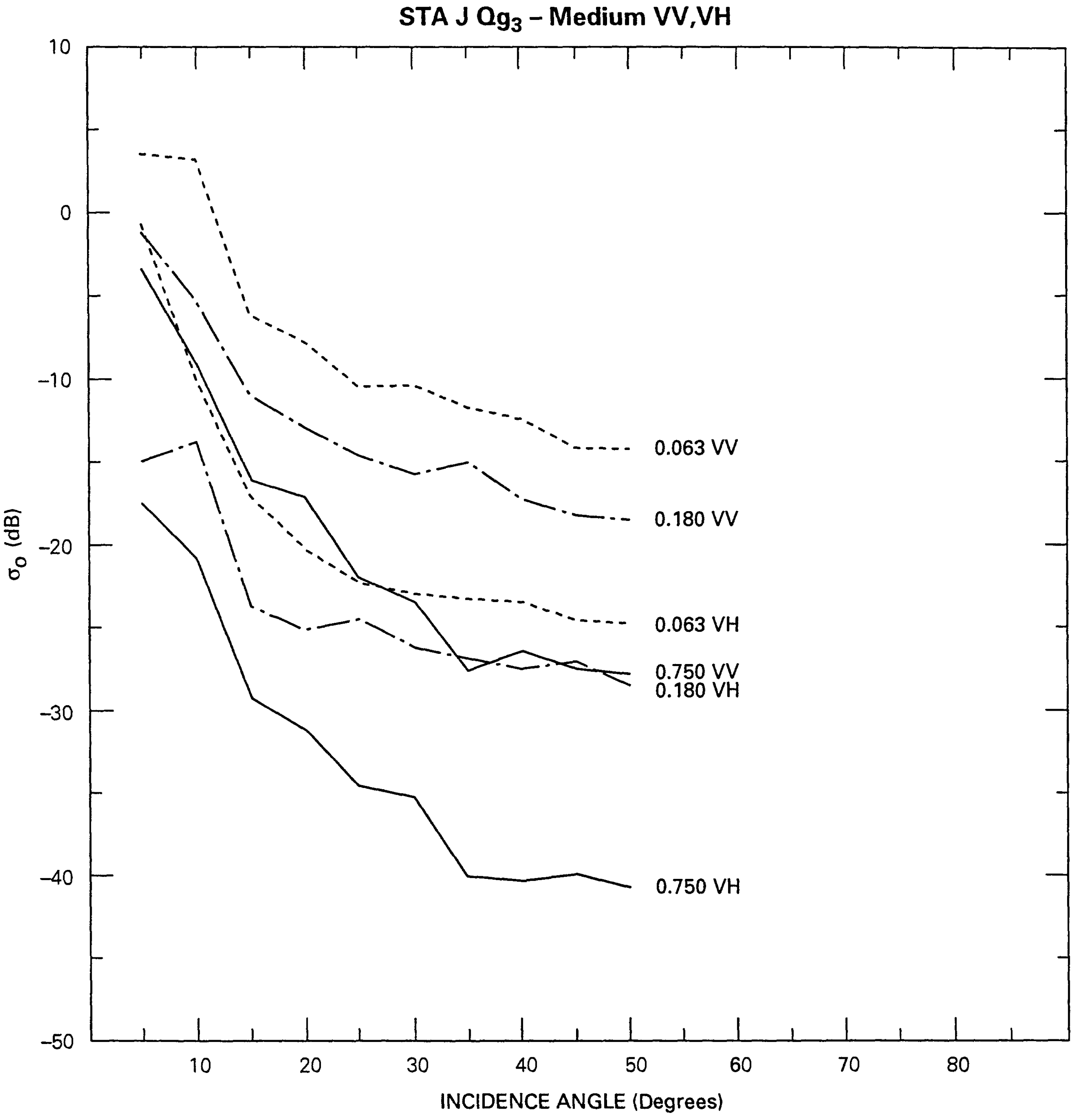

STA J $Qg_3$ – Medium VV,VH

Figure 27c

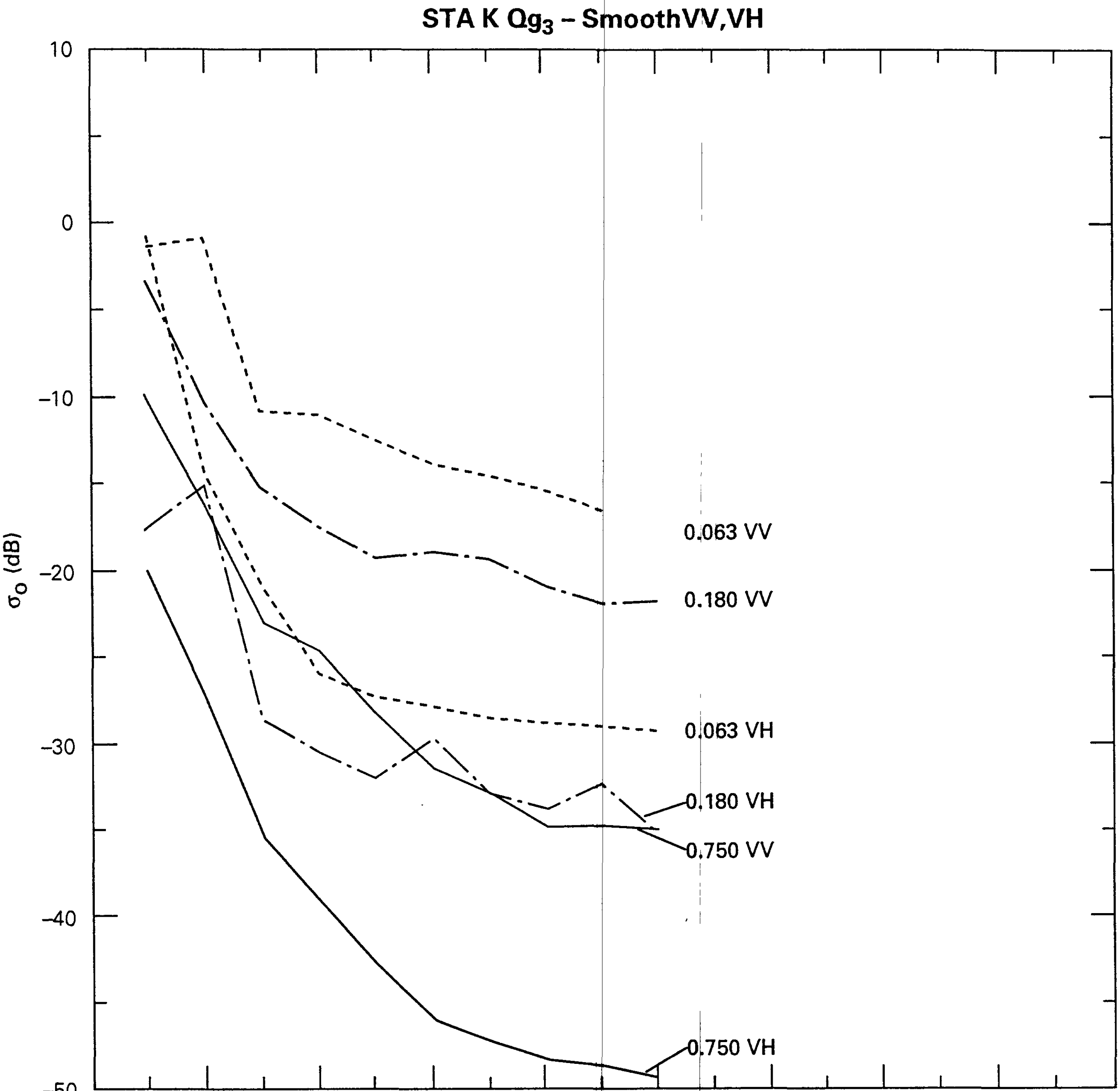
STA K Qg3 – SmoothVV,VH
10
0
–10
–20
–30
–40
–50
σo (dB)
10
20
30
40
50
60
70
80
INCIDENCE ANGLE (Degrees)
0.063 VV
0.180 VV
0.063 VH
0.180 VH
0.750 VV
0.750 VH

Figure 28

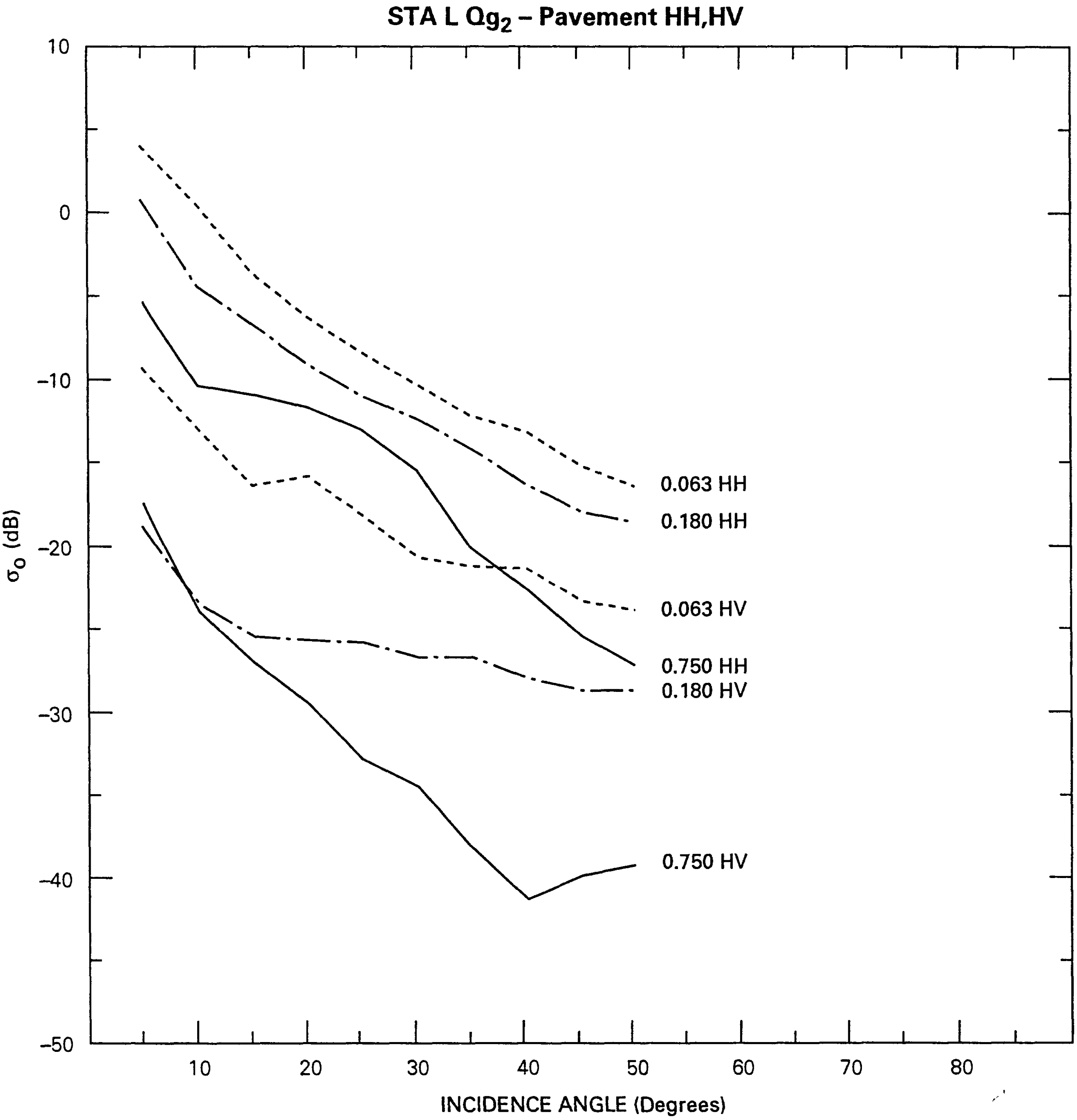 
STA L $Qg_2$ – Pavement HH,HV

Figure 29

### TABLE 4 - AVERAGE SURFACE ROUGHNESS PARAMETERS (Ground Level Profiles)

| Station | Unit Symbol | Total Relief (cm) | Mean Relief (cm) | Standard Deviation (cm) | Variance (cm Sq.) | Mean Slope at 3 cm Sample Interval (Degrees) | Mean Slope at 25 cm Sample Interval (Degrees) | Surface Correlation Length* (cm) |
|---|---|---|---|---|---|---|---|---|
| | | | SALTPAN SURFACES | | | | | |
| A | Qh | 62.5 | 27.4 | 16.9 | 286.2 | 33.5 | 27.8 | 25 |
| B | Qhr-1** | 50.7 | 22.7 | 16.7 | 279.1 | 32.4 | 31.9 | 16 |
| C | Qhr-2 | 33.4 | 17.6 | 8.7 | 77.4 | 32.6 | 26.8 | 7.5 |
| D | Qch | 12.9 | 5.7 | 2.3 | 13.3 | 16 | 10.7 | 8.5 |
| E | Qhs-1 | 8.8 | 4.8 | 2.2 | 4.7 | 13.6 | 7.8 | 9.7 |
| F | Qhs-2 | 6 | 3.3 | 1.1 | 1.2 | 9.7 | 4.9 | 4 |
| G | Qf-1 | 4.4 | 1 | 0.5 | 0.9 | 5.9 | 1.7 | 8.5 |
| H | Qf-2 | 0.8 | 0.4 | 0.2 | 0.3 | 1.6 | 0.5 | 4.2 |
| | | | FAN GRAVEL SURFACES | | | | | |
| I | Qg3-1 | 24.4 | 12.3 | 7 | 49.1 | 25.3 | 21.6 | 2.5 |
| J | Qg3-2 | 11.2 | 5.3 | 2.6 | 6.7 | 16.9 | 9.5 | 2.5 |
| K | Qg3-3 | 2.5 | 1.8 | 0.9 | 0.9 | 8.9 | 3.8 | 5.2 |
| L | Qg2-Pavement | 4.1 | 1.3 | 0.9 | 0.9 | 6.9 | 1.9 | 9.5 |

* The surface correlation length is the lag displacement distance at which the autocorrelation of two identical topographic profiles drops to 1/e, or 0.368.

** Numbers 1-3 designate increasingly smoother facies

Table 4

Table 5

| | | | RELIEF STATISTICS | | | |
|---|---|---|---|---|---|---|
| | | | | | | |
| **STA A UNIT Qh** | | | | | | |
| | | | | | | |
| **DATA** | | **HELX** | **GRX** | **HELY** | **GRY** | **UNITS** |
| | | | | | | |
| No. Sample pts. | | 490 | 813 | 649 | 972 | |
| Sample Interval | | 0.013 | 0.003 | 0.13 | 0.003 | Meters |
| Profile Length | | 50.47 | 2.44 | 81.37 | 2.92 | Meters |
| Variance | | 1.10E-01 | 2.80E-02 | 1.40E-02 | 2.90E-02 | Meters Sq. |
| Standard Dev. | | 0.1 | 1.70E-01 | 0.12 | 1.70E-01 | Meters |
| Total Relief | | 0.557 | 0.566 | 0.596 | 0.683 | Meters |

## Table 6

| | | | RELIEF STATISTICS | | | |
|---|---|---|---|---|---|---|
| | | | | | | |
| STA B Qhr | | | | | | |
| | | | | | | |
| DATA | | HELX | GRX | HELY | GRY | UNITS |
| | | | | | | |
| No. Sample pts. | | 790 | 395 | 972 | 413 | |
| Sampe Interval | | 0.103 | 0.003 | 0.104 | 0.003 | Meters |
| Profile Length | | 81.23 | 1.19 | 101.09 | 1.24 | Meters |
| Variance | | 0.008 | 0.032 | 0.02 | 0.024 | Meters Sq. |
| Standard Dev. | | 0.09 | 0.18 | 0.14 | 0.15 | Meters |
| Total Relief | | 0.495 | 0.544 | 0.683 | 0.47 | Meters |

Table 7

| | | | RELIEF STATISTICS | | | |
|---|---|---|---|---|---|---|
| | | | | | | |
| STA D Qch | | | | | | |
| | | | | | | |
| DATA | | HELX | GRX | HELY | GRY | UNITS |
| | | | | | | |
| No. Sample pts. | | 874 | 472 | 735 | 478 | |
| Sampe Interval | | 0.106 | 0.003 | 0.126 | 0.0029 | Meters |
| Profile Length | | 92.64 | 1.42 | 92.61 | 1.39 | Meters |
| Variance | | 0.03 | 0.002 | 0.02 | 5.26E-04 | Meters Sq. |
| Standard Dev. | | 0.16 | 0.05 | 0.14 | 2.29E-02 | Meters |
| Total Relief | | 0.941 | 0.169 | 0.639 | 0.09 | Meters |

# Table 8

| | | | RELIEF STATISTICS | | | |
|---|---|---|---|---|---|---|
| | | | | | | |
| **STA E Qhs** | | | | | | |
| | | | | | | |
| **DATA** | | **HELX** | **GRX** | **HELY** | **GRY** | **UNITS** |
| | | | | | | |
| No. Sample pts. | | 464 | 483 | 869 | 453 | |
| Sample Interval | | 0.103 | 0.0024 | 0.108 | 0.0024 | Meters |
| Profile Length | | 47.79 | 1.16 | 93.85 | 1.09 | Meters |
| Variance | | 5.80E-04 | 2.20E-02 | 1.30E-03 | 2.14E-02 | Meters Sq. |
| Standard Dev. | | 0.024 | 4.87E-04 | 0.036 | 4.59E-04 | Meters |
| Total Relief | | 0.132 | 0.08 | 0.218 | 0.096 | Meters |

Table 9

| | | | RELIEF STATISTICS | | | |
|---|---|---|---|---|---|---|
| | | | | | | |
| **STA H Qf** | | | | | | |
| | | | | | | |
| **DATA** | | **HELX** | **GRX** | **HELY** | **GRY** | **UNITS** |
| | | | | | | |
| No. Sample pts. | | None | 361 | None | 436 | |
| Sample Interval | | | 0.003 | | 0.003 | Meters |
| Profile Length | | | 1.08 | | 1.31 | Meters |
| Variance | | | 3.00E-06 | | 2.20E-06 | Meters Sq. |
| Standard Dev. | | | 1.70E-03 | | 1.50E-03 | Meters |
| Total Relief | | | 0.009 | | 0.008 | Meters |

Table 10

| | | | RELIEF STATISTICS | | | |
|---|---|---|---|---|---|---|
| | | | | | | |
| **STA I QG3-ROUGH** | | | | | | |
| | | | | | | |
| **DATA** | | **HELX** | **GRX** | **HELY** | **GRY** | **UNITS** |
| | | | | | | |
| No. Sample pts. | | 402 | 460 | 629 | 475 | |
| Sample Interval | | 0.125 | 0.003 | 0.13 | 0.003 | Meters |
| Profile Length | | 50.25 | 1.38 | 81.77 | 1.42 | Meters |
| Variance | | 4.00E-02 | 6.00E-03 | 3.00E-02 | 5.00E-03 | Meters Sq. |
| Standard Dev. | | 0.2 | 8.00E-02 | 0.16 | 7.00E-02 | Meters |
| Total Relief | | 0.67 | 0.26 | 0.92 | 0.227 | Meters |

Table 11

| | | | RELIEF STATISTICS | | | |
|---|---|---|---|---|---|---|
| | | | | | | |
| **STA J QG3-MODERATE** | | | | | | |
| | | | | | | |
| **DATA** | | **HELX** | **GRX** | **HELY** | **GRY** | **UNITS** |
| | | | | | | |
| No. Sample pts. | | 582 | 375 | 486 | 483 | |
| Sample Interval | | 0.107 | 0.003 | 0.123 | 0.003 | Meters |
| Profile Length | | 62.27 | 1.12 | 59.78 | 1.45 | Meters |
| Variance | | 4.00E-02 | 3.85E-04 | 4.00E-02 | 7.60E-04 | Meters Sq. |
| Standard Dev. | | 0.2 | 2.40E-02 | 0.2 | 2.76E-02 | Meters |
| Total Relief | | 1.11 | 0.099 | 0.943 | 0.124 | Meters |

Table 12

| | | RELIEF STATISTICS | | | |
|---|---|---|---|---|---|
| STA K QG3-SMOOTH | | | | | |
| DATA | HELX | GRX | HELY | GRY | UNITS |
| No. Sample pts. | 682 | 383 | 680 | 486 | |
| Sample Interval | 0.107 | 0.003 | 0.122 | 0.003 | Meters |
| Profile Length | 72.97 | 1.15 | 82.96 | 1.46 | Meters |
| Variance | 1.00E-02 | 4.80E-05 | 2.00E-02 | 1.53E-05 | Meters Sq. |
| Standard Dev. | 0.1 | 6.90E-03 | 0.13 | 3.90E-03 | Meters |
| Total Relief | 0.48 | 0.028 | 0.546 | 0.023 | Meters |

Table 13

| | | | RELIEF STATISTICS | | | |
|---|---|---|---|---|---|---|
| | | | | | | |
| **STA L QG3-DESERT PAVEMENT** | | | | | | |
| | | | | | | |
| **DATA** | | **HELX** | **GRX** | **HELY** | **GRY** | **UNITS** |
| | | | | | | |
| No. Sample pts. | | 351 | 269 | 703 | 260 | |
| Sample Interval | | 0.106 | 0.006 | 0.128 | 0.006 | Meters |
| Profile Length | | 37.21 | 1.61 | 8.98 | 1.56 | Meters |
| Variance | | 1.00E-02 | 9.00E-05 | 7.00E-02 | 7.70E-05 | Meters Sq. |
| Standard Dev. | | 0.117 | 9.50E-03 | 0.26 | 8.80E-03 | Meters |
| Total Relief | | 0.5 | 0.041 | 0.971 | 0.041 | Meters |

Table 14

| | | | SLOPE STATISTICS | | | | |
|---|---|---|---|---|---|---|---|
| STA A Gx | | | | | | | |
| Sample Interval (meters) | Variance (Degrees Sq) | Standard Deviation (Degrees) | Absolute Average (Degrees) | Absolute Variance (Degrees Sq) | Curvature Variance (Degrees Sq) | Log10(A) | B |
| 0.003 | 1849 | 43 | 36.7 | 501.3 | 1379 | 0.5 | -0.029 |
| 0.006 | 1842 | 43 | 36 | 544 | 818 | 0.459 | -0.028 |
| 0.012 | 1743 | 41.8 | 34.6 | 547 | 376.6 | 0.416 | -0.028 |
| 0.024 | 1614 | 40.2 | 33 | 529 | 139 | 0.387 | -0.029 |
| 0.06 | 1590 | 40 | 33.3 | 491 | 40.3 | 0.417 | -0.03 |
| 0.12 | 1490 | 38.6 | 33.4 | 390 | 18.3 | 0.51 | -0.034 |
| 0.24 | 1051 | 32.4 | 26.8 | 357 | 8.2 | 0.372 | -0.036 |

Table 15

|  |  |  | SLOPE STATISTICS |  |  |  |  |
|---|---|---|---|---|---|---|---|
|  |  |  |  |  |  |  |  |
| STA B Qhr Gx |  |  |  |  |  |  |  |
|  |  |  |  |  |  |  |  |
| Sample Interval (meters) | Variance (Degrees Sq) | Standard Deviation (Degrees) | Absolute Average (Degrees) | Absolute Variance (Degrees Sq) | Curvature Variance (Degrees Sq) | Log10(A) | B |
|  |  |  |  |  |  |  |  |
| 0.003 | 1469 | 38.3 | 31.8 | 463 | 1063.4 | 0.405 | -0.029 |
| 0.006 | 1418 | 37.7 | 30.9 | 464 | 436.9 | 0.382 | -0.029 |
| 0.012 | 1398 | 37.4 | 30.5 | 468 | 174 | 0.369 | -0.029 |
| 0.03 | 1405 | 37.5 | 30.4 | 477 | 53.9 | 0.354 | -0.029 |
| 0.06 | 1443 | 38 | 31 | 482 | 22.6 | 0.365 | -0.029 |
| 0.08 | 1472 | 38.4 | 31.5 | 476 | 14.9 | 0.377 | -0.03 |
| 0.12 | 1513 | 38.9 | 32.4 | 468 | 9.4 | 0.395 | -0.03 |

## Table 16

| | | | SLOPE STATISTICS | | | | |
|---|---|---|---|---|---|---|---|
| STA D Qhr Gx | | | | | | | |
| Sample Interval (meters) | Variance (Degrees Sq) | Standard Deviation (Degrees) | Absolute Average (Degrees) | Absolute Variance (Degrees Sq) | Curvature Variance (Degrees Sq) | Log10(A) | B |
| 0.003 | 858 | 29.3 | 23.5 | 315 | 845 | 0.293 | -0.033 |
| 0.006 | 765 | 27.7 | 21.5 | 313 | 371 | 0.242 | -0.033 |
| 0.012 | 648 | 25.5 | 19.4 | 286 | 126 | 0.194 | -0.034 |
| 0.03 | 494 | 22.2 | 16.9 | 227 | 38 | 0.186 | -0.038 |
| 0.06 | 343 | 18.5 | 14.6 | 152 | 12.7 | 0.238 | -0.05 |
| 0.08 | 281 | 16.8 | 13.8 | 116 | 8.5 | 0.293 | -0.059 |
| 0.12 | 158 | 12.6 | 11.4 | 60 | 4 | 0.407 | -0.086 |

Table 17

| | | | SLOPE STATISTICS | | | | |
|---|---|---|---|---|---|---|---|
| STA E Qhs Gx | | | | | | | |
| Sample Interval (meters) | Variance (Degrees Sq) | Standard Deviation (Degrees) | Absolute Average (Degrees) | Absolute Variance (Degrees Sq) | Curvature Variance (Degrees Sq) | Log10(A) | B |
| 0.002 | 935 | 30.6 | 23.3 | 390 | 1230 | 0.265 | -0.033 |
| 0.005 | 754 | 27.4 | 22 | 273 | 420 | 0.316 | -0.036 |
| 0.009 | 626 | 25 | 20.2 | 218 | 146 | 0.335 | -0.041 |
| 0.024 | 432 | 20.8 | 17.4 | 131 | 33.3 | 0.423 | -0.053 |
| 0.047 | 237 | 15.4 | 12.8 | 79 | 11.8 | 0.387 | -0.07 |
| 0.061 | 156 | 12.5 | 10.3 | 55.4 | 6.8 | 0.344 | -0.081 |
| 0.094 | 72.6 | 8.5 | 6.8 | 31.8 | 2.6 | 0.214 | -0.1 |

Table 18

| | | | SLOPE STATISTICS | | | | |
|---|---|---|---|---|---|---|---|
| STA H Qf Gx | | | | | | | |
| Sample Interval (meters) | Variance (Degrees Sq) | Standard Deviation (Degrees) | Absolute Average (Degrees) | Absolute Variance (Degrees Sq) | Curvature Variance (Degrees Sq) | Log10(A) | B |
| 0.003 | 140.5 | 11.9 | 6.3 | 101 | 325.5 | -0.106 | -0.051 |
| 0.006 | 67.2 | 8.2 | 5.3 | 39 | 88.9 | 0.017 | -0.085 |
| 0.012 | 27.7 | 5.3 | 4 | 11.7 | 24.3 | 0.178 | -0.158 |
| 0.024 | 8 | 2.8 | 2.3 | 2.9 | 4.8 | 0.263 | -0.313 |
| 0.06 | 2.2 | 1.5 | 1.2 | 0.7 | 0.73 | -0.387 | -0.707 |
| 0.12 | 0.62 | 0.79 | 0.73 | 0.18 | 0.18 | 0.504 | -1.38 |
| 0.24 | 0.17 | 0.41 | 0.39 | 0.07 | 0.05 | 0.38 | -2.41 |

Table 19

| | | | SLOPE STATISTICS | | | | |
|---|---|---|---|---|---|---|---|
| STA I Qg3-Rough Gx | | | | | | | |
| Sample Interval (meters) | Variance (Degrees Sq) | Standard Deviation (Degrees) | Absolute Average (Degrees) | Absolute Variance (Degrees Sq) | Curvature Variance (Degrees Sq) | Log10(A) | B |
| 0.003 | 1208 | 34.8 | 27.9 | 439 | 935 | 0.322 | -0.029 |
| 0.006 | 1177 | 34.3 | 26.9 | 464 | 397 | 0.282 | -0.029 |
| 0.012 | 1152 | 34 | 26 | 480 | 191 | 0.252 | -0.029 |
| 0.024 | 1157 | 34 | 26.4 | 461 | 87 | 0.268 | -0.03 |
| 0.06 | 1083 | 33 | 27 | 356 | 34.9 | 0.378 | -0.034 |
| 0.12 | 912 | 30.2 | 25.3 | 282 | 12.7 | 0.406 | -0.04 |
| 0.24 | 565 | 23.8 | 20.6 | 150 | 4.8 | 0.494 | -0.054 |

Table 20

| | | | SLOPE STATISTICS | | | | |
|---|---|---|---|---|---|---|---|
| STA J Qg3-Moderate Gx | | | | | | | |
| Sample Interval (meters) | Variance (Degrees Sq) | Standard Deviation (Degrees) | Absolute Average (Degrees) | Absolute Variance (Degrees Sq) | Curvature Variance (Degrees Sq) | Log10(A) | B |
| 0.003 | 1160 | 34 | 28.4 | 353 | 1234 | 0.403 | -0.032 |
| 0.006 | 1056 | 32.5 | 26 | 387 | 615 | 0.318 | -0.031 |
| 0.012 | 937 | 30.6 | 23.9 | 368 | 258 | 0.278 | -0.037 |
| 0.024 | 779 | 28 | 22 | 297 | 111 | 0.296 | -0.037 |
| 0.06 | 477 | 21.8 | 17.7 | 165 | 24.8 | 0.361 | -0.051 |
| 0.12 | 223 | 15 | 12.8 | 61.8 | 6.9 | 0.473 | -0.085 |
| 0.24 | 65.4 | 8.1 | 6.8 | 23.2 | 1.9 | 0.38 | -0.137 |

Table 21

| | | | SLOPE STATISTICS | | | | |
|---|---|---|---|---|---|---|---|
| STA K Qg3-Smooth Gx | | | | | | | |
| Sample Interval (meters) | Variance (Degrees Sq) | Standard Deviation (Degrees) | Absolute Average (Degrees) | Absolute Variance (Degrees Sq) | Curvature Variance (Degrees Sq) | Log10(A) | B |
| 0.003 | 658 | 25.6 | 19.2 | 288 | 1281 | 0.214 | -0.036 |
| 0.006 | 429 | 20.7 | 15.7 | 184 | 415 | 0.176 | -0.041 |
| 0.012 | 269 | 16 | 12 | 113 | 138 | 0.183 | -0.052 |
| 0.024 | 133 | 11.5 | 8.7 | 57 | 36.9 | 0.187 | -0.074 |
| 0.06 | 36.6 | 6.1 | 4.9 | 12.6 | 5.8 | 0.333 | -0.166 |
| 0.12 | 16.8 | 4.1 | 3.3 | 5.8 | 1.4 | 0.337 | -0.249 |
| 0.24 | 5.9 | 2.4 | 2.2 | 1.5 | 0.42 | 0.533 | -0.49 |

Table 22

| | | | SLOPE STATISTICS | | | | |
|---|---|---|---|---|---|---|---|
| STA L Qg3-Pavement Gx | | | | | | | |
| Sample Interval (meters) | Variance (Degrees Sq) | Standard Deviation (Degrees) | Absolute Average (Degrees) | Absolute Variance (Degrees Sq) | Curvature Variance (Degrees Sq) | Log10(A) | B |
| 0.006 | 513 | 22.7 | 17.5 | 207 | 1162 | 0.214 | -0.038 |
| 0.012 | 295 | 17.1 | 12.4 | 140 | 393 | 0.098 | -0.043 |
| 0.024 | 139 | 11.8 | 8.3 | 70.4 | 98.5 | 0.025 | -0.056 |
| 0.048 | 74.4 | 8.6 | 5.8 | 40.4 | 29.6 | 0.012 | -0.078 |
| 0.12 | 27.6 | 5.3 | 3.6 | 15 | 5.4 | 0.057 | -0.15 |
| 0.24 | 6.6 | 2.6 | 1.9 | 2.9 | 1.4 | 0.119 | -0.3 |
| 0.48 | 3 | 1.7 | 1.4 | 0.95 | 0.27 | 0.294 | -0.536 |

Table 23a

| | | | SLOPE STATISTICS | | | | |
|---|---|---|---|---|---|---|---|
| | | | | | | | |
| STA A Qh Hx | | | | | | | |
| | | | | | | | |
| Sample Interval (meters) | Variance (Degrees Sq) | Standard Deviation (Degrees) | Absolute Average (Degrees) | Absolute Variance (Degrees Sq) | Curvature Variance (Degrees Sq) | Log10(A) | B |
| | | | | | | | |
| 0.1 | 550.9 | 23.5 | 19.1 | 185 | 401.7 | 0.364 | -0.045 |
| 0.21 | 476.4 | 21.8 | 17.9 | 154.6 | 261.7 | 0.381 | -0.05 |
| 0.41 | 320.9 | 17.9 | 14.8 | 102.6 | 99.2 | -0.404 | -0.063 |
| 0.82 | 133 | 11.5 | 9.3 | 45.7 | 26.3 | 0.371 | -0.095 |
| 2.06 | 16.5 | 4 | 3.2 | 5.9 | 3.7 | 0.309 | -0.24 |
| 4.11 | 5.5 | 2.3 | 1.9 | 1.9 | 1 | 0.32 | -0.421 |
| 8.23 | 1.4 | 1.2 | 0.9 | 0.5 | 0.2 | 0.325 | -0.844 |
| 10.29 | 0.8 | 0.9 | 0.7 | 0.3 | 0.2 | 0.323 | -1.1 |
| 20.57 | 0.2 | 0.5 | 0.4 | 0.1 | 0.04 | 0.365 | -2.11 |

Table 23b

| | | | SLOPE STATISTICS | | | | |
|---|---|---|---|---|---|---|---|
| STA A Qh Hy | | | | | | | |
| Sample Interval (meters) | Variance (Degrees Sq) | Standard Deviation (Degrees) | Absolute Average (Degrees) | Absolute Variance (Degrees Sq) | Curvature Variance (Degrees Sq) | Log10(A) | B |
| 0.13 | 488.6 | 22.1 | 18.1 | 159.8 | 448 | 0.378 | -0.04 |
| 0.25 | 399.6 | 20 | 16.5 | 126 | 258.1 | 0.41 | -0.055 |
| 0.5 | 240.5 | 25.5 | 12.7 | 78.8 | 91.3 | 0.389 | -0.07 |
| 1.01 | 81.1 | 9 | 7.2 | 29.1 | 22.2 | 0.315 | -0.11 |
| 2.52 | 11.5 | 3.4 | 2.7 | 4.2 | 3.1 | 0.283 | -0.277 |
| 5.04 | 2.85 | 1.7 | 1.3 | 1.2 | 0.8 | 0.239 | -0.55 |
| 10.09 | 0.92 | 0.96 | 0.78 | 0.32 | 0.22 | 0.341 | -1.07 |
| 12.61 | 0.56 | 0.76 | 0.61 | 0.21 | 0.14 | 0.331 | -1.34 |
| 25.22 | 0.17 | 0.41 | 0.35 | 0.05 | 0.04 | 0.395 | -2.6 |

## Table 24a

| | | | SLOPE STATISTICS | | | | |
|---|---|---|---|---|---|---|---|
| STA B Qhr Hx | | | | | | | |
| | | | | | | | |
| Sample Interval (meters) | Variance (Degrees Sq) | Standard Deviation (Degrees) | Absolute Average (Degrees) | Absolute Variance (Degrees Sq) | Curvature Variance (Degrees Sq) | Log10(A) | B |
| | | | | | | | |
| 0.1 | 447.6 | 21.2 | 17.4 | 145.3 | 563.8 | 0.386 | -0.051 |
| 0.21 | 326.9 | 18.1 | 14.8 | 108.1 | 291.7 | 0.36 | -0.058 |
| 0.41 | 157.5 | 12.5 | 10.2 | 54.2 | 74.3 | 0.336 | -0.08 |
| 0.82 | 51.1 | 7.1 | 5.8 | 17.7 | 18.3 | 0.321 | -0.137 |
| 2.06 | 7.3 | 2.7 | 2.2 | 2.6 | 2.7 | 0.266 | -0.33 |
| 4.12 | 2.2 | 1.5 | 1.2 | 0.75 | 0.72 | 0.348 | -0.69 |
| 8.24 | 0.61 | 0.78 | 0.63 | 0.22 | 0.17 | 0.323 | -1.27 |
| 10.29 | 0.41 | 0.64 | 0.51 | 0.15 | 0.11 | 0.32 | -1.57 |
| 20.59 | 0.11 | 0.33 | 0.27 | 0.04 | 0.03 | 0.315 | -2.97 |

## Table 24b

| | | | SLOPE STATISTICS | | | | |
|---|---|---|---|---|---|---|---|
| STA B Qhr Hy | | | | | | | |
| Sample Interval (meters) | Variance (Degrees Sq) | Standard Deviation (Degrees) | Absolute Average (Degrees) | Absolute Variance (Degrees Sq) | Curvature Variance (Degrees Sq) | Log10(A) | B |
| 0.1 | 289.2 | 17 | 13.8 | 97.5 | 297.2 | 0.32 | -0.057 |
| 0.21 | 224.8 | 15 | 12.2 | 76.2 | 164.2 | 0.319 | -0.064 |
| 0.42 | 122.8 | 11.1 | 8.9 | 44.1 | 48.5 | 0.274 | -0.083 |
| 0.83 | 42.1 | 6.5 | 5.1 | 16.2 | 11.5 | 0.206 | -0.128 |
| 2.08 | 7 | 2.6 | 2 | 2.9 | 1.6 | 0.149 | -0.289 |
| 4.16 | 1.9 | 1.4 | 1.1 | 0.75 | 0.43 | 0.179 | -0.568 |
| 8.32 | 0.49 | 0.7 | 0.58 | 0.21 | 0.1 | 0.211 | -1.13 |
| 10.4 | 0.3 | 0.55 | 0.48 | 0.12 | 0.06 | 0.295 | -1.58 |
| 20.8 | 0.09 | 0.3 | 0.31 | 0.04 | 0.02 | 0.411 | -2.92 |

## Table 25a

| | | | SLOPE STATISTICS | | | | |
|---|---|---|---|---|---|---|---|
| STA D Qch Hx | | | | | | | |
| Sample Interval (meters) | Variance (Degrees Sq) | Standard Deviation (Degrees) | Absolute Average (Degrees) | Absolute Variance (Degrees Sq) | Curvature Variance (Degrees Sq) | Log10(A) | B |
| 0.11 | 77.6 | 8.8 | 6.9 | 31.5 | 129.2 | 0.185 | -0.092 |
| 0.21 | 46.2 | 6.8 | 5.3 | 18.1 | 47.8 | 0.252 | -0.133 |
| 0.42 | 20 | 4.5 | 3.5 | 8.1 | 9.3 | 0.155 | -0.173 |
| 0.85 | 9.2 | 3 | 2.4 | 3.5 | 2.6 | 0.237 | -0.287 |
| 2.11 | 3.61 | 1.9 | 1.5 | 1.6 | 0.38 | 0.134 | -0.396 |
| 4.23 | 2.3 | 1.5 | 1.2 | 1 | 0.1 | 0.164 | -0.533 |
| 8.45 | 1.3 | 1.1 | 0.85 | 0.64 | 0.025 | 0.155 | -0.723 |
| 10.57 | 0.96 | 0.98 | 0.72 | 0.51 | 0.017 | 0.129 | -0.81 |
| 21.14 | 0.21 | 0.46 | 0.37 | 0.13 | 0.005 | 0.14 | -1.65 |

## Table 25b

|  |  |  | SLOPE STATISTICS |  |  |  |  |
|---|---|---|---|---|---|---|---|
| STA D Hy |  |  |  |  |  |  |  |
| Sample Interval (meters) | Variance (Degrees Sq) | Standard Deviation (Degrees) | Absolute Average (Degrees) | Absolute Variance (Degrees Sq) | Curvature Variance (Degrees Sq) | Log10(A) | B |
| 0.13 | 48 | 6.9 | 5.5 | 18.2 | 61.9 | 0.225 | -0.123 |
| 0.25 | 32.9 | 5.7 | 4.6 | 11.7 | 27 | 0.255 | -0.155 |
| 0.51 | 16.6 | 4.1 | 3.2 | 6 | 6.5 | 0.277 | -0.277 |
| 1.01 | 7.2 | 2.7 | 2.1 | 2.7 | 1.6 | 0.24 | -0.326 |
| 2.53 | 3.3 | 1.8 | 1.4 | 1.3 | 0.24 | 0.219 | -0.476 |
| 5.05 | 2.3 | 1.5 | 1.2 | 0.93 | 0.07 | 0.228 | -0.606 |
| 10.1 | 1.2 | 1.1 | 0.87 | 0.46 | 0.02 | 0.266 | -0.859 |
| 12.63 | 0.9 | 0.95 | 0.71 | 0.38 | 0.011 | 0.214 | -0.96 |
| 25.25 | 0.27 | 0.52 | 0.42 | 0.096 | 0.002 | 0.33 | -2.05 |

## Table 26a

| | | | SLOPE STATISTICS | | | | |
|---|---|---|---|---|---|---|---|
| STA E Qhs Hx | | | | | | | |
| Sample Interval (meters) | Variance (Degrees Sq) | Standard Deviation (Degrees) | Absolute Average (Degrees) | Absolute Variance (Degrees Sq) | Curvature Variance (Degrees Sq) | Log10(A) | B |
| 0.1 | 41 | 6.4 | 4.9 | 16.9 | 48.4 | 0.185 | -0.13 |
| 0.21 | 29.2 | 5.4 | 4.2 | 11.4 | 24.7 | 0.236 | -0.166 |
| 0.41 | 13.3 | 3.7 | 2.9 | 5 | 6.4 | 0.242 | -0.253 |
| 0.83 | 3.8 | 2 | 1.5 | 1.4 | 1.3 | 0.318 | -0.458 |
| 2.06 | 0.67 | 0.82 | 0.66 | 0.23 | 0.19 | 0.288 | -1.2 |
| 4.13 | 0.19 | 0.42 | 0.35 | 0.067 | 0.048 | 0.418 | -2.13 |
| 8.26 | 0.055 | 0.23 | 0.2 | 0.017 | 0.013 | 0.359 | -4.62 |
| 10.32 | 0.038 | 0.2 | 0.16 | 0.013 | 0.008 | 0.335 | -5.19 |
| 20.65 | 0.01 | 0.1 | 0.08 | 0.003 | 0.002 | 0.14 | -9.83 |

## Table 26b

| | | | SLOPE STATISTICS | | | | |
|---|---|---|---|---|---|---|---|
| STA E Qhs Hy | | | | | | | |
| Sample Interval (meters) | Variance (Degrees Sq) | Standard Deviation (Degrees) | Absolute Average (Degrees) | Absolute Variance (Degrees Sq) | Curvature Variance (Degrees Sq) | Log10(A) | B |
| 0.11 | 70.9 | 8.4 | 6.8 | 24.2 | 112.6 | 0.31 | -0.113 |
| 0.22 | 43.4 | 6.7 | 5.4 | 14.7 | 46.2 | 0.315 | -0.147 |
| 0.43 | 16.2 | 4 | 3.2 | 5.8 | 10.5 | 0.294 | -0.233 |
| 0.86 | 4.1 | 2 | 1.6 | 1.6 | 2.3 | 0.243 | -0.444 |
| 2.15 | 0.87 | 0.93 | 0.75 | 0.3 | 0.37 | 0.327 | -1.06 |
| 4.31 | 0.22 | 0.47 | 0.38 | 0.08 | 0.09 | 0.306 | -2.05 |
| 8.61 | 0.088 | 0.3 | 0.23 | 0.034 | 0.023 | 0.218 | -2.86 |
| 10.76 | 0.068 | 0.26 | 0.21 | 0.024 | 0.015 | 0.283 | -3.53 |
| 21.53 | 0.017 | 0.13 | 0.11 | 0.007 | 0.004 | 0.228 | -6.53 |

## Table 27a

|  |  |  | SLOPE STATISTICS |  |  |  |  |
|---|---|---|---|---|---|---|---|
|  |  |  |  |  |  |  |  |
| STA I Qg3-Rough Hx |  |  |  |  |  |  |  |
|  |  |  |  |  |  |  |  |
| Sample Interval (meters) | Variance (Degrees Sq) | Standard Deviation (Degrees) | Absolute Average (Degrees) | Absolute Variance (Degrees Sq) | Curvature Variance (Degrees Sq) | Log10(A) | B |
|  |  |  |  |  |  |  |  |
| 0.13 | 161.4 | 12.7 | 9.7 | 67.9 | 154 | 0.186 | -0.066 |
| 0.25 | 126.7 | 11.3 | 8.7 | 51.4 | 67.8 | 0.209 | -0.076 |
| 0.5 | 86 | 9.3 | 7.1 | 35.5 | 20 | 0.185 | -0.089 |
| 1 | 51.8 | 7.2 | 5.3 | 23.5 | 5 | 0.144 | -0.112 |
| 2.4 | 24.1 | 4.9 | 3.8 | 9.7 | 0.97 | 0.254 | -0.195 |
| 5.01 | 10.6 | 3.2 | 2.5 | 4.3 | 0.24 | 0.265 | -0.313 |
| 10.02 | 2.6 | 1.6 | 1.4 | 0.88 | 0.062 | 0.402 | -0.738 |
| 12.52 | 1.7 | 1.3 | 1.1 | 0.56 | 0.033 | 0.431 | -0.868 |
| 25.04 | 0.54 | 0.73 | 0.6 | 0.19 | 0.009 | 0.35 | -1.58 |

## Table 27b

|  |  |  | SLOPE STATISTICS |  |  |  |  |
|---|---|---|---|---|---|---|---|
| STA I Qg3-Rough Hx |  |  |  |  |  |  |  |
| Sample Interval (meters) | Variance (Degrees Sq) | Standard Deviation (Degrees) | Absolute Average (Degrees) | Absolute Variance (Degrees Sq) | Curvature Variance (Degrees Sq) | Log10(A) | B |
| 0.13 | 84.2 | 9.2 | 6.9 | 36.3 | 117.9 | 0.18 | -0.091 |
| 0.26 | 56 | 7.5 | 5.8 | 22.9 | 43.1 | 0.214 | -0.117 |
| 0.52 | 32.6 | 5.7 | 4.3 | 14.5 | 10.6 | 0.115 | -0.131 |
| 1.04 | 19.9 | 4.5 | 3.1 | 10.3 | 2.9 | -0.002 | -0.139 |
| 2.6 | 9.4 | 3.1 | 2.1 | 4.9 | 0.48 | -0.027 | -0.193 |
| 5.21 | 4.1 | 2 | 1.6 | 1.7 | 0.12 | 0.118 | -0.359 |
| 10.41 | 1.4 | 1.2 | 1 | 0.4 | 0.03 | 0.428 | -0.88 |
| 13.02 | 1 | 1 | 0.88 | 0.33 | 0.017 | 0.434 | -1.09 |
| 26.03 | 0.35 | 0.59 | 0.48 | 0.13 | 0.005 | 0.285 | -1.577 |

## Table 28a

|  |  |  | SLOPE STATISTICS |  |  |  |  |
|---|---|---|---|---|---|---|---|
| STA J Qg3-Moderate Hx |  |  |  |  |  |  |  |
| Sample Interval (meters) | Variance (Degrees Sq) | Standard Deviation (Degrees) | Absolute Average (Degrees) | Absolute Variance (Degrees Sq) | Curvature Variance (Degrees Sq) | Log10(A) | B |
| 0.11 | 129.5 | 11.4 | 8.7 | 54 | 117.7 | 0.177 | -0.072 |
| 0.21 | 102.2 | 10.1 | 7.8 | 41.4 | 58.4 | 0.194 | -0.082 |
| 0.43 | 65.3 | 8.1 | 6.1 | 28 | 16.8 | 0.154 | -0.098 |
| 0.85 | 35.3 | 5.9 | 4.5 | 15.2 | 4.4 | 0.183 | -0.143 |
| 2.14 | 13.4 | 3.7 | 2.8 | 5.5 | 0.76 | 0.221 | -0.239 |
| 4.27 | 4.67 | 2.16 | 1.7 | 1.8 | 0.18 | 0.258 | -0.412 |
| 8.54 | 1.69 | 1.3 | 1 | 0.7 | 0.042 | 0.237 | -0.687 |
| 10.68 | 1.2 | 1.1 | 0.92 | 0.43 | 0.029 | 0.343 | -0.913 |
| 21.35 | 0.66 | 0.81 | 0.75 | 0.2 | 0.008 | 0.539 | -1.47 |

Table 28b

| | | | SLOPE STATISTICS | | | | |
|---|---|---|---|---|---|---|---|
| STA J Qg3-Moderate Hy | | | | | | | |
| Sample Interval (meters) | Variance (Degrees Sq) | Standard Deviation (Degrees) | Absolute Average (Degrees) | Absolute Variance (Degrees Sq) | Curvature Variance (Degrees Sq) | Log10(A) | B |
| 0.12 | 123.5 | 11.1 | 8.5 | 50.6 | 144.5 | 0.198 | -0.076 |
| 0.25 | 90.3 | 9.5 | 7.4 | 35.7 | 64.4 | 0.206 | 0.089 |
| 0.49 | 53.5 | 7.3 | 5.5 | 23 | 15.5 | 0.162 | -0.111 |
| 0.98 | 30.9 | 5.6 | 4.2 | 13.1 | 3.9 | 0.172 | -0.149 |
| 2.46 | 15.9 | 4 | 3 | 7.1 | 0.75 | 0.12 | -0.189 |
| 4.91 | 6.6 | 2.6 | 2 | 2.5 | 0.18 | 0.267 | -0.363 |
| 9.82 | 1.9 | 1.4 | 1.2 | 0.59 | 0.044 | 0.397 | -0.762 |
| 12.28 | 1.5 | 1.2 | 1 | 0.43 | 0.024 | 0.491 | -1.02 |
| 24.57 | 0.48 | 0.69 | 0.69 | 0.087 | 0.007 | 0.803 | -1.98 |

Table 29a

| | | | SLOPE STATISTICS | | | | |
|---|---|---|---|---|---|---|---|
| STA K Qg3-Smooth Hx | | | | | | | |
| Sample Interval (meters) | Variance (Degrees Sq) | Standard Deviation (Degrees) | Absolute Average (Degrees) | Absolute Variance (Degrees Sq) | Curvature Variance (Degrees Sq) | Log10(A) | B |
| 0.11 | 51.7 | 7.2 | 5.4 | 22.5 | 51.4 | 0.077 | -0.097 |
| 0.21 | 39.5 | 6.3 | 4.8 | 16.4 | 24.9 | 0.146 | -0.121 |
| 0.43 | 22.7 | 4.8 | 3.7 | 9.3 | 7.7 | 0.177 | -0.169 |
| 0.85 | 9.2 | 3 | 2.3 | 3.9 | 1.6 | 0.133 | -0.249 |
| 2.13 | 3.2 | 1.8 | 1.3 | 1.5 | 0.26 | 0.1 | -0.404 |
| 4.27 | 1.7 | 1.3 | 0.96 | 0.76 | 0.072 | 0.125 | -0.594 |
| 8.53 | 0.82 | 0.9 | 0.7 | 0.34 | 0.017 | 0.245 | -1.04 |
| 10.67 | 0.6 | 0.78 | 0.6 | 0.25 | 0.011 | 0.268 | -1.31 |
| 21.33 | 0.21 | 0.46 | 0.4 | 0.06 | 0.003 | 0.471 | -2.43 |

## Table 29b

| | | | SLOPE STATISTICS | | | | |
|---|---|---|---|---|---|---|---|
| STA K Qg3-Smooth Hy | | | | | | | |
| Sample Interval (meters) | Variance (Degrees Sq) | Standard Deviation (Degrees) | Absolute Average (Degrees) | Absolute Variance (Degrees Sq) | Curvature Variance (Degrees Sq) | Log10(A) | B |
| 0.12 | 69.6 | 8.3 | 6.5 | 27 | 58.7 | 0.241 | -0.107 |
| 0.24 | 55.6 | 7.5 | 5.9 | 21.2 | 31.6 | 0.186 | -0.108 |
| 0.49 | 34.4 | 5.9 | 4.6 | 13.5 | 10.5 | 0.098 | -0.12 |
| 0.97 | 15 | 3.9 | 3 | 5.9 | 2.4 | 0.126 | -0.19 |
| 2.43 | 4.85 | 2.2 | 1.6 | 2.2 | 0.38 | 0.078 | -0.314 |
| 4.86 | 2.2 | 1.5 | 1.1 | 0.89 | 0.092 | 0.229 | -0.618 |
| 9.72 | 0.82 | 0.9 | 0.72 | 0.3 | 0.023 | 0.301 | -1.07 |
| 12.16 | 0.57 | 0.75 | 0.62 | 0.19 | 0.014 | 0.376 | -1.39 |
| 24.31 | 0.14 | 0.37 | 0.35 | 0.048 | 0.004 | 0.418 | -2.54 |

## Table 30a

|  |  | SLOPE STATISTICS |  |  |  |  |  |
|---|---|---|---|---|---|---|---|
| STA. L Hx |  |  |  |  |  |  |  |
|  |  |  |  |  |  |  |  |
| Sample Interval (Meters) | Variance (Degrees Sq) | Standard Devaition (Degrees) | Absolute Average (Degrees) | Absolute Variance (Degrees Sq) | Curvature Variance (Degrees Sq) | Log10(A) | B |
|  |  |  |  |  |  |  |  |
| 0.11 | 81.8 | 9 | 7 | 32.8 | 103 | 0.084 | -0.07 |
| 0.21 | 55.32 | 7.4 | 5.9 | 20.5 | 44.3 | 0.214 | -0.112 |
| 0.42 | 28.47 | 5.3 | 4.1 | 11.7 | 11 | 0.143 | -0.143 |
| 0.85 | 12.63 | 3.6 | 2.6 | 5.9 | 2.4 | 0.111 | -0.213 |
| 2.11 | 6.63 | 2.6 | 2 | 2.7 | 0.35 | 0.237 | -0.358 |
| 4.23 | 3.68 | 1.9 | 1.5 | 1.4 | 0.09 | 0.275 | -0.519 |
| 8.45 | 1.41 | 1.2 | 0.93 | 0.56 | 0.022 | 0.23 | -0.761 |
| 10.56 | 1.13 | 1.1 | 0.85 | 0.45 | 0.015 | 0.29 | -0.94 |
| 21.13 | 0.05 | 0.22 | 0.49 | 0.5 | 0.005 | 0.851 | -2.91 |

## Table 30b

| | | | SLOPE STATISTICS | | | | |
|---|---|---|---|---|---|---|---|
| STA L Qg2-Smooth Hy | | | | | | | |
| Sample Interval (meters) | Variance (Degrees Sq) | Standard Deviation (Degrees) | Absolute Average (Degrees) | Absolute Variance (Degrees Sq) | Curvature Variance (Degrees Sq) | Log10(A) | B |
| 0.13 | 34.6 | 5.9 | 4.5 | 14.6 | 52.2 | 0.071 | -0.116 |
| 0.26 | 21.9 | 4.7 | 3.6 | 9.1 | 18 | 0.092 | -0.151 |
| 0.51 | 12 | 3.5 | 2.6 | 5.6 | 3.8 | -0.058 | -0.156 |
| 1.02 | 7.4 | 2.7 | 2 | 3.6 | 1.09 | -0.073 | -0.192 |
| 2.55 | 2.7 | 1.7 | 1.2 | 1.6 | 0.018 | -0.066 | -0.312 |
| 5.11 | 1.25 | 1.11 | 0.91 | 0.83 | 0.05 | 0.05 | -0.537 |
| 10.21 | 0.46 | 0.68 | 0.64 | 0.32 | 0.01 | 0.1 | -0.854 |
| 12.77 | 0.35 | 0.6 | 0.6 | 0.25 | 0.008 | 0.152 | -0.998 |
| 25.54 | 0.18 | 0.43 | 0.54 | 0.13 | 0.002 | 0.421 | -1.72 |

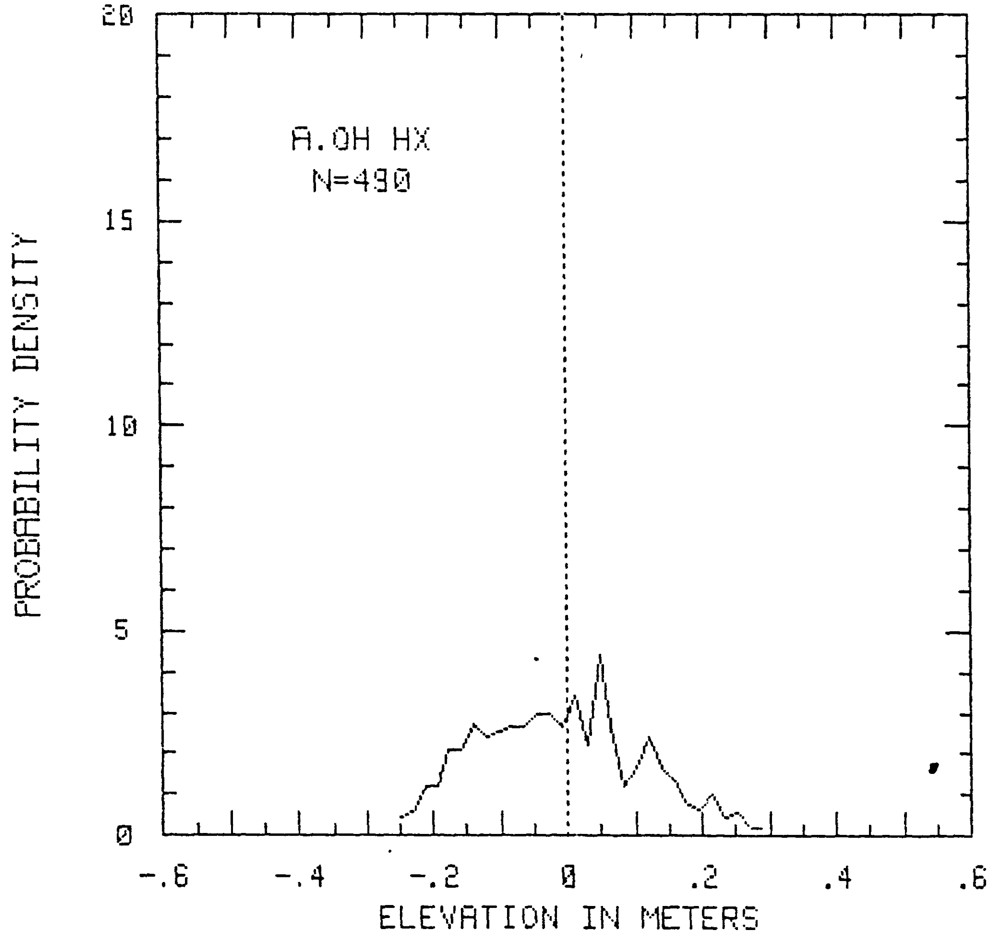
A.OH HX
N=490
PROBABILITY DENSITY
ELEVATION IN METERS
20
15
10
5
0
-.6
-.4
-.2
0
.2
.4
.6

Figure 30a

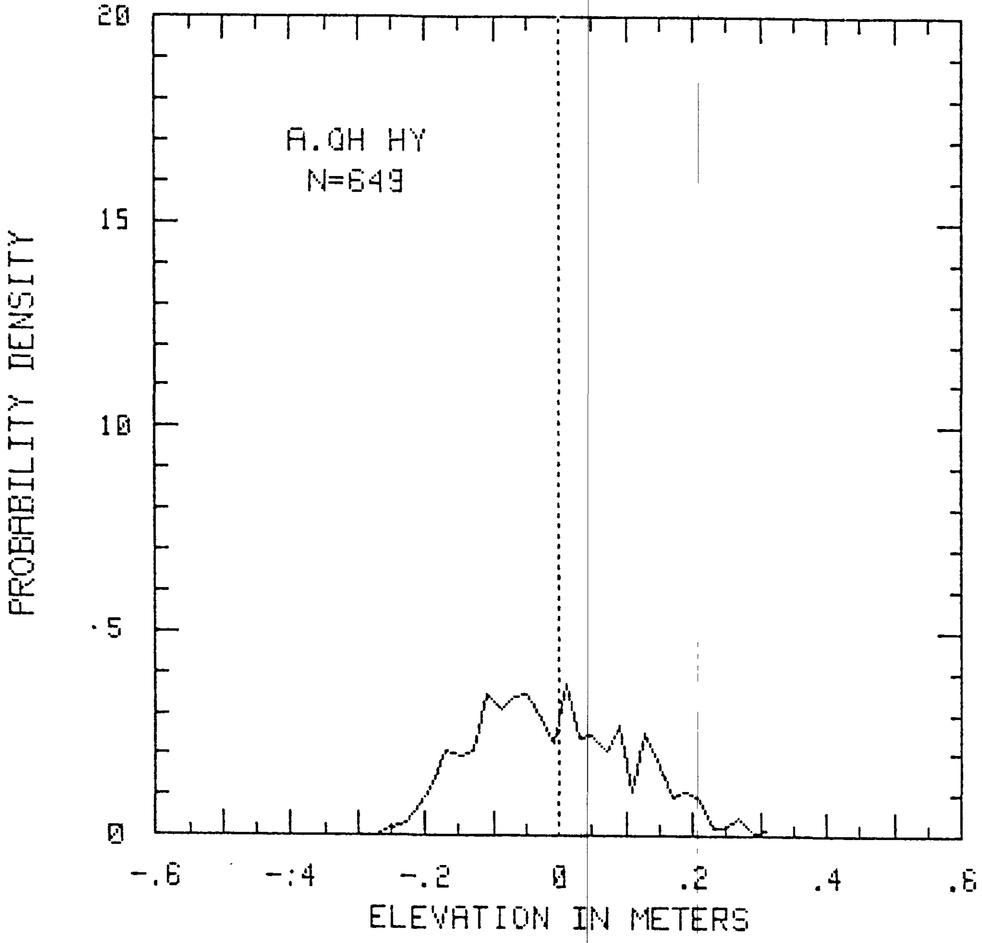
A.QH HY
N=649
PROBABILITY DENSITY
20
15
10
5
0
-.6
-.4
-.2
0
.2
.4
.6
ELEVATION IN METERS

Figure 30b

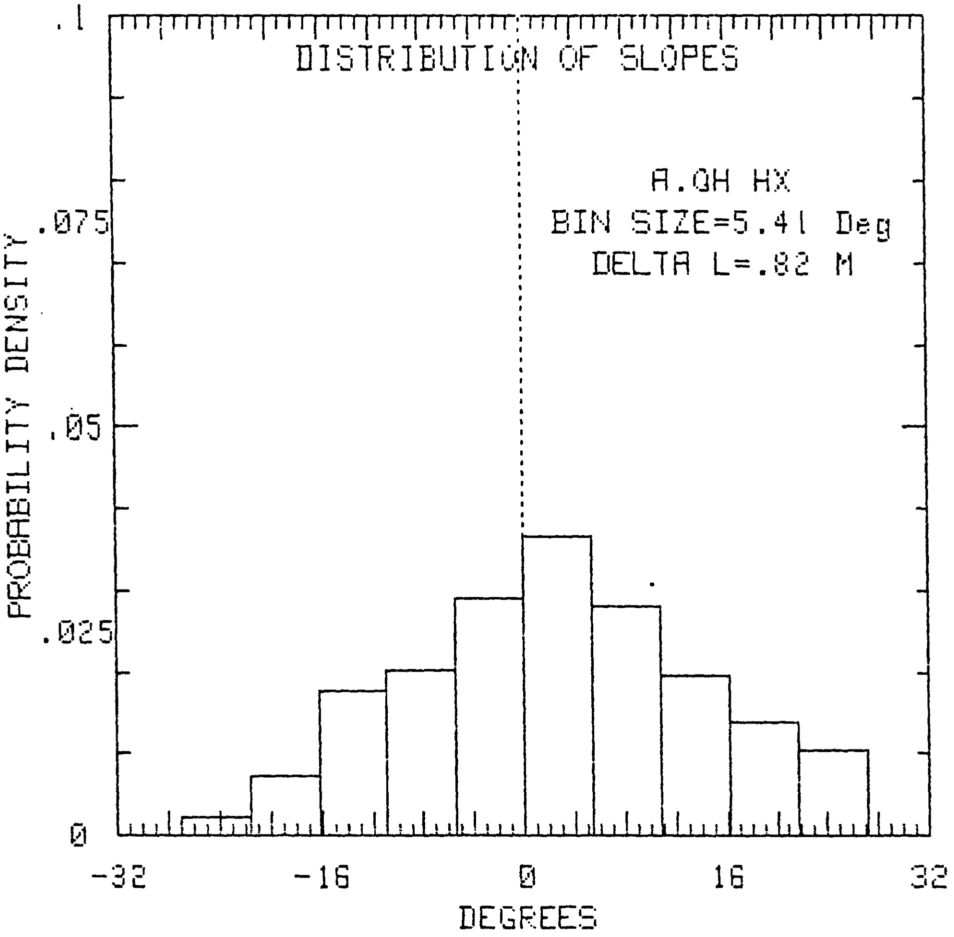
DISTRIBUTION OF SLOPES
A.QH HX
BIN SIZE=5.41 Deg
DELTA L=.82 M
PROBABILITY DENSITY
.1
.075
.05
.025
0
-32
-16
0
16
32
DEGREES

Figure 30c

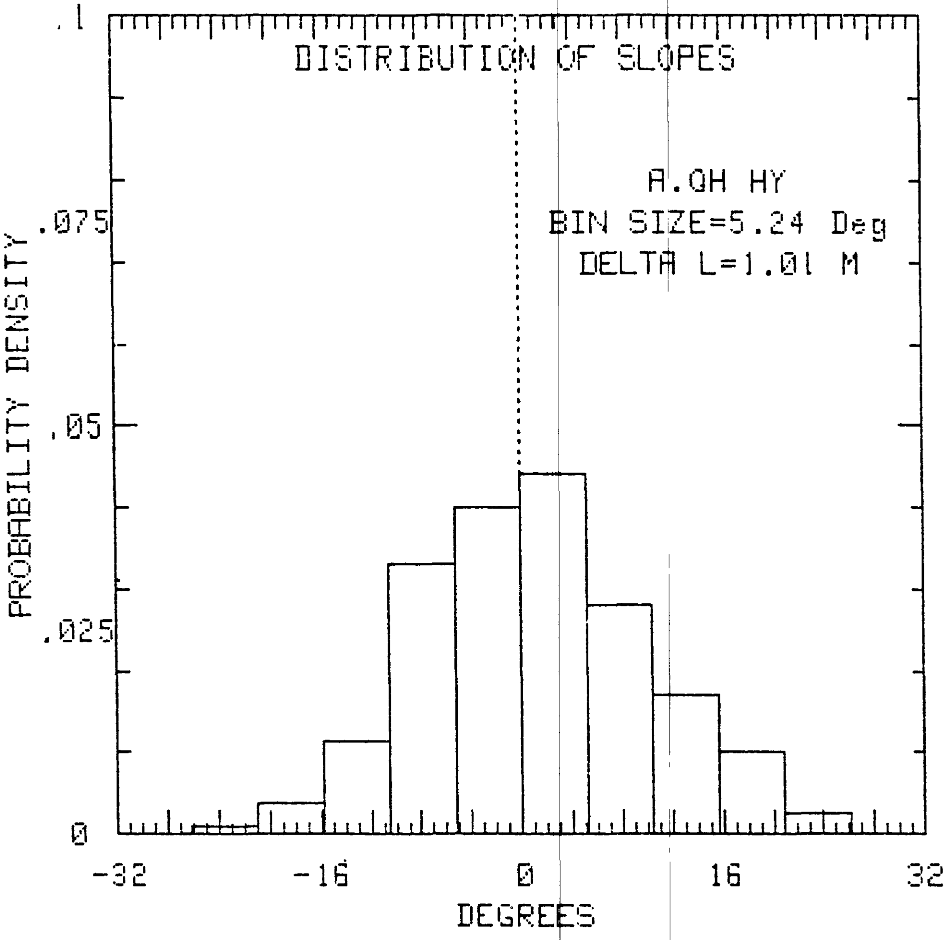
DISTRIBUTION OF SLOPES
A.QH HY
BIN SIZE=5.24 Deg
DELTA L=1.01 M
PROBABILITY DENSITY
.1
.075
.05
.025
0
-32
-16
0
16
32
DEGREES

Figure 30d

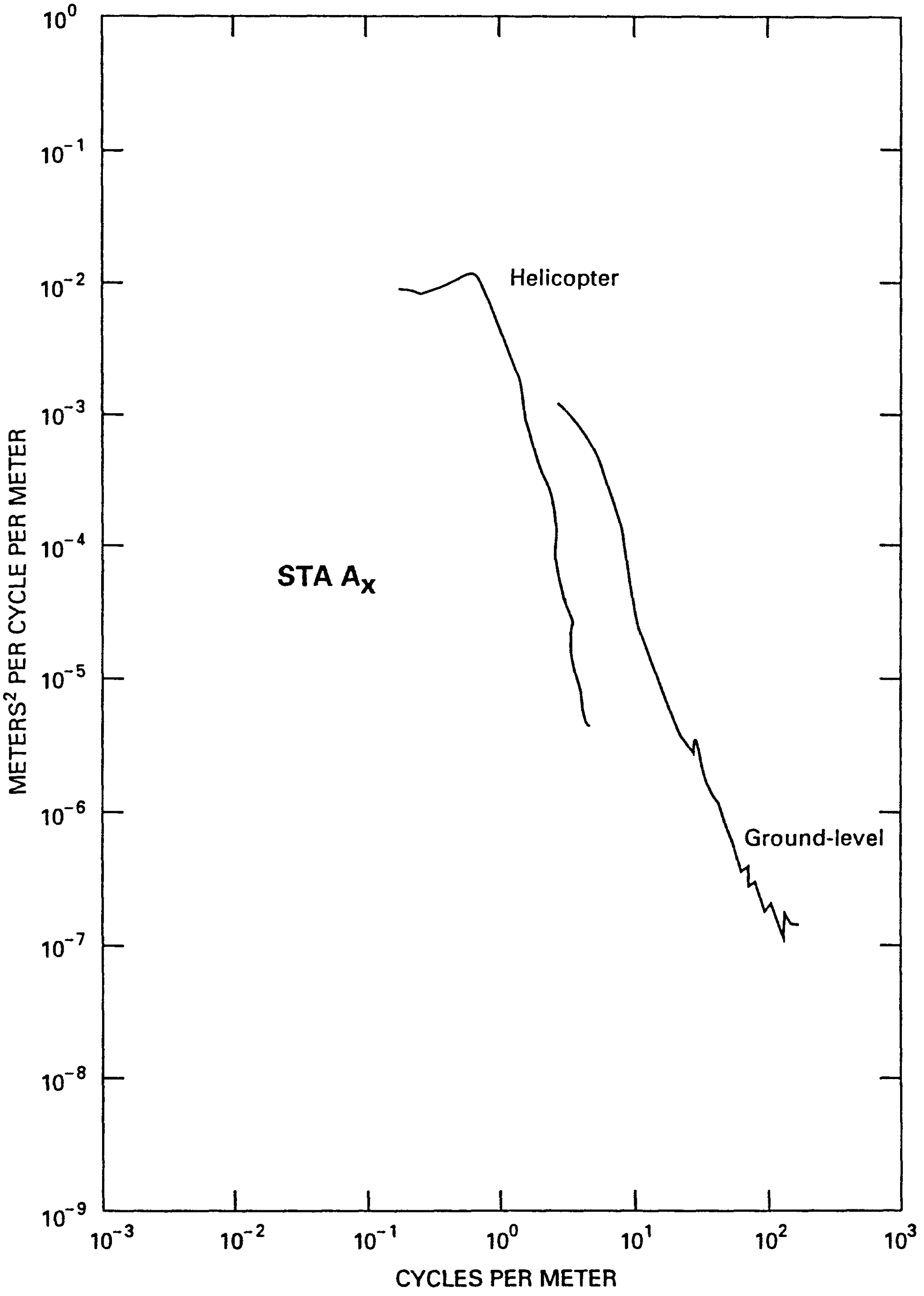
10^0
10^-1
10^-2
10^-3
10^-4
10^-5
10^-6
10^-7
10^-8
10^-9
METERS² PER CYCLE PER METER
Helicopter
Ground-level
STA A_X
10^-3
10^-2
10^-1
10^0
10^1
10^2
10^3
CYCLES PER METER

Figure 30e

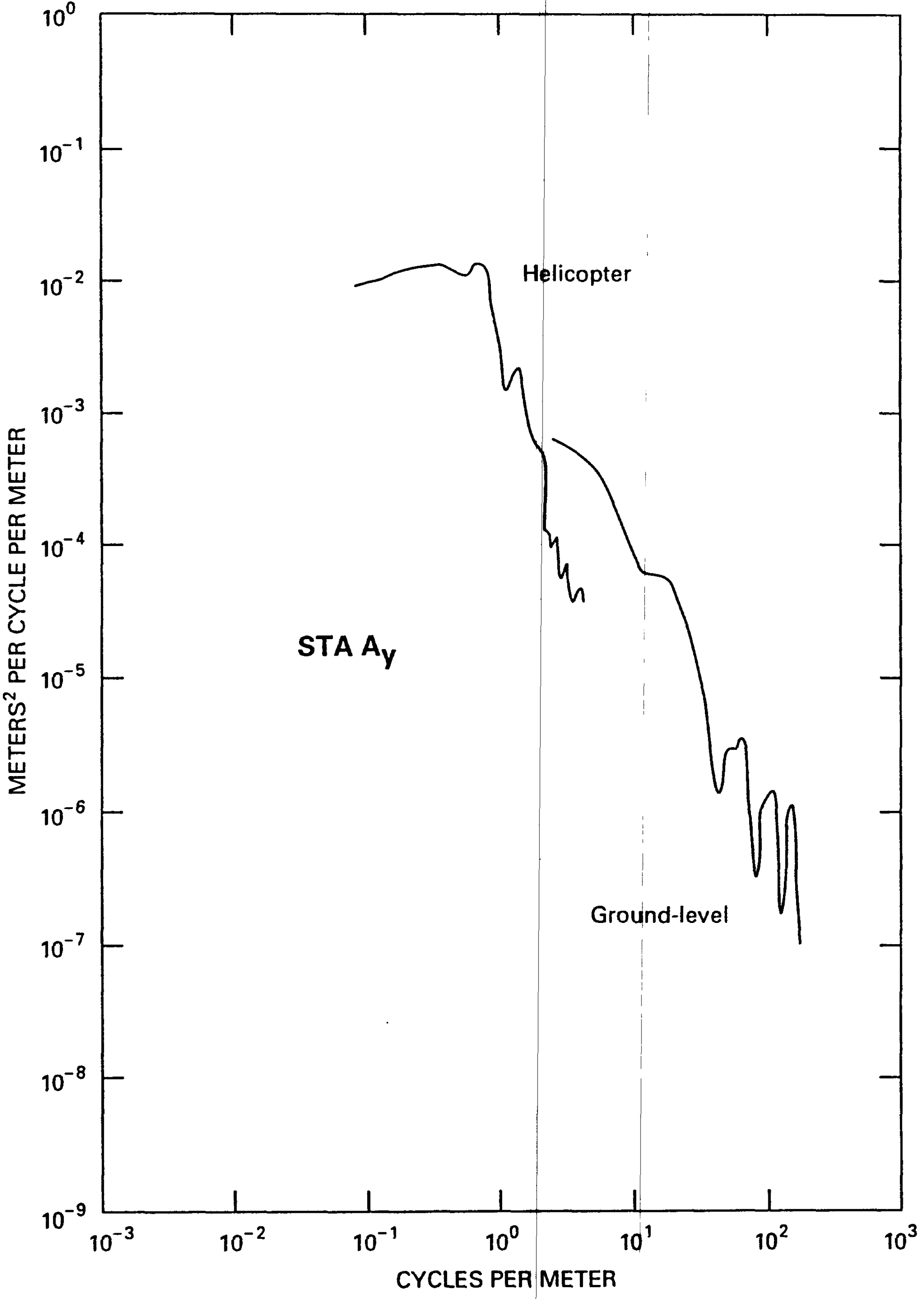

10^0
10^-1
10^-2
10^-3
10^-4
10^-5
10^-6
10^-7
10^-8
10^-9
METERS² PER CYCLE PER METER
Helicopter
Ground-level
STA A_y
10^-3
10^-2
10^-1
10^0
10^1
10^2
10^3
CYCLES PER METER

Figure 30f

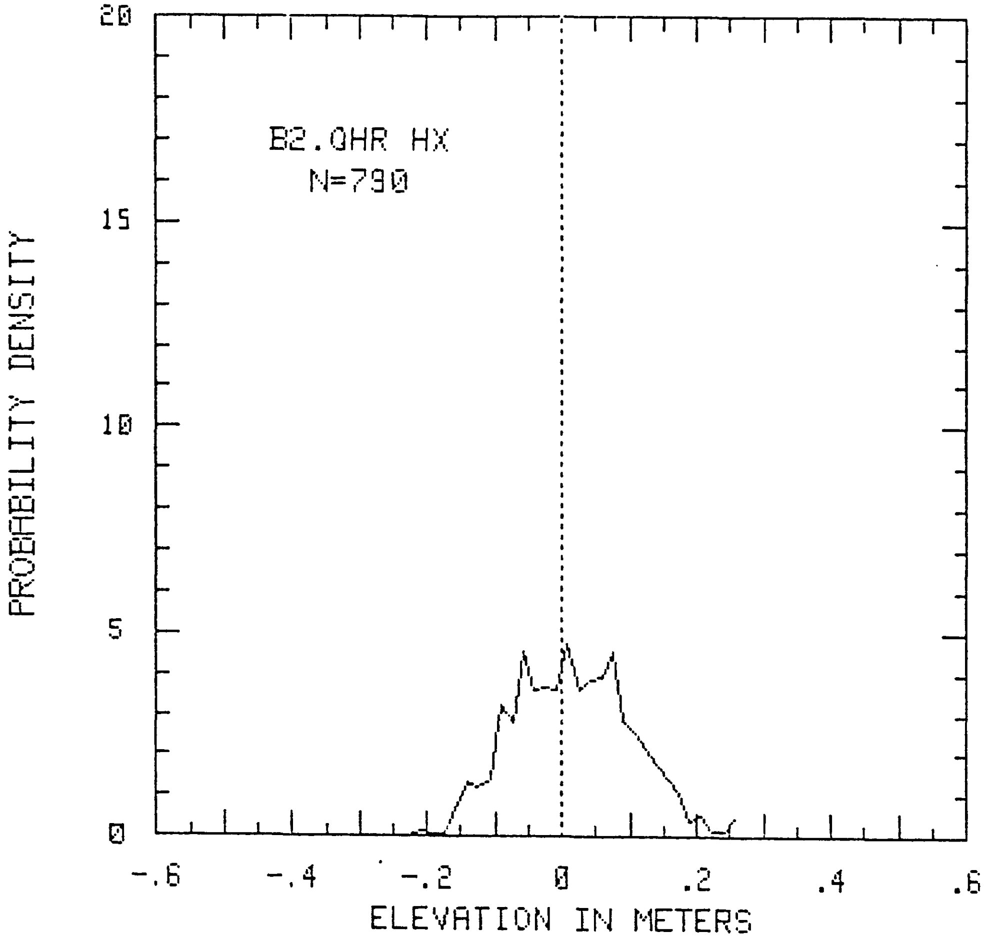
B2.QHR HX
N=790
PROBABILITY DENSITY
20
15
10
5
0
-.6
-.4
-.2
0
.2
.4
.6
ELEVATION IN METERS

Figure 31a

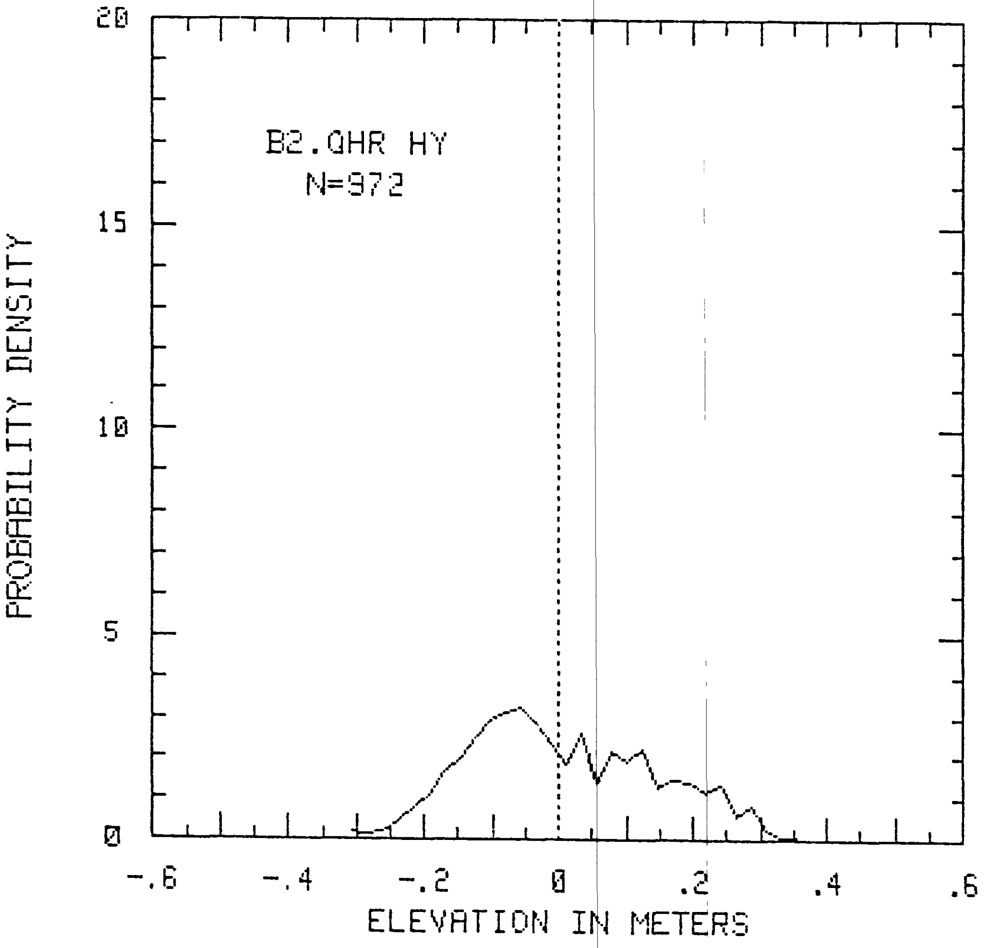
B2.QHR HY
N=972
PROBABILITY DENSITY
ELEVATION IN METERS
20
15
10
5
0
-.6
-.4
-.2
0
.2
.4
.6

Figure 31b

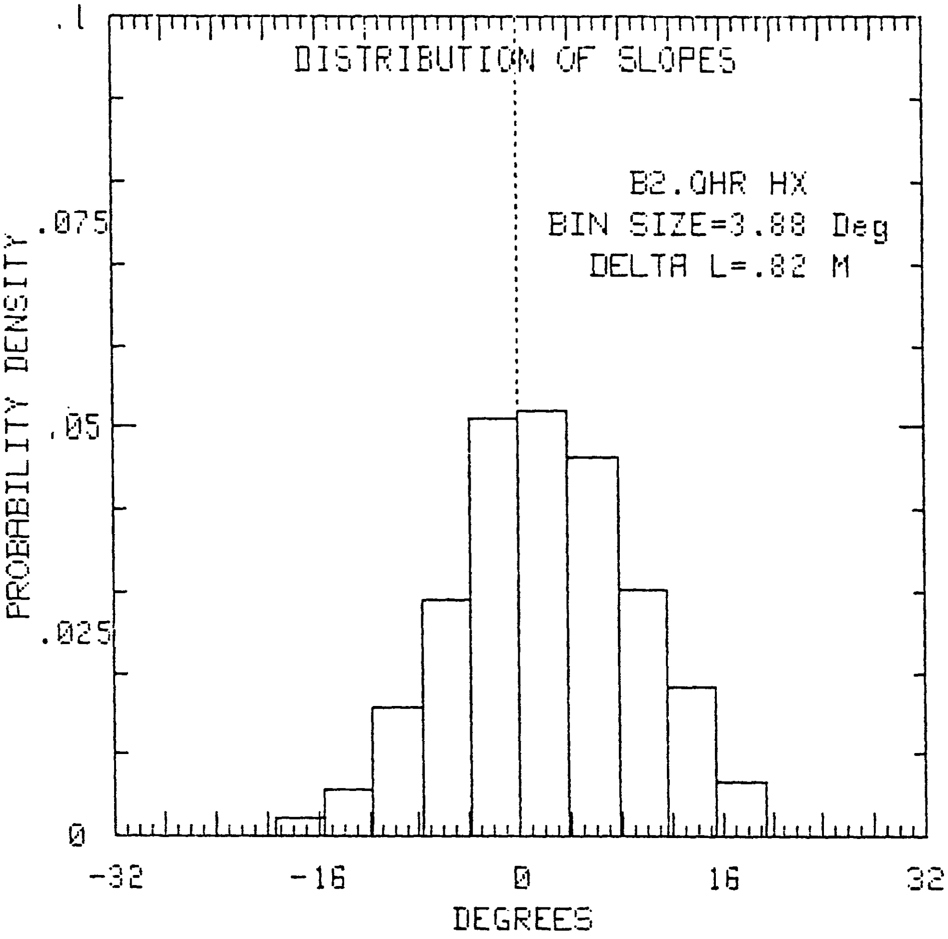
DISTRIBUTION OF SLOPES
B2.0HR HX
BIN SIZE=3.88 Deg
DELTA L=.82 M
PROBABILITY DENSITY
.1
.075
.05
.025
0
-32
-16
0
16
32
DEGREES

Figure 31c

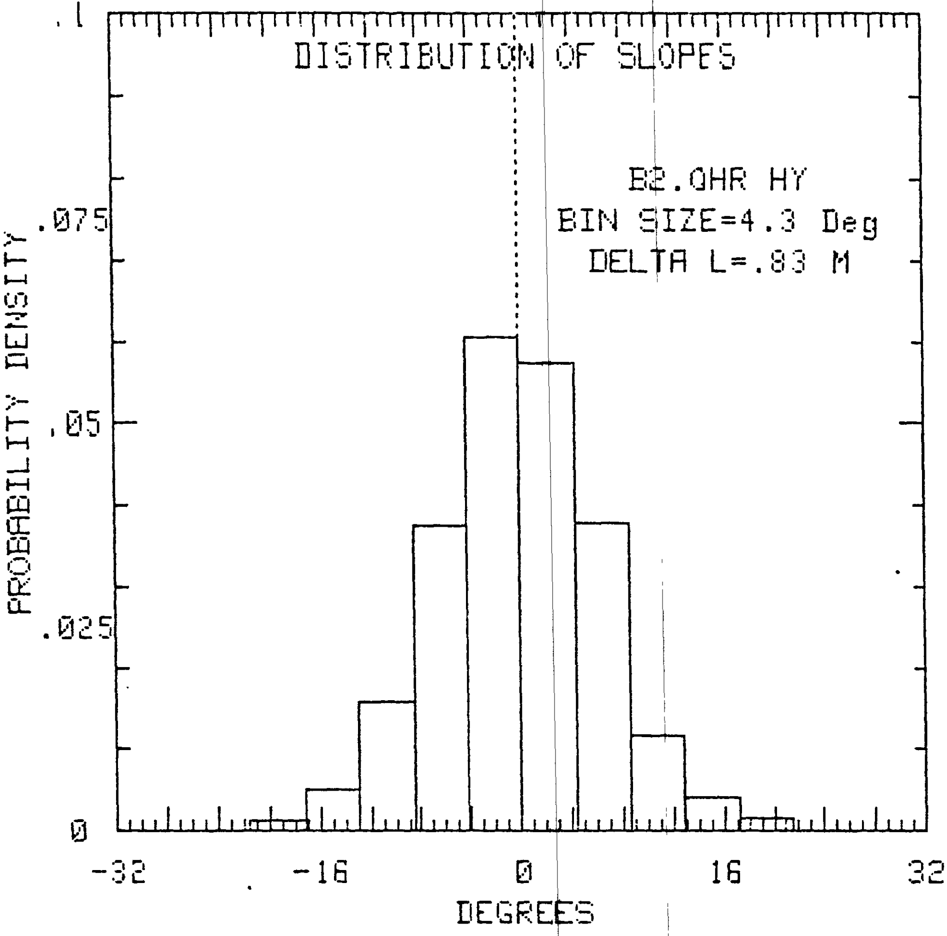
DISTRIBUTION OF SLOPES
B2.0HR HY
BIN SIZE=4.3 Deg
DELTA L=.83 M
PROBABILITY DENSITY
.1
.075
.05
.025
0
-32
-16
0
16
32
DEGREES

Figure 31d

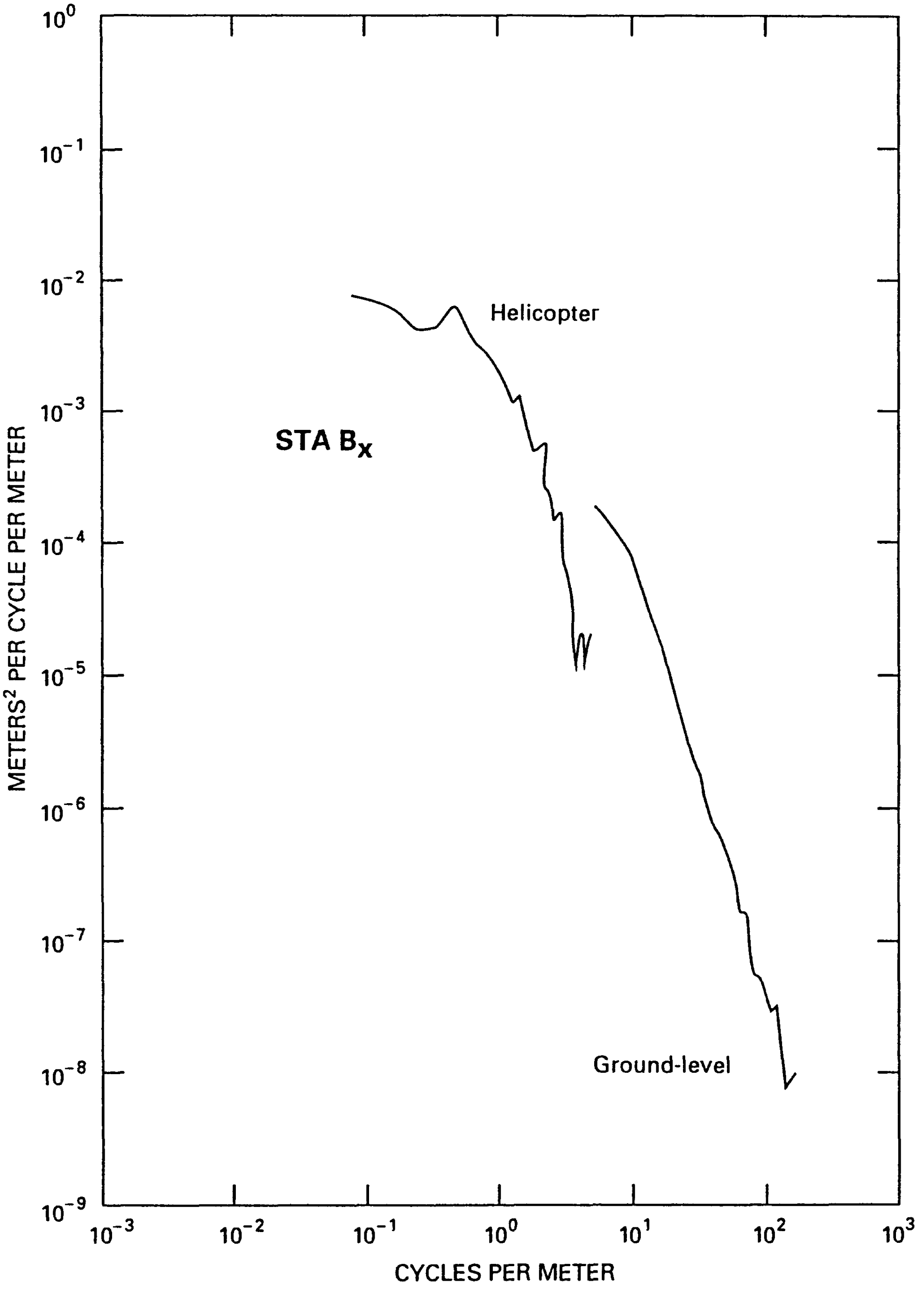

STA $B_X$
Helicopter
Ground-level
METERS$^2$ PER CYCLE PER METER
CYCLES PER METER
$10^0$
$10^{-1}$
$10^{-2}$
$10^{-3}$
$10^{-4}$
$10^{-5}$
$10^{-6}$
$10^{-7}$
$10^{-8}$
$10^{-9}$
$10^{-3}$
$10^{-2}$
$10^{-1}$
$10^0$
$10^1$
$10^2$
$10^3$

Figure 31e

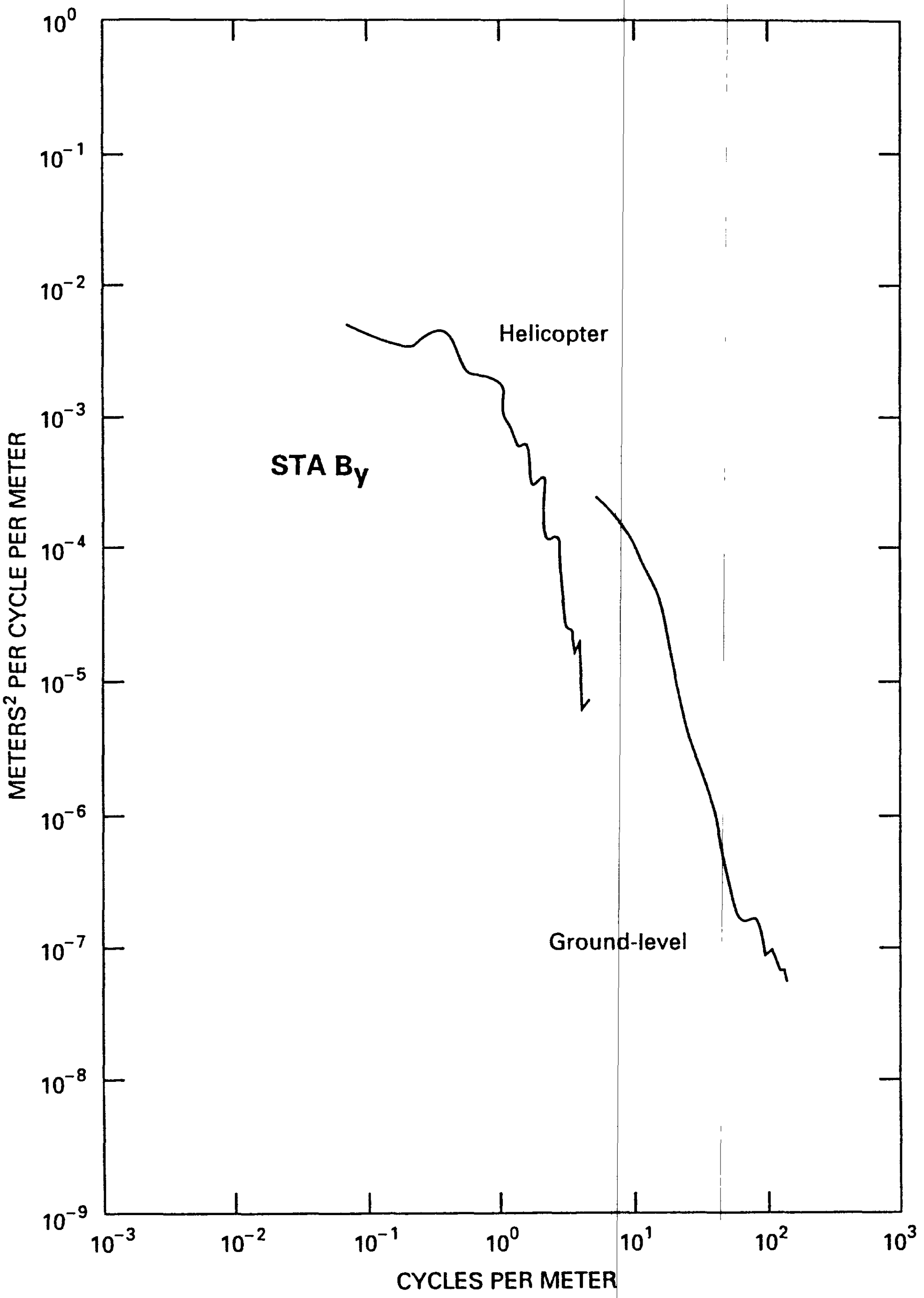
STA $B_y$
Helicopter
Ground-level
METERS² PER CYCLE PER METER
CYCLES PER METER
$10^0$
$10^{-1}$
$10^{-2}$
$10^{-3}$
$10^{-4}$
$10^{-5}$
$10^{-6}$
$10^{-7}$
$10^{-8}$
$10^{-9}$
$10^{-3}$
$10^{-2}$
$10^{-1}$
$10^0$
$10^1$
$10^2$
$10^3$

Figure 31f

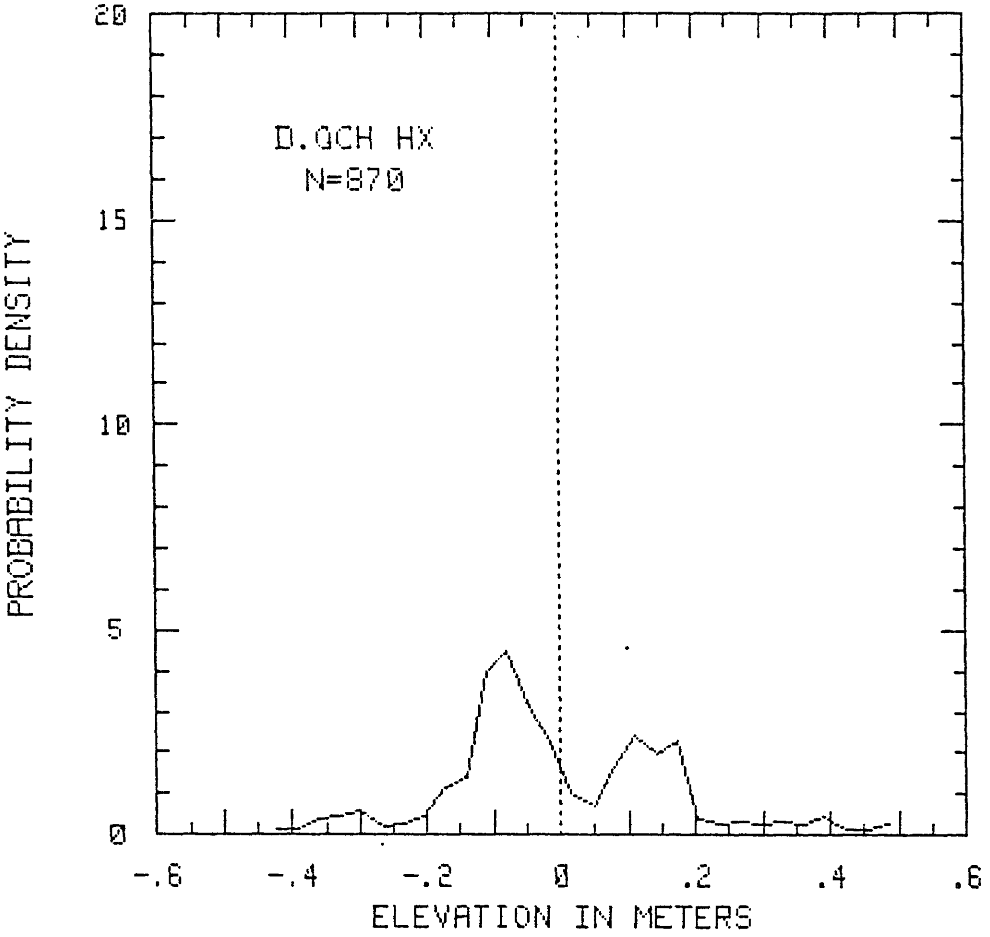
D.QCH HX
N=870
PROBABILITY DENSITY
20
15
10
5
0
-.6
-.4
-.2
0
.2
.4
.6
ELEVATION IN METERS

Figure 32a

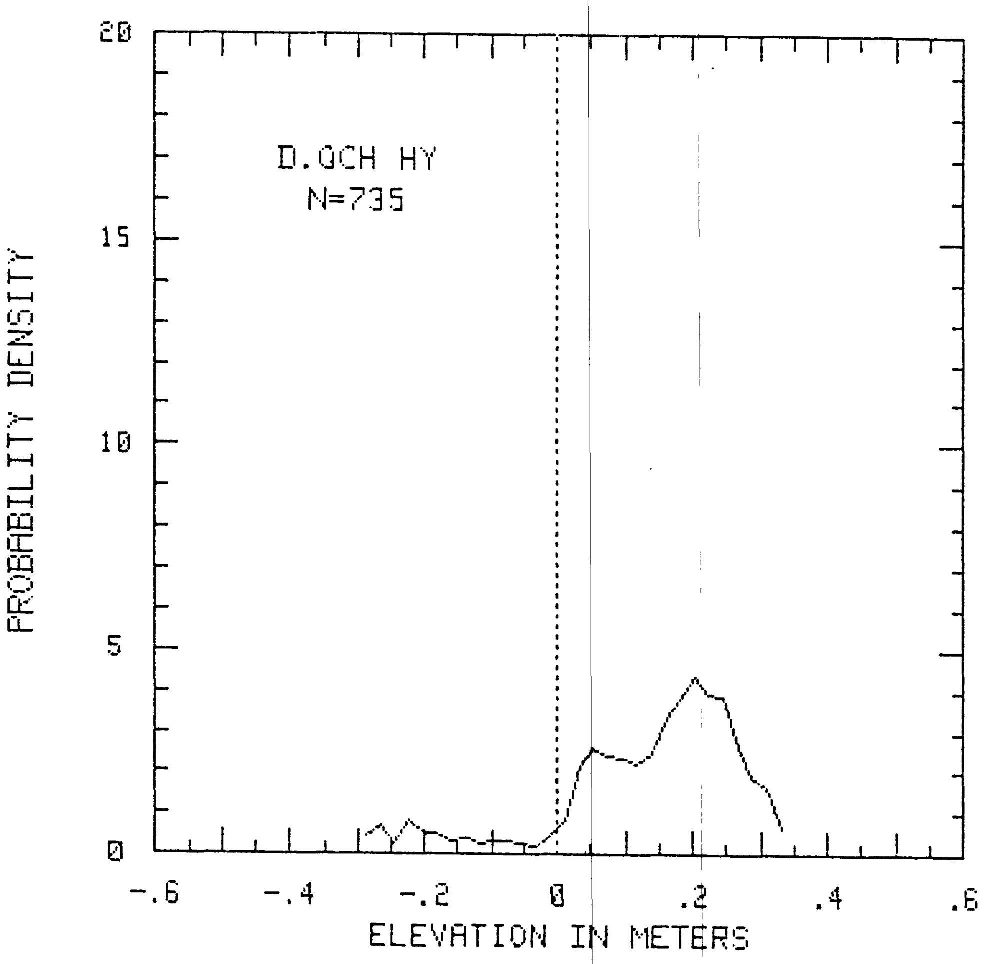
D.QCH HY
N=735
PROBABILITY DENSITY
ELEVATION IN METERS
0
5
10
15
20
-.6
-.4
-.2
0
.2
.4
.6

Figure 32b

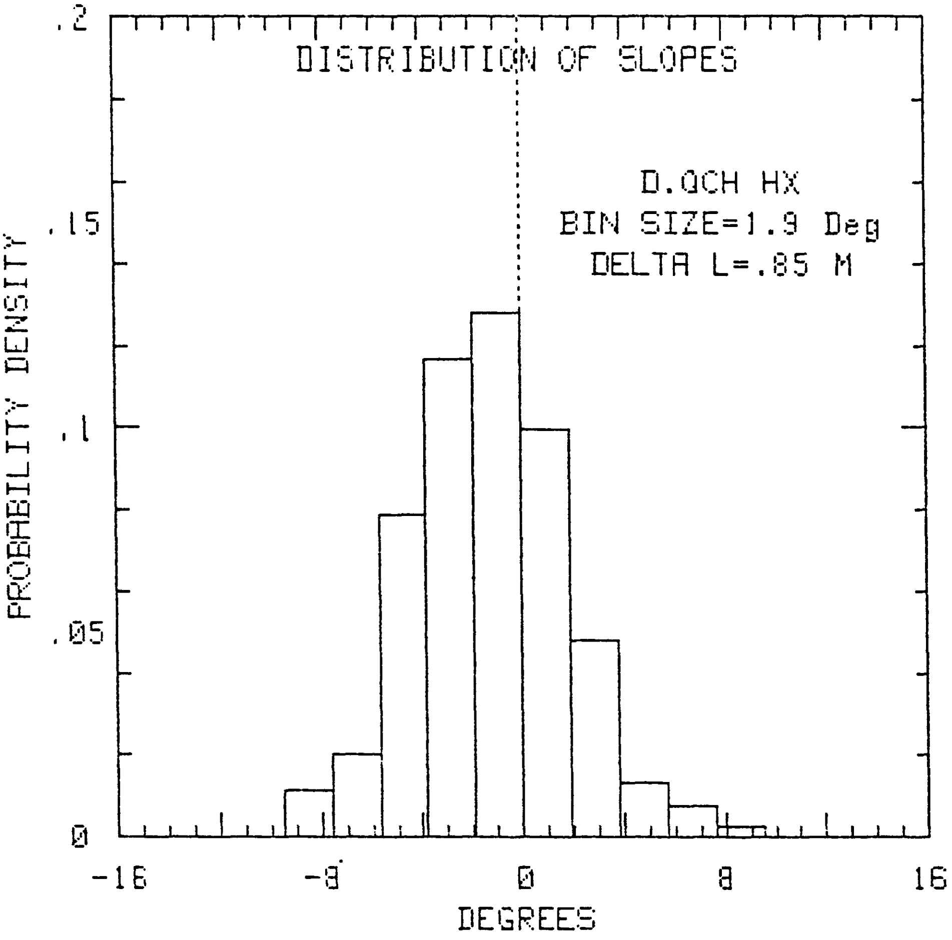
DISTRIBUTION OF SLOPES
D.QCH HX
BIN SIZE=1.9 Deg
DELTA L=.85 M
PROBABILITY DENSITY
.2
.15
.1
.05
0
-16
-8
0
8
16
DEGREES

Figure 32c

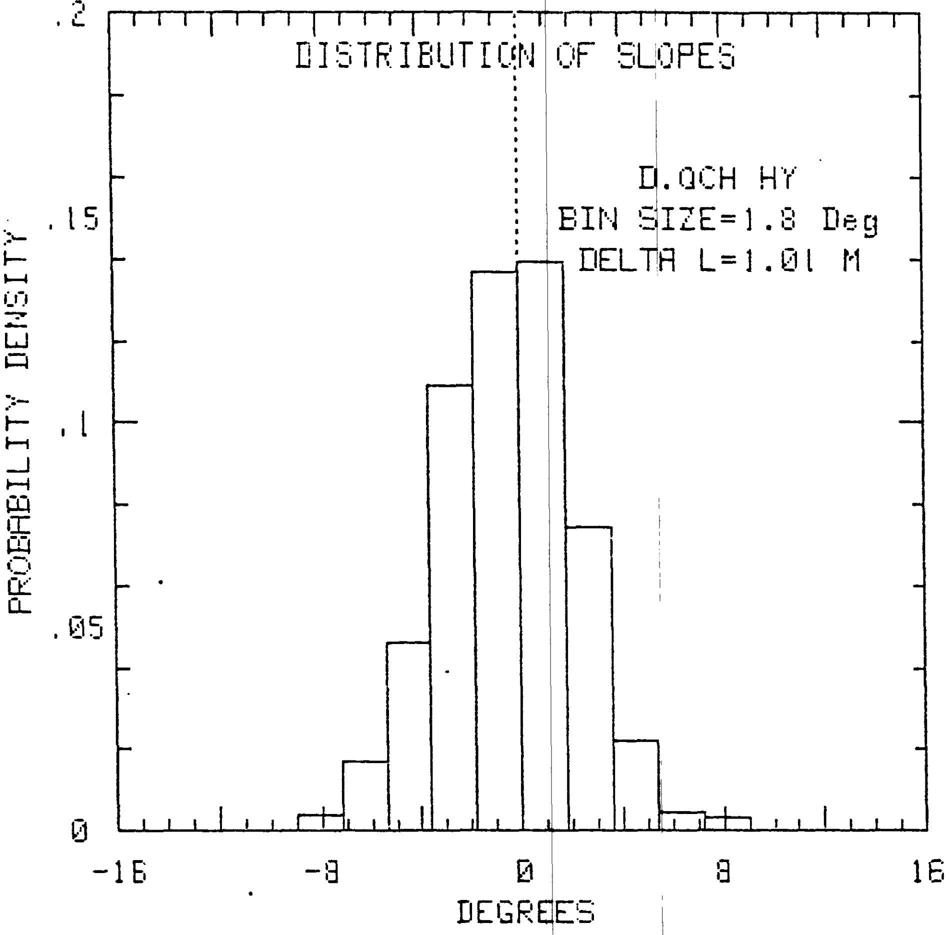
DISTRIBUTION OF SLOPES
D.QCH HY
BIN SIZE=1.8 Deg
DELTA L=1.01 M
PROBABILITY DENSITY
.2
.15
.1
.05
0
-16
-8
0
8
16
DEGREES

Figure 32d

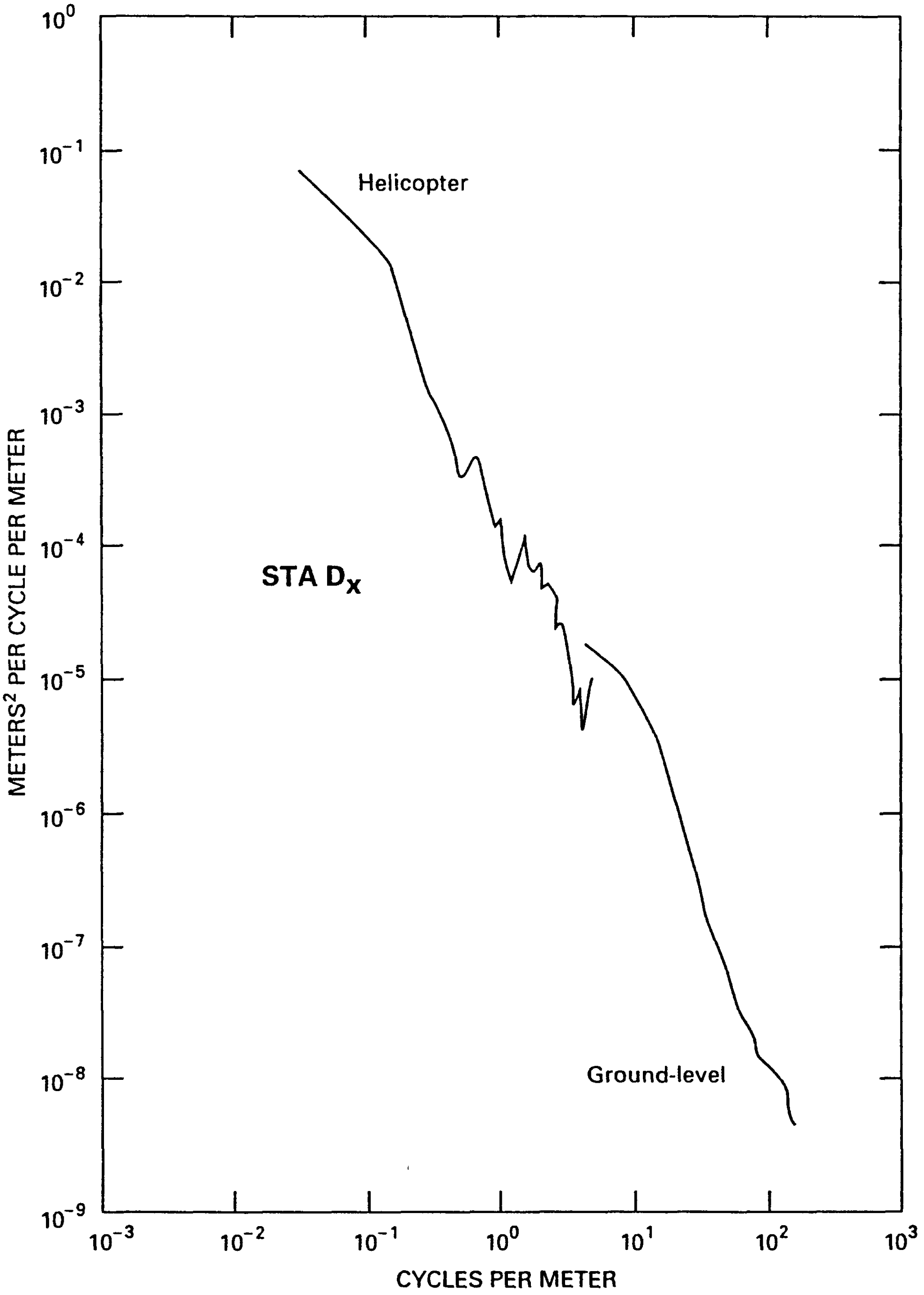

Helicopter
Ground-level
STA $D_x$
METERS$^2$ PER CYCLE PER METER
CYCLES PER METER
$10^0$
$10^{-1}$
$10^{-2}$
$10^{-3}$
$10^{-4}$
$10^{-5}$
$10^{-6}$
$10^{-7}$
$10^{-8}$
$10^{-9}$
$10^{-3}$
$10^{-2}$
$10^{-1}$
$10^0$
$10^1$
$10^2$
$10^3$

Figure 32e

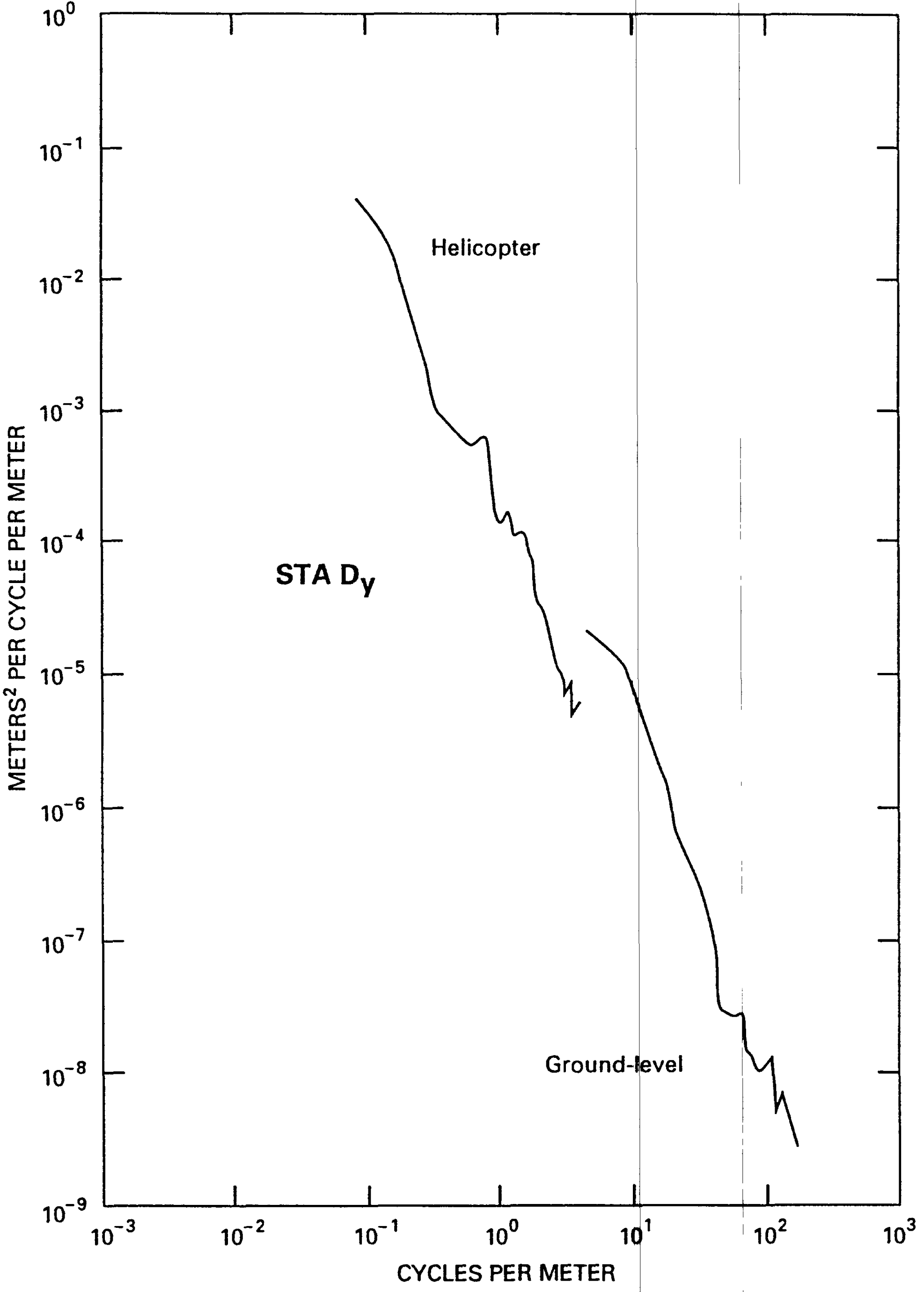
10^0
10^-1
10^-2
10^-3
10^-4
10^-5
10^-6
10^-7
10^-8
10^-9
METERS² PER CYCLE PER METER
Helicopter
STA D_y
Ground-level
10^-3
10^-2
10^-1
10^0
10^1
10^2
10^3
CYCLES PER METER

Figure 32f

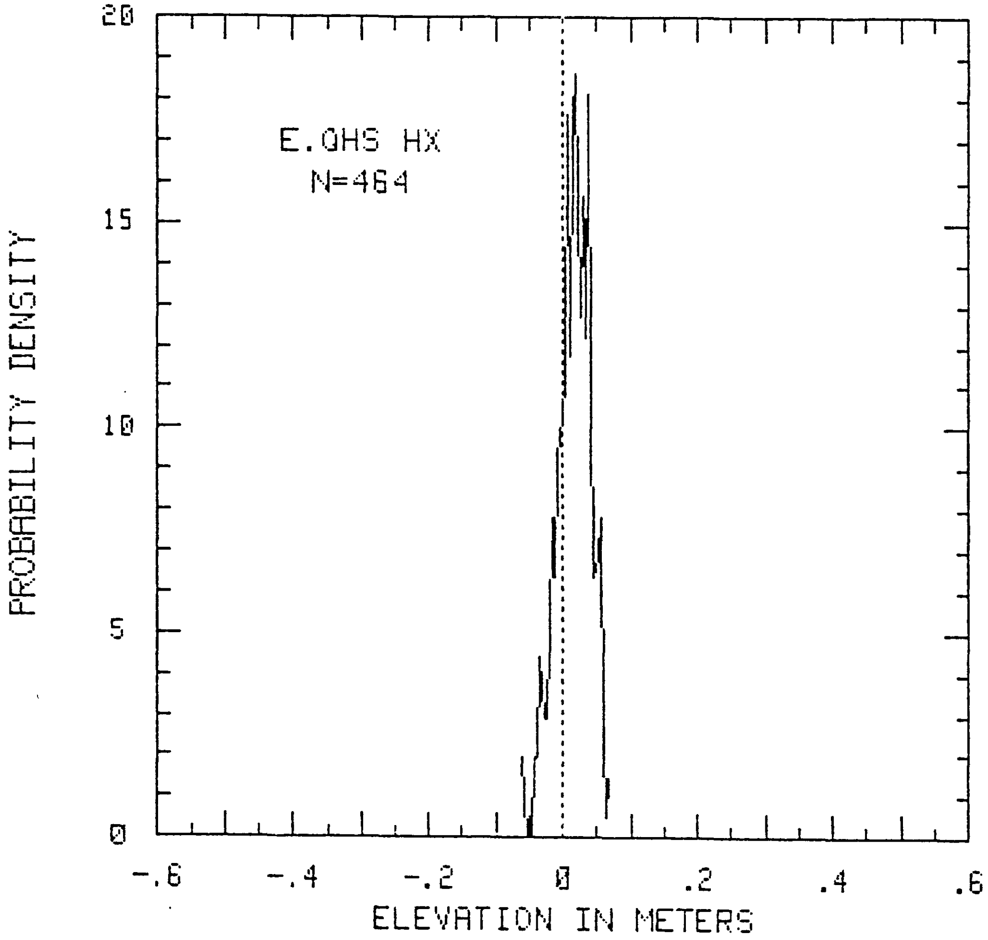
E.QHS HX
N=464
PROBABILITY DENSITY
0
5
10
15
20
-.6
-.4
-.2
0
.2
.4
.6
ELEVATION IN METERS

Figure 33a

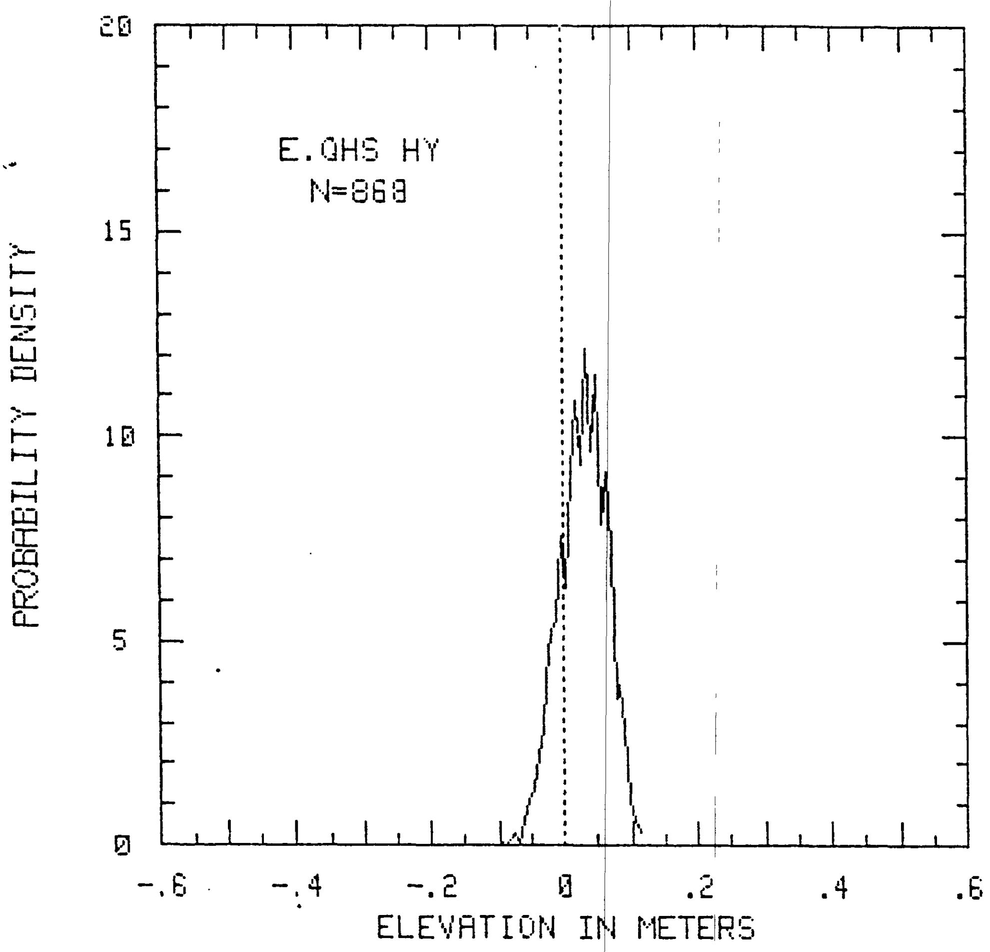
E.QHS HY
N=868
PROBABILITY DENSITY
ELEVATION IN METERS
0
5
10
15
20
-.6
-.4
-.2
0
.2
.4
.6

Figure 33b

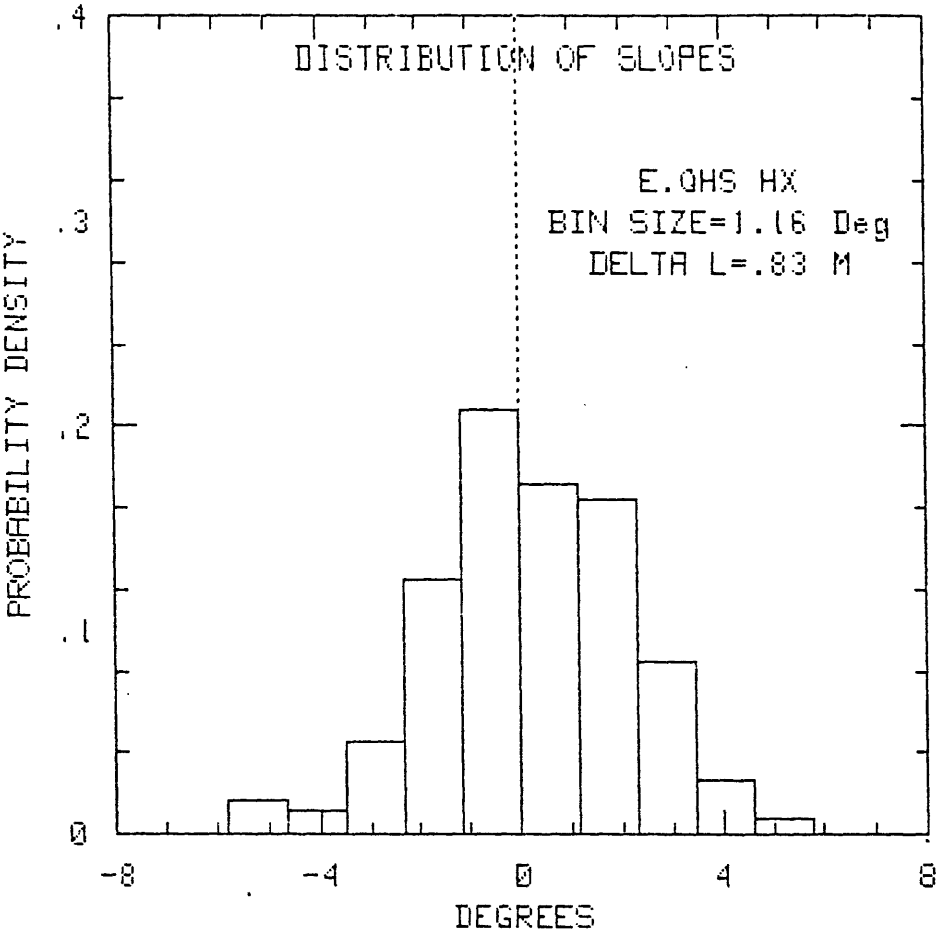
DISTRIBUTION OF SLOPES
E.QHS HX
BIN SIZE=1.16 Deg
DELTA L=.83 M
PROBABILITY DENSITY
.4
.3
.2
.1
0
-8
-4
0
4
8
DEGREES

Figure 33c

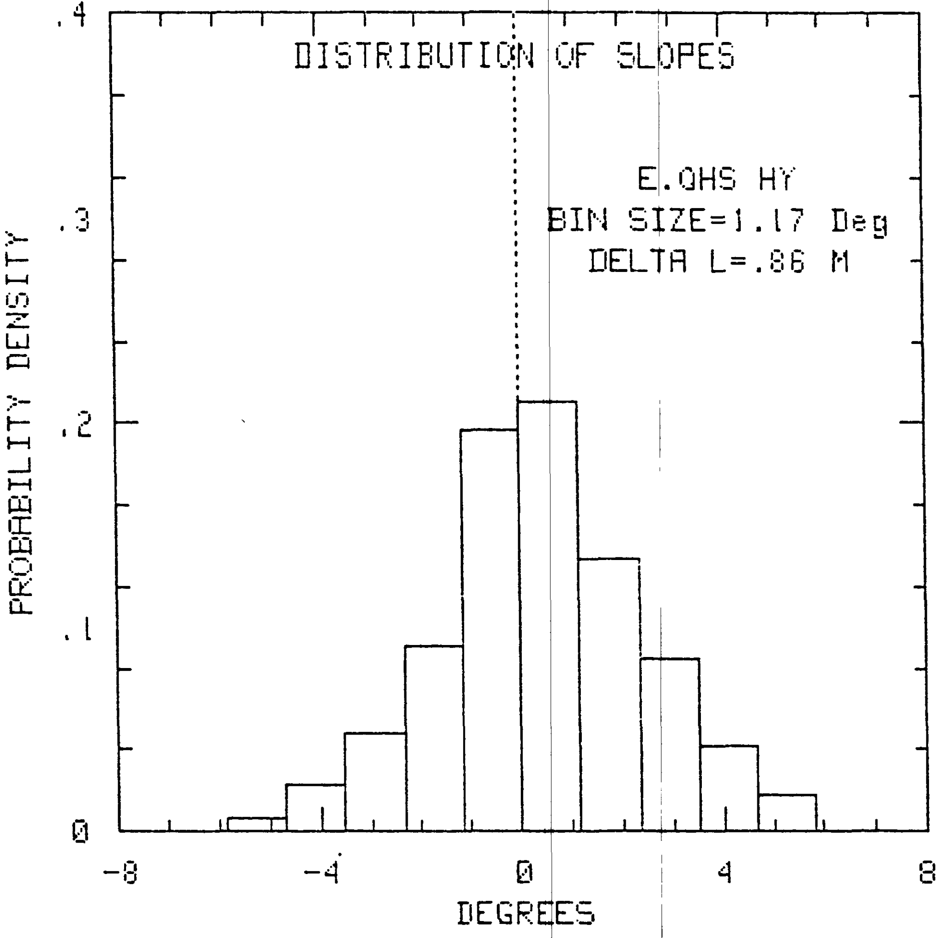
DISTRIBUTION OF SLOPES
E.QHS HY
BIN SIZE=1.17 Deg
DELTA L=.86 M
PROBABILITY DENSITY
.4
.3
.2
.1
0
-8
-4
0
4
8
DEGREES

Figure 33d

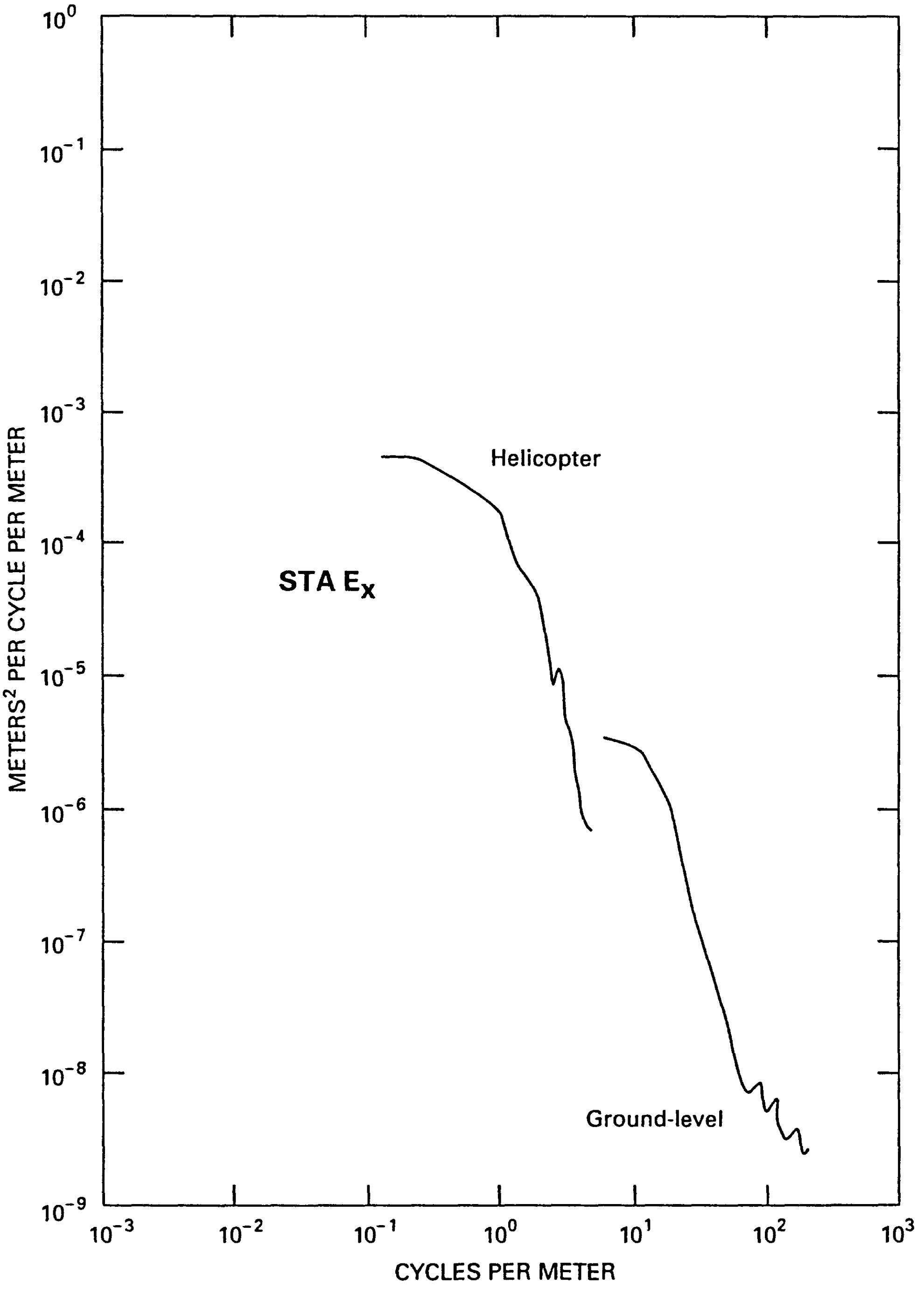

$10^{0}$
$10^{-1}$
$10^{-2}$
$10^{-3}$
$10^{-4}$
$10^{-5}$
$10^{-6}$
$10^{-7}$
$10^{-8}$
$10^{-9}$
METERS$^2$ PER CYCLE PER METER
Helicopter
STA $E_X$
Ground-level
$10^{-3}$
$10^{-2}$
$10^{-1}$
$10^{0}$
$10^{1}$
$10^{2}$
$10^{3}$
CYCLES PER METER

Figure 33e

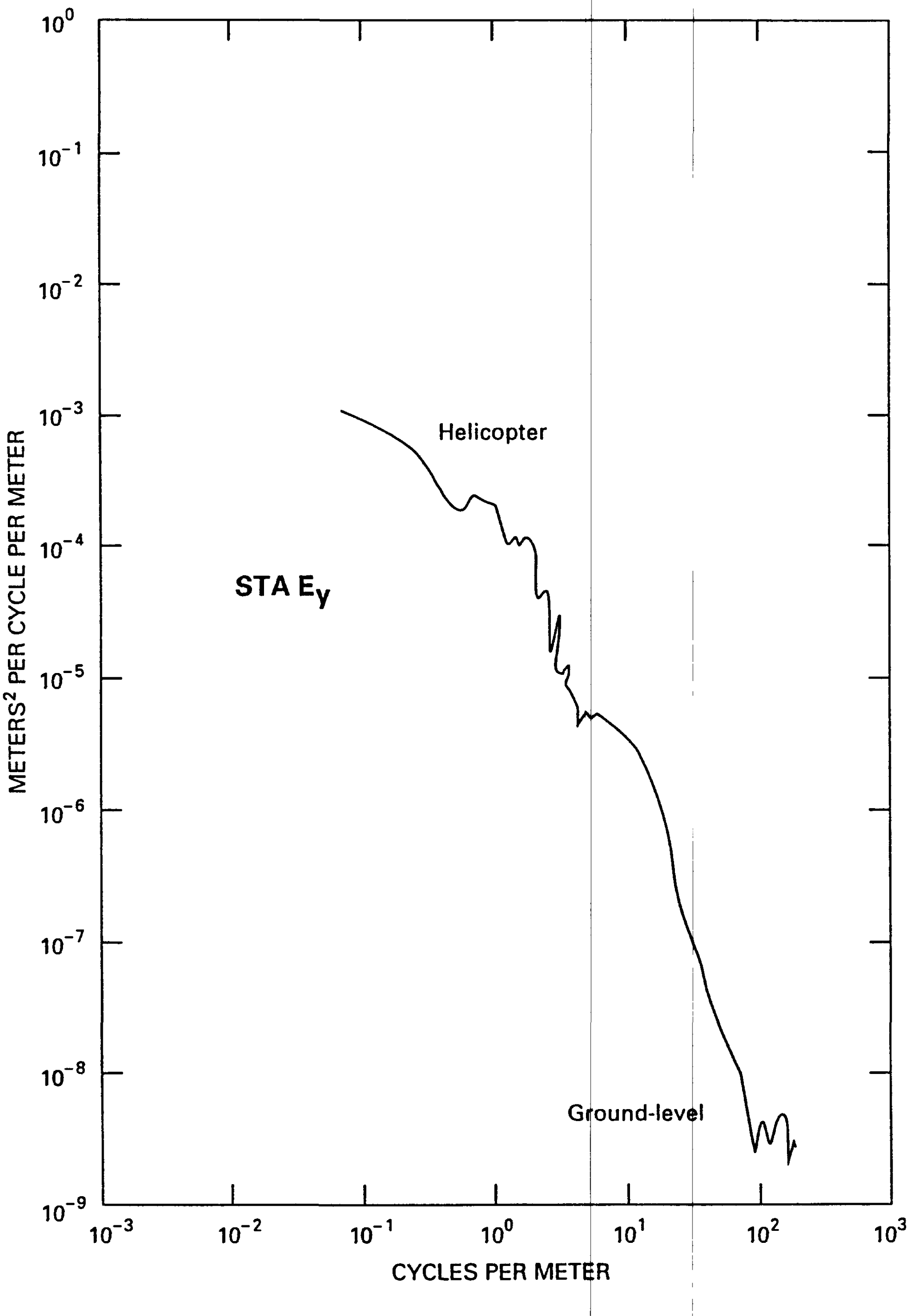

$10^0$
$10^{-1}$
$10^{-2}$
$10^{-3}$
$10^{-4}$
$10^{-5}$
$10^{-6}$
$10^{-7}$
$10^{-8}$
$10^{-9}$
METERS$^2$ PER CYCLE PER METER
Helicopter
STA $E_y$
Ground-level
$10^{-3}$
$10^{-2}$
$10^{-1}$
$10^0$
$10^1$
$10^2$
$10^3$
CYCLES PER METER

Figure 33f

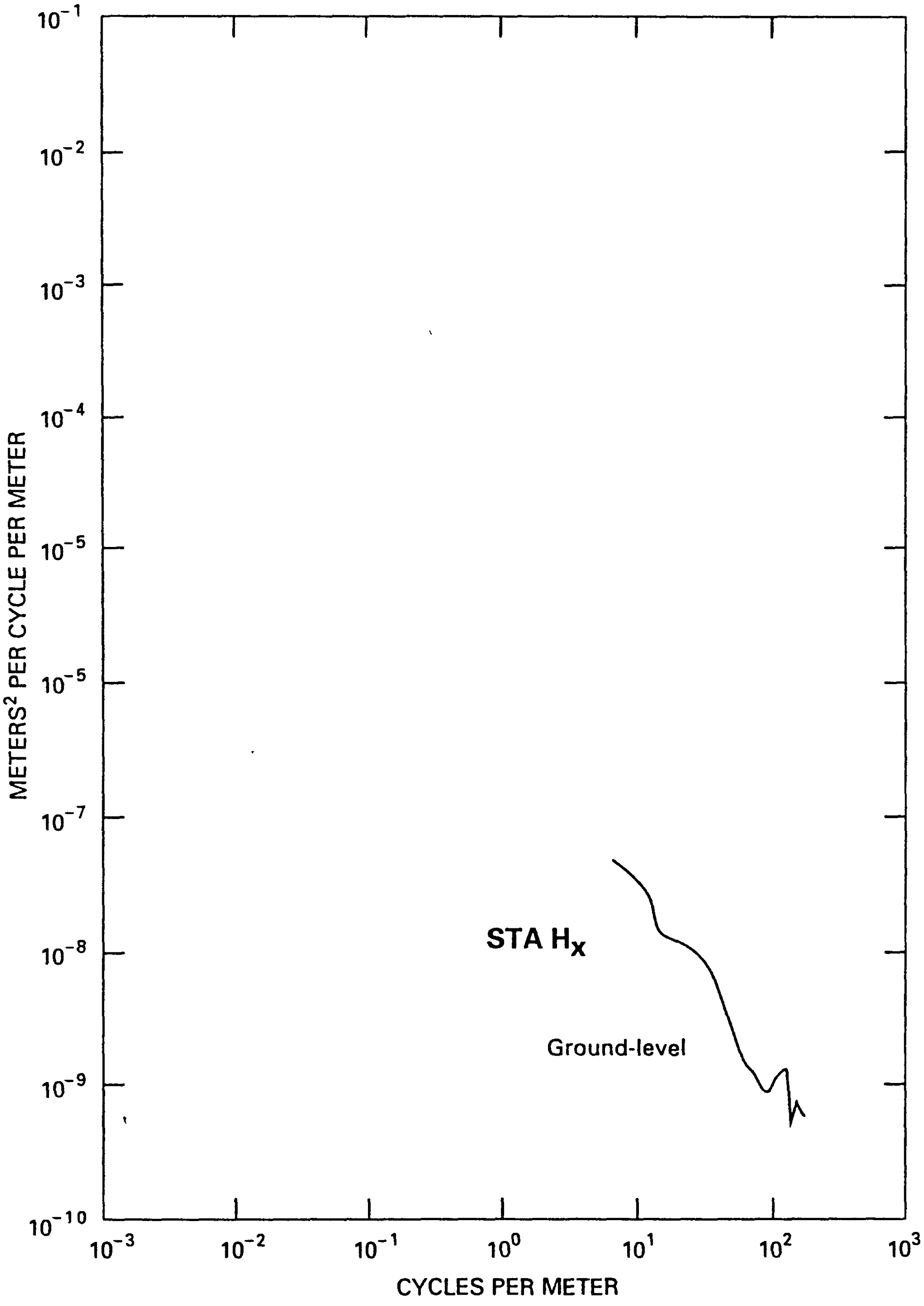
METERS$^2$ PER CYCLE PER METER
CYCLES PER METER
$10^{-1}$
$10^{-2}$
$10^{-3}$
$10^{-4}$
$10^{-5}$
$10^{-5}$
$10^{-7}$
$10^{-8}$
$10^{-9}$
$10^{-10}$
$10^{-3}$
$10^{-2}$
$10^{-1}$
$10^{0}$
$10^{1}$
$10^{2}$
$10^{3}$
STA $H_x$
Ground-level

Figure 34

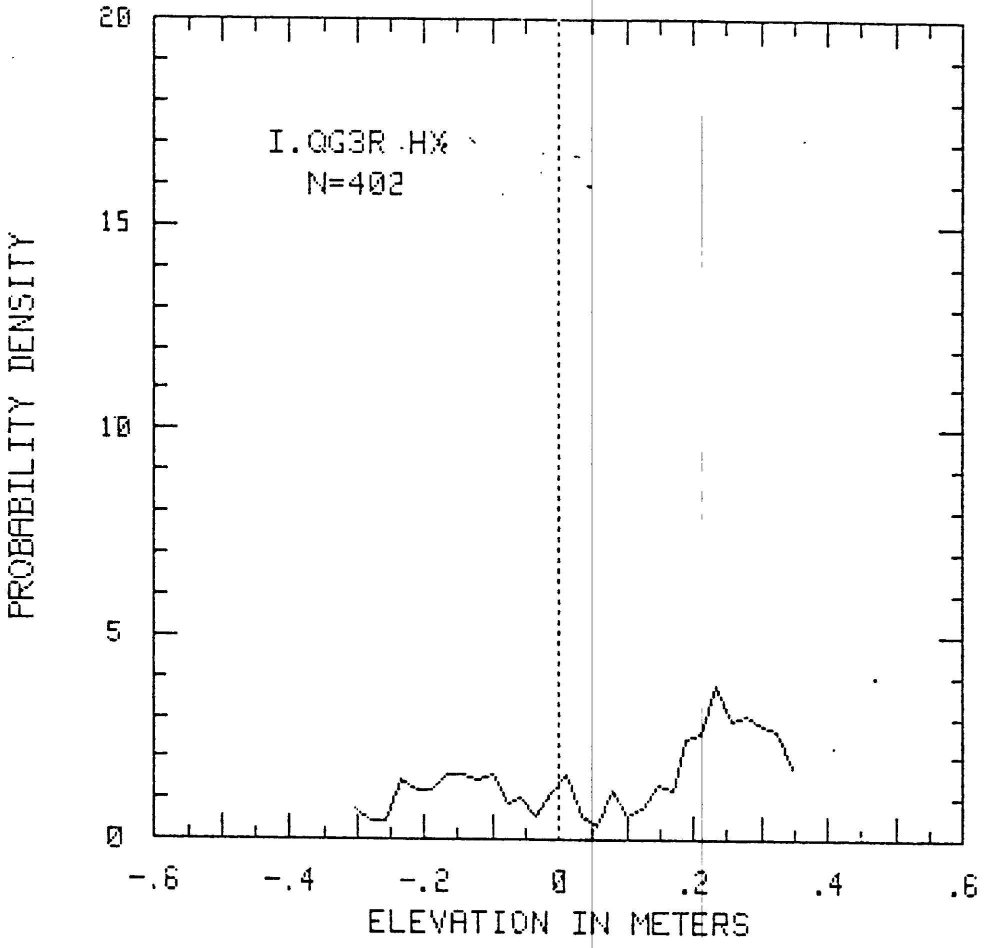
I.QG3R HX
N=402
PROBABILITY DENSITY
0
5
10
15
20
-.6
-.4
-.2
0
.2
.4
.6
ELEVATION IN METERS

Figure 35a

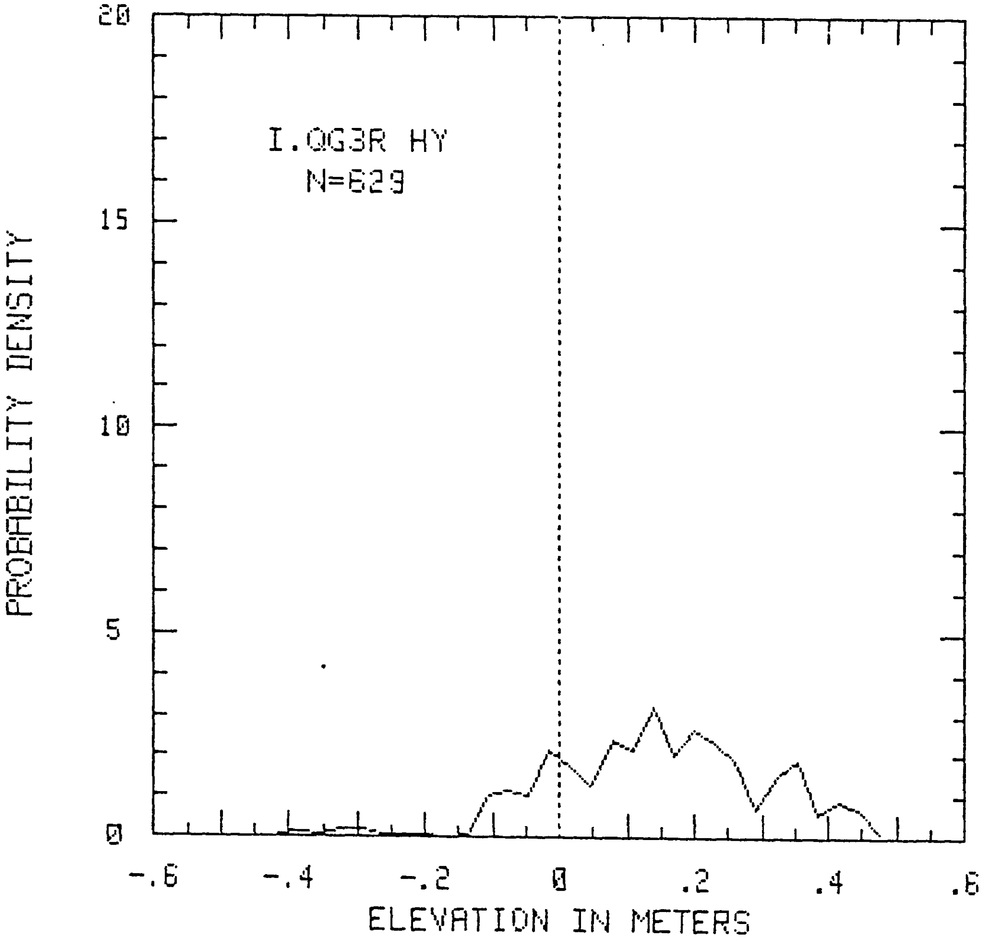
I.QG3R HY
N=629
PROBABILITY DENSITY
20
15
10
5
0
-.6
-.4
-.2
0
.2
.4
.6
ELEVATION IN METERS

Figure 35b

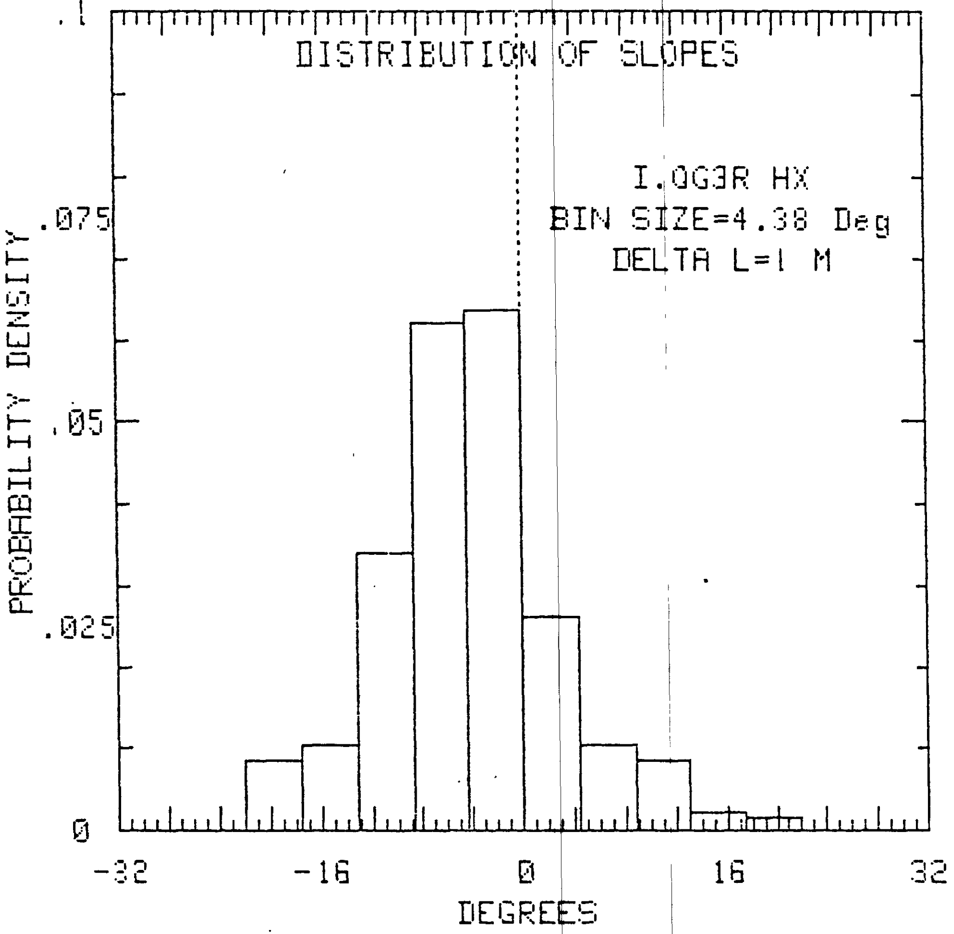
DISTRIBUTION OF SLOPES
I.0G3R HX
BIN SIZE=4.38 Deg
DELTA L=1 M
PROBABILITY DENSITY
.1
.075
.05
.025
0
-32
-16
0
16
32
DEGREES

Figure 35c

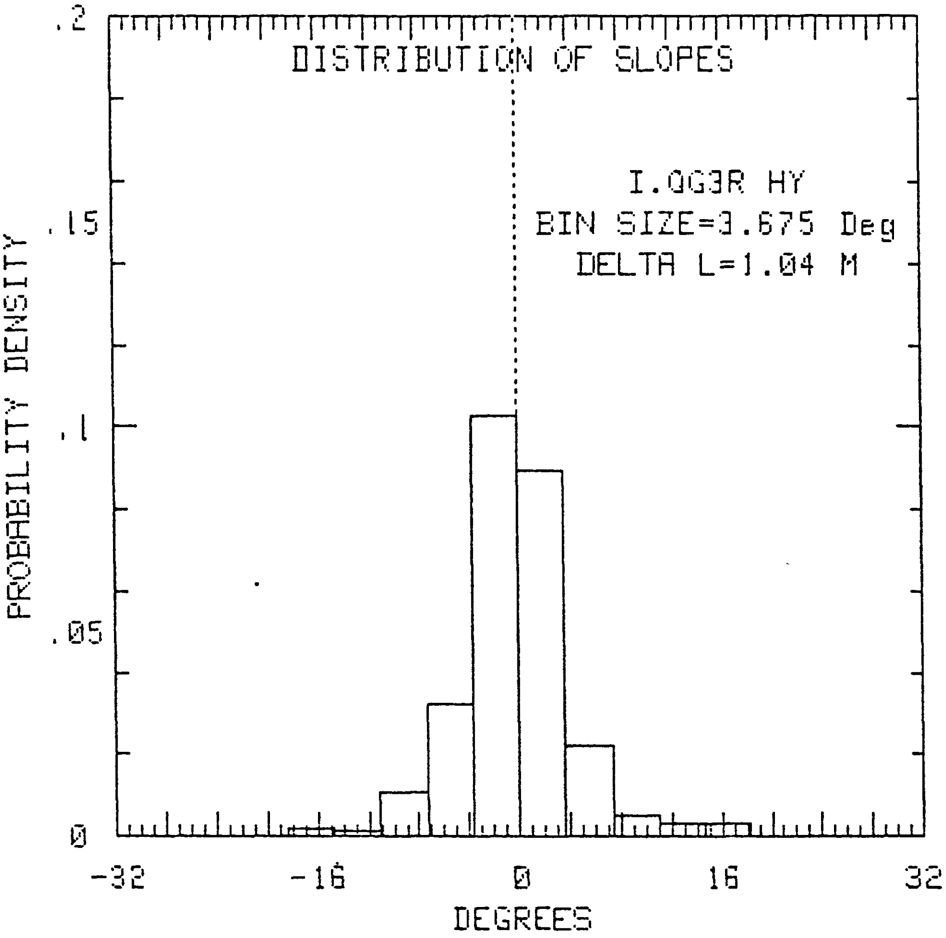
DISTRIBUTION OF SLOPES
I.QG3R HY
BIN SIZE=3.675 Deg
DELTA L=1.04 M
PROBABILITY DENSITY
.2
.15
.1
.05
0
-32
-16
0
16
32
DEGREES

Figure 35d

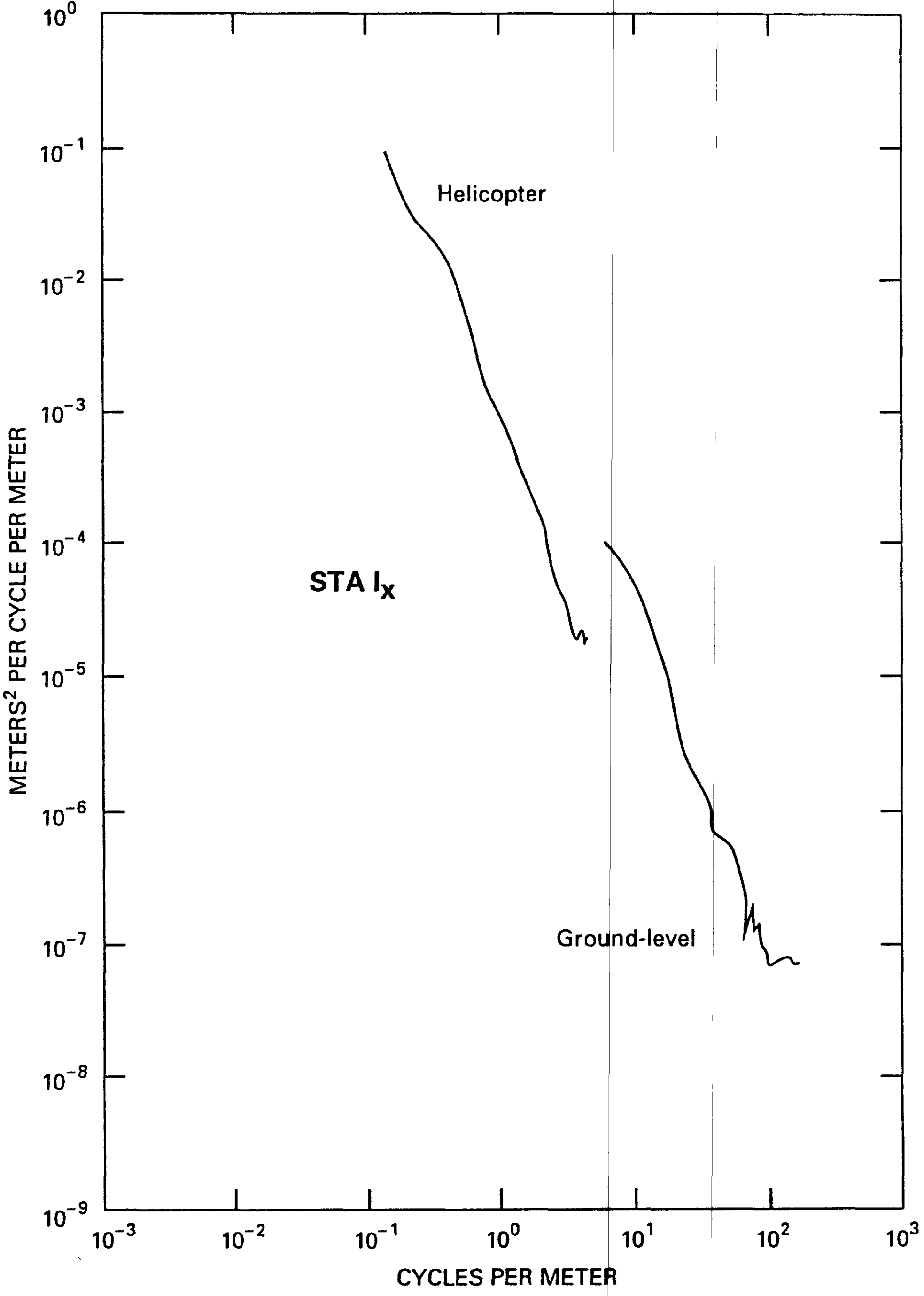
10⁰
10⁻¹
10⁻²
10⁻³
10⁻⁴
10⁻⁵
10⁻⁶
10⁻⁷
10⁻⁸
10⁻⁹
METERS² PER CYCLE PER METER
Helicopter
STA $I_X$
Ground-level
10⁻³
10⁻²
10⁻¹
10⁰
10¹
10²
10³
CYCLES PER METER

Figure 35e

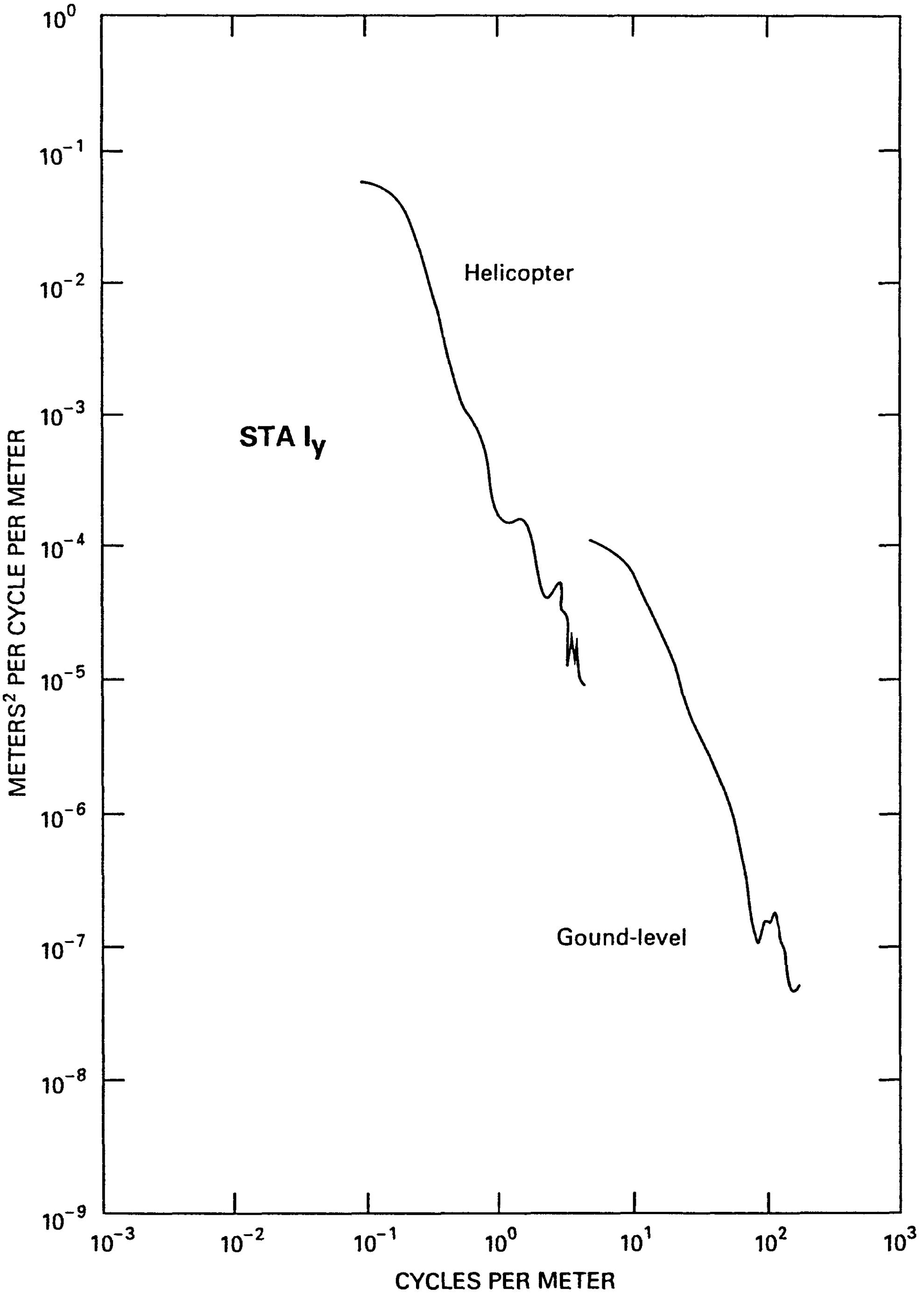
STA $I_y$
Helicopter
Gound-level
METERS$^2$ PER CYCLE PER METER
CYCLES PER METER
$10^0$
$10^{-1}$
$10^{-2}$
$10^{-3}$
$10^{-4}$
$10^{-5}$
$10^{-6}$
$10^{-7}$
$10^{-8}$
$10^{-9}$
$10^{-3}$
$10^{-2}$
$10^{-1}$
$10^0$
$10^1$
$10^2$
$10^3$

Figure 35f

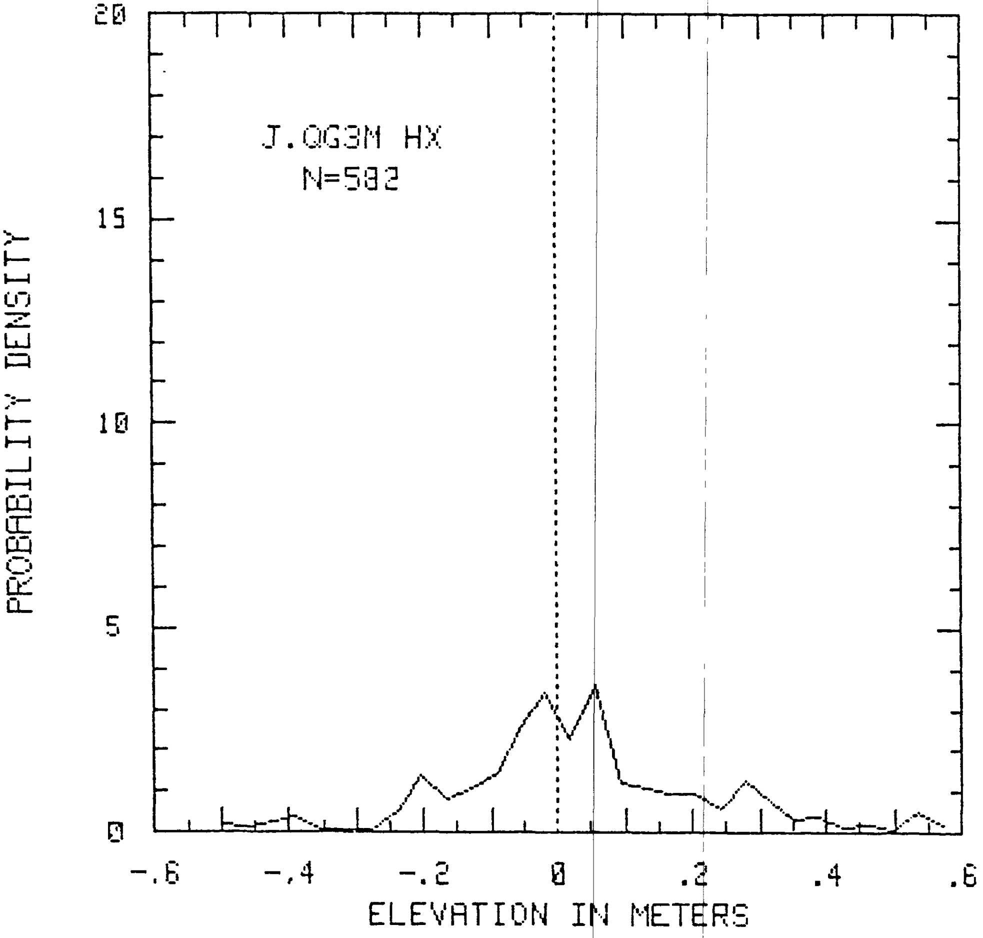
J.QG3M HX
N=582
PROBABILITY DENSITY
ELEVATION IN METERS
20
15
10
5
0
-.6
-.4
-.2
0
.2
.4
.6

Figure 36a

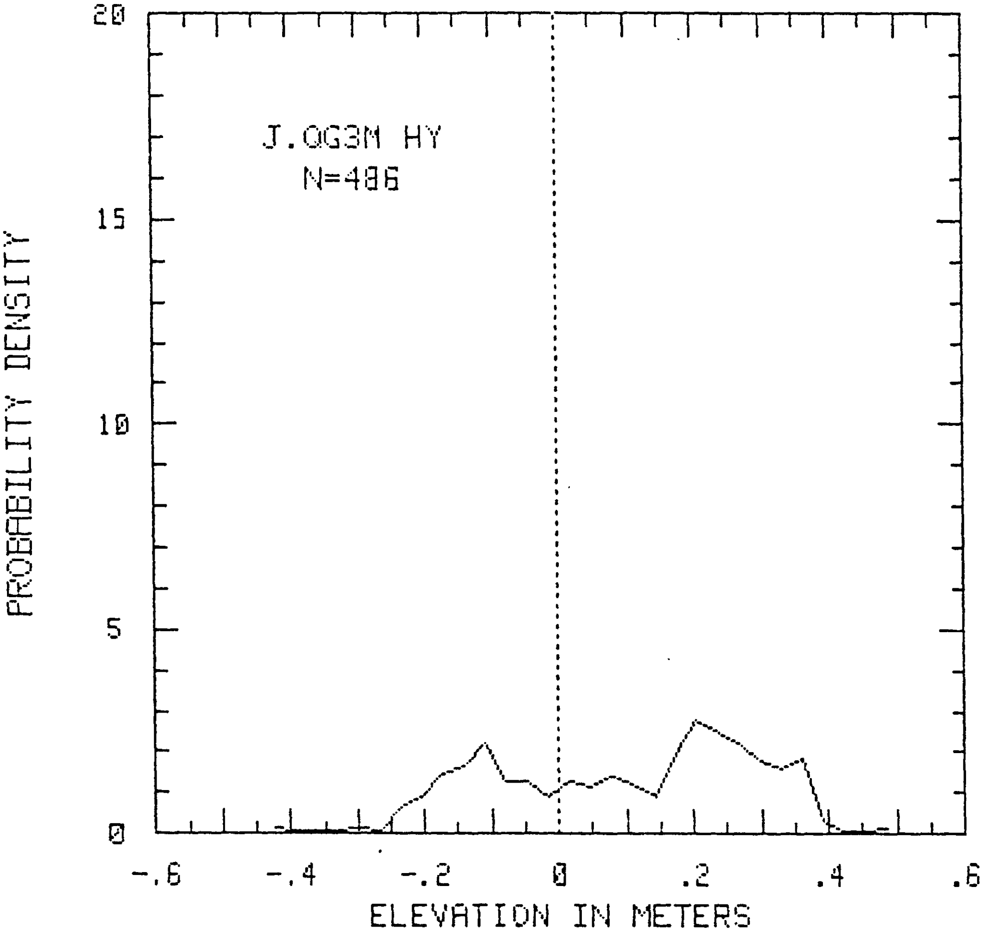
J.OG3M HY
N=486
PROBABILITY DENSITY
20
15
10
5
0
-.6
-.4
-.2
0
.2
.4
.6
ELEVATION IN METERS

Figure 36b

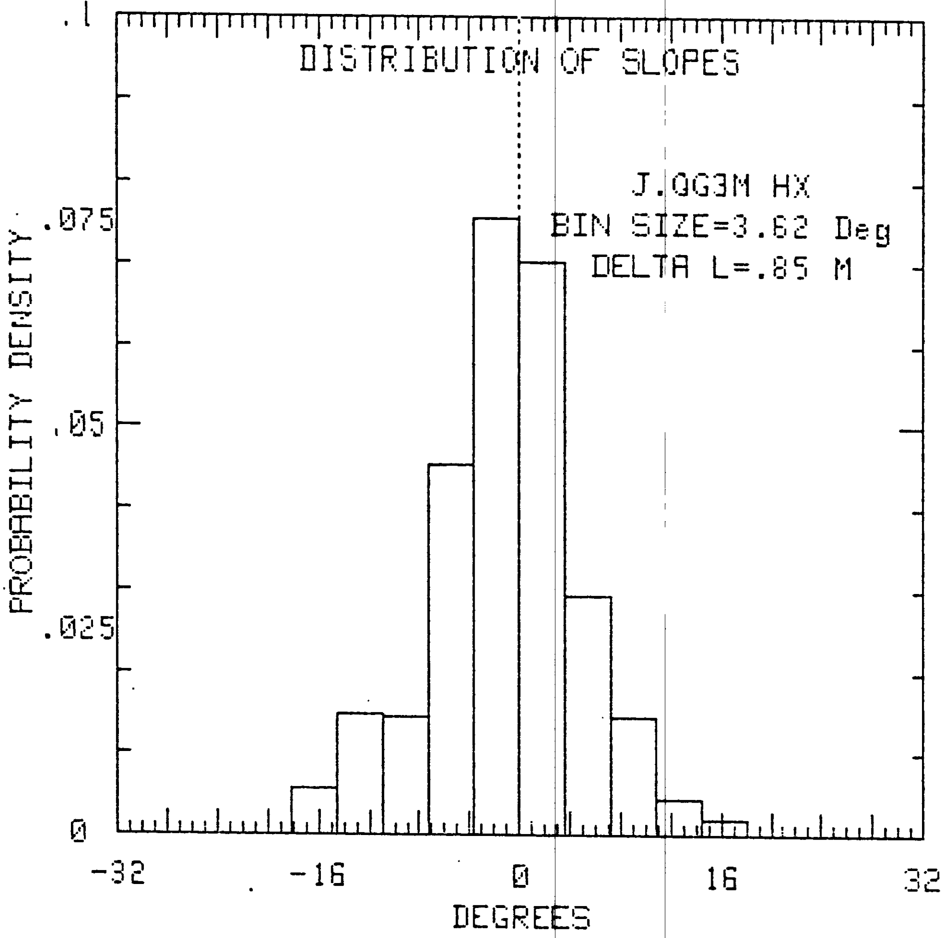
DISTRIBUTION OF SLOPES
J.QG3M HX
BIN SIZE=3.62 Deg
DELTA L=.85 M
PROBABILITY DENSITY
.1
.075
.05
.025
0
-32
-16
0
16
32
DEGREES

Figure 36c

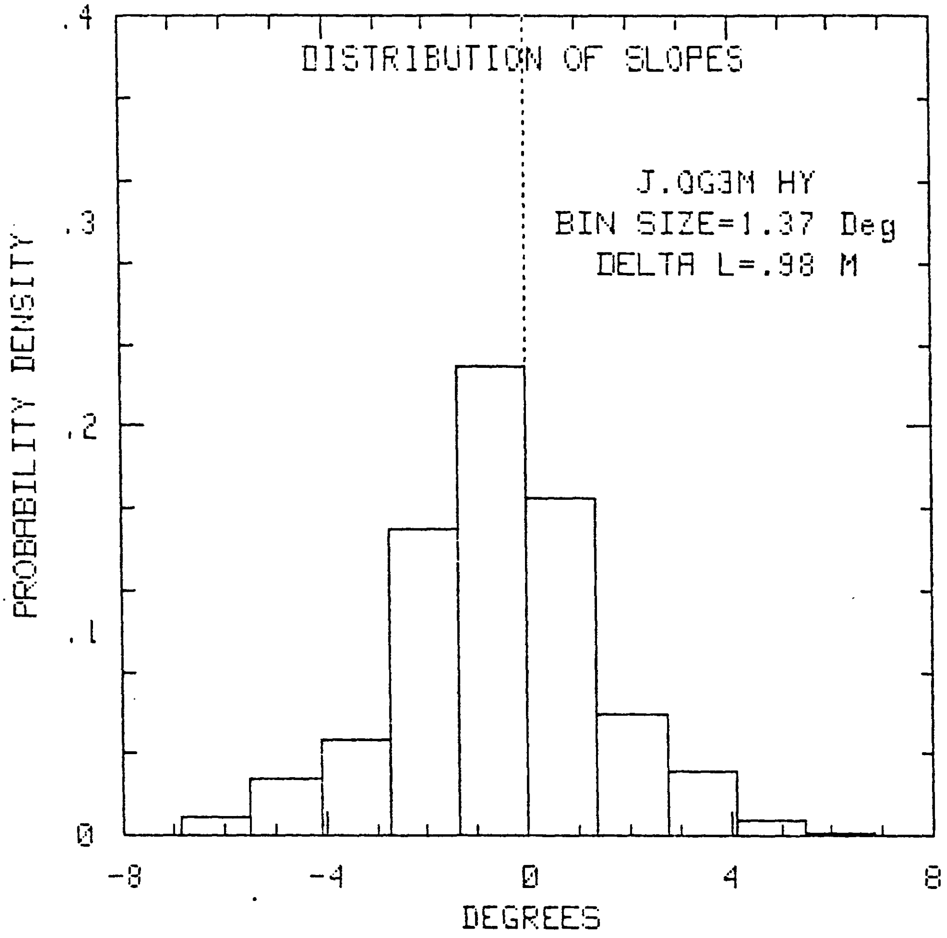
DISTRIBUTION OF SLOPES
J.OG3M HY
BIN SIZE=1.37 Deg
DELTA L=.98 M
PROBABILITY DENSITY
.4
.3
.2
.1
0
-8
-4
0
4
8
DEGREES

Figure 36d

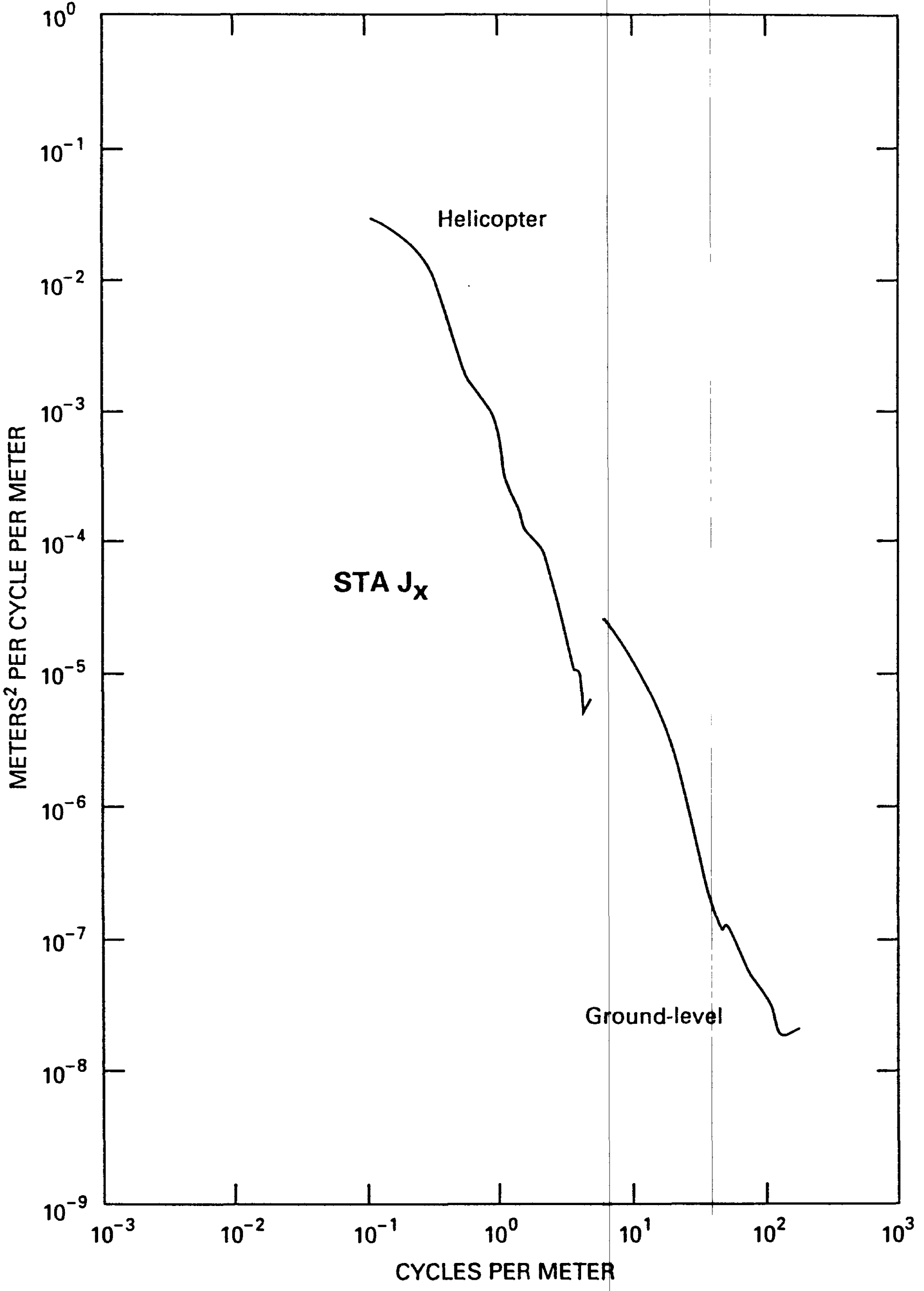

10^0
10^-1
10^-2
10^-3
10^-4
10^-5
10^-6
10^-7
10^-8
10^-9
METERS² PER CYCLE PER METER
Helicopter
STA J_X
Ground-level
10^-3
10^-2
10^-1
10^0
10^1
10^2
10^3
CYCLES PER METER

Figure 36e

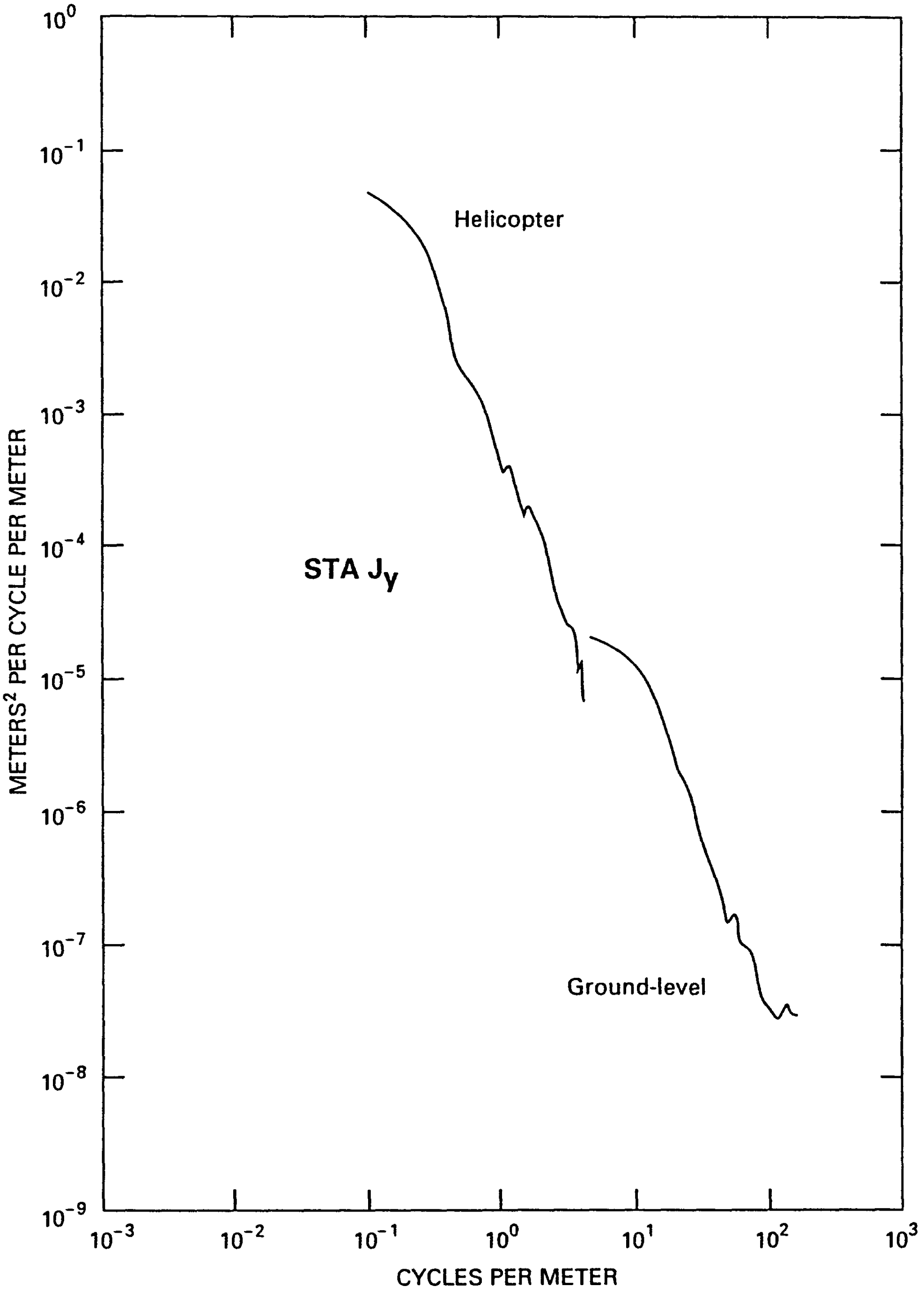
10^0
10^-1
10^-2
10^-3
10^-4
10^-5
10^-6
10^-7
10^-8
10^-9
METERS² PER CYCLE PER METER
Helicopter
STA Jy
Ground-level
10^-3
10^-2
10^-1
10^0
10^1
10^2
10^3
CYCLES PER METER

Figure 36f

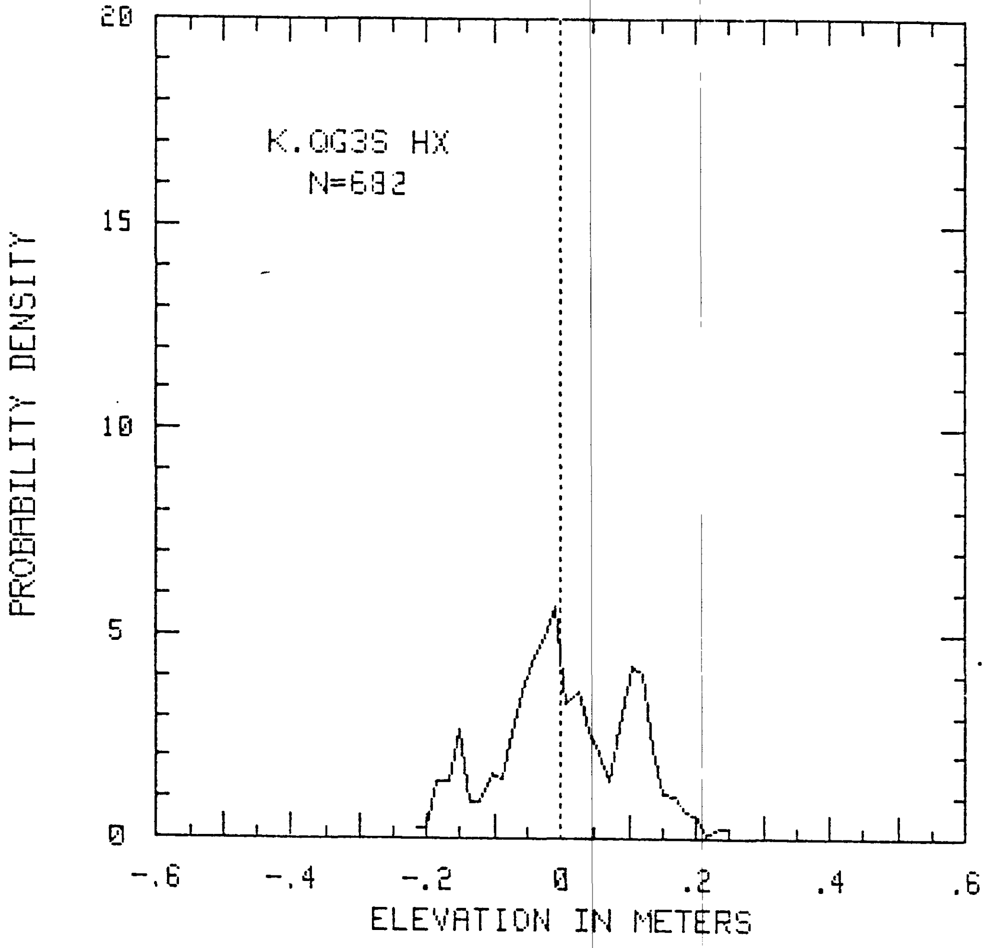
K.OG3S HX
N=682
PROBABILITY DENSITY
20
15
10
5
0
-.6
-.4
-.2
0
.2
.4
.6
ELEVATION IN METERS

Figure 37a

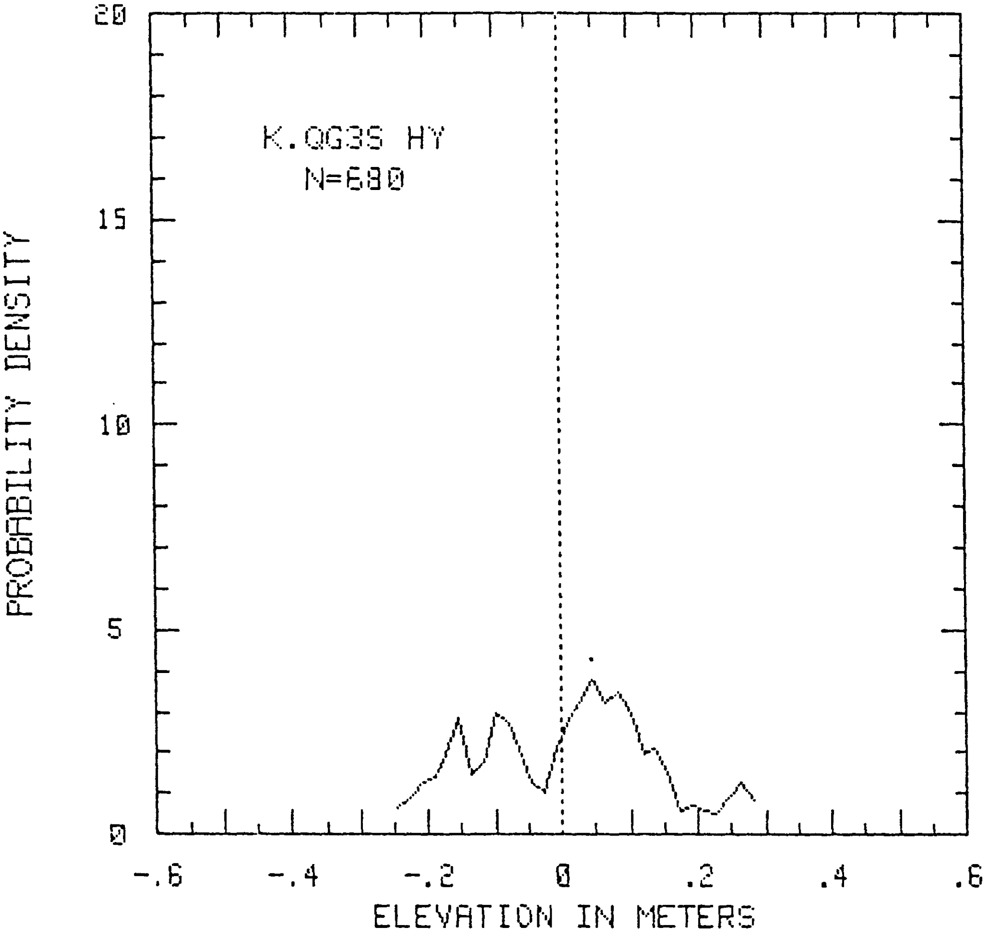
K.QG3S HY
N=680
PROBABILITY DENSITY
ELEVATION IN METERS
20
15
10
5
0
-.6
-.4
-.2
0
.2
.4
.6

Figure 37b

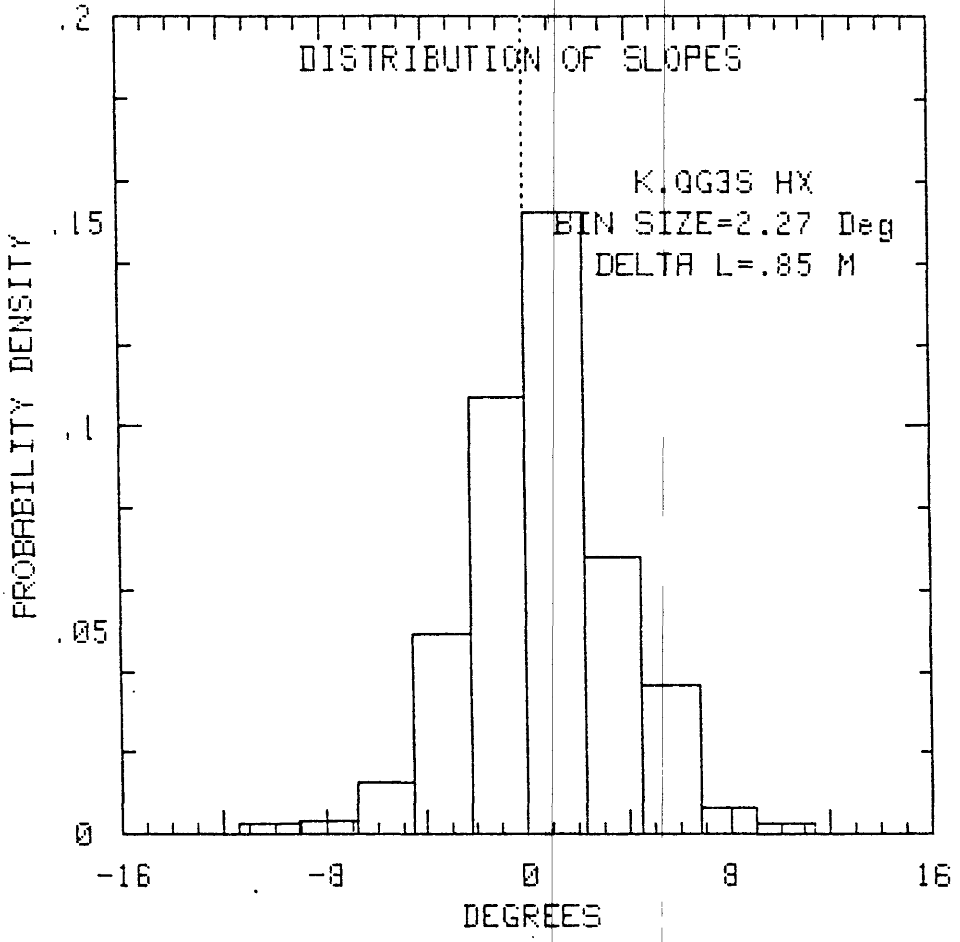
DISTRIBUTION OF SLOPES
K.QG3S HX
BIN SIZE=2.27 Deg
DELTA L=.85 M
PROBABILITY DENSITY
.2
.15
.1
.05
0
-16
-8
0
8
16
DEGREES

Figure 37c

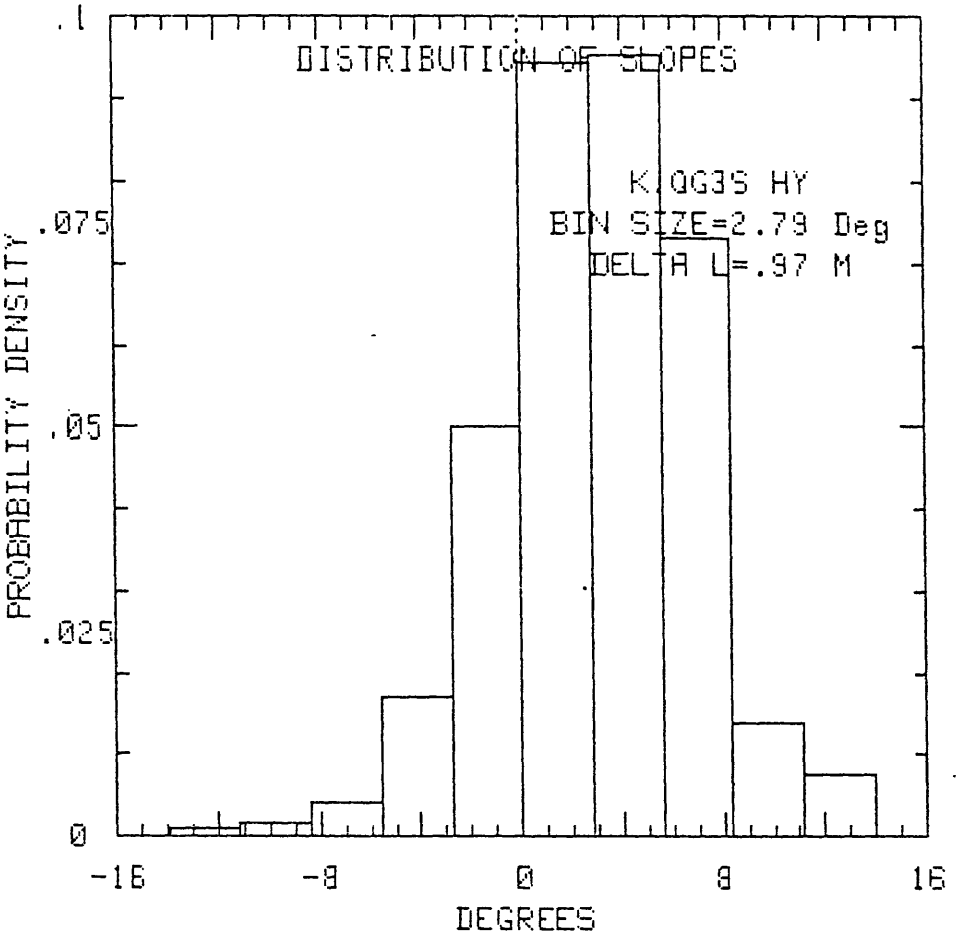
DISTRIBUTION OF SLOPES
K.QG3S HY
BIN SIZE=2.79 Deg
DELTA L=.97 M
PROBABILITY DENSITY
.1
.075
.05
.025
0
-16
-8
0
8
16
DEGREES

Figure 37d

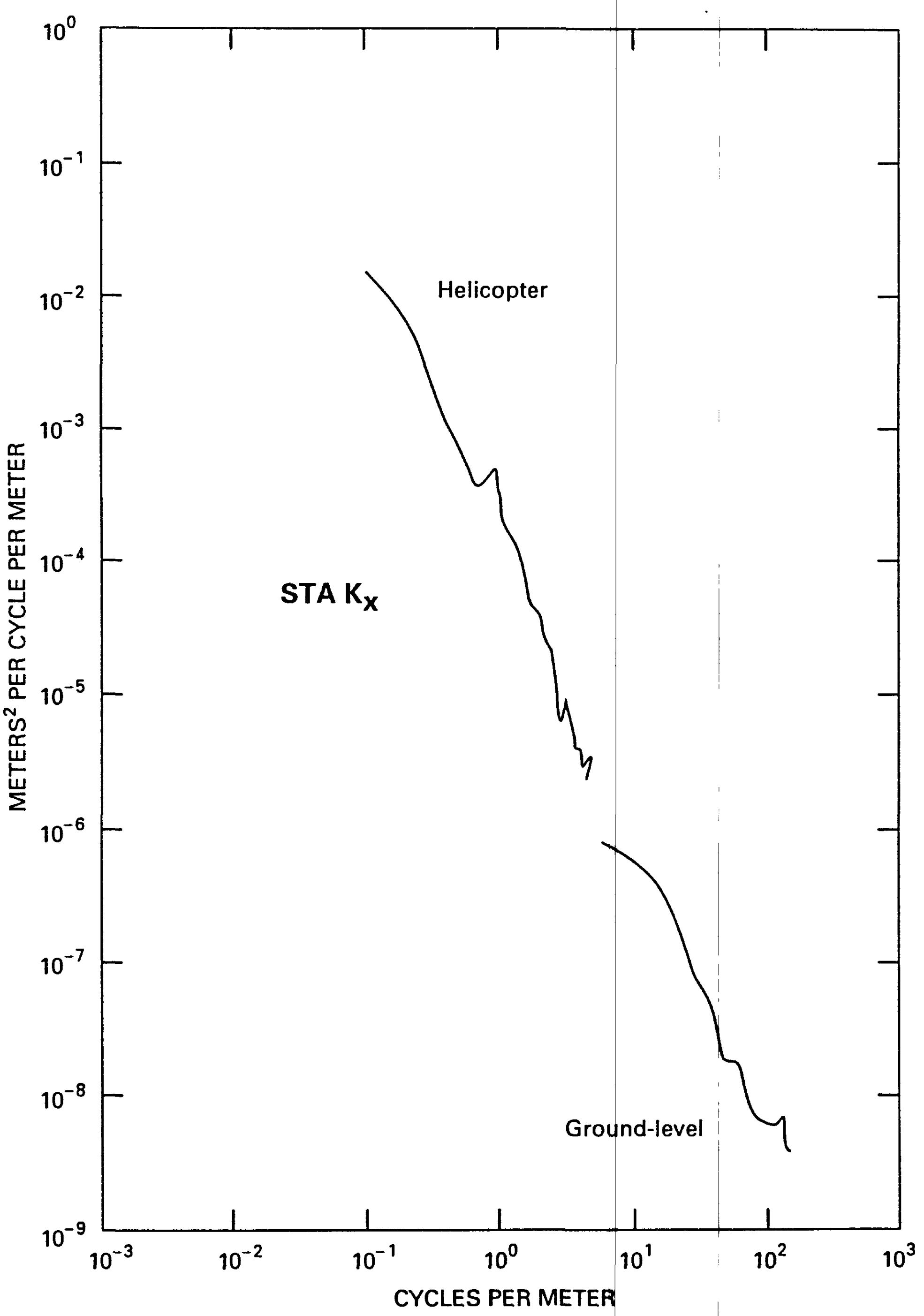
10^0
10^-1
10^-2
10^-3
10^-4
10^-5
10^-6
10^-7
10^-8
10^-9
METERS² PER CYCLE PER METER
Helicopter
STA Kx
Ground-level
10^-3
10^-2
10^-1
10^0
10^1
10^2
10^3
CYCLES PER METER

Figure 37e

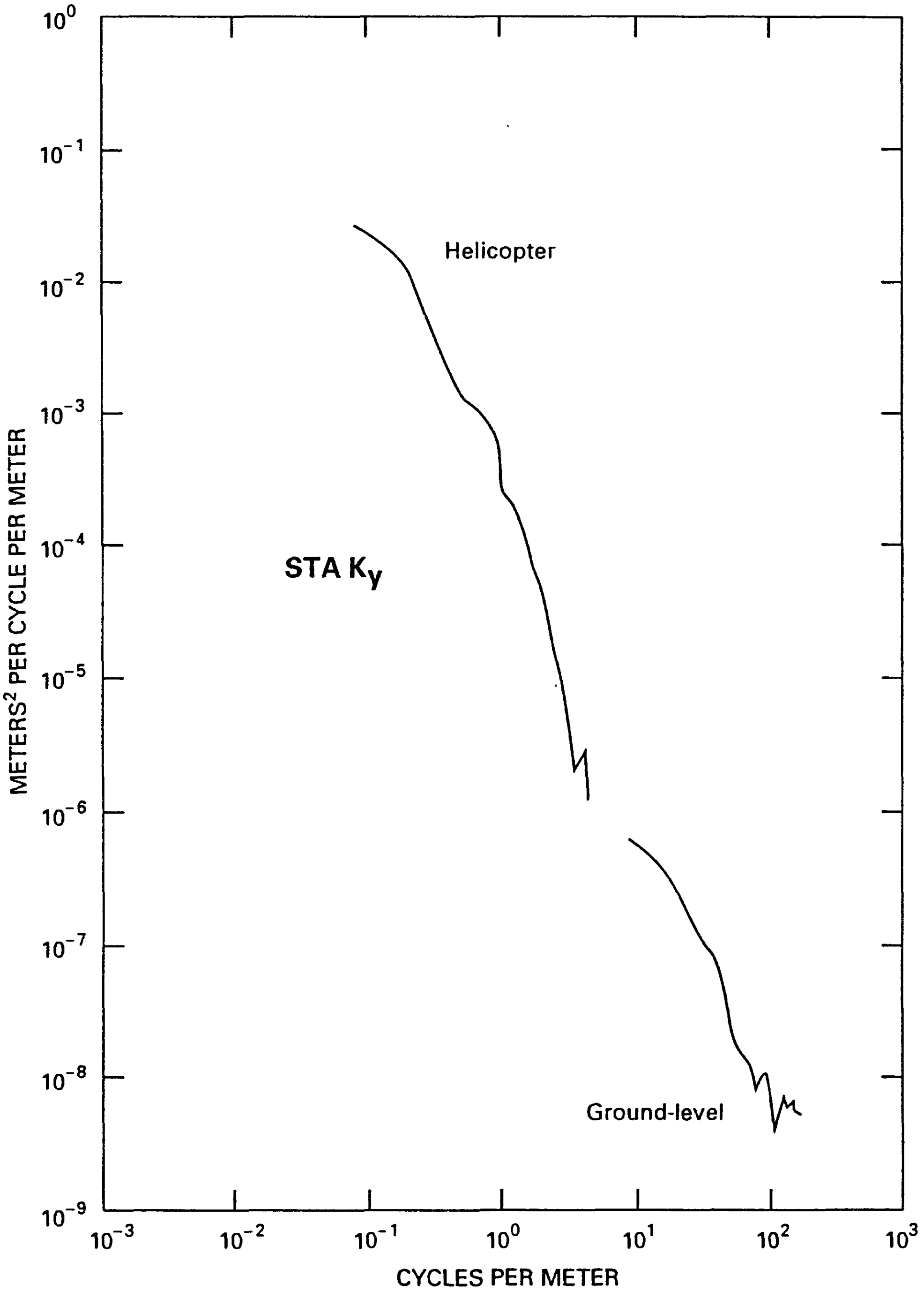
10^0
10^-1
10^-2
10^-3
10^-4
10^-5
10^-6
10^-7
10^-8
10^-9
METERS² PER CYCLE PER METER
10^-3
10^-2
10^-1
10^0
10^1
10^2
10^3
CYCLES PER METER
Helicopter
STA K_y
Ground-level

Figure 37f

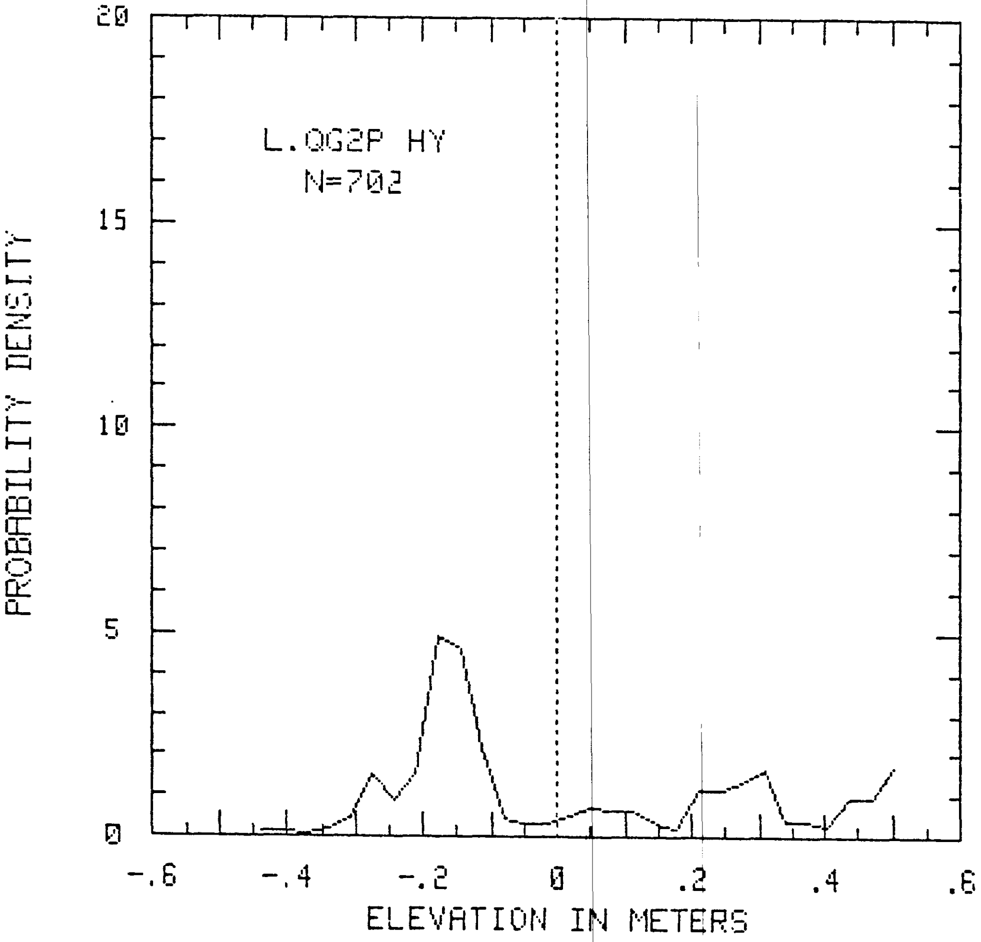
L.QG2P HY
N=702
PROBABILITY DENSITY
20
15
10
5
0
-.6
-.4
-.2
0
.2
.4
.6
ELEVATION IN METERS

Figure 38a

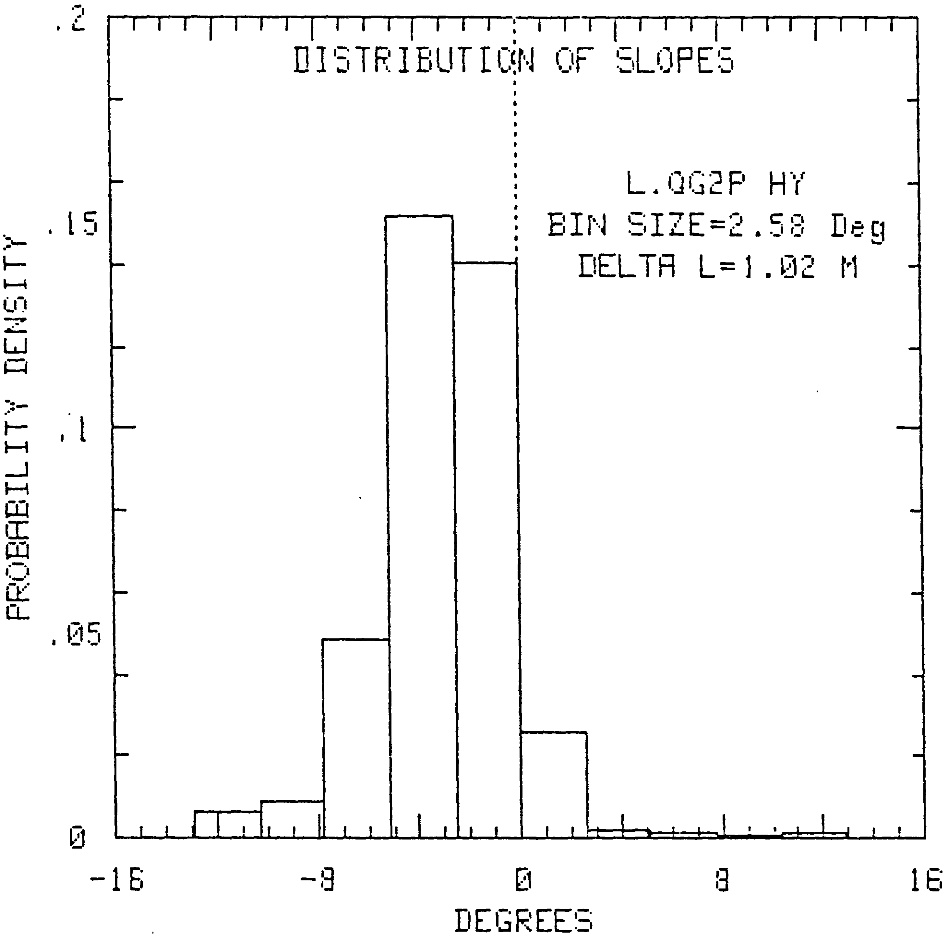
DISTRIBUTION OF SLOPES
L.QG2P HY
BIN SIZE=2.58 Deg
DELTA L=1.02 M
PROBABILITY DENSITY
.2
.15
.1
.05
0
-16
-8
0
8
16
DEGREES

Figure 38b

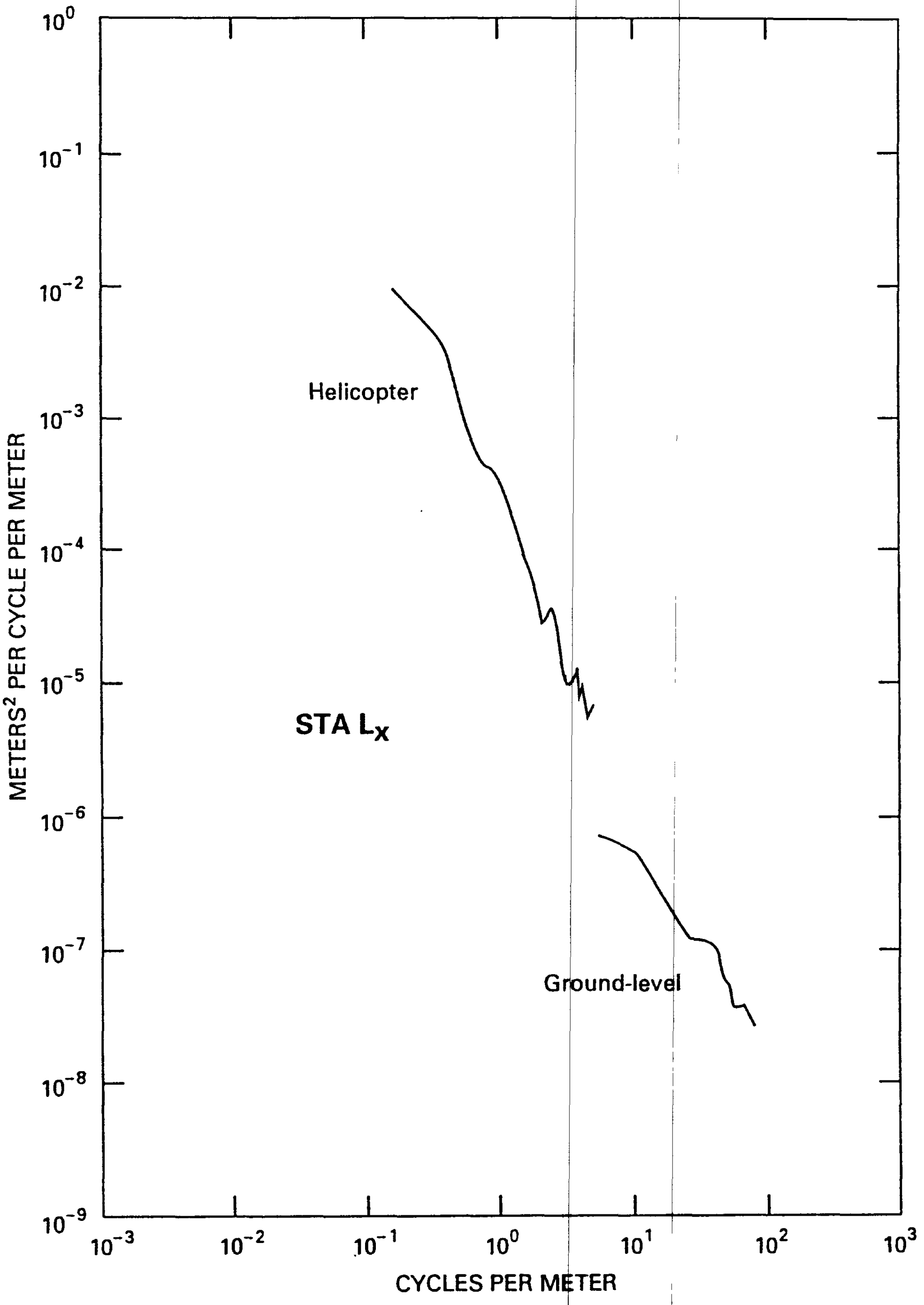
$10^0$
$10^{-1}$
$10^{-2}$
$10^{-3}$
$10^{-4}$
$10^{-5}$
$10^{-6}$
$10^{-7}$
$10^{-8}$
$10^{-9}$
METERS$^2$ PER CYCLE PER METER
Helicopter
STA $L_X$
Ground-level
$10^{-3}$
$10^{-2}$
$10^{-1}$
$10^0$
$10^1$
$10^2$
$10^3$
CYCLES PER METER

Figure 38c

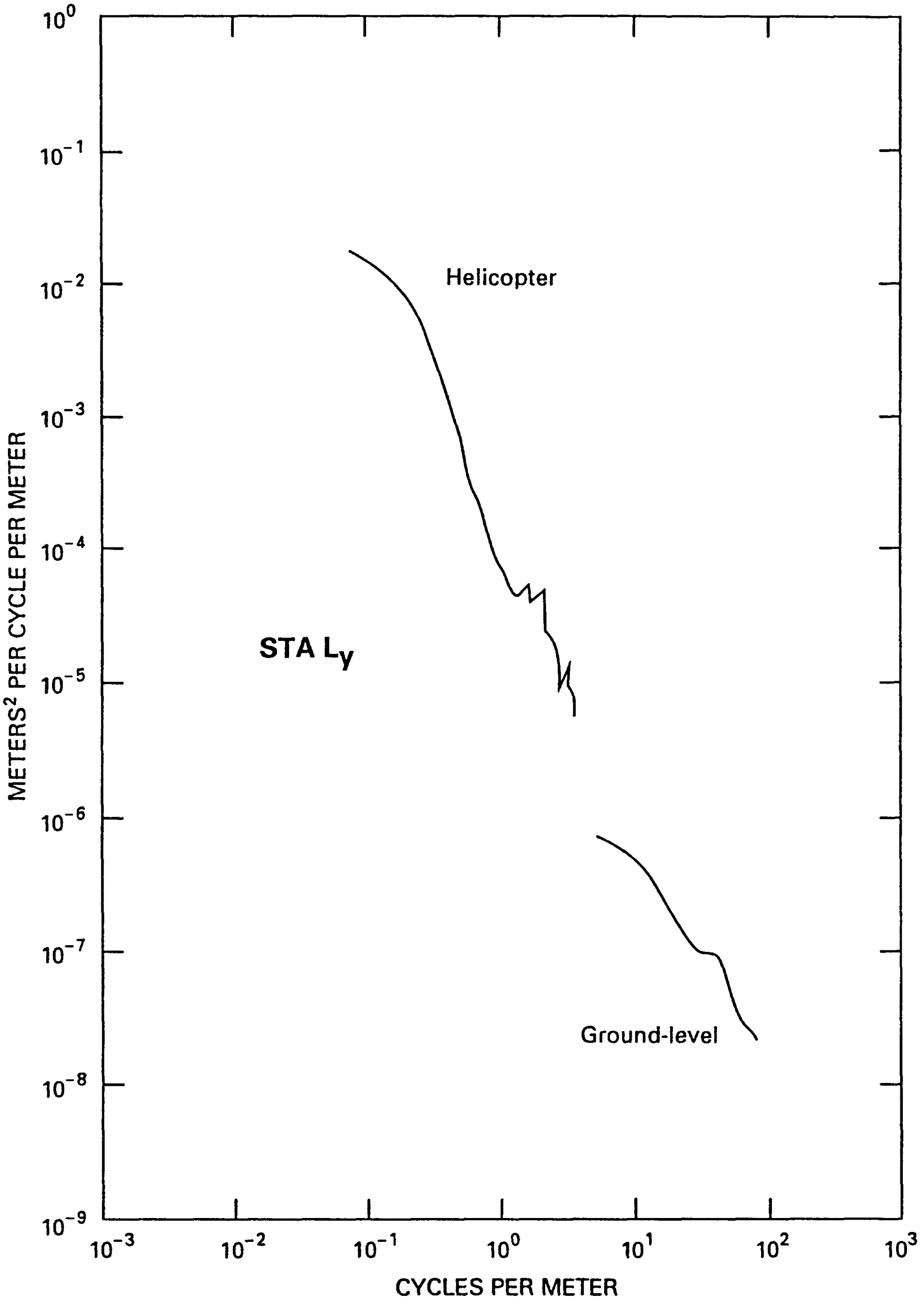

$10^0$
$10^{-1}$
$10^{-2}$
$10^{-3}$
$10^{-4}$
$10^{-5}$
$10^{-6}$
$10^{-7}$
$10^{-8}$
$10^{-9}$
METERS$^2$ PER CYCLE PER METER
Helicopter
STA $L_y$
Ground-level
$10^{-3}$
$10^{-2}$
$10^{-1}$
$10^0$
$10^1$
$10^2$
$10^3$
CYCLES PER METER

Figure 38d

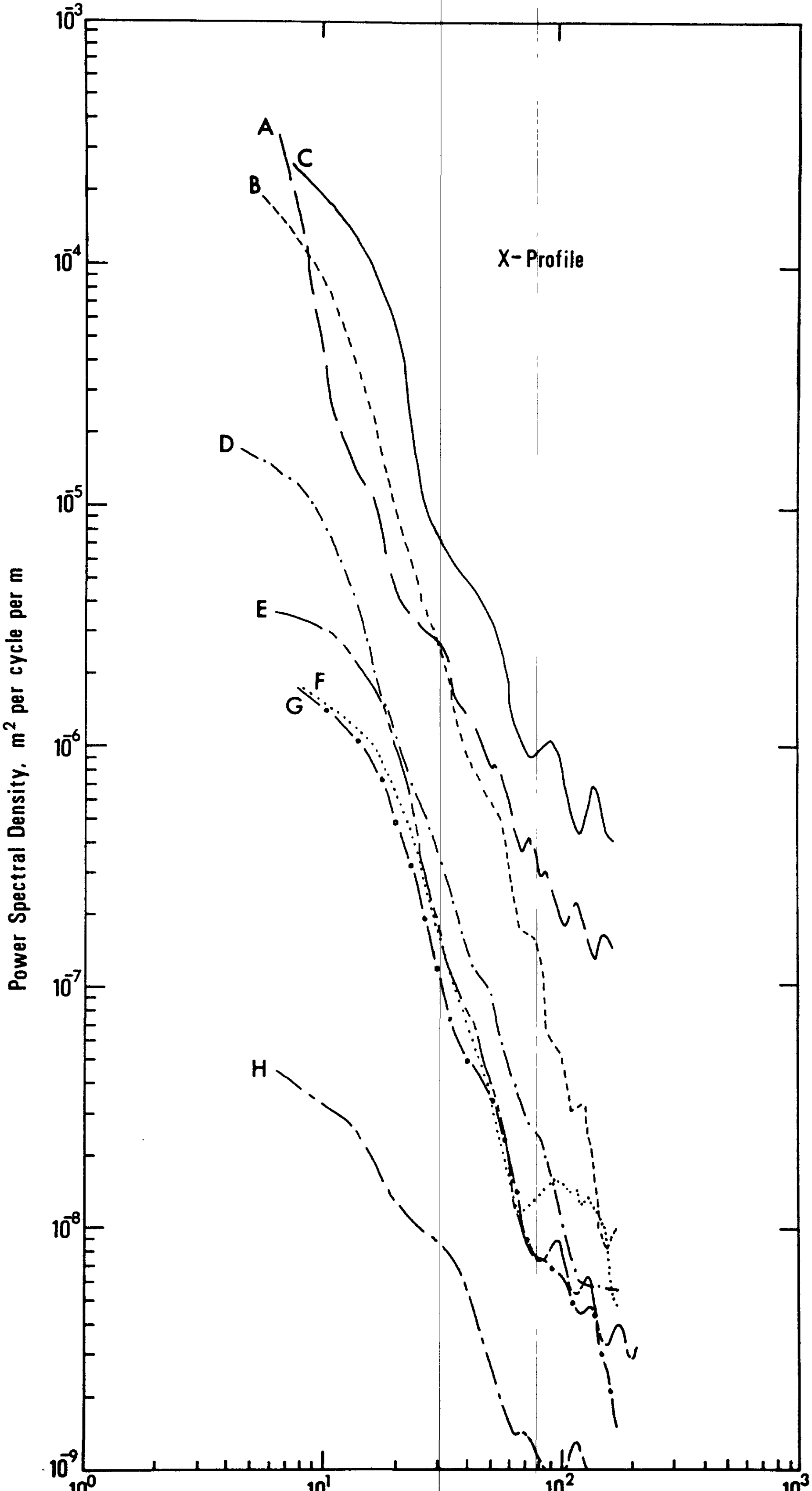
X- Profile
A
B
C
D
E
F
G
H
10⁻³
10⁻⁴
10⁻⁵
10⁻⁶
10⁻⁷
10⁻⁸
10⁻⁹
10⁰
10¹
10²
10³
Power Spectral Density, m² per cycle per m
Frequency, cycles per m

Figure 39a

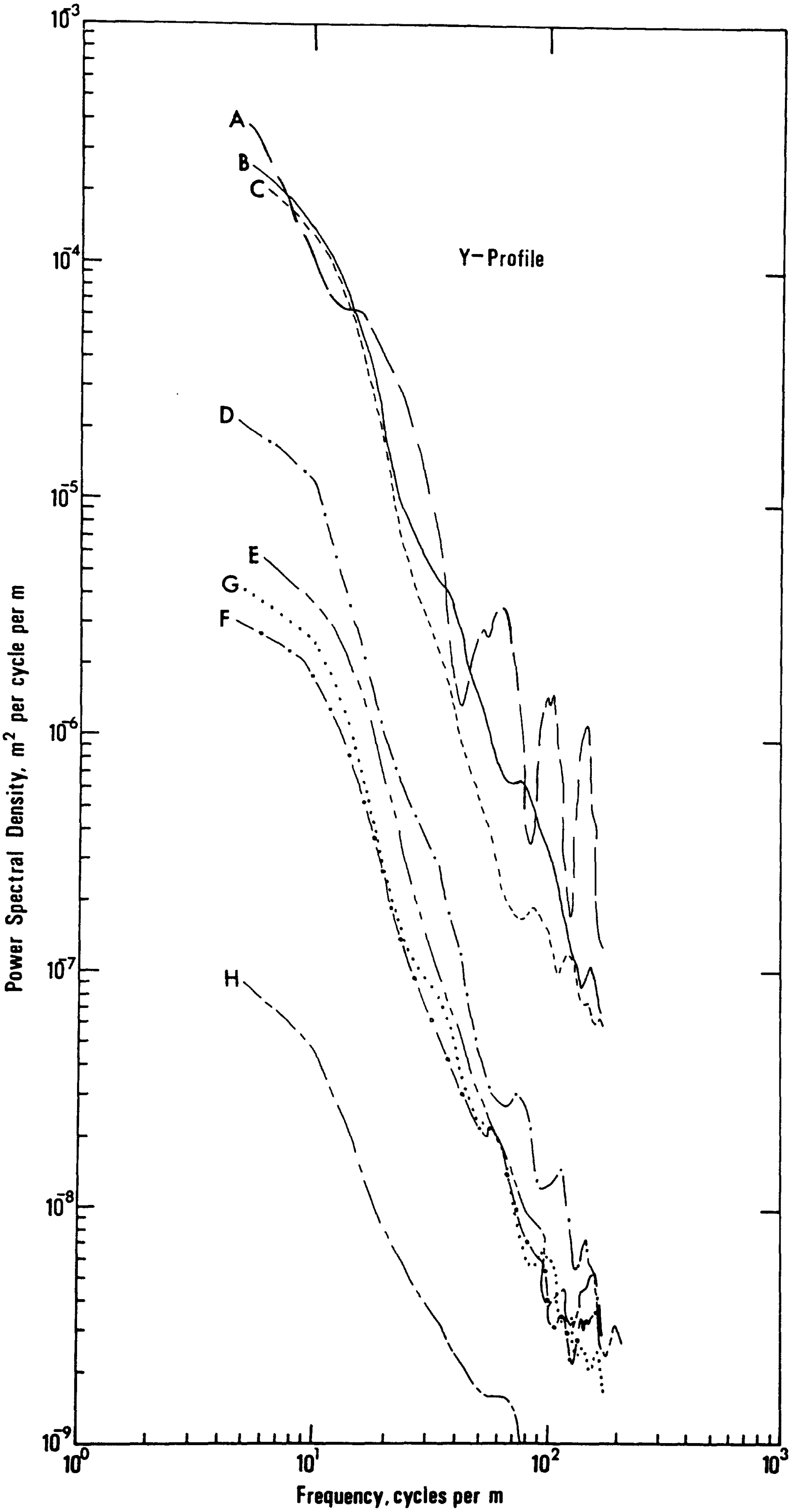
10⁻³
10⁻⁴
10⁻⁵
10⁻⁶
10⁻⁷
10⁻⁸
10⁻⁹
A
B
C
D
E
G
F
H
Y-Profile
Power Spectral Density, m² per cycle per m
10⁰
10¹
10²
10³
Frequency, cycles per m

Figure 39b

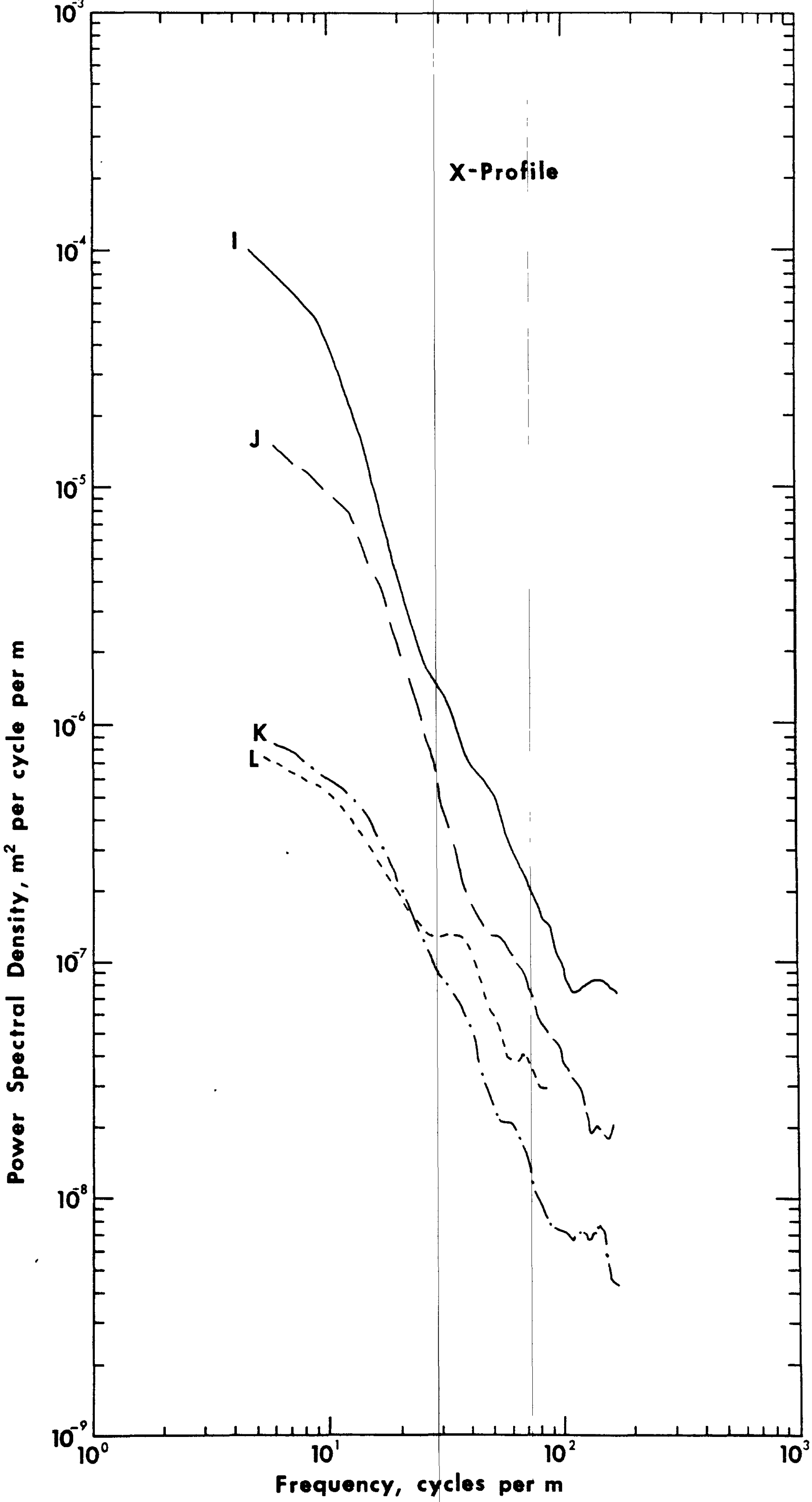
X-Profile
I
J
K
L
Power Spectral Density, m² per cycle per m
10⁻³
10⁻⁴
10⁻⁵
10⁻⁶
10⁻⁷
10⁻⁸
10⁻⁹
10⁰
10¹
10²
10³
Frequency, cycles per m

Figure 39c

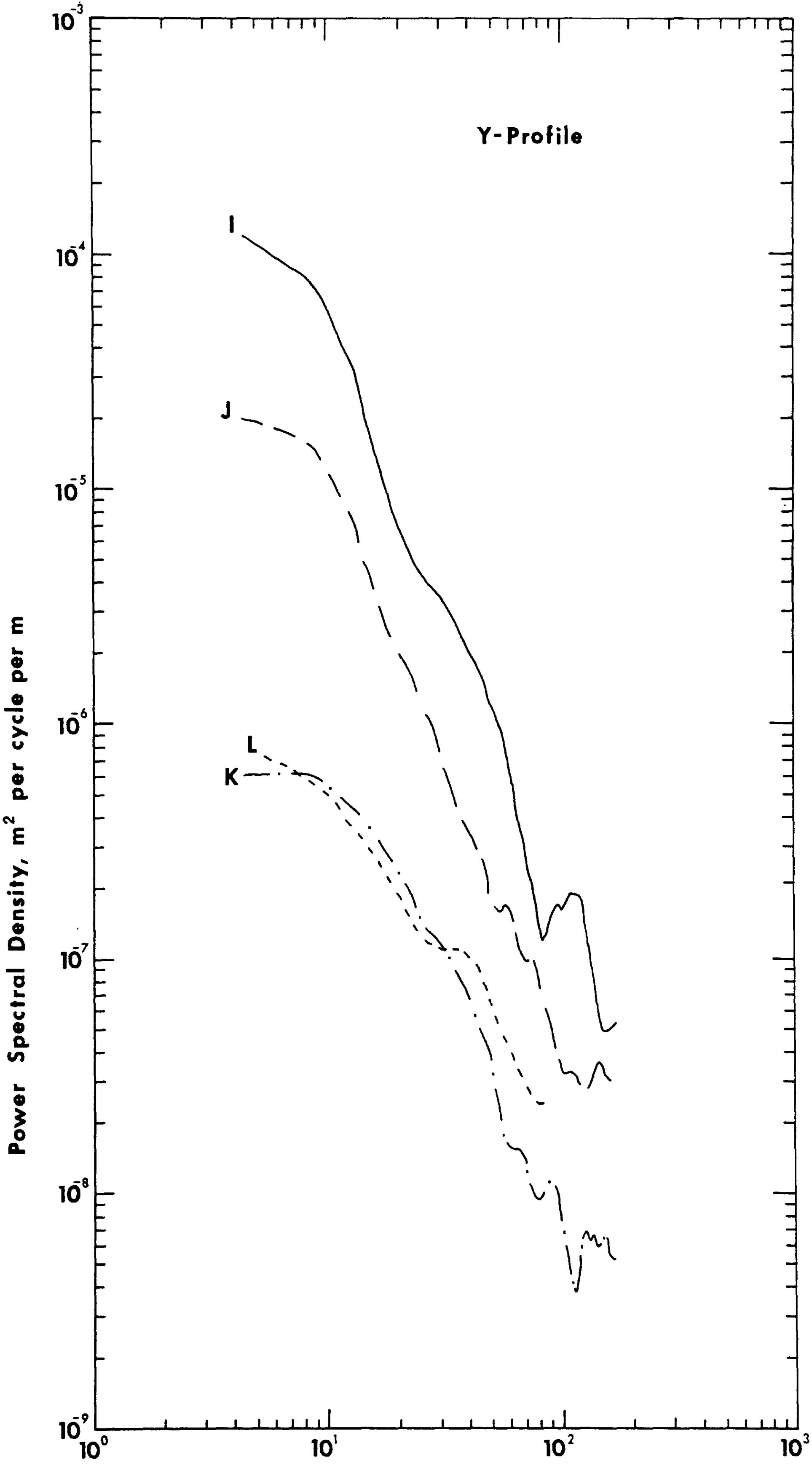
Y-Profile
I
J
K
L
Power Spectral Density, m$^2$ per cycle per m
$10^{-3}$
$10^{-4}$
$10^{-5}$
$10^{-6}$
$10^{-7}$
$10^{-8}$
$10^{-9}$
$10^0$
$10^1$
$10^2$
$10^3$
Frequency, cycles per m

Figure 39d

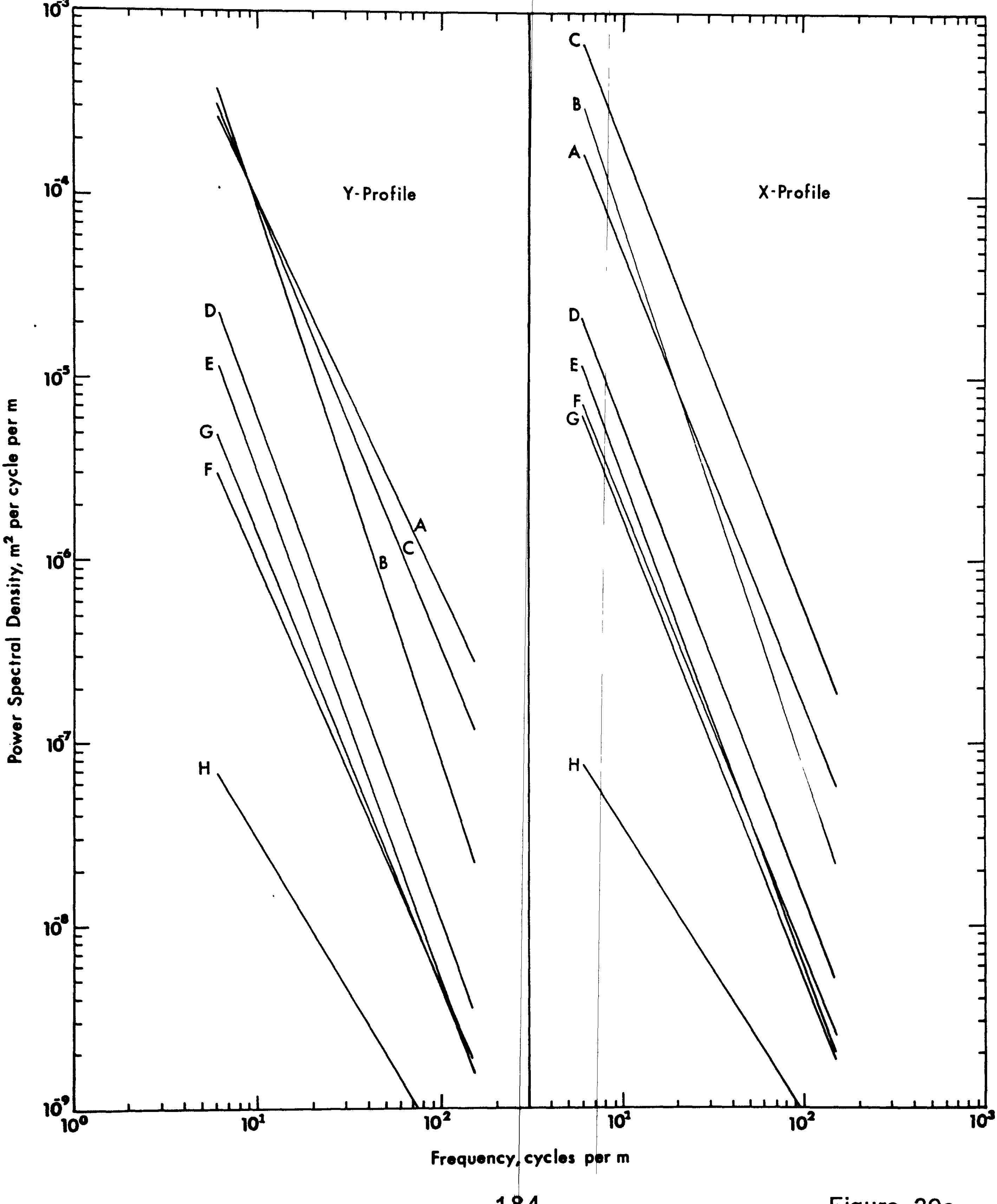

Power Spectral Density, m² per cycle per m
Frequency, cycles per m
Y-Profile
X-Profile
10⁻³
10⁻⁴
10⁻⁵
10⁻⁶
10⁻⁷
10⁻⁸
10⁻⁹
10⁰
10¹
10²
10¹
10²
10³
A
B
C
D
E
F
G
H
C
B
A
D
E
F
G
H

Figure 39e

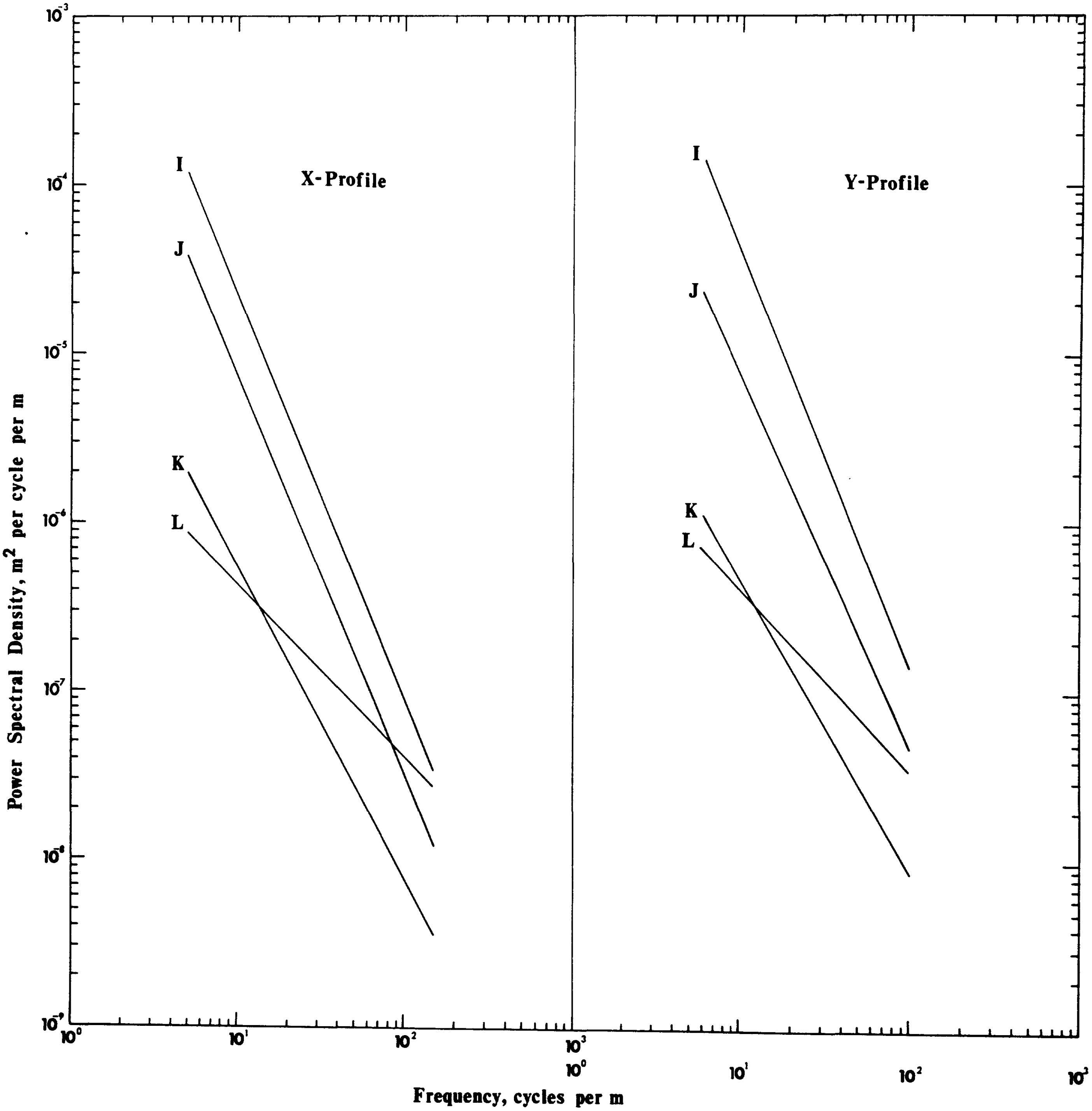

X-Profile
Y-Profile
I
J
K
L
I
J
K
L
Power Spectral Density, m² per cycle per m
Frequency, cycles per m
10⁻³
10⁻⁴
10⁻⁵
10⁻⁶
10⁻⁷
10⁻⁸
10⁻⁹
10⁰
10¹
10²
10³
10⁰
10¹
10²
10³

Figure 39f

## TABLE 31 - Regression Line-fits For Power Spectral Density Functions*

| STATION (UNIT) | LOG10(A) | A | B | TOTAL VARIANCE IN INTEGRATED SPECTRUM |
|---|---|---|---|---|
| | | GROUND-LEVEL PROFILES** | | |
| Ax (Qh) | -0.2641 | 0.544346 | -2.469964 | 7.52E+03 |
| Ay | 0.6980 | 4.88506 | -2.132259 | 5.34E+03 |
| Bx (Qhr) | -1.0982 | 0.079767 | -2.962868 | 2.48E+03 |
| By | -1.1500 | 0.070795 | -3.033413 | 3.23E+03 |
| Dx (Qch) | -1.4072 | 0.03916 | -2.579806 | 2.13E+02 |
| Dy | -1.7142 | 0.019309 | -2.736138 | 2.47E+02 |
| Ex (Qhs) | -1.8855 | 0.013017 | -2.67874 | 6.60E+01 |
| Ey | -2.0751 | 0.008412 | -2.76845 | 8.24E+01 |
| Hx (Qf) | -1.5784 | 0.0264 | -1.56253 | 1.04E+01 |
| Hy | -1.8861 | 0.012997 | -1.681062 | 1.24E+00 |
| Ix (Qg3 rough) | -0.4623 | 0.34488 | -2.413144 | 1.17E+03 |
| Iy | -0.3040 | 0.496549 | -2.462884 | 1.44E+03 |
| Jx (Qg3 mod.) | -0.9022 | 0.125251 | -2.386939 | 2.35E+02 |
| Jy | -0.5168 | 0.304199 | -2.199021 | 2.75E+02 |
| Kx (Qg3 sm.) | -0.9784 | 0.10511 | -1.863331 | 1.56E+01 |
| Ky | -0.7352 | 0.183978 | -1.701661 | 1.34E+01 |
| Lx (Qg2) | 0.5767 | 3.772731 | -1.029388 | 1.56E+01 |
| Ly | 0.4654 | 2.920287 | -1.07673 | 1.49E+01 |
| | | | | |
| | | HELICOPTER PROFILES*** | | |
| Ax | -2.9428 | 0.001141 | -2.093369 | 2.05E-02 |
| Ay | -3.0851 | 0.000822 | -1.617652 | 1.39E-02 |
| Bx | -3.5031 | 0.000314 | -1.513427 | 3.35E-03 |
| By | -3.5673 | 0.000271 | -1.569992 | 2.18E-03 |
| Dx | -4.2178 | 0.00006 | -1.667845 | 1.63E-03 |
| Dy | -4.1144 | 0.000077 | -2.035621 | 4.35E-03 |
| Ex | -4.1487 | 0.000071 | -1.45248 | 5.34E-04 |
| Ey | -4.3136 | 0.000048 | -0.911129 | 2.73E-04 |
| Ix | -3.0738 | 0.000844 | -2.952064 | 1.61E-01 |
| Iy | -2.5046 | 0.003129 | -2.544404 | 8.17E-01 |
| Jx | -3.3694 | 0.000427 | -2.397352 | 1.72E-02 |
| Jy | -3.4221 | 0.000378 | -2.46453 | 2.61E-02 |
| Kx | -4.2888 | 0.000051 | -2.412363 | 7.54E-03 |
| Ky | -3.7641 | 0.000172 | -2.463676 | 2.19E-02 |

*The results of fitting a regression line of the form:
LOG10(PSD) =log10(A) + B*LOG10(FREQ)
where A=PSD for FREQ=1

** Ground PSD data high-pass filtered
*** Helicopter PSD data not filtered

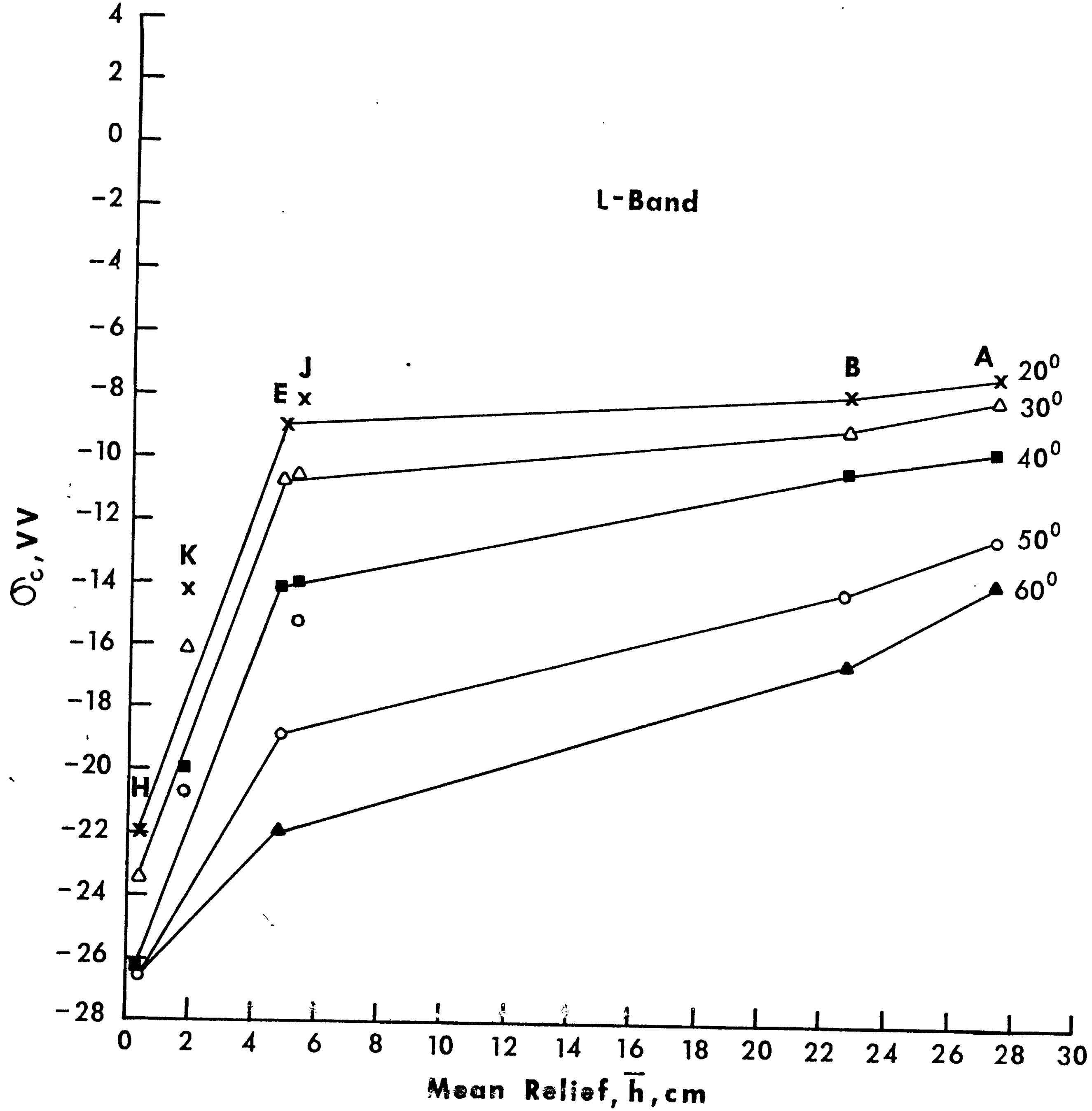
L-Band
4
2
0
-2
-4
-6
-8
-10
-12
-14
-16
-18
-20
-22
-24
-26
-28
$\sigma_c$, VV
0
2
4
6
8
10
12
14
16
18
20
22
24
26
28
30
Mean Relief, $\overline{h}$, cm
H
K
E
J
B
A
20°
30°
40°
50°
60°

Figure 40a

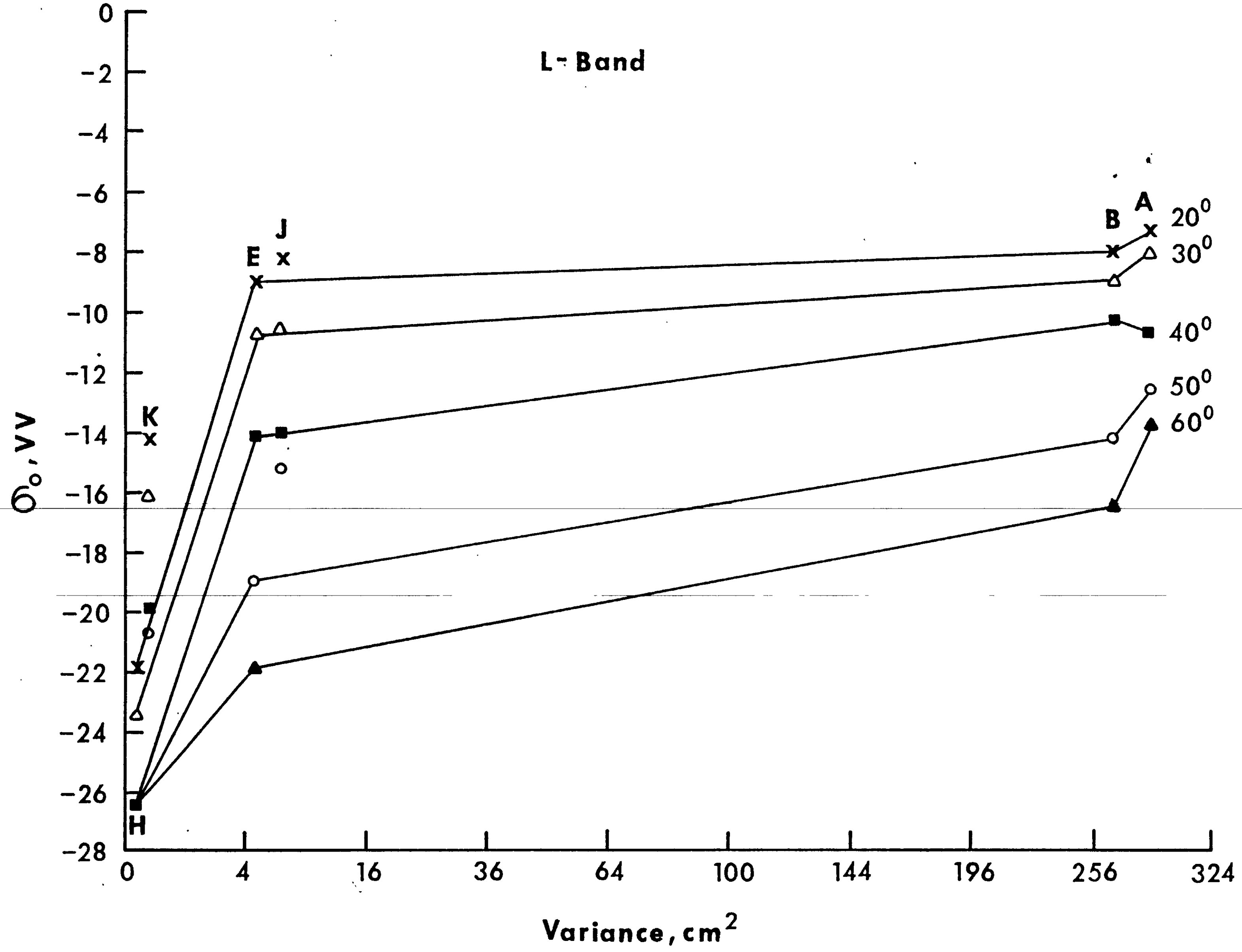
L- Band
$\sigma_o$, VV
0
-2
-4
-6
-8
-10
-12
-14
-16
-18
-20
-22
-24
-26
-28
0
4
16
36
64
100
144
196
256
324
Variance, cm$^2$
A
B
E
J
K
H
20°
30°
40°
50°
60°

Figure 40b

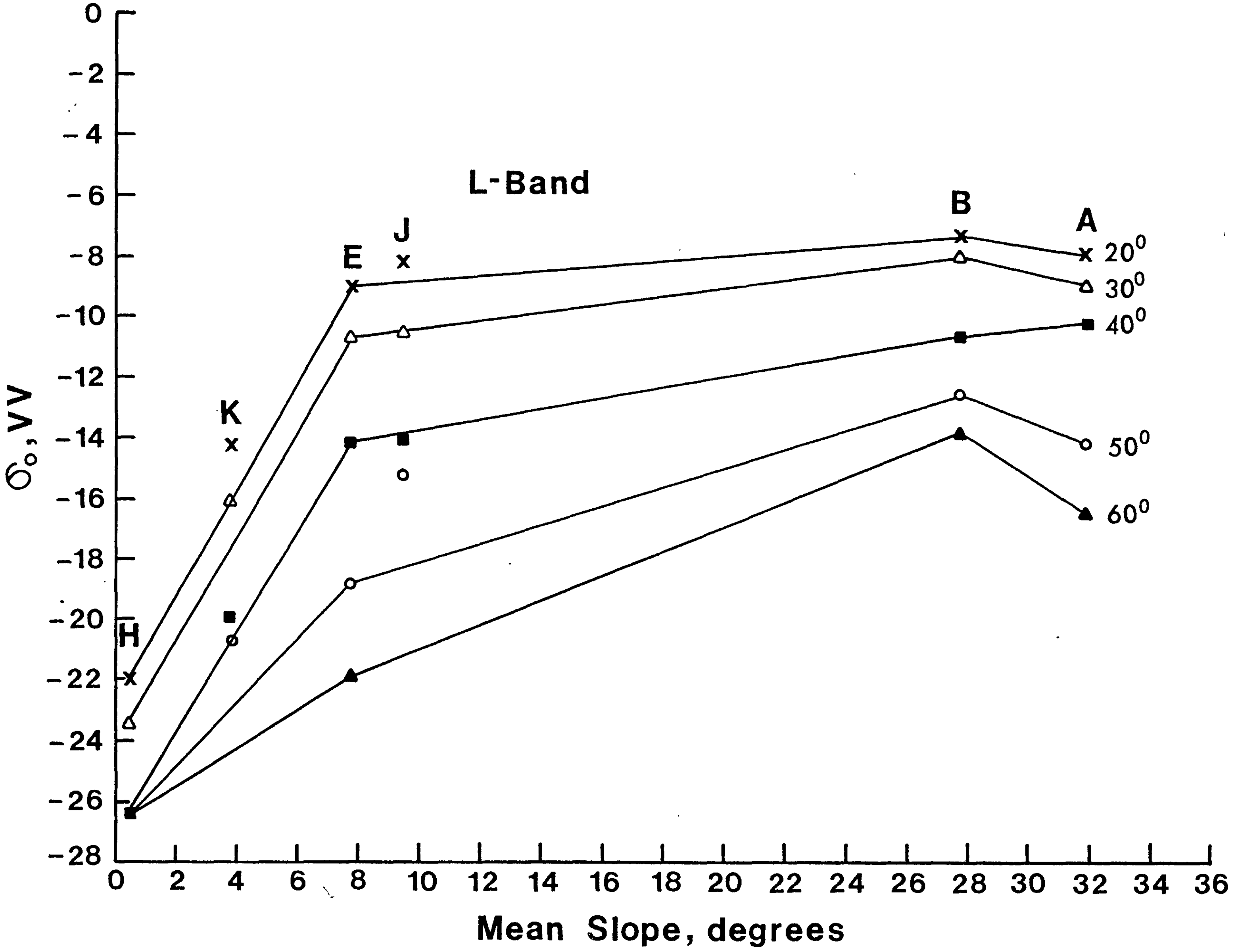
L-Band
$\sigma_o$, VV
0
-2
-4
-6
-8
-10
-12
-14
-16
-18
-20
-22
-24
-26
-28
0
2
4
6
8
10
12
14
16
18
20
22
24
26
28
30
32
34
36
Mean Slope, degrees
H
K
E
J
B
A
$20^0$
$30^0$
$40^0$
$50^0$
$60^0$

Figure 40c

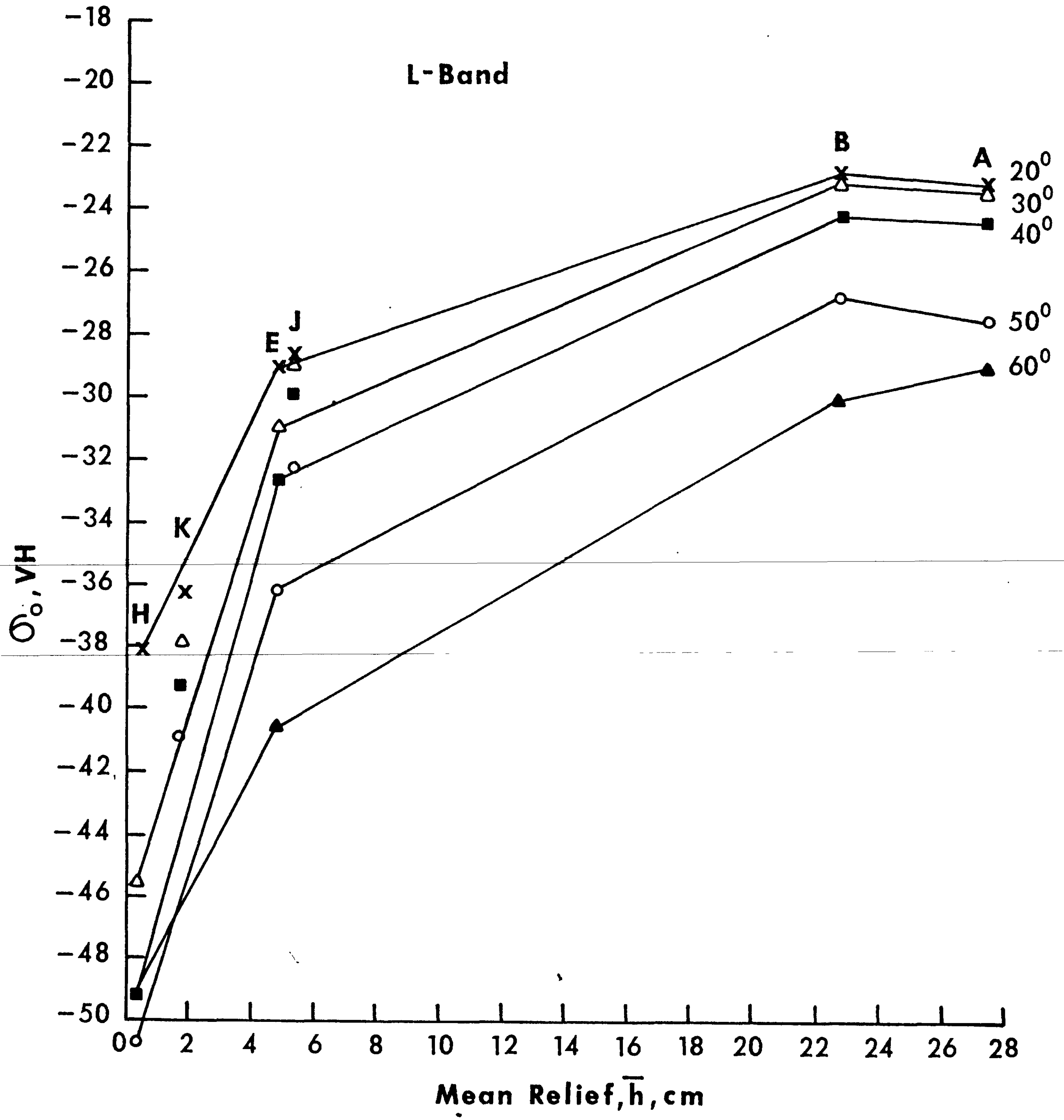
L-Band
$\sigma_o$, VH
-18
-20
-22
-24
-26
-28
-30
-32
-34
-36
-38
-40
-42
-44
-46
-48
-50
0
2
4
6
8
10
12
14
16
18
20
22
24
26
28
Mean Relief, $\overline{h}$, cm
A
B
E
J
K
H
20°
30°
40°
50°
60°

Figure 41a

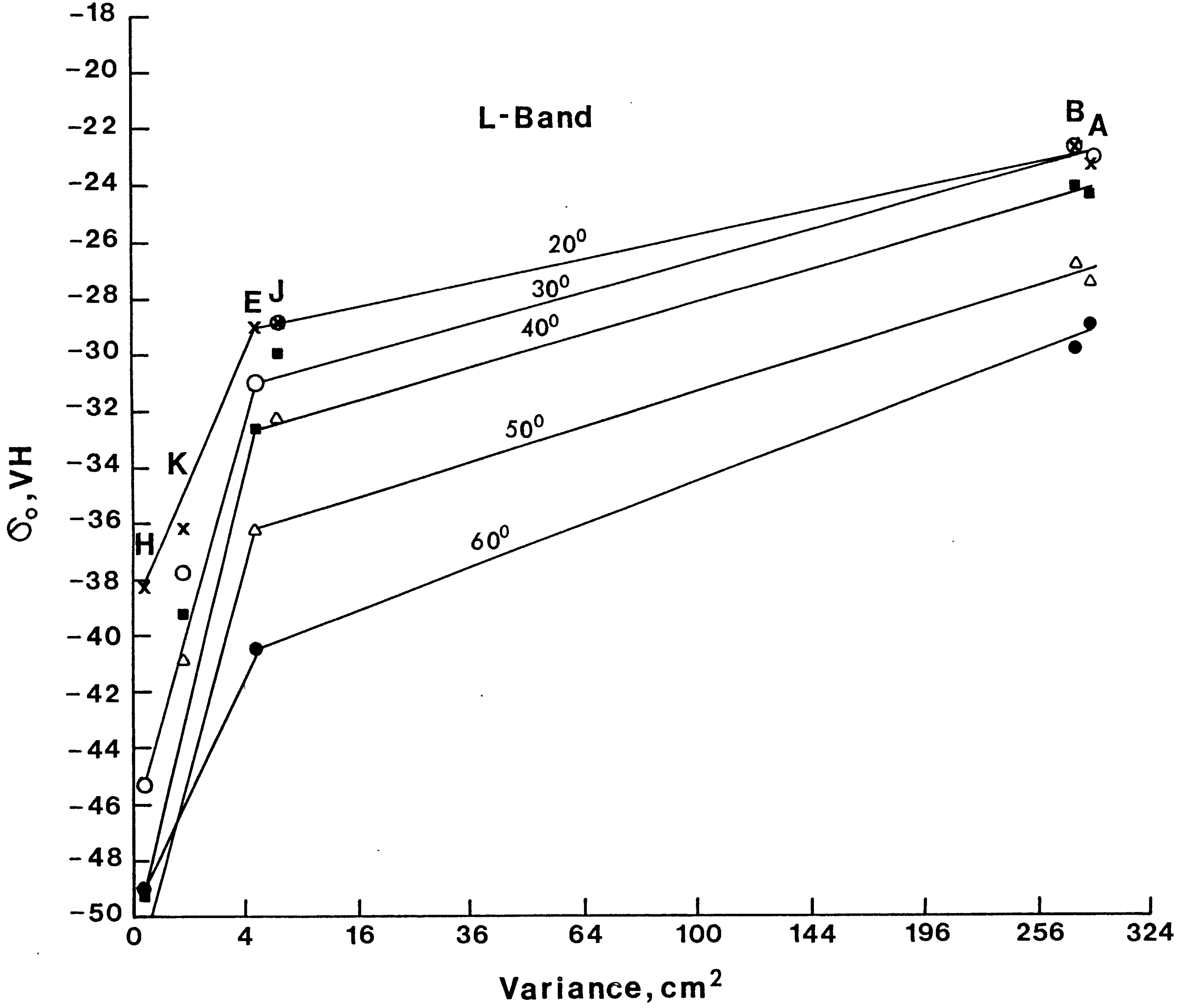
L-Band
$\sigma_o$, VH
-18
-20
-22
-24
-26
-28
-30
-32
-34
-36
-38
-40
-42
-44
-46
-48
-50
Variance, cm²
0
4
16
36
64
100
144
196
256
324
20°
30°
40°
50°
60°
H
K
E
J
B
A

Figure 41b

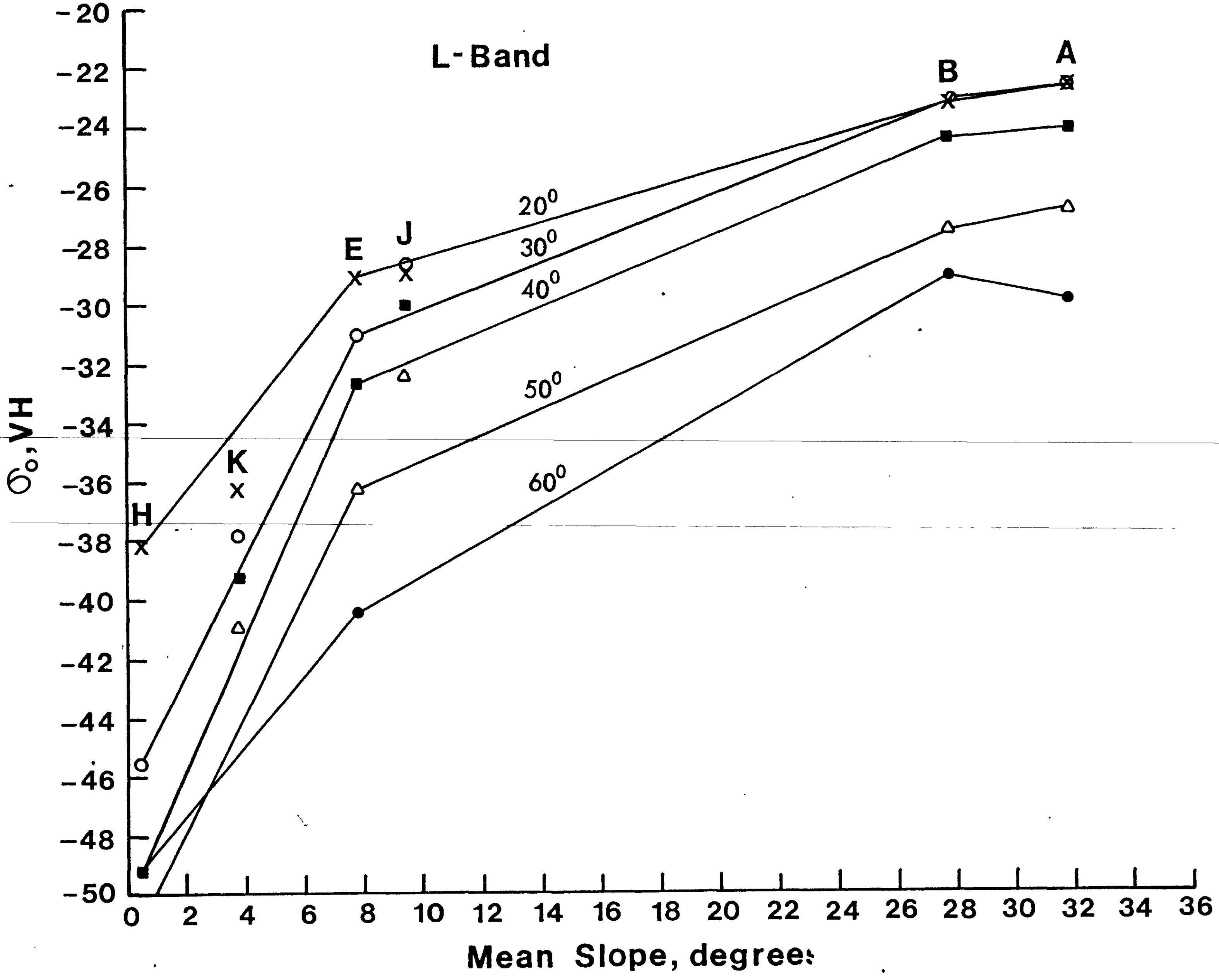
L-Band
A
B
E
J
K
H
20°
30°
40°
50°
60°
σ°, VH
-20
-22
-24
-26
-28
-30
-32
-34
-36
-38
-40
-42
-44
-46
-48
-50
0
2
4
6
8
10
12
14
16
18
20
22
24
26
28
30
32
34
36
Mean Slope, degrees

Figure 41c

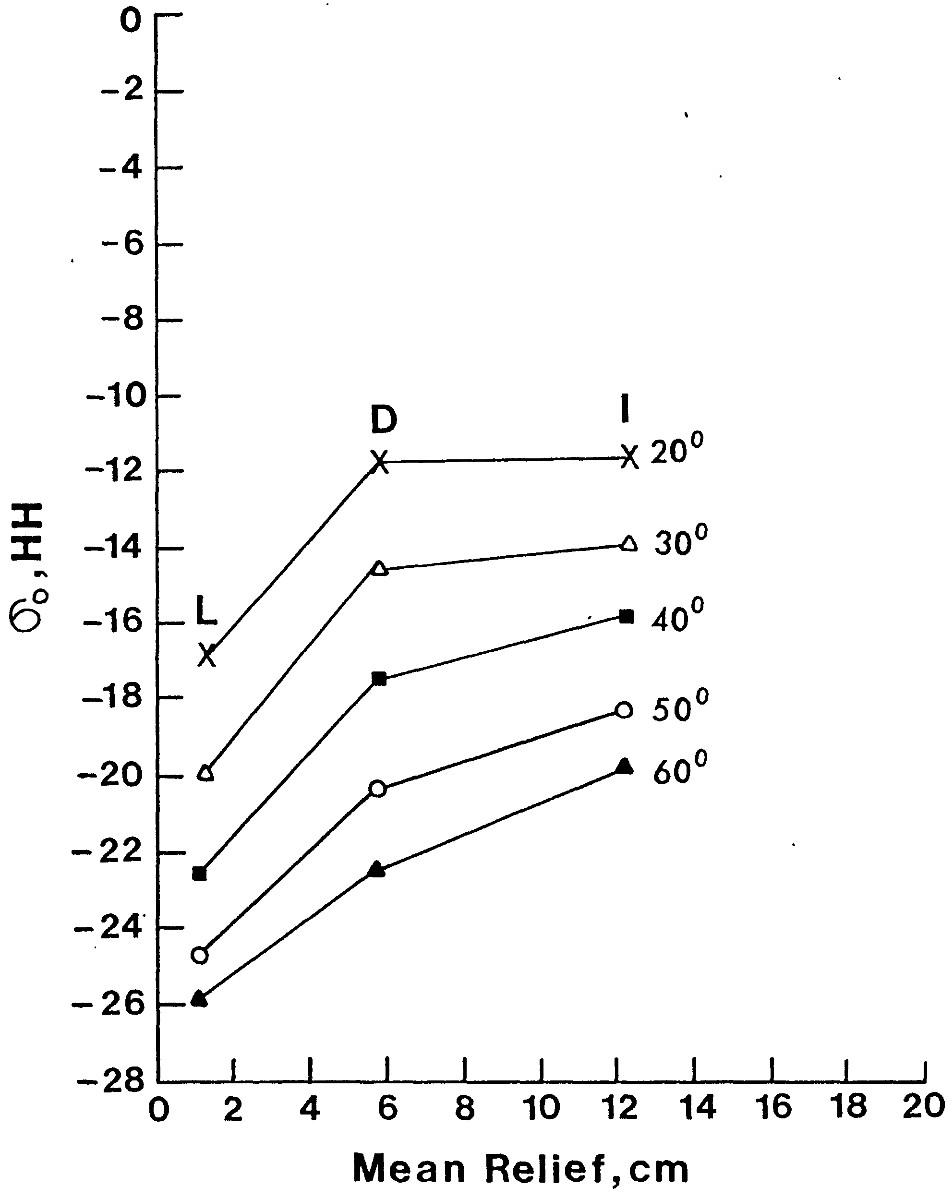
0
-2
-4
-6
-8
-10
-12
-14
-16
-18
-20
-22
-24
-26
-28
$\sigma^o$, HH
L
D
I
$20^0$
$30^0$
$40^0$
$50^0$
$60^0$
0
2
4
6
8
10
12
14
16
18
20
Mean Relief, cm

Figure 42a

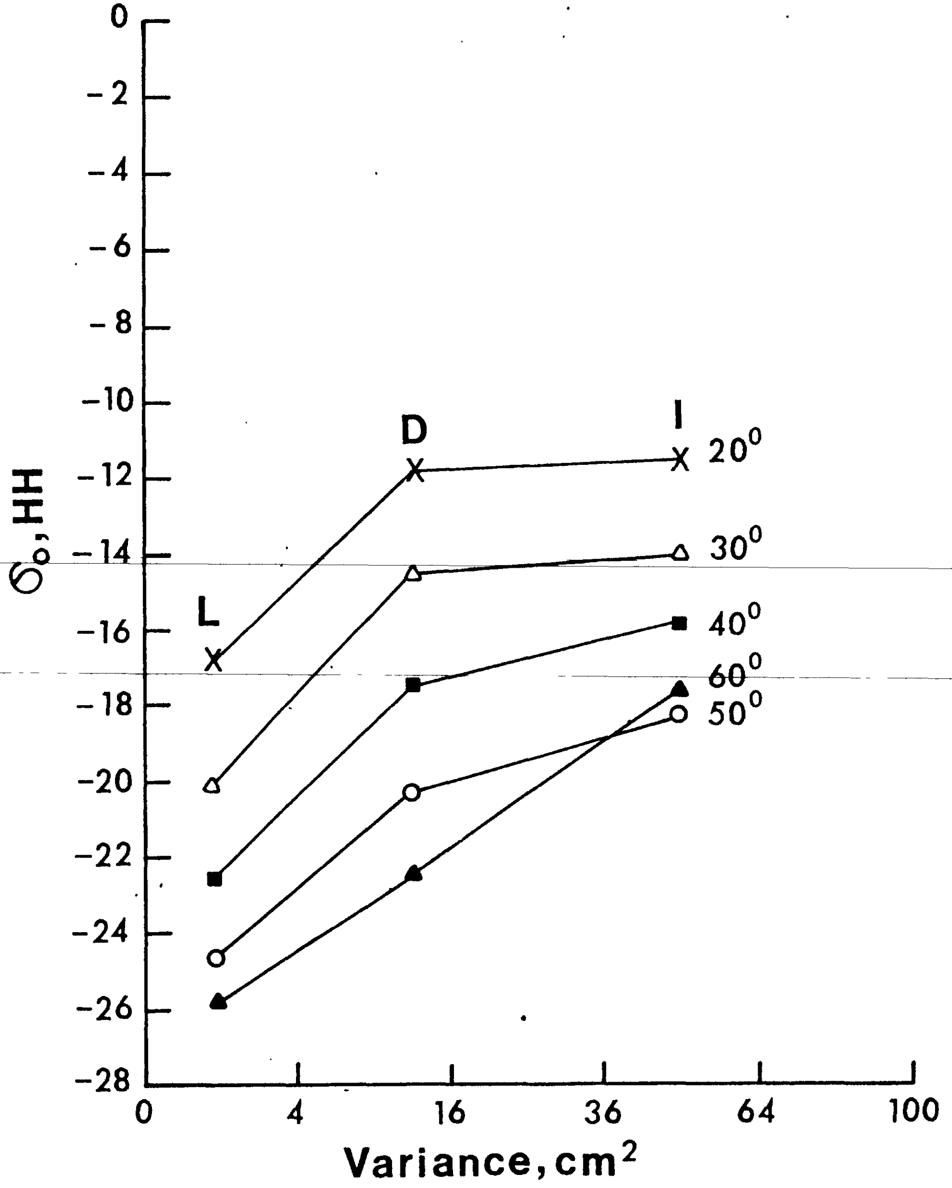

$\sigma_o$, HH
0
-2
-4
-6
-8
-10
-12
-14
-16
-18
-20
-22
-24
-26
-28
L
D
I
$20^0$
$30^0$
$40^0$
$60^0$
$50^0$
0
4
16
36
64
100
Variance, cm$^2$

Figure 42b

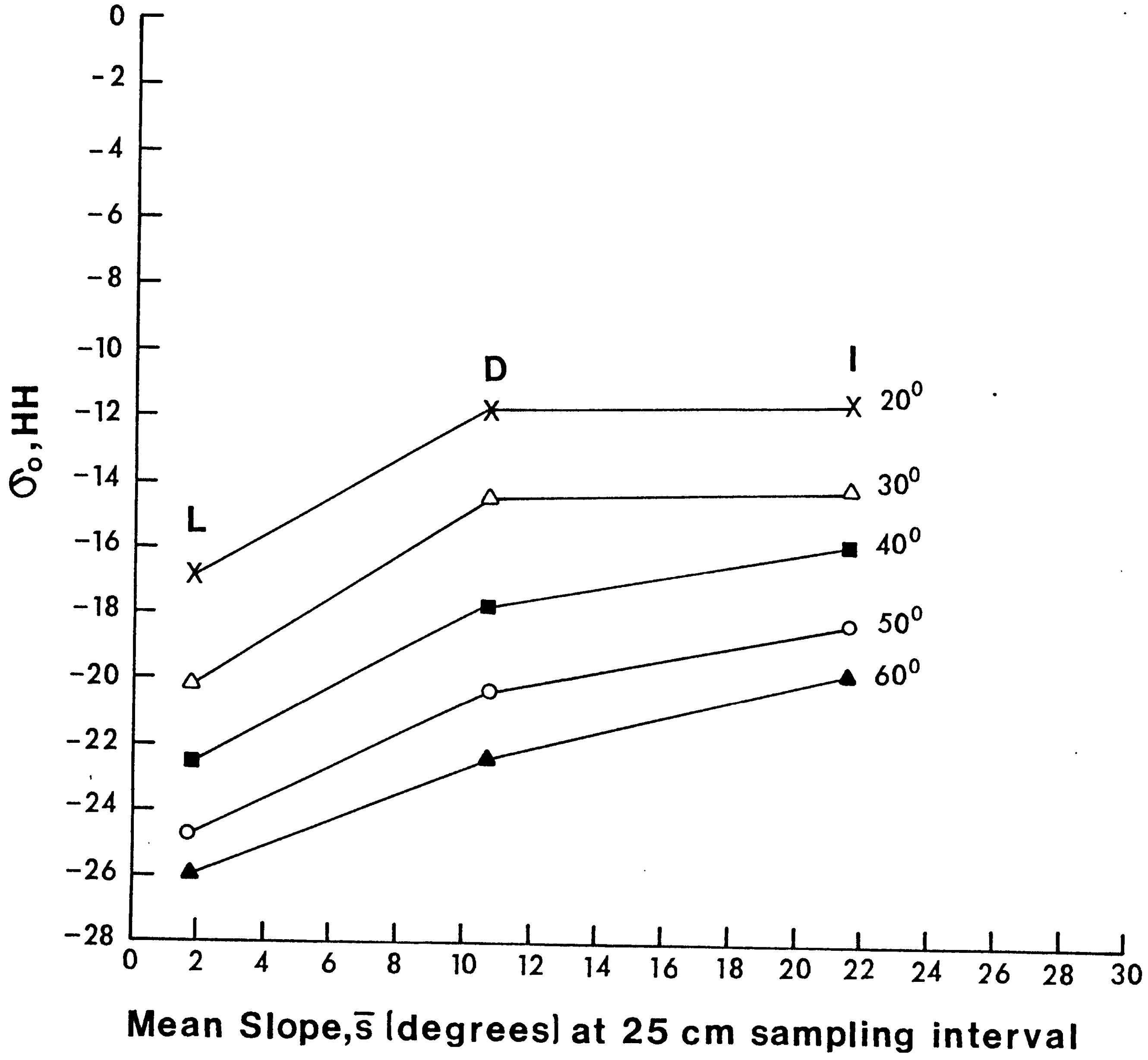
$\sigma_o$, HH
0
-2
-4
-6
-8
-10
-12
-14
-16
-18
-20
-22
-24
-26
-28
L
D
I
20°
30°
40°
50°
60°
0
2
4
6
8
10
12
14
16
18
20
22
24
26
28
30
Mean Slope, $\bar{s}$ (degrees) at 25 cm sampling interval

Figure 42c

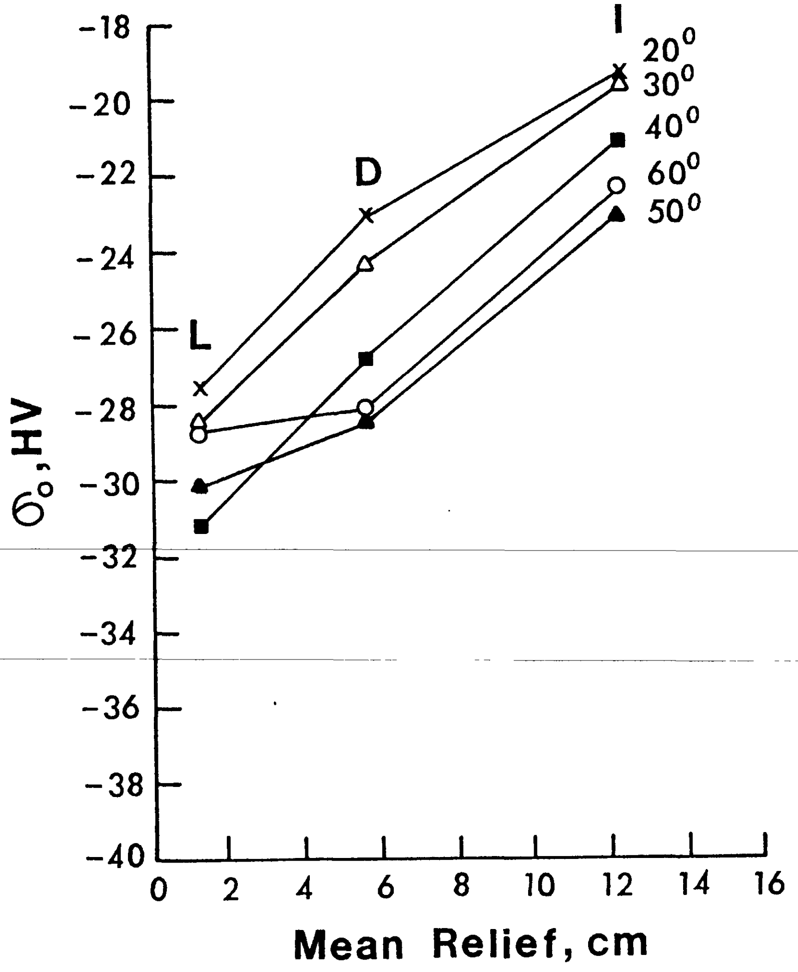

$\sigma_o$, HV
-18
-20
-22
-24
-26
-28
-30
-32
-34
-36
-38
-40
0
2
4
6
8
10
12
14
16
Mean Relief, cm
L
D
I
20°
30°
40°
60°
50°

Figure 43a

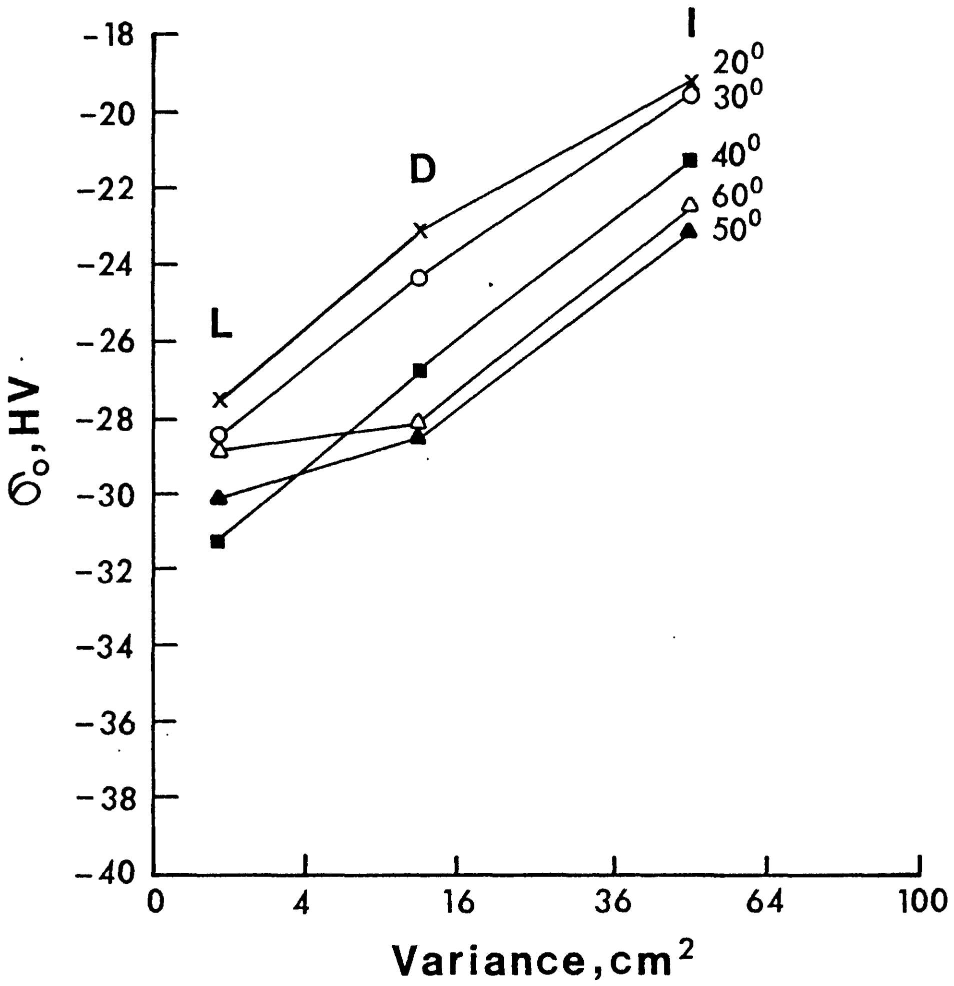
-18
-20
-22
-24
-26
-28
-30
-32
-34
-36
-38
-40
$\sigma_o$,HV
0
4
16
36
64
100
Variance,cm$^2$
L
D
I
20$^0$
30$^0$
40$^0$
60$^0$
50$^0$

Figure 43b

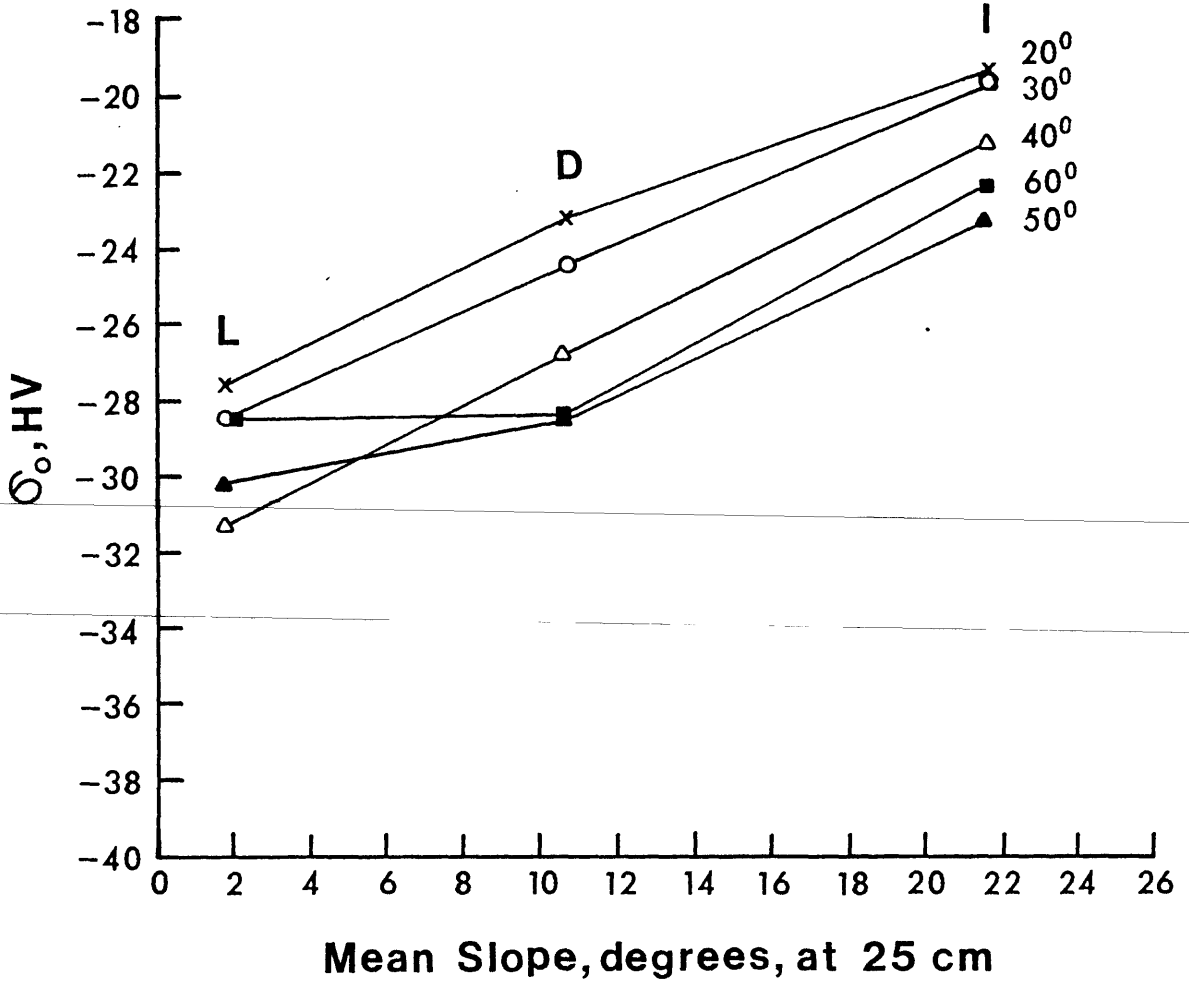
L
D
I
20⁰
30⁰
40⁰
60⁰
50⁰
−18
−20
−22
−24
−26
−28
−30
−32
−34
−36
−38
−40
σ₀, HV
0
2
4
6
8
10
12
14
16
18
20
22
24
26
Mean Slope, degrees, at 25 cm

Figure 43c

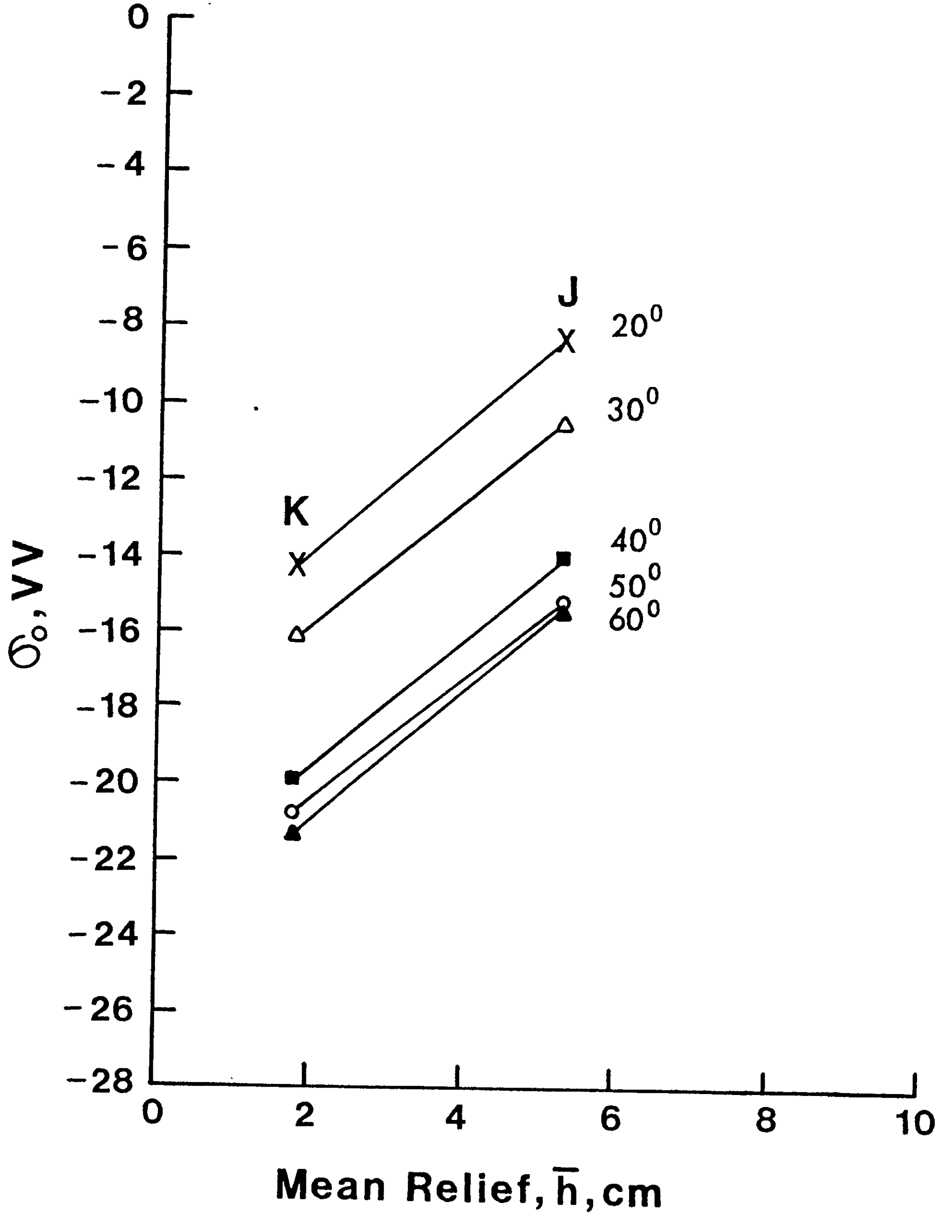
0
−2
−4
−6
−8
−10
−12
−14
−16
−18
−20
−22
−24
−26
−28
$\sigma_o$, VV
0
2
4
6
8
10
Mean Relief, $\bar{h}$, cm
K
J
$20^0$
$30^0$
$40^0$
$50^0$
$60^0$

Figure 44

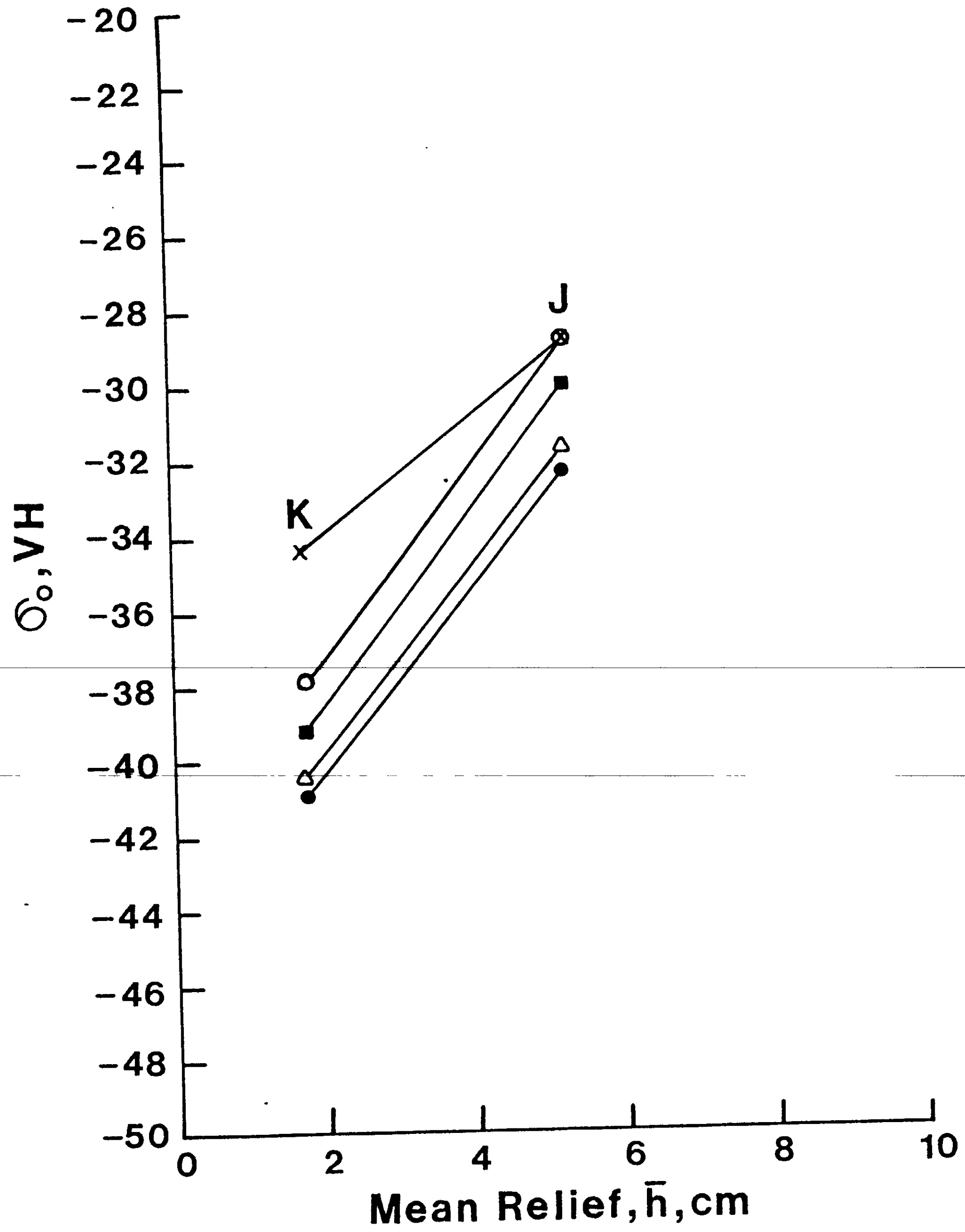
-20
-22
-24
-26
-28
-30
-32
-34
-36
-38
-40
-42
-44
-46
-48
-50
$\sigma_o$, VH
J
K
0
2
4
6
8
10
Mean Relief, $\bar{h}$, cm

Figure 45

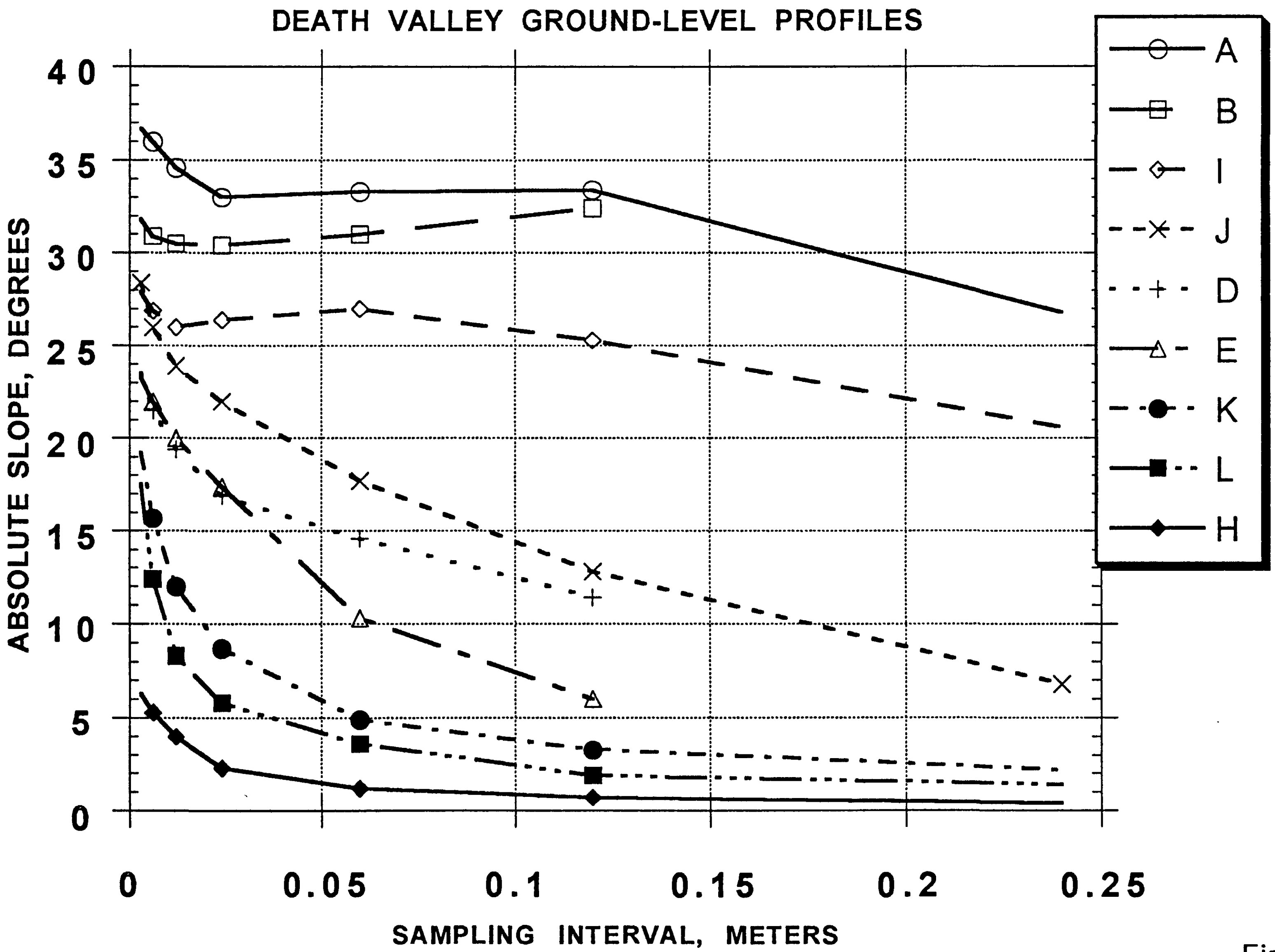
DEATH VALLEY GROUND-LEVEL PROFILES
ABSOLUTE SLOPE, DEGREES
40
35
30
25
20
15
10
5
0
0
0.05
0.1
0.15
0.2
0.25
SAMPLING INTERVAL, METERS
A
B
I
J
D
E
K
L
H

Figure 46a

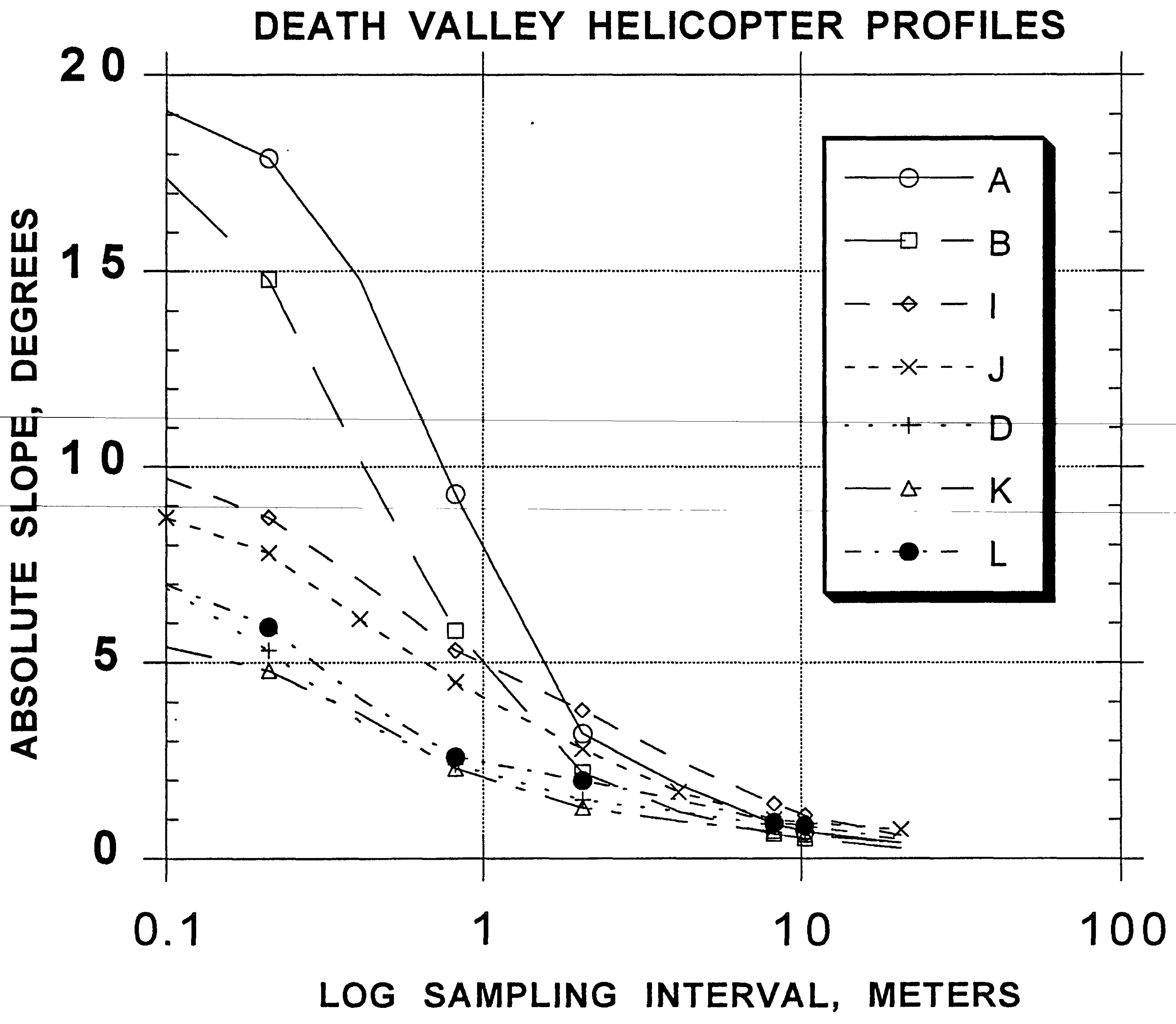
DEATH VALLEY HELICOPTER PROFILES
ABSOLUTE SLOPE, DEGREES
20
15
10
5
0
0.1
1
10
100
LOG SAMPLING INTERVAL, METERS
A
B
I
J
D
K
L

Figure 46b

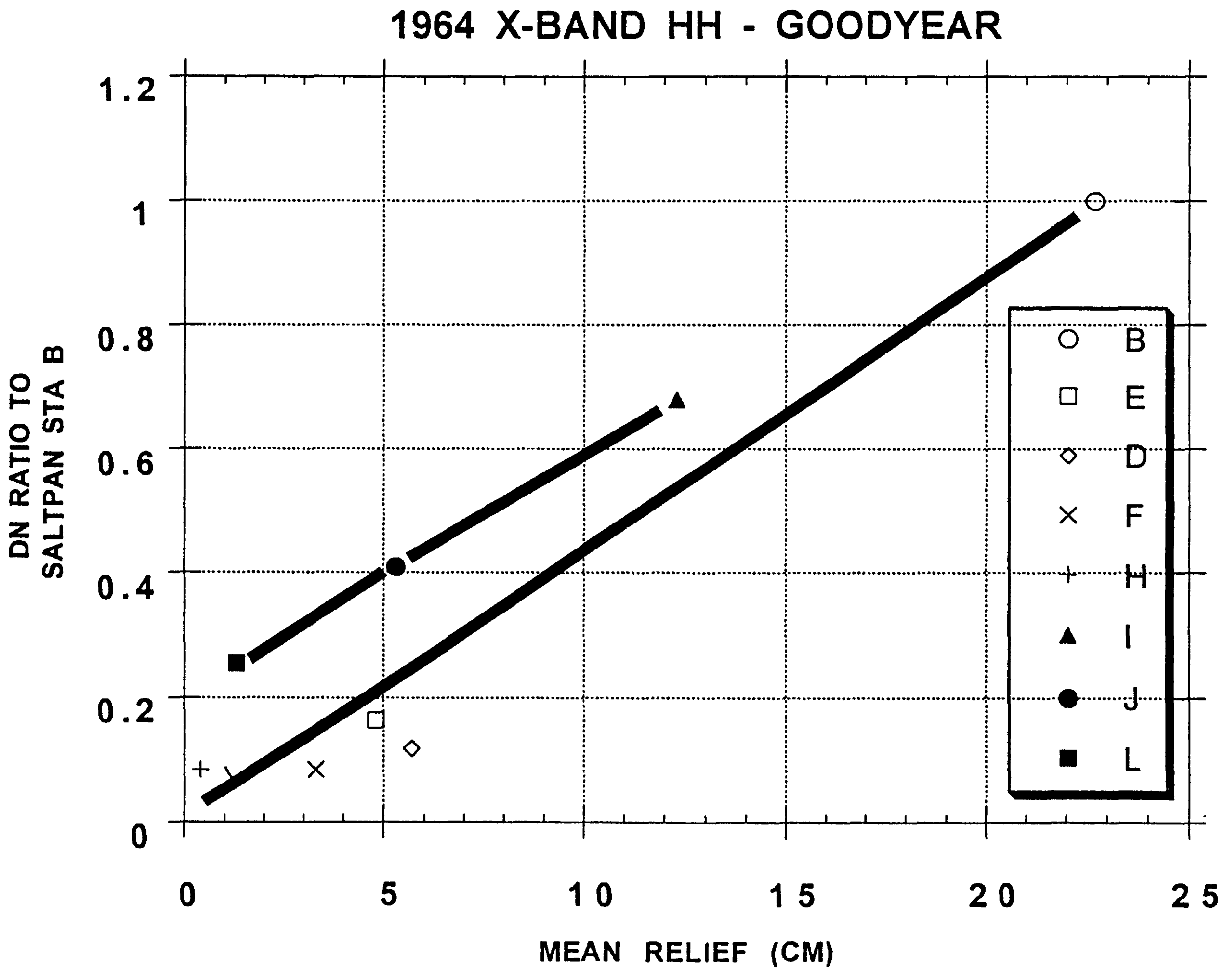
1964 X-BAND HH - GOODYEAR
DN RATIO TO SALTPAN STA B
1.2
1
0.8
0.6
0.4
0.2
0
0
5
10
15
20
25
MEAN RELIEF (CM)
○ B
□ E
◇ D
× F
+ H
▲ I
● J
■ L

Figure 47a

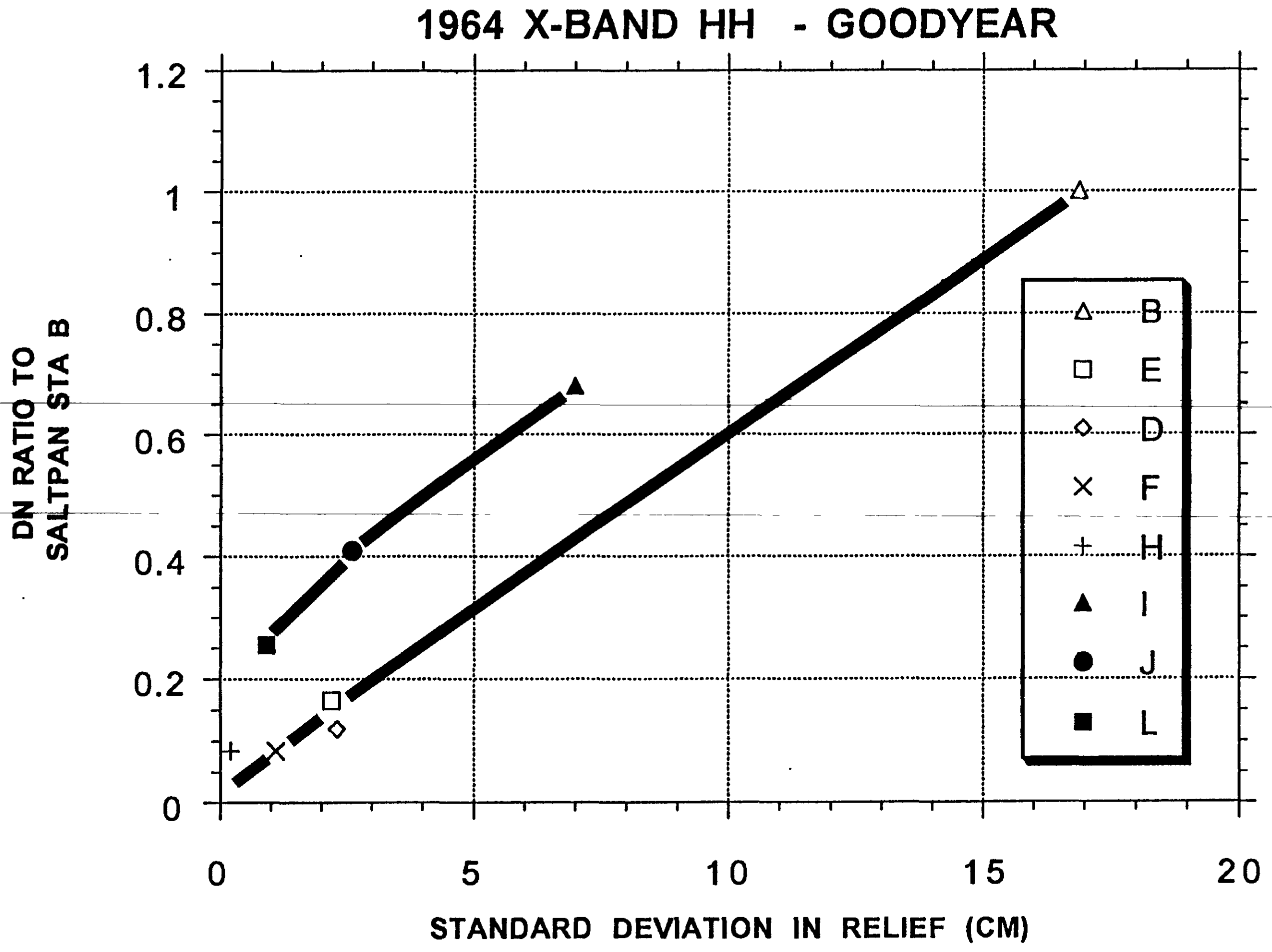
1964 X-BAND HH - GOODYEAR
DN RATIO TO SALTPAN STA B
1.2
1
0.8
0.6
0.4
0.2
0
0
5
10
15
20
STANDARD DEVIATION IN RELIEF (CM)
△ B
□ E
◇ D
× F
+ H
▲ I
● J
■ L

Figure 47b

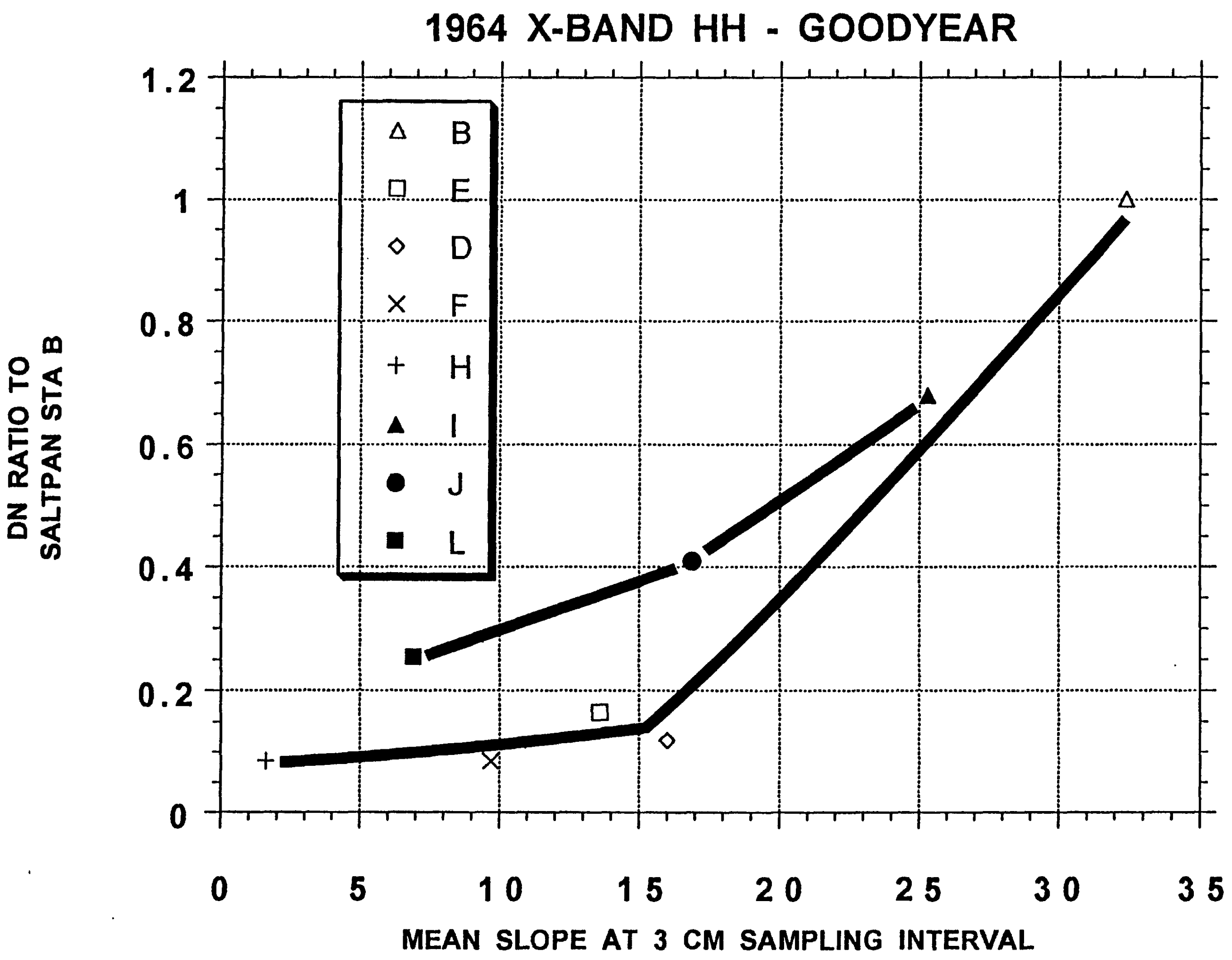
1964 X-BAND HH - GOODYEAR
DN RATIO TO
SALTPAN STA B
1.2
1
0.8
0.6
0.4
0.2
0
0
5
10
15
20
25
30
35
MEAN SLOPE AT 3 CM SAMPLING INTERVAL
△ B
□ E
◇ D
× F
+ H
▲ I
● J
■ L

Figure 47c

1976 X-BAND (HH)- GOODYEAR

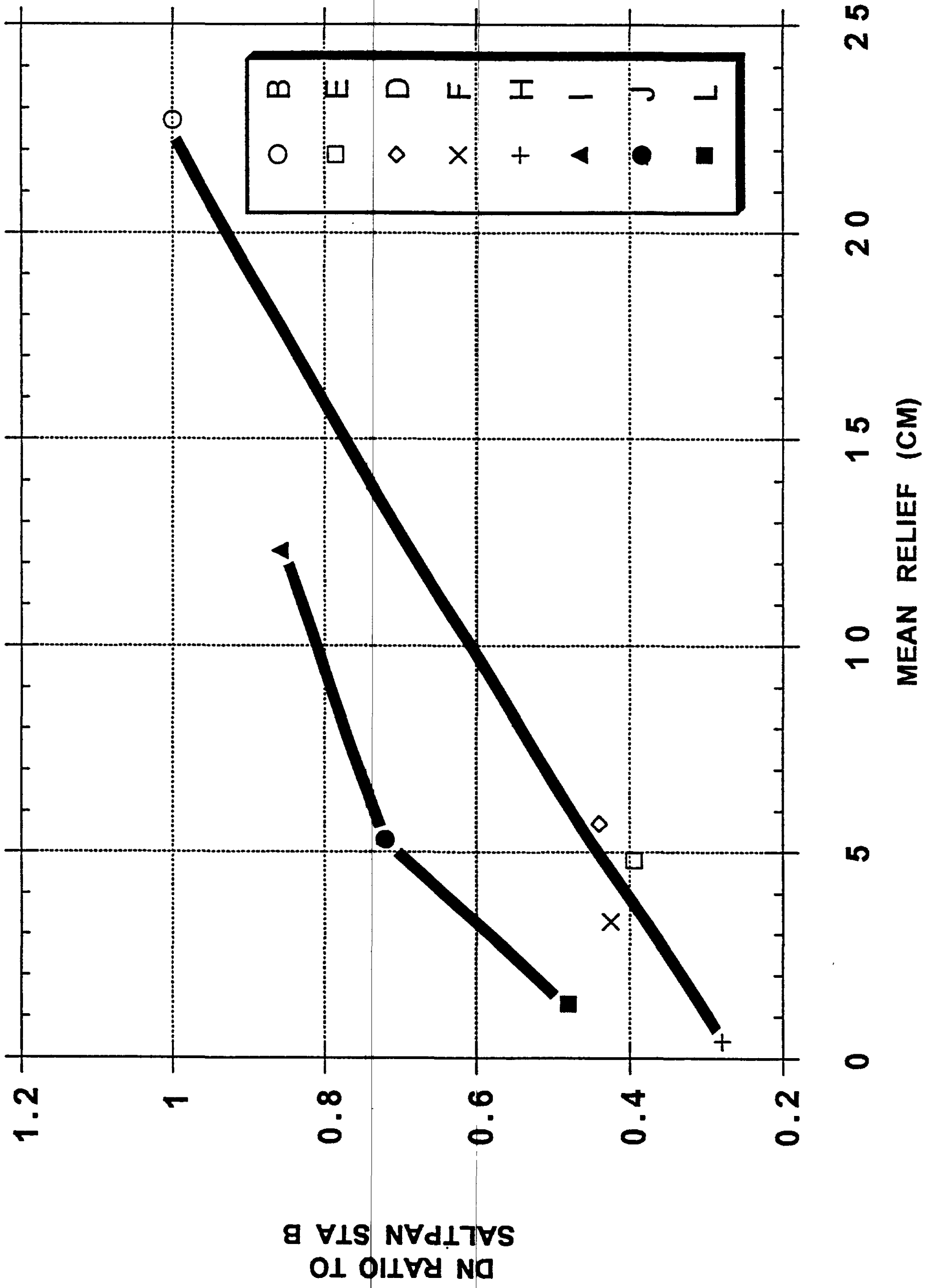

Figure 48a

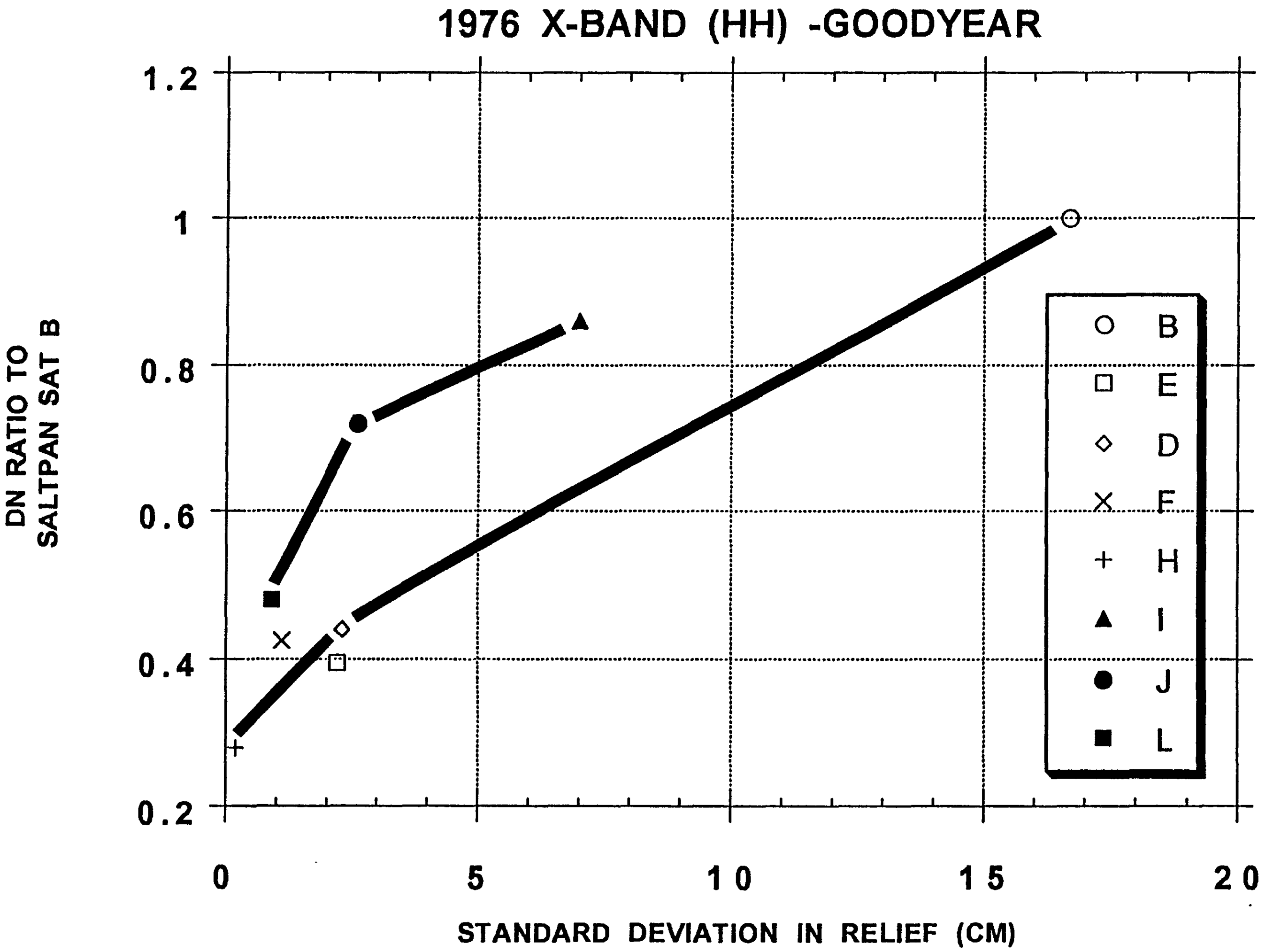
1976 X-BAND (HH) -GOODYEAR
DN RATIO TO SALTPAN SAT B
1.2
1
0.8
0.6
0.4
0.2
0
5
10
15
20
STANDARD DEVIATION IN RELIEF (CM)
○ B
□ E
◇ D
× F
+ H
▲ I
● J
■ L

Figure 48b

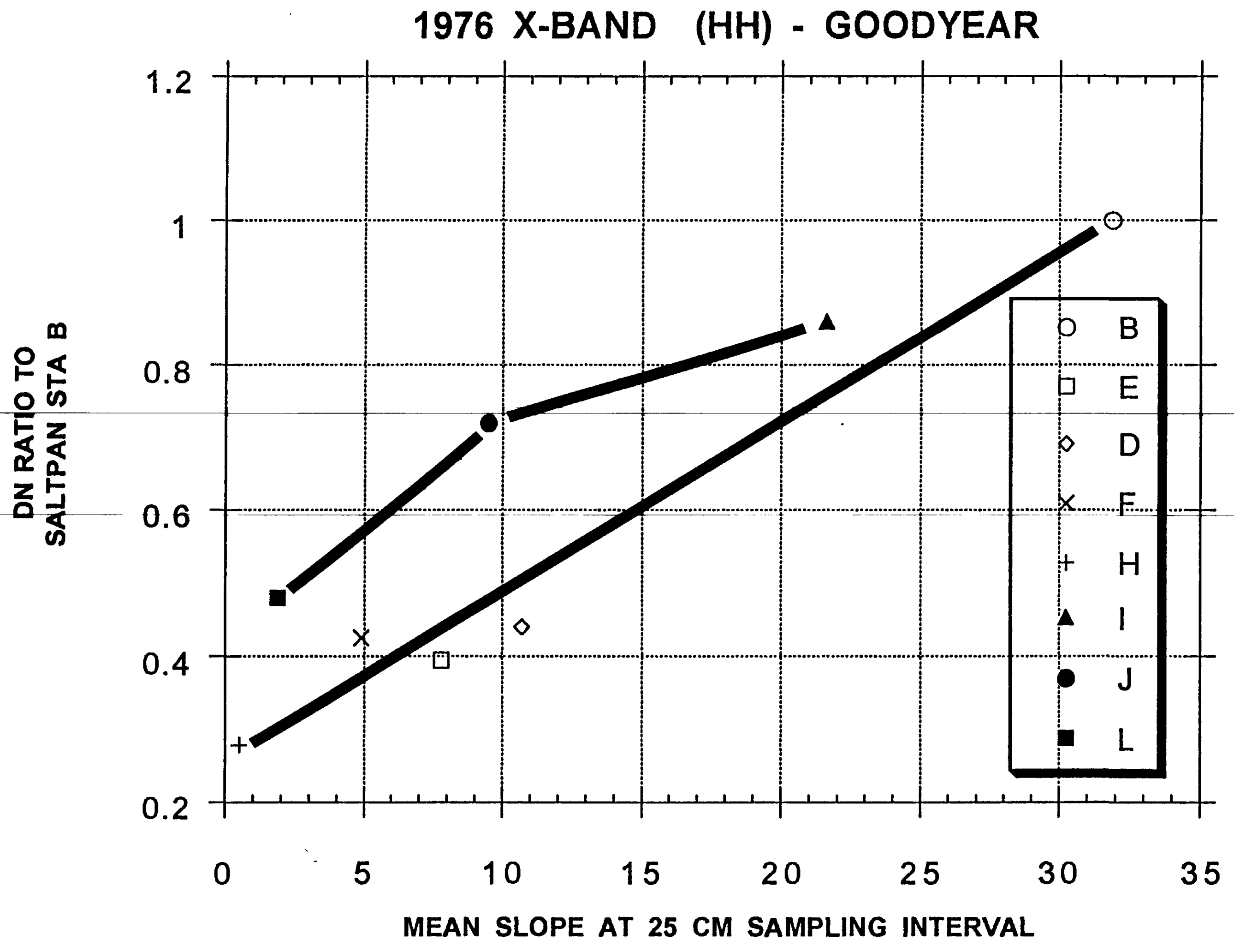
1976 X-BAND (HH) - GOODYEAR
DN RATIO TO SALTPAN STA B
1.2
1
0.8
0.6
0.4
0.2
0
5
10
15
20
25
30
35
MEAN SLOPE AT 25 CM SAMPLING INTERVAL
○ B
□ E
◇ D
× F
+ H
▲ I
● J
■ L

Figure 48c

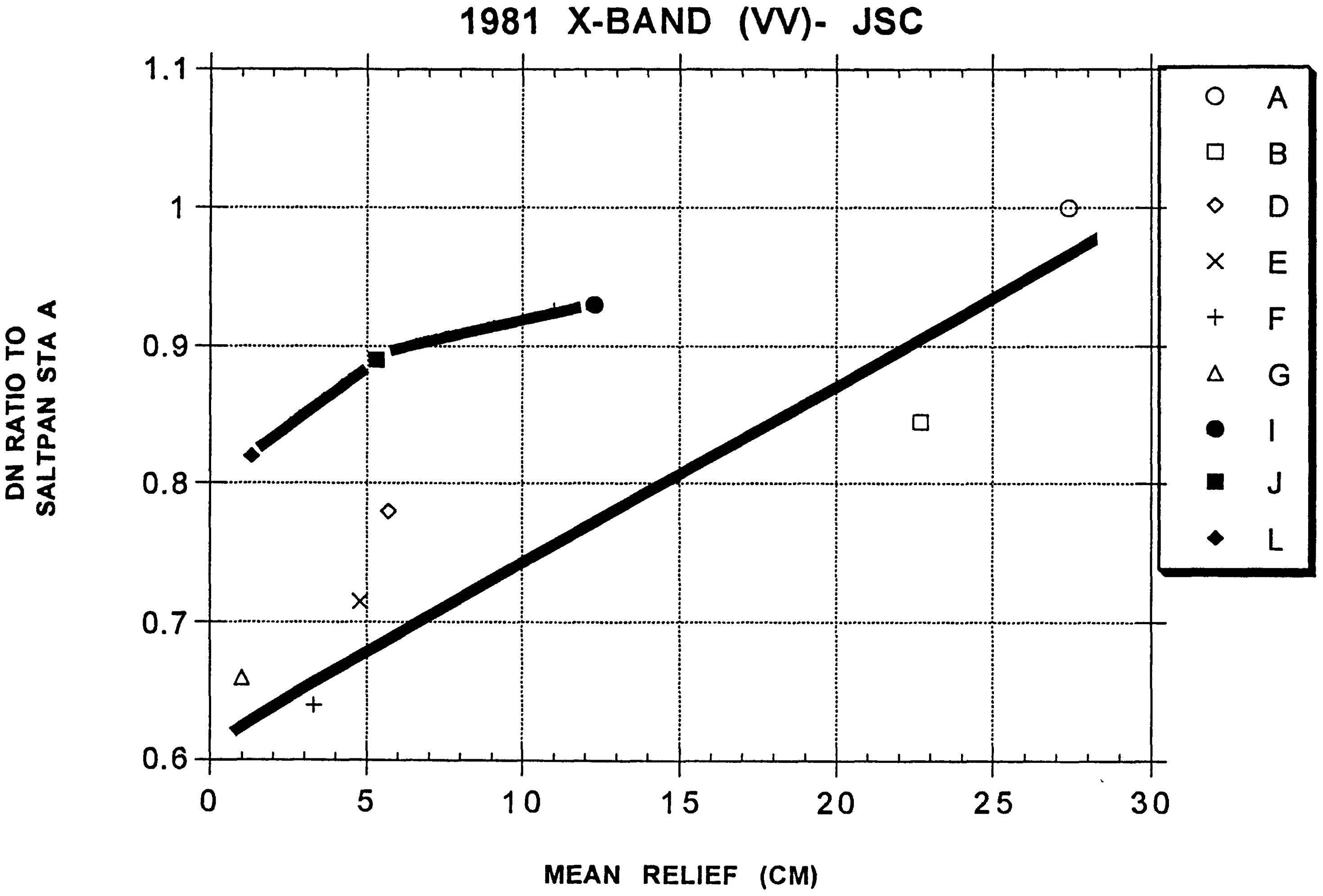
1981 X-BAND (VV)- JSC
DN RATIO TO SALTPAN STA A
1.1
1
0.9
0.8
0.7
0.6
0
5
10
15
20
25
30
MEAN RELIEF (CM)
○ A
□ B
◇ D
× E
+ F
△ G
● I
■ J
◆ L

Figure 49a

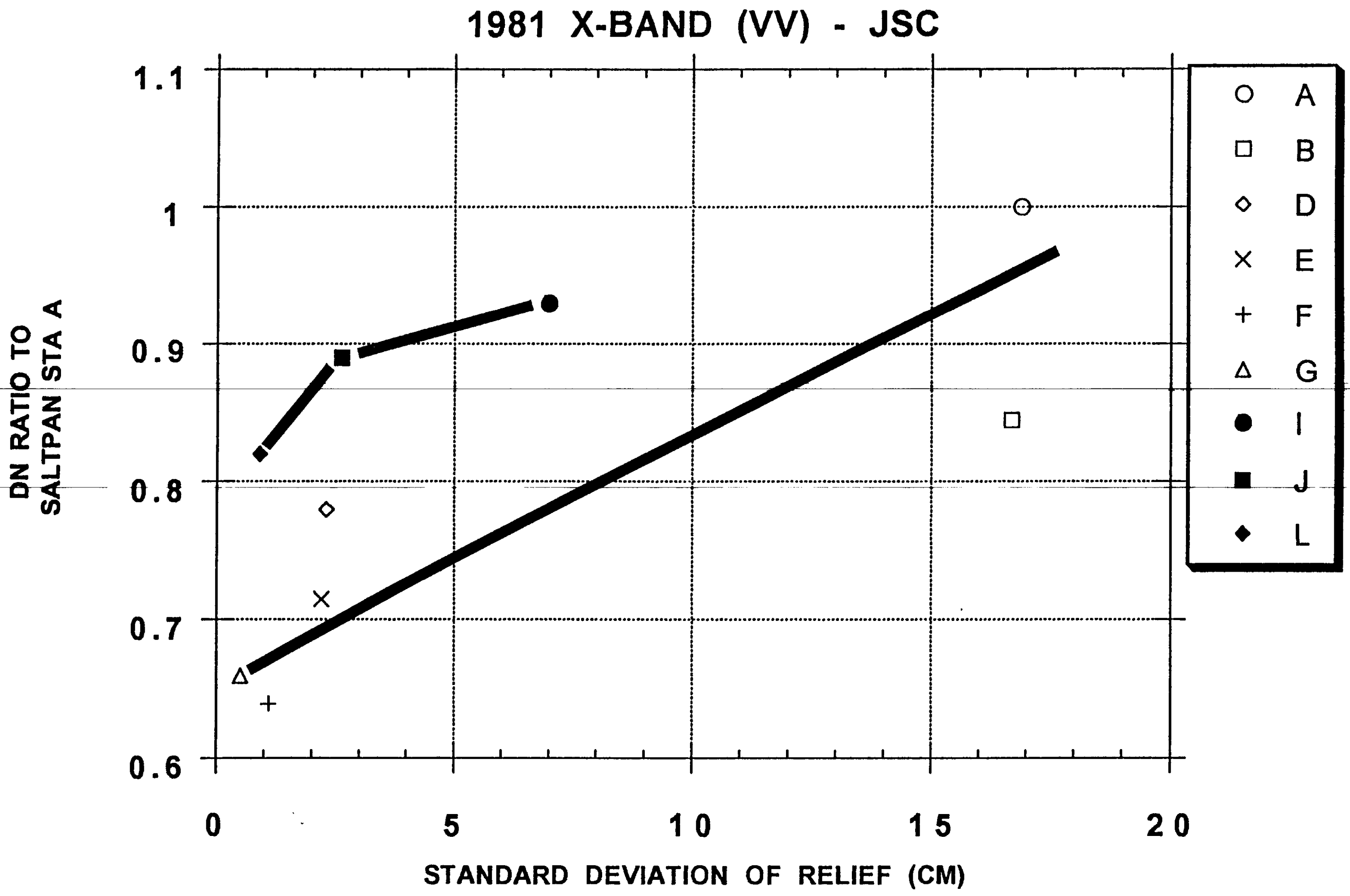
1981 X-BAND (VV) - JSC
DN RATIO TO SALTPAN STA A
1.1
1
0.9
0.8
0.7
0.6
0
5
10
15
20
STANDARD DEVIATION OF RELIEF (CM)
○ A
□ B
◇ D
× E
+ F
△ G
● I
■ J
◆ L

Figure 49b

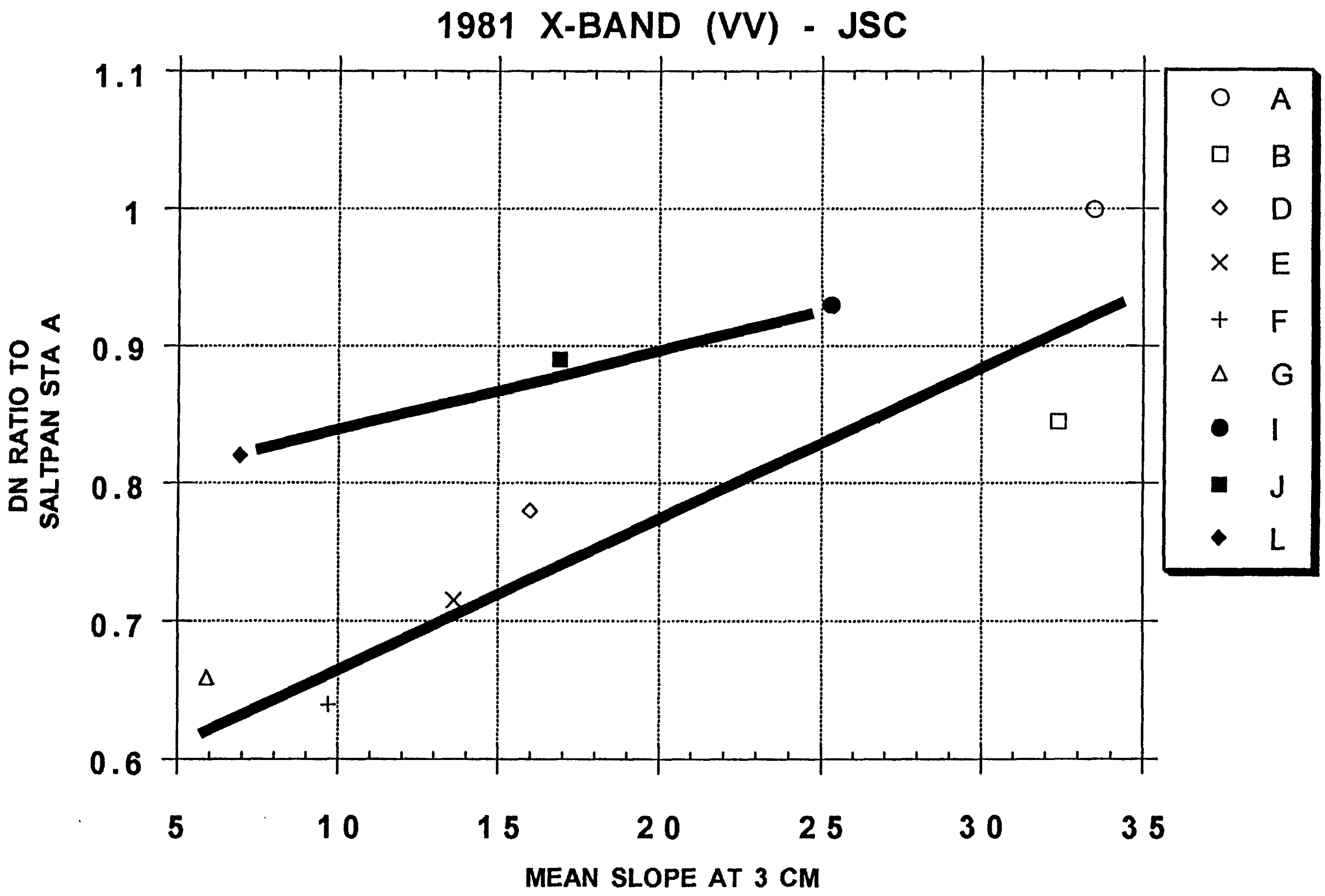
1981 X-BAND (VV) - JSC
DN RATIO TO SALTPAN STA A
1.1
1
0.9
0.8
0.7
0.6
5
10
15
20
25
30
35
MEAN SLOPE AT 3 CM
○ A
□ B
◇ D
× E
+ F
△ G
● I
■ J
◆ L

Figure 49c

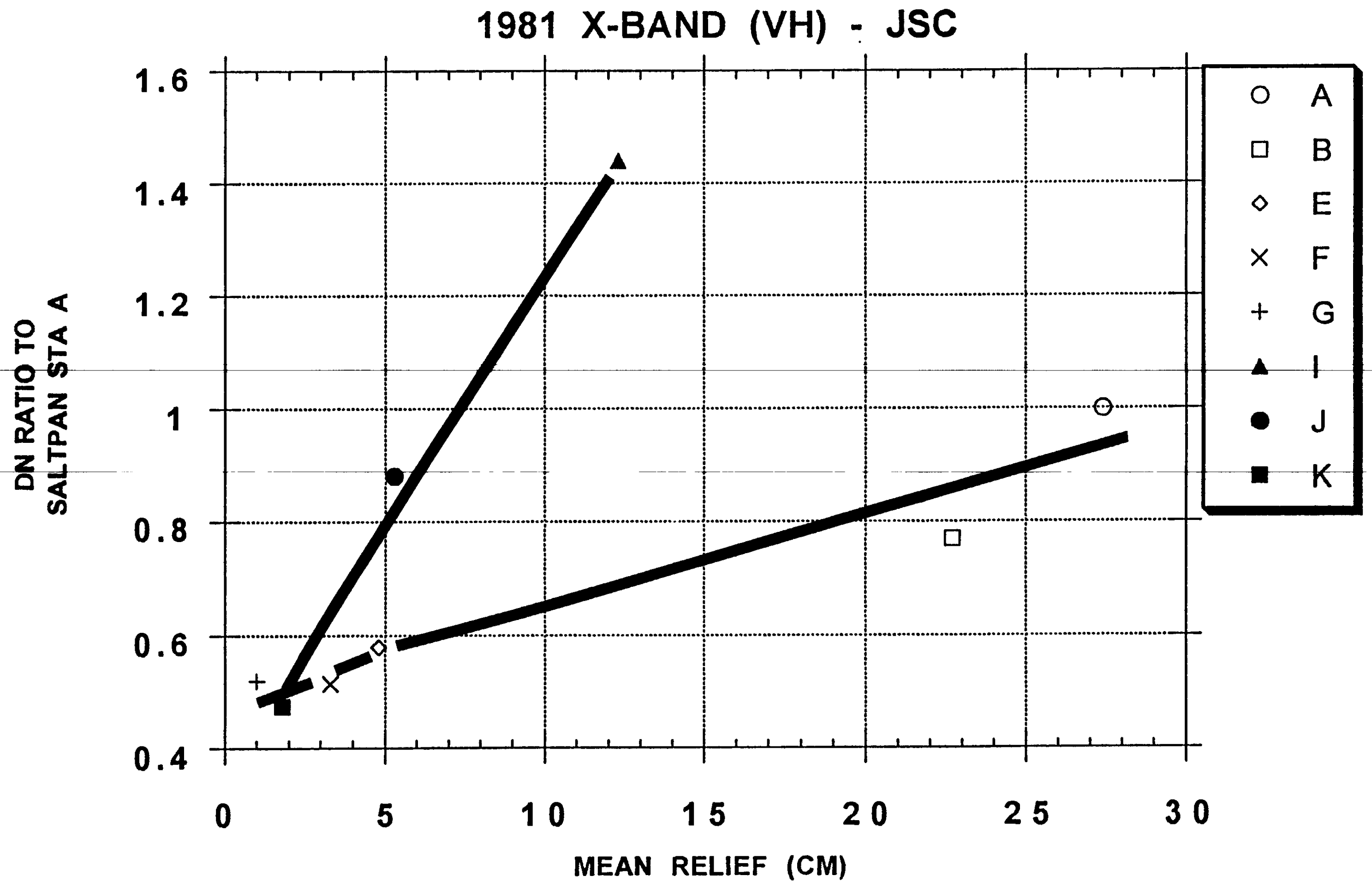
1981 X-BAND (VH) - JSC
DN RATIO TO SALTPAN STA A
1.6
1.4
1.2
1
0.8
0.6
0.4
0
5
10
15
20
25
30
MEAN RELIEF (CM)
○ A
□ B
◇ E
× F
+ G
▲ I
● J
■ K

Figure 49d

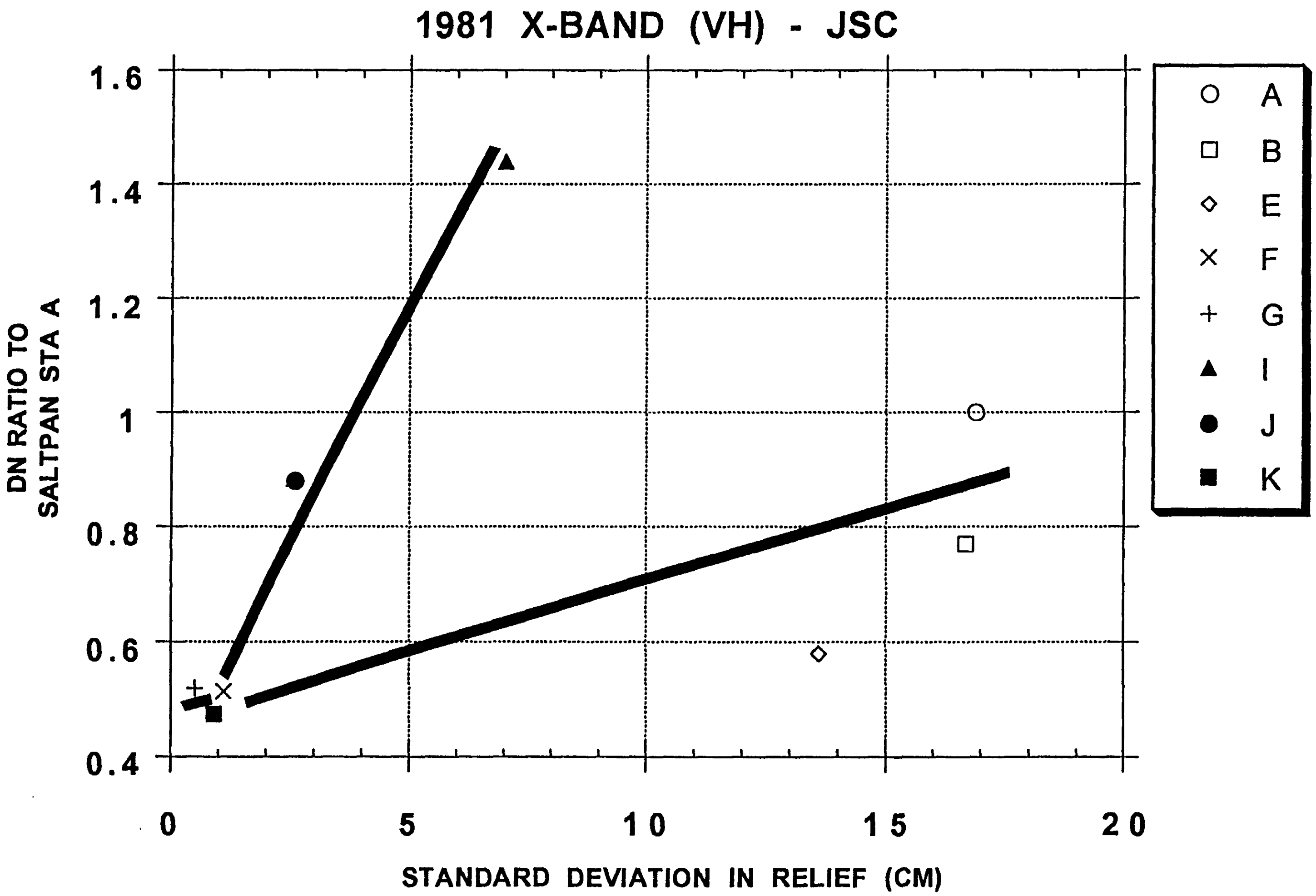
1981 X-BAND (VH) - JSC
DN RATIO TO SALTPAN STA A
1.6
1.4
1.2
1
0.8
0.6
0.4
0
5
10
15
20
STANDARD DEVIATION IN RELIEF (CM)
○ A
□ B
◇ E
× F
+ G
▲ I
● J
■ K

Figure 49e

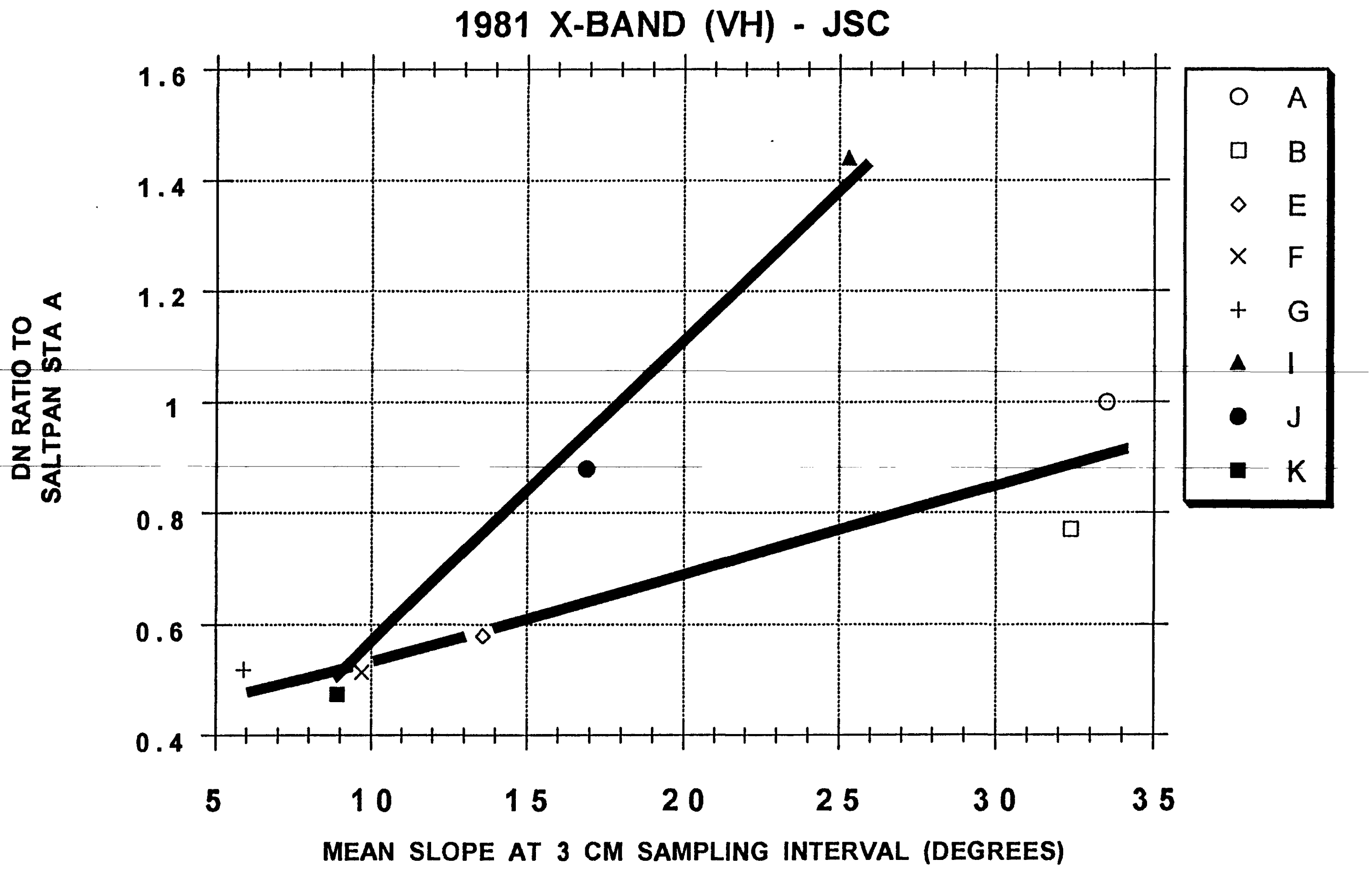

1981 X-BAND (VH) - JSC

Figure 49f

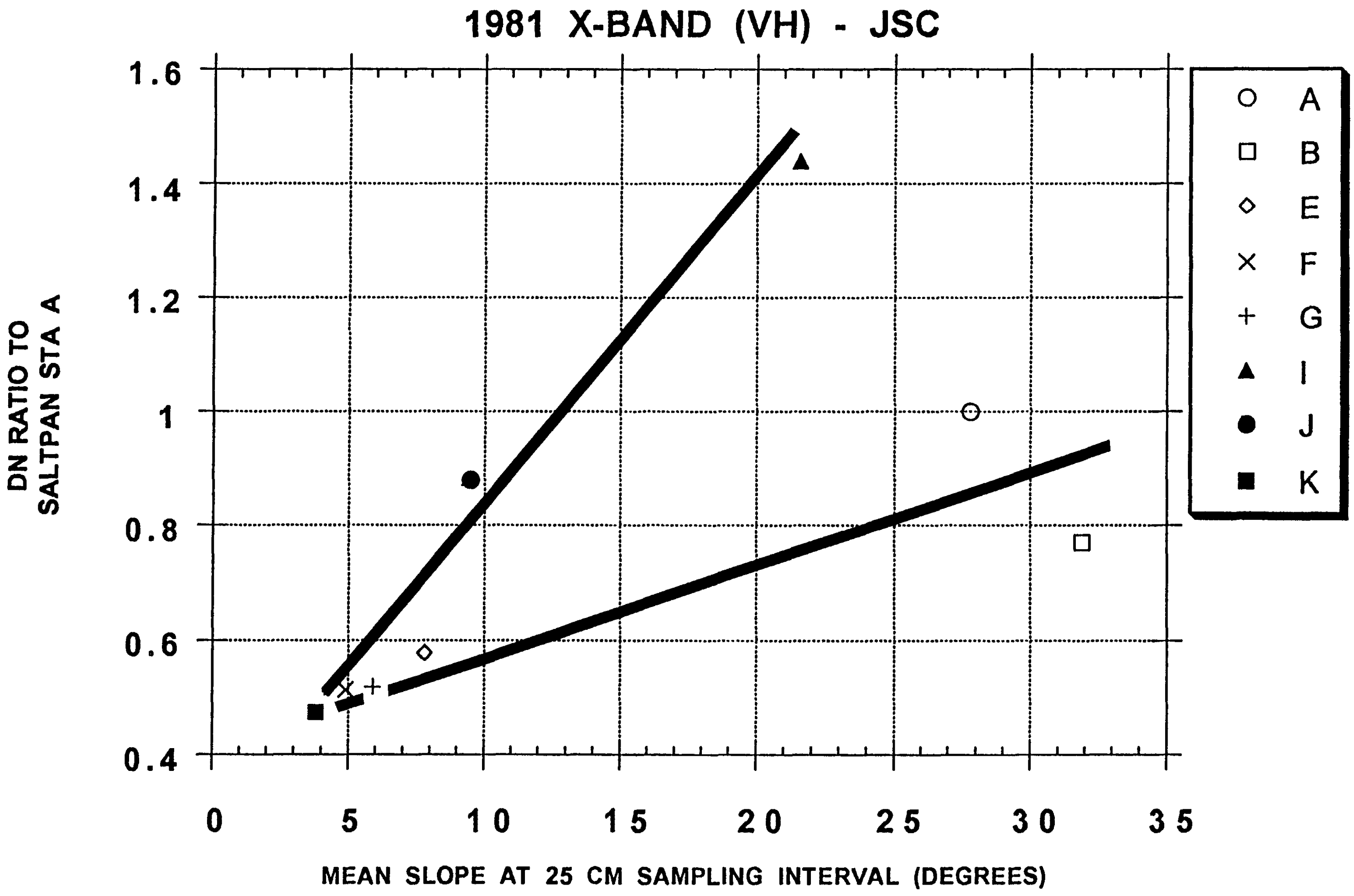
1981 X-BAND (VH) - JSC
DN RATIO TO SALTPAN STA A
1.6
1.4
1.2
1
0.8
0.6
0.4
0
5
10
15
20
25
30
35
MEAN SLOPE AT 25 CM SAMPLING INTERVAL (DEGREES)
○ A
□ B
◇ E
× F
+ G
▲ I
● J
■ K

Figure 49g

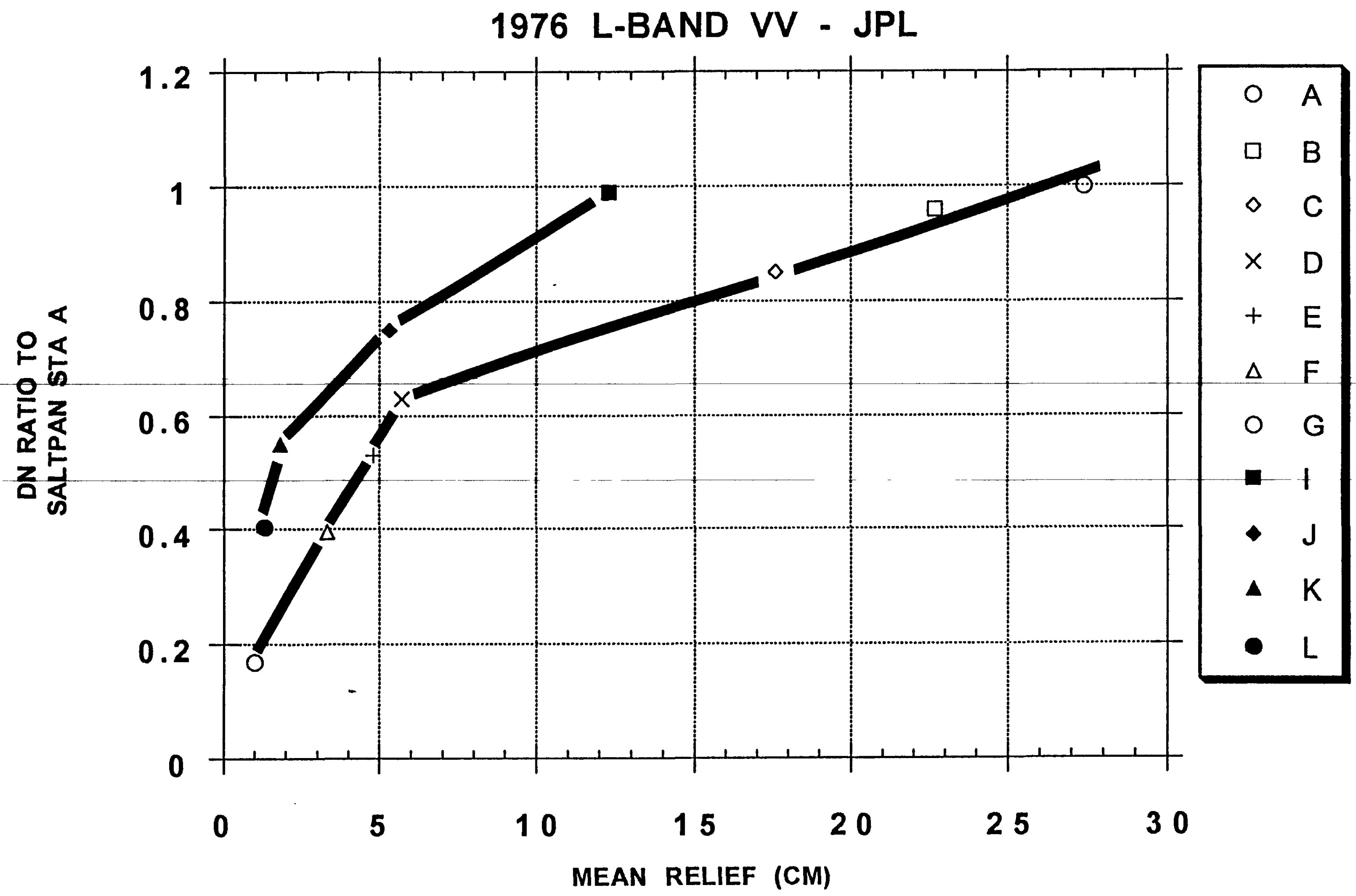
1976 L-BAND VV - JPL
DN RATIO TO SALTPAN STA A
1.2
1
0.8
0.6
0.4
0.2
0
0
5
10
15
20
25
30
MEAN RELIEF (CM)
○ A
□ B
◇ C
× D
+ E
△ F
○ G
■ I
◆ J
▲ K
● L

Figure 50a

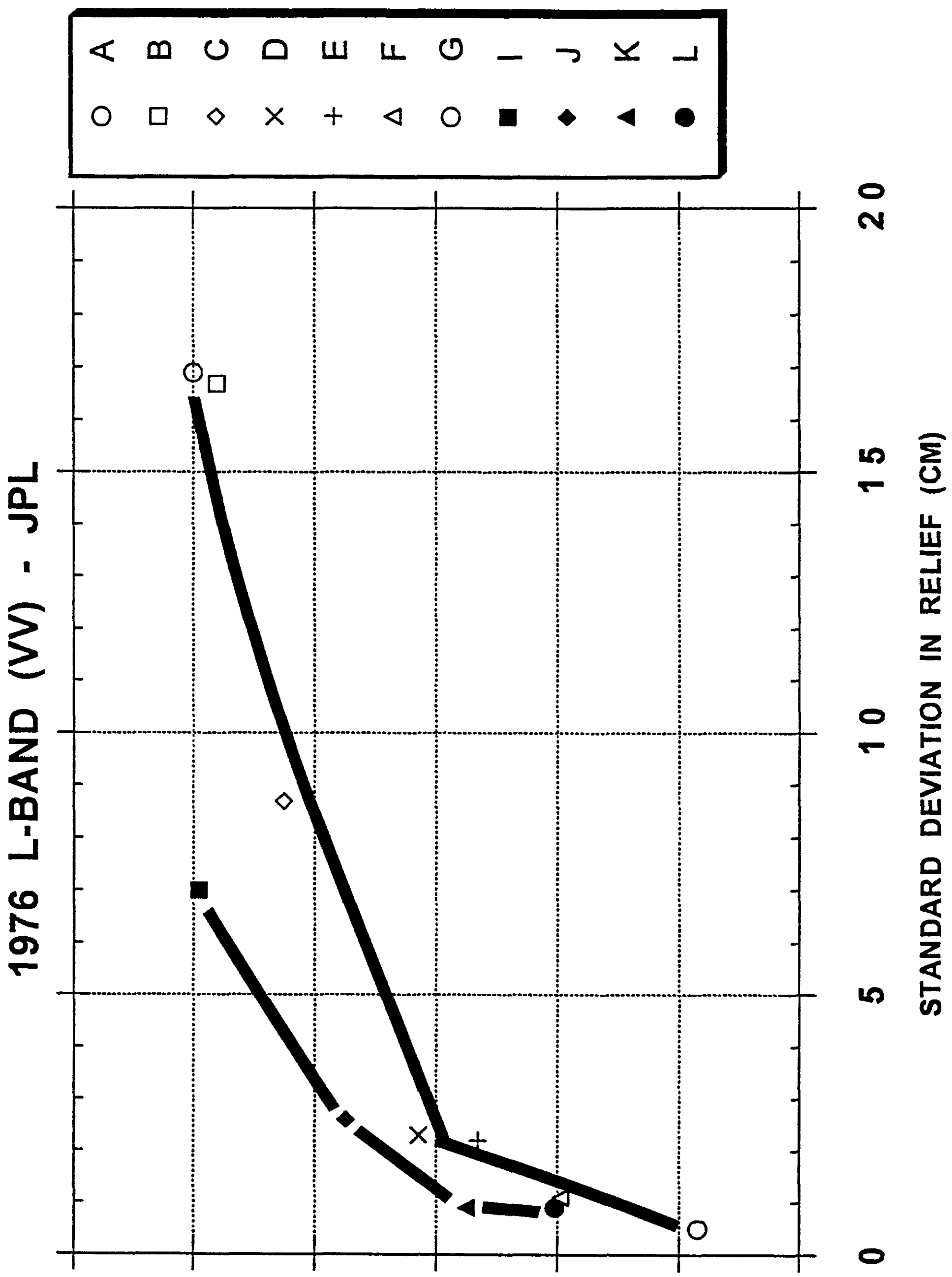
1976 L-BAND (VV) - JPL
DN RATIO TO SALTPAN STA A
1.2
1
0.8
0.6
0.4
0.2
0
0
5
10
15
20
STANDARD DEVIATION IN RELIEF (CM)
○ A
□ B
◇ C
× D
+ E
△ F
○ G
■ I
◆ J
▲ K
● L

Figure 50b

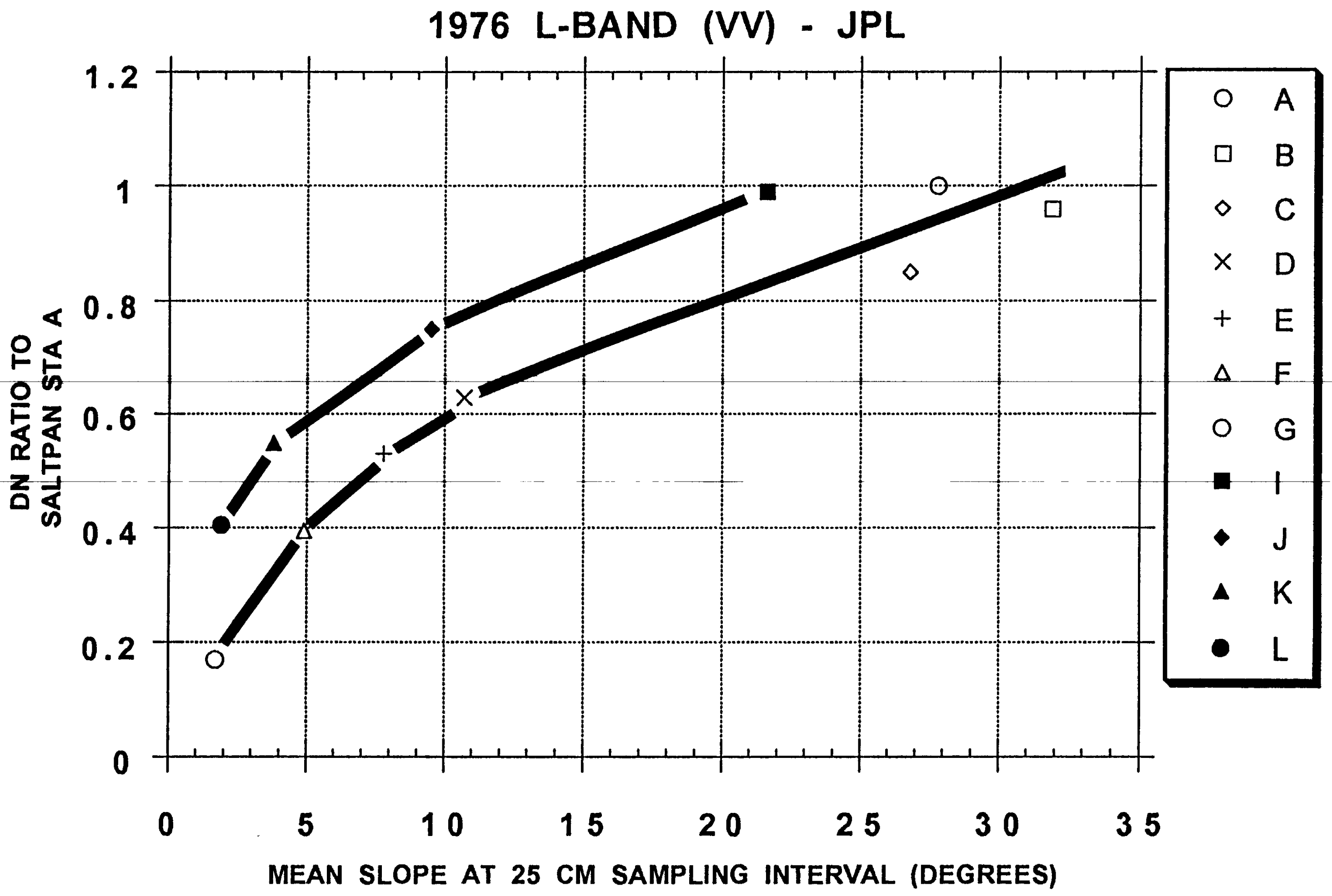
1976 L-BAND (VV) - JPL
DN RATIO TO SALTPAN STA A
1.2
1
0.8
0.6
0.4
0.2
0
0
5
10
15
20
25
30
35
MEAN SLOPE AT 25 CM SAMPLING INTERVAL (DEGREES)
○ A
□ B
◇ C
× D
+ E
△ F
○ G
■ I
◆ J
▲ K
● L

Figure 50c

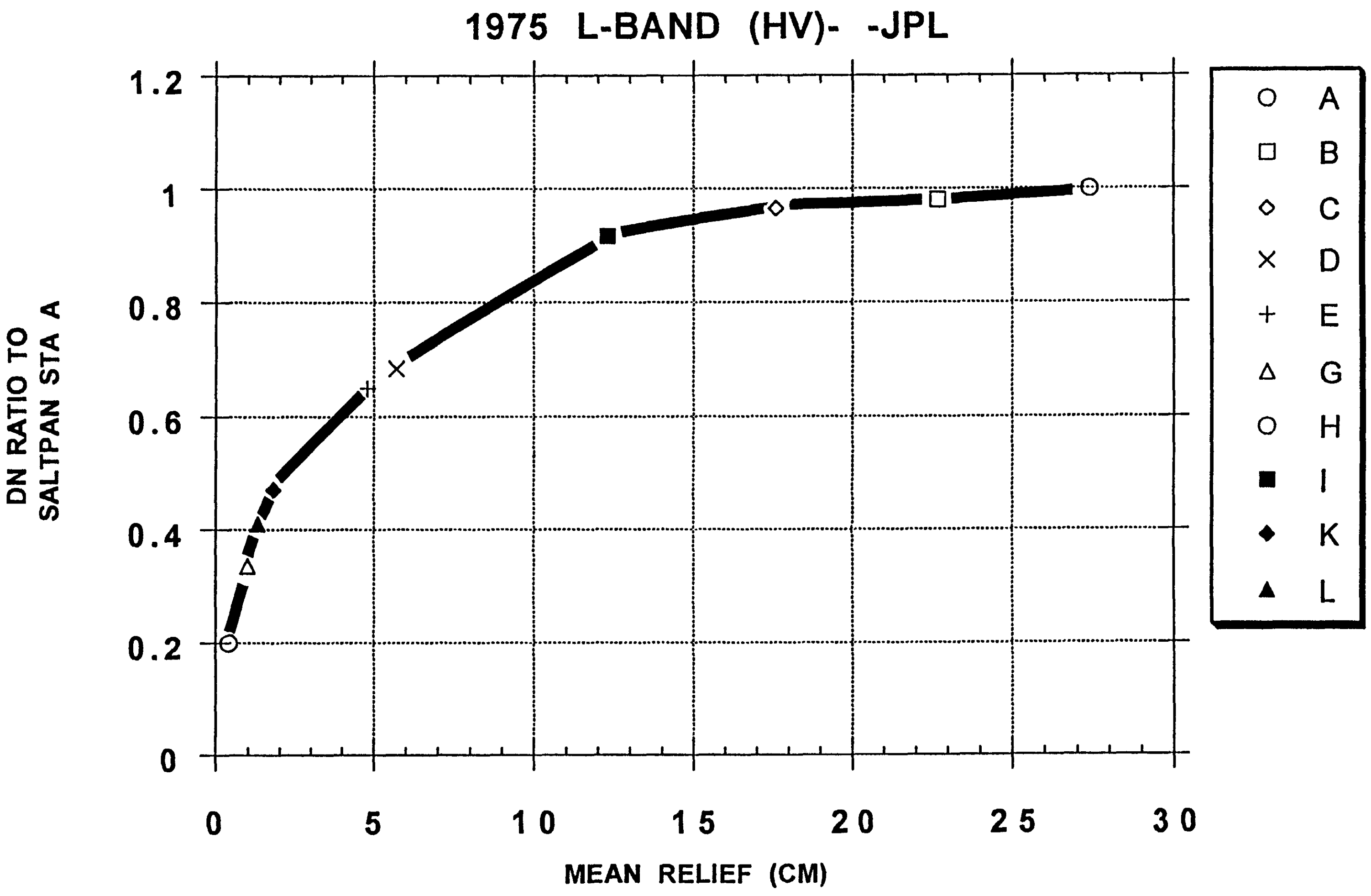
1975 L-BAND (HV)- -JPL
DN RATIO TO SALTPAN STA A
1.2
1
0.8
0.6
0.4
0.2
0
0
5
10
15
20
25
30
MEAN RELIEF (CM)
○ A
□ B
◇ C
× D
+ E
△ G
○ H
■ I
◆ K
▲ L

Figure 51a

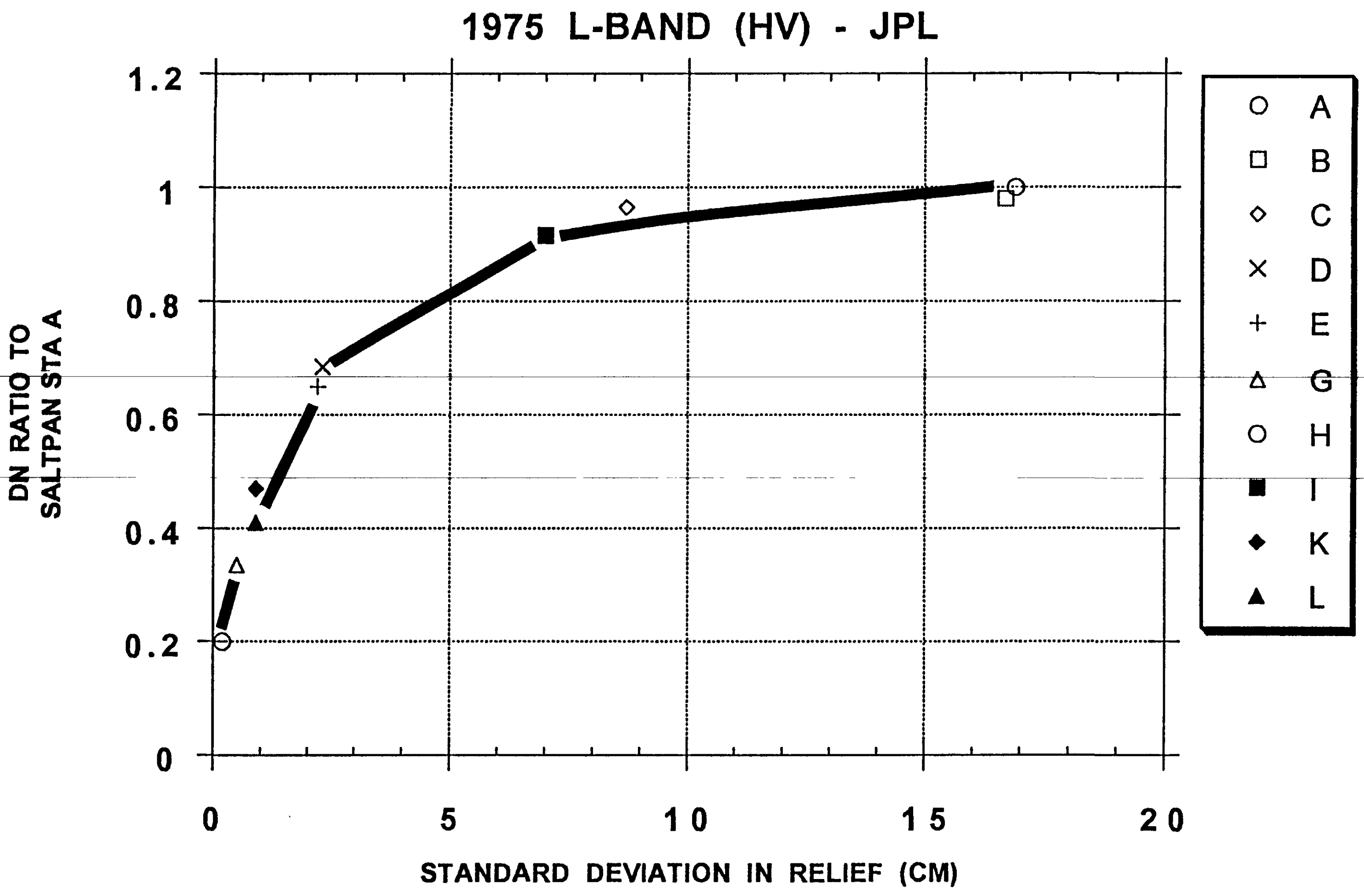
1975 L-BAND (HV) - JPL
DN RATIO TO SALTPAN STA A
1.2
1
0.8
0.6
0.4
0.2
0
0
5
10
15
20
STANDARD DEVIATION IN RELIEF (CM)
○ A
□ B
◇ C
× D
+ E
△ G
○ H
■ I
◆ K
▲ L

Figure 51b

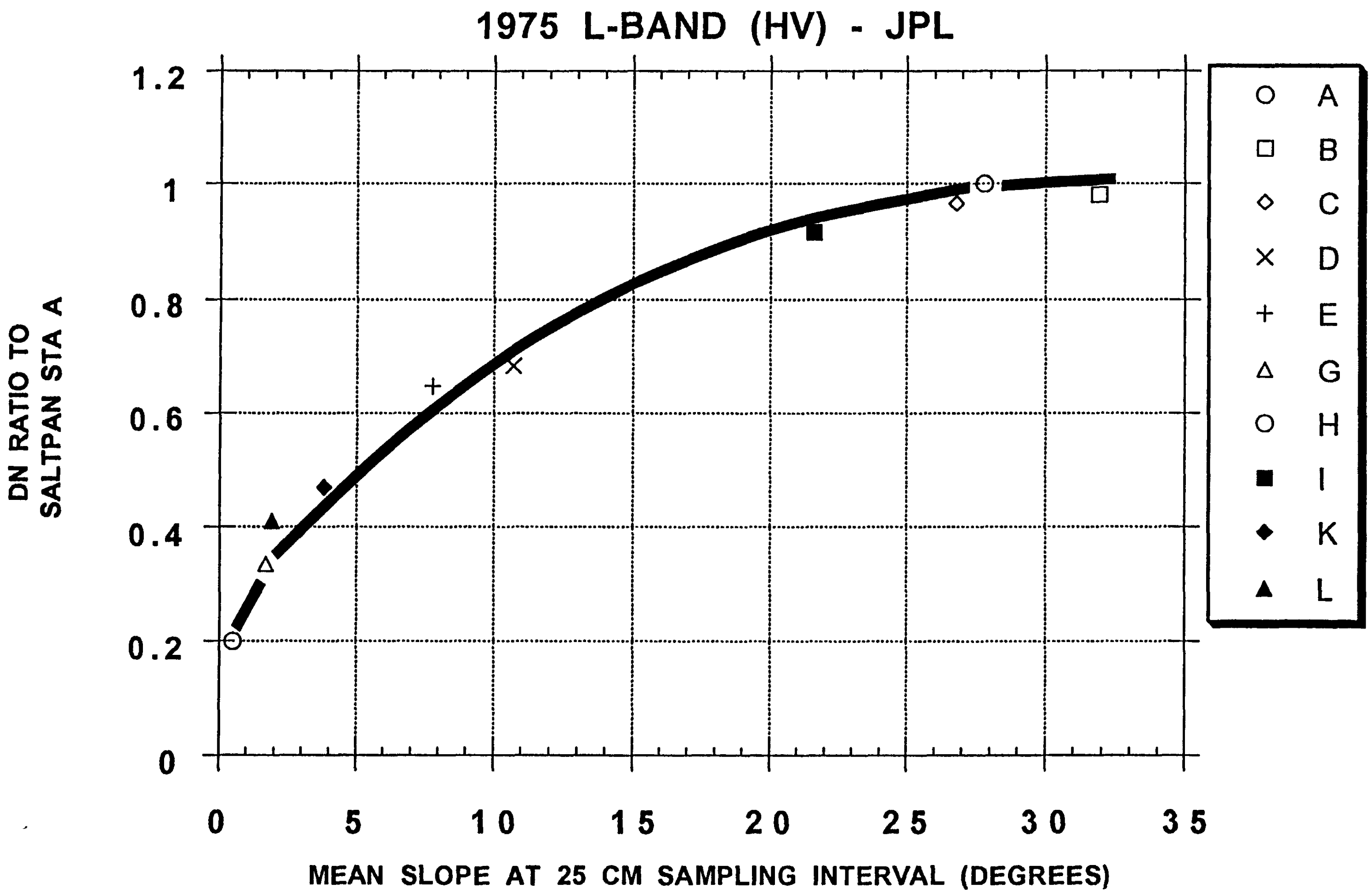
1975 L-BAND (HV) - JPL
DN RATIO TO SALTPAN STA A
1.2
1
0.8
0.6
0.4
0.2
0
0
5
10
15
20
25
30
35
MEAN SLOPE AT 25 CM SAMPLING INTERVAL (DEGREES)
○ A
□ B
◇ C
× D
+ E
△ G
○ H
■ I
◆ K
▲ L

Figure 51c

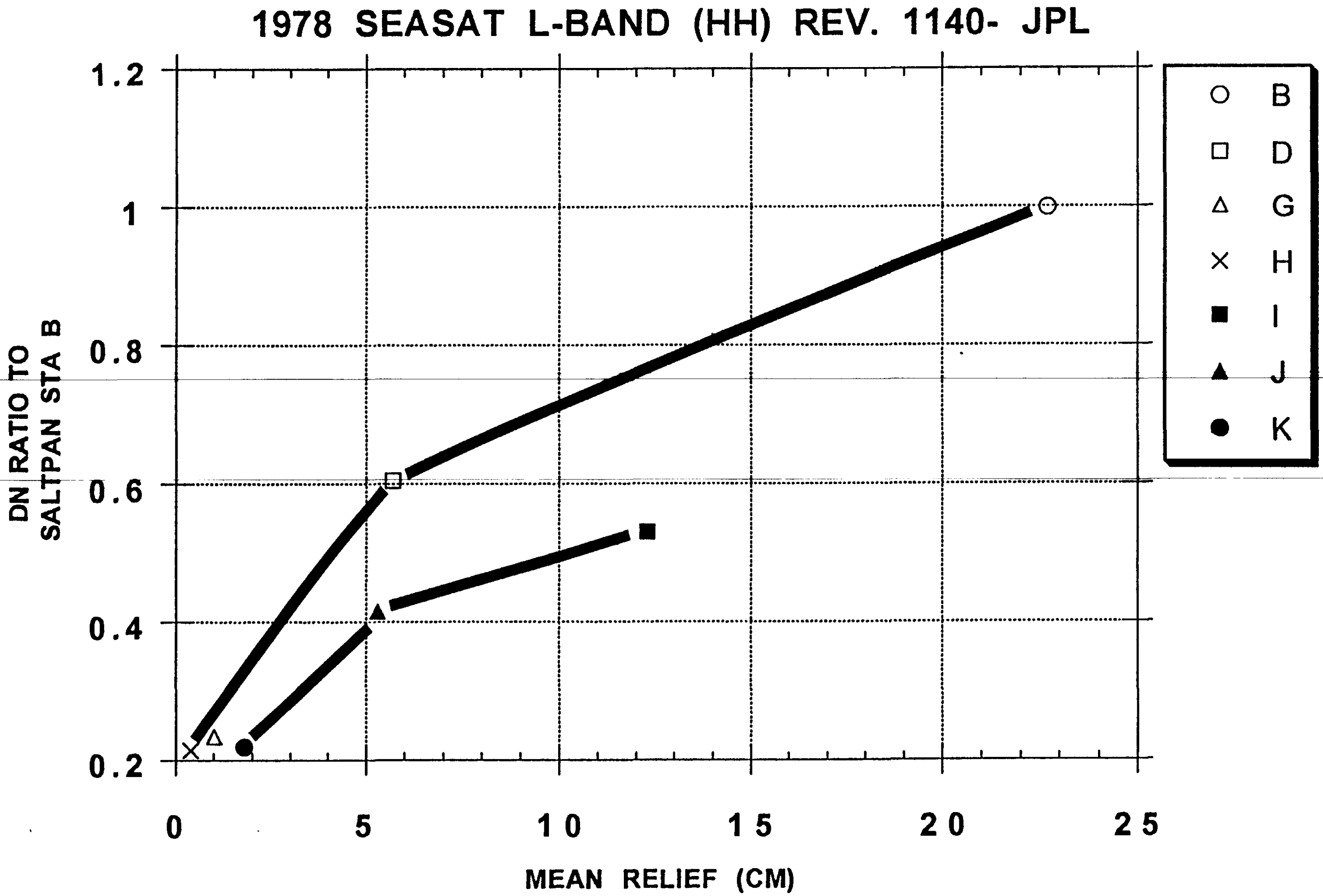
1978 SEASAT L-BAND (HH) REV. 1140- JPL
DN RATIO TO SALTPAN STA B
1.2
1
0.8
0.6
0.4
0.2
0
5
10
15
20
25
MEAN RELIEF (CM)
○ B
□ D
△ G
× H
■ I
▲ J
● K

Figure 52a

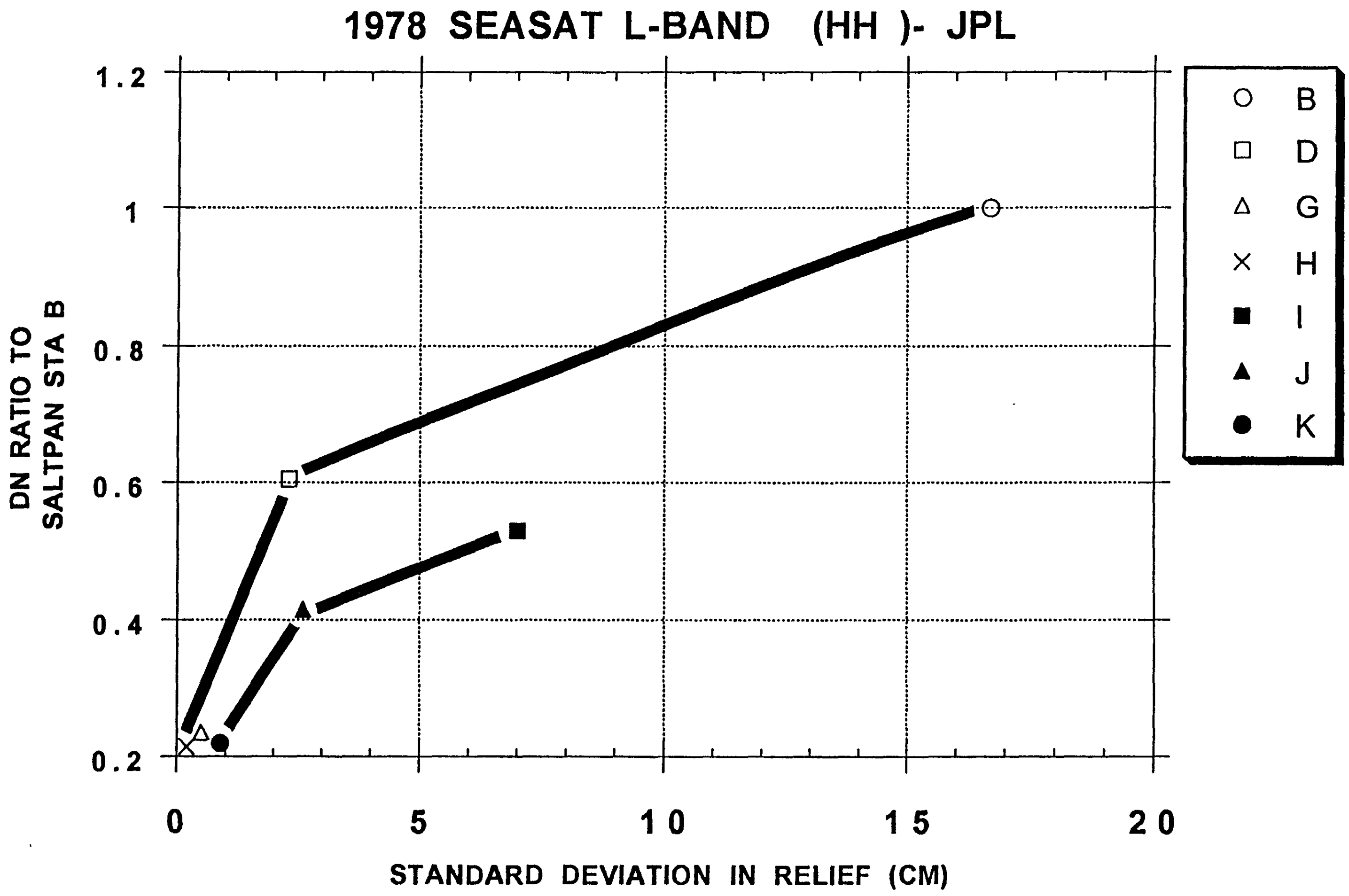
1978 SEASAT L-BAND (HH )- JPL
DN RATIO TO SALTPAN STA B
1.2
1
0.8
0.6
0.4
0.2
0
5
10
15
20
STANDARD DEVIATION IN RELIEF (CM)
○ B
□ D
△ G
× H
■ I
▲ J
● K

Figure 52b

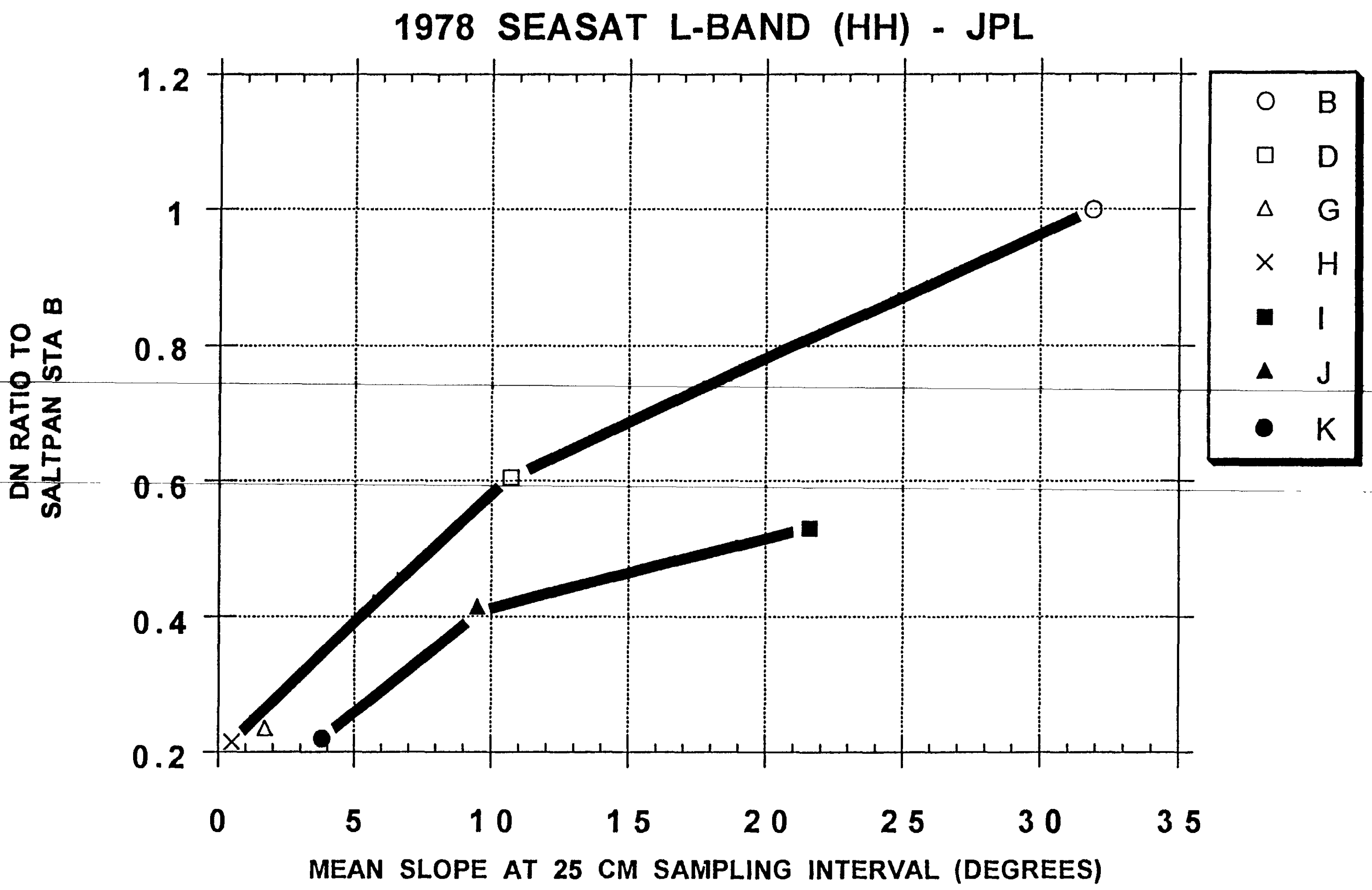
1978 SEASAT L-BAND (HH) - JPL
DN RATIO TO SALTPAN STA B
1.2
1
0.8
0.6
0.4
0.2
0
5
10
15
20
25
30
35
MEAN SLOPE AT 25 CM SAMPLING INTERVAL (DEGREES)
○ B
□ D
△ G
× H
■ I
▲ J
● K

Figure 52c

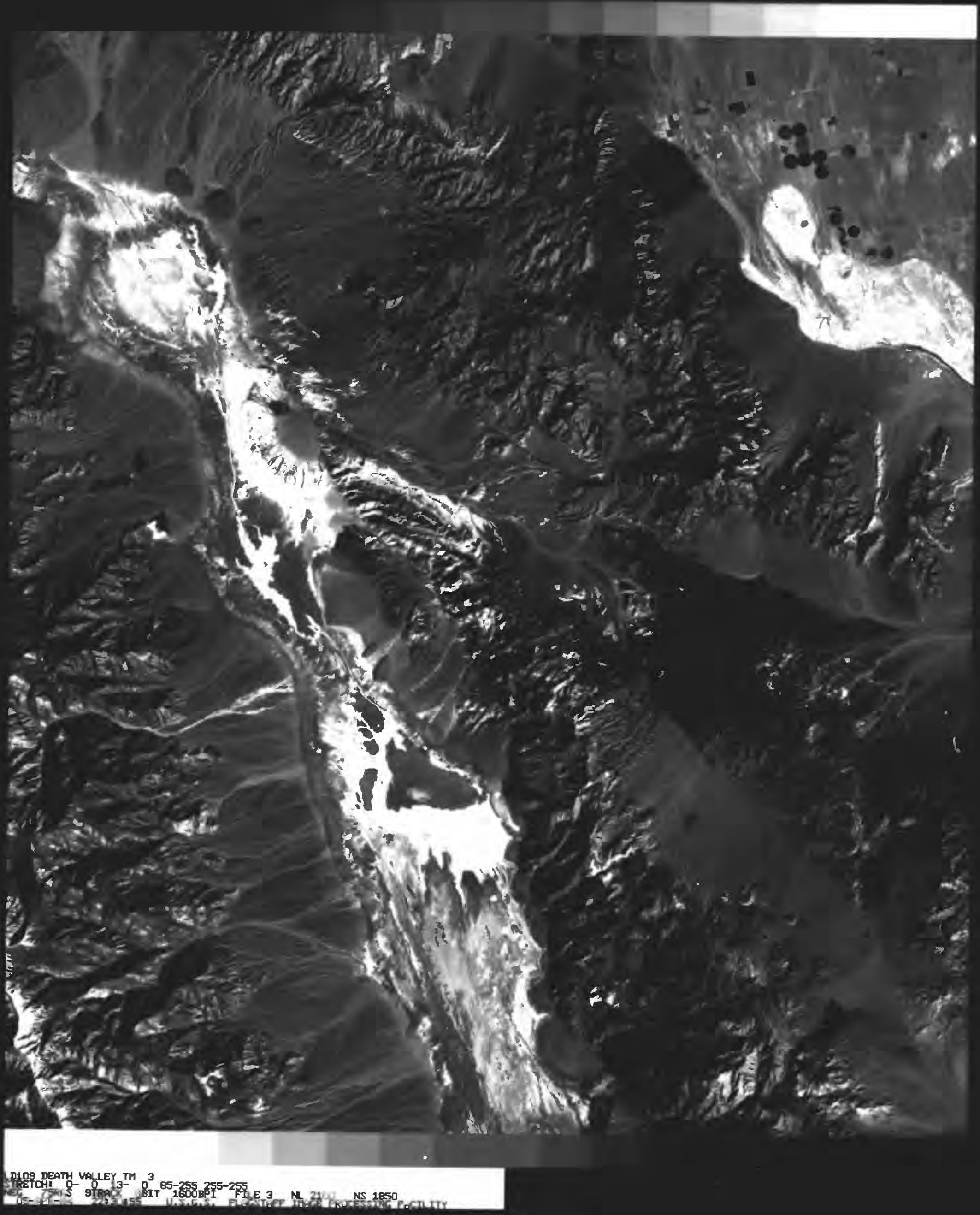
LD109 DEATH VALLEY TM 3
STRETCH: 0- 0 13- 0 85-255 255-255
9TRACK BIT 1600BPI FILE 3 NL NS 1850
U.S.G.S. FLAGSTAFF IMAGE PROCESSING FACILITY

Figure 53a


D109 DEATH VALLEY TM 5
STRETCH: 0- 0 4- 0 136-255 255-255
NEG 9TRACK 8BIT 1600BPI FILE 5 NL NS 1850
U.S.G.S. FLAGSTAFF IMAGE PROCESSING FACILITY

Figure 53b

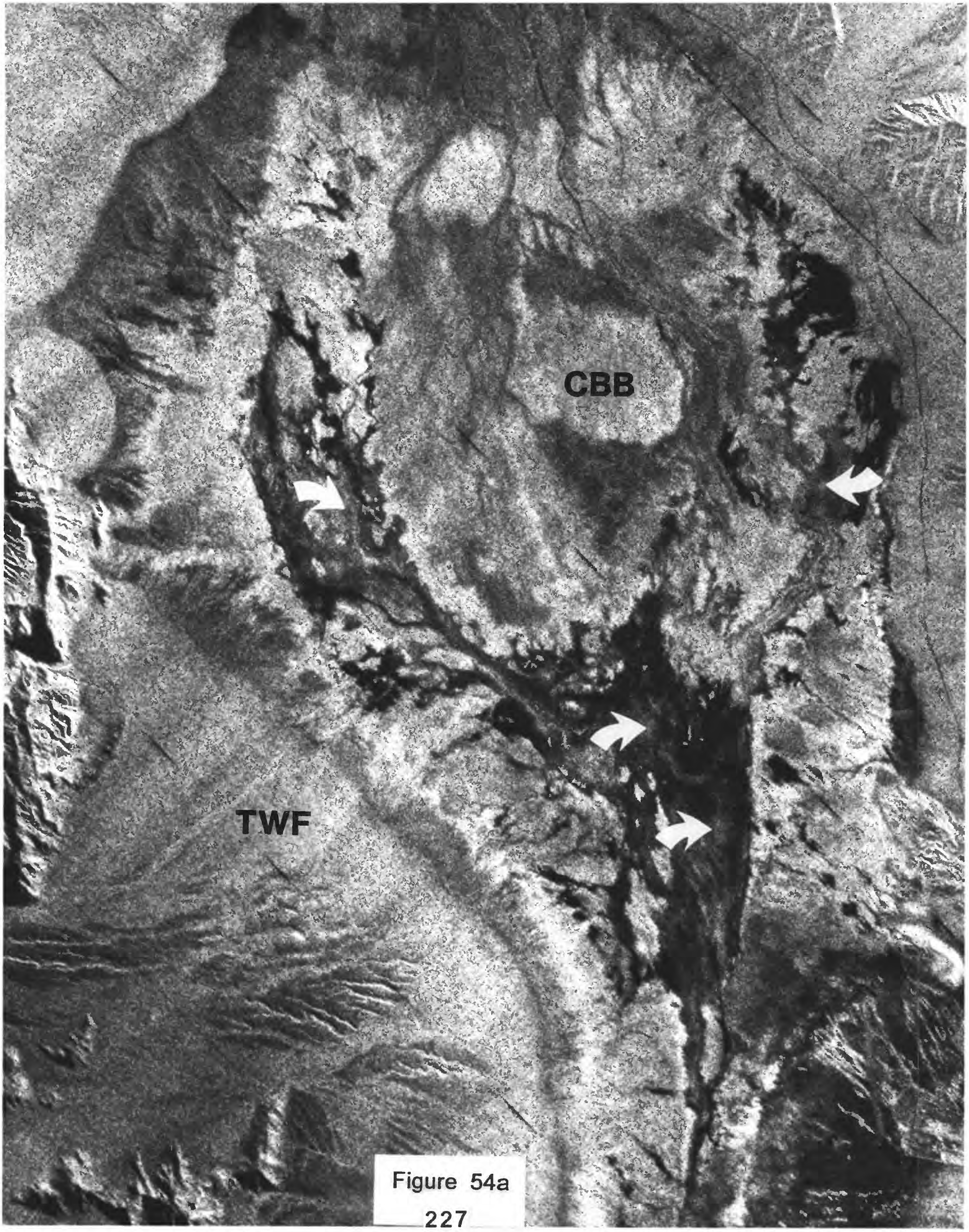

Figure 54a

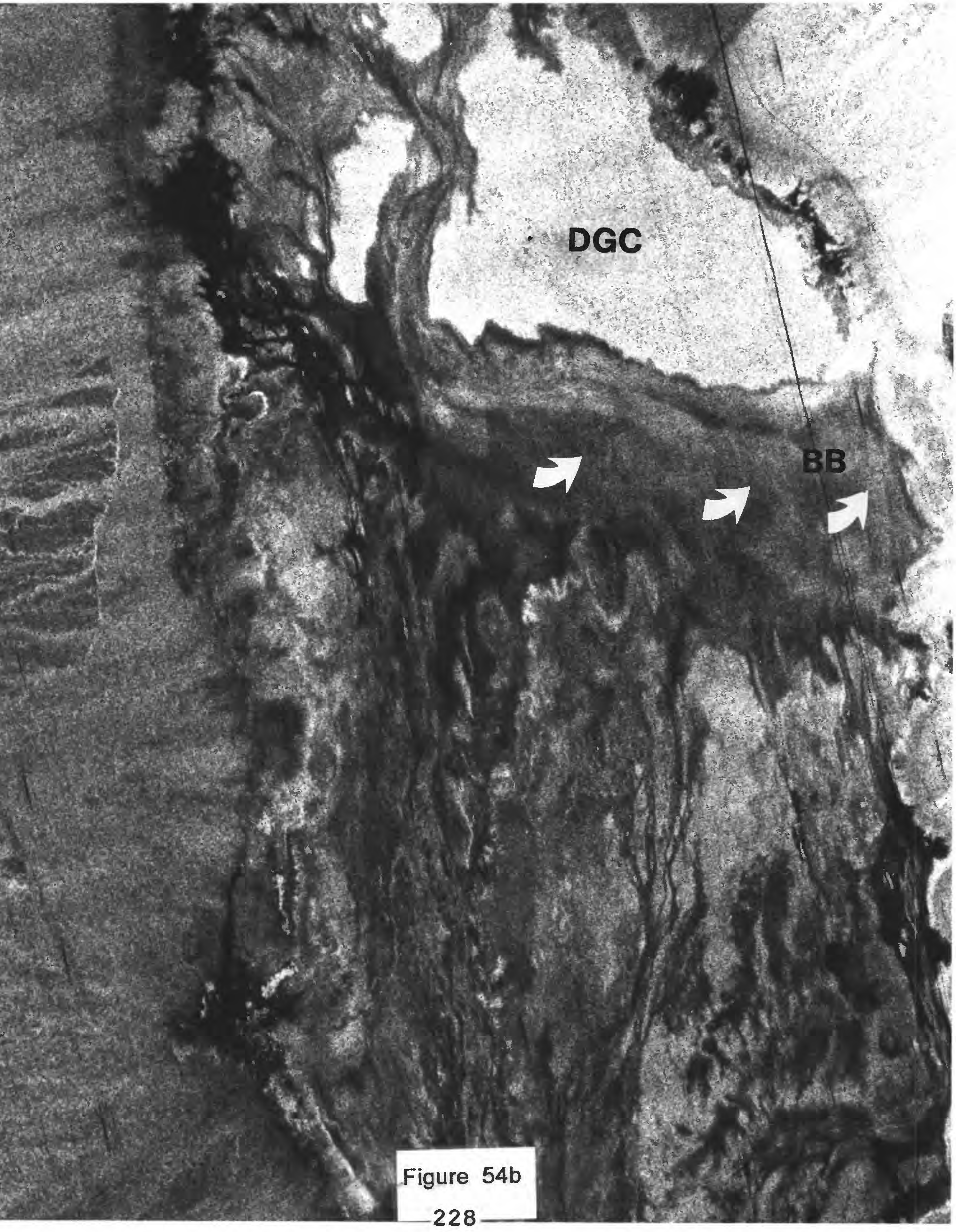

Figure 54b

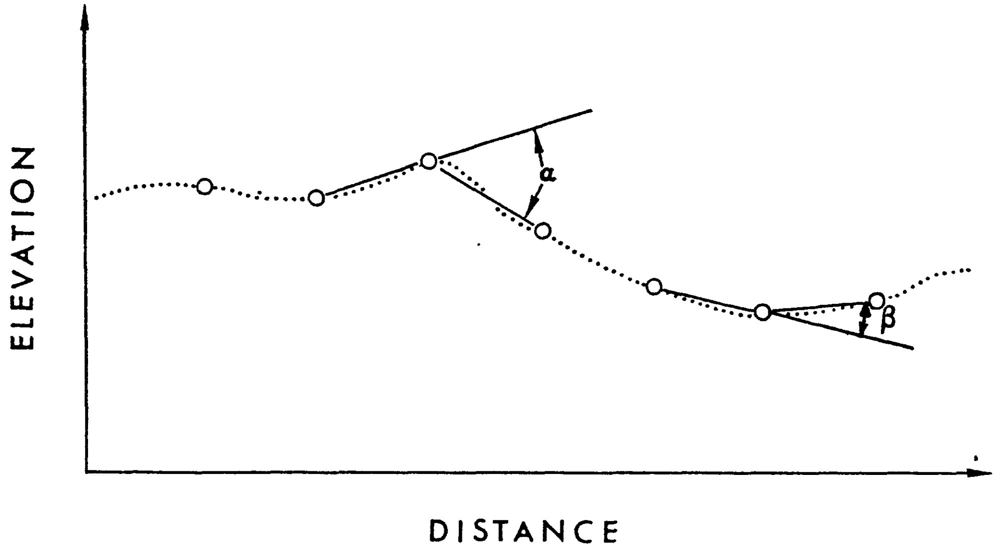

Figure A1

| TABLE 31 - | Laboratory- Measured Physical Properties | | | | | | | |
|---|---|---|---|---|---|---|---|---|
| | For Death Valley Samples * | | | | | | | |
| Station | Unit/Area | Dielectric | Properties | | Wt. % H20 | Year | | |
| | | Real Component | Imaginary Component | Resultant | (wet/dry) | | | |
| A | Qh DGC** | 2.38 | -0.41 | 2.42 | dry | 1977 | | |
| A | Qh DGC | 2.25 | -0.1 | 2.25 | dry | 1977 | | |
| B | Qhr CBB | 1.77 | 0.41 | 1.82 | 5.43 | 1977 | | |
| E | | 2.54 | 0.26 | 2.56 | 5.94 | 1977 | | |
| D | | 1.14 | 0.27 | 1.17 | 6.14 | 1977 | | |
| G | | 14.28 | -8.49 | 16.62 | 23.24 | 1977 | | |
| H | | 15.97 | -4.12 | 16.5 | 24.68 | 1977 | | |
| A | Qh DGC | 2.38 | -0.41 | 2.42 | dry | 1981 | | |
| A | Qh DGC | 2.25 | -0.1 | 2.25 | dry | 1981 | | |
| B | Qhr BWB | 3.04 | -0.26 | 3.05 | dry | 1981 | | |
| E | Qhs CBB | 2.48 | -0.32 | 2.5 | 2.03 | 1981 | | |
| E | Qhs CBB | 2.71 | -0.26 | 2.72 | 1.7 | 1981 | | |
| G | Qf CBB | 3.2 | -2.33 | 3.96 | moist | 1981 | | |
| G | Qf CBB | 3.34 | -1.27 | 3.57 | moist | 1981 | | |
| G | Qf CBB | 2.91 | -2.14 | 3.61 | moist | 1981 | | |
| G | Qf CBB | 4.45 | -2.36 | 5.04 | moist | 1981 | | |
| G | Qf CBB | 12.3 | -8.82 | 15.13 | 20.7 | 1981 | | |
| G | Qf CBB | 8.99 | -9.56 | 13.12 | 19.43 | 1981 | | |
| G | Qf CBB | 9.77 | -10.17 | 14.1 | 18.06 | 1981 | | |
| H | Qf BWB | 2.45 | -1.14 | 2.7 | 1.24 | 1981 | | |
| J | Qg3 FCF | 3.87 | -0.13 | 3.87 | 0.68 | 1981 | | |
| K | Qg3 ADF | 2.87 | -0.4 | 2.9 | 1.4 | 1981 | | |

| | | | | | | | | |
|---|---|---|---|---|---|---|---|---|
| **Table 31 Cont.** | | | | | | | | |
| *Dielectric Property Measurements by U.S. Army White Sands Missile Range Calibration Laboratory, White Sands, NM | | | | | | | | |
| (1977 measurements by H.F. Gonzalez, Secondary Standa | | | | Branch) | | | | |
| (1981 Measurements by James A. Harmon; Chief, Calibration Division Quality Assurance Office) | | | | | | | | |
| | | | | | | | | |
| The estimated uncertainty of the dielectric constant parameters measurements is within 0.5 of the indicated value | | | | | | | | |
| | | | | | | | | |
| ** | | | | | | | | |
| DGC - Devil's Golf Course | | | | | | | | |
| CBB - CottonBall Basin | | | | | | | | |
| BWB - Bad Water Basin | | | | | | | | |
| FCF - Furnace Creek Fan | | | | | | | | |
| ADF - Artist's Drive Fan | | | | | | | | |

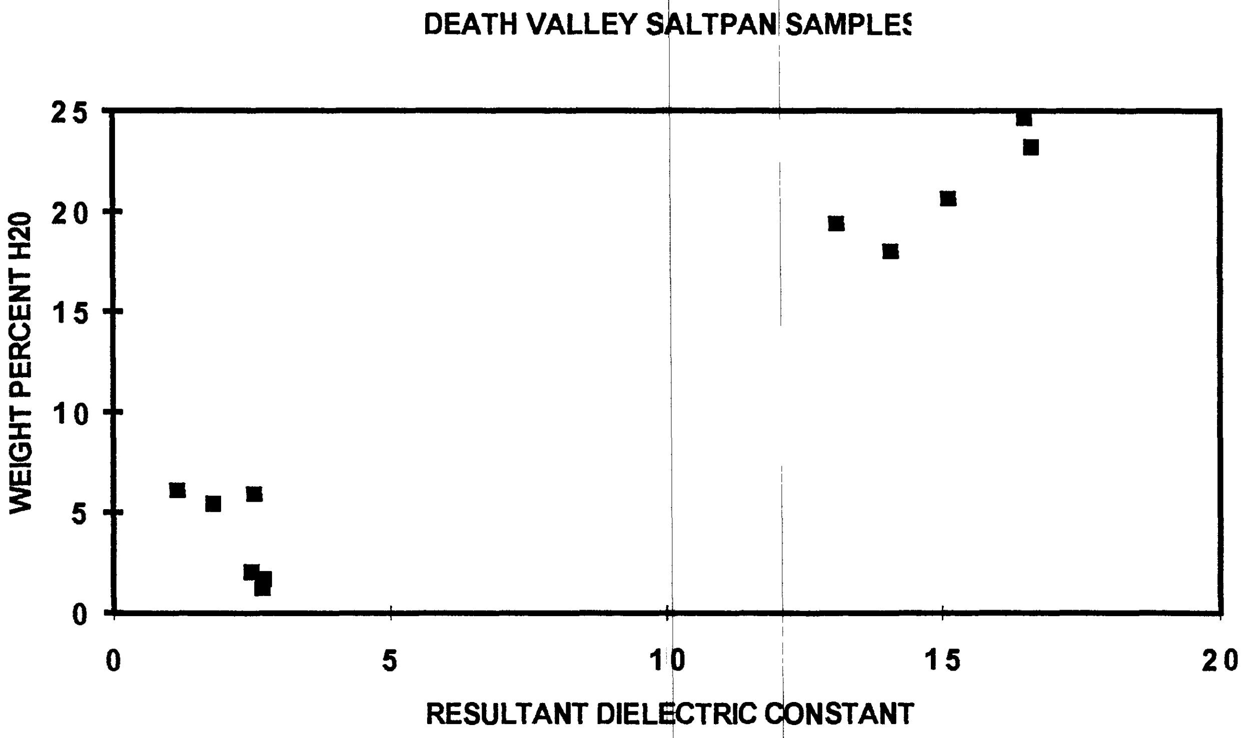
DEATH VALLEY SALTPAN SAMPLE
WEIGHT PERCENT H20
25
20
15
10
5
0
0
5
10
15
20
RESULTANT DIELECTRIC CONSTANT

Figure B1